

UNIVERSITÉ SORBONNE PARIS NORD
INSTITUT GALILÉE
LABORATOIRE DE PHYSIQUE DES LASERS

Thèse présentée par

Yanliang Guo

Pour obtenir le grade de

Docteur de l'Université Sorbonne Paris Nord

Sujet :

Annular quantum gases in a bubble-shaped trap: from equilibrium to strong rotations

A soutenir le 13 janvier 2021 devant le jury composé de :

M.	Frédéric CHEVY	Rapporteur
Mme	Donatella CASSETTARI	Rapporteuse
M.	Jean-Philippe BRANTUT	Examineur
M.	Olivier GORCEIX	Examineur
M.	Jook WALRAVEN	Examineur
M.	Laurent LONGCHAMBON	Co-Encadrant de thèse
Mme	Hélène PERRIN	Directrice de thèse

Contents

General Introduction	7
1 A Bose-Einstein condensate and its excitations	11
1.1 Bose-Einstein condensation	11
1.1.1 The ideal Bose gas	11
1.1.2 Weakly interacting BEC	13
1.1.3 Bose gases in the 2D regime or quasi-2D regime	15
1.2 Superfluid dynamics of the condensate	16
1.2.1 Hydrodynamic formulation	16
1.2.2 Bogoliubov approach for a uniform gas	18
1.2.3 Quantized vortices	20
1.2.4 Collective modes of a trapped condensate	22
2 RF-dressed adiabatic potential	25
2.1 An angular momentum coupled to an rf field	26
2.1.1 Magnetic interaction	26
2.1.2 Description of the rf field mode	27
2.1.3 Quantum description of the rf field and magnetic resonance	28
2.2 Adiabatic potentials for rf dressed atoms	32
2.2.1 Adiabatic potential	32
2.2.2 Adiabaticity condition	34
2.2.3 Local Rabi coupling	35
2.3 A dressed quadrupole trap	37
2.3.1 Principle of the bubble trap	37
2.3.2 Circular polarization	38
2.3.3 Linear polarization	40
2.3.4 Elliptical polarization	41
2.3.5 Determining the local Rabi coupling experimentally	42
3 The superfluid recipe	45
3.1 The ingredients and utensils	45
3.1.1 The cold Atom source: Rubidium 87	45

3.1.2	Laser system	46
3.2	The casseroles and the recipe: experimental sequence	47
3.2.1	2D+3D MOT	48
3.2.2	Magnetic transport	48
3.2.3	Plugged quadrupole trap	49
3.2.4	Dressed quadrupole trap: the bubble trap	50
3.3	Degustation: Imaging system	52
3.3.1	Absorption imaging	53
3.3.2	Horizontal imaging system	55
3.3.3	Vertical imaging system	56
4	A microgravity bubble trap	59
4.1	Gravity compensation mechanism	60
4.1.1	Analytical predictions	60
4.1.2	Experimental verification of the threshold	61
4.2	Detailed study of the bubble trap in microgravity	62
4.2.1	Experimental sequence	63
4.2.2	Fine alignment of the rf field parameters	64
4.2.3	Experimental results with a pure circular polarization	68
4.3	Interpretation of the results	71
4.3.1	Improved analytical model	71
4.3.2	Numerical simulation of the experiment	72
5	Superfluid flow in a ring trap	77
5.1	Theory of rotating annular superfluids	78
5.1.1	A single atom rotating in a ring trap	78
5.1.2	Phase jump and persistent flow	80
5.2	Experimental realization of an annular trap	81
5.2.1	Principle of the ring trap	81
5.2.2	Loading atoms into the ring trap	83
5.2.3	Imaging the annular gas	84
5.3	Preparation and detection of a quantized flow	86
5.3.1	Rotating the deformed bubble	86
5.3.2	A rotating laser stirrer	89
5.4	Improvement of the detection of the flow	92
5.4.1	Our strategy for magnifying the effect of the circulation	93
5.4.2	Statistics on the hole area	95
5.4.3	Splitting into singly-charged vortices	96
5.5	Conclusions	97
6	Fast rotating superfluid	99
6.1	Theory of rotating superfluids	100
6.1.1	Motivations for fast rotation	100
6.1.2	GPE solution in the rotating frame	104
6.1.3	Collective modes of a rotating trapped superfluid	106

6.2	Fast rotating superfluids in a bubble trap	111
6.2.1	Potential in the rotating frame	111
6.2.2	Experimental rotation protocol	112
6.3	Measurement of the rotation rate	114
6.3.1	Analysis of the in situ atomic density distribution	114
6.3.2	Exciting the quadrupole modes of a rotating superfluid	115
6.3.3	Analysis of the vortex density in the time-of-flight images	116
6.3.4	Size of the expanding cloud	118
6.4	A long-lived dynamical ring	120
6.4.1	Formation of the dynamical ring	120
6.4.2	Time evolution of the effective rotation frequency	121
6.5	Evidence of superfluidity	123
6.5.1	The most direct proof we are waiting for	123
6.5.2	Estimating the ring temperature	124
6.5.3	Analysis of the in situ azimuthal density profile	125
6.5.4	Properties of the dynamical ring	126
6.6	Quadrupole modes of the dynamical ring	128
6.7	Outlook	130
6.7.1	Reaching the giant vortex regime	130
6.7.2	Dissipation of the supersonic flow	131
	General conclusion	133
	Appendices	137
	A Measurement of the gradient of the quadrupole trap	139
	B Loading atoms to the equator of the compressed bubble trap	141
	Bibliography	145

General Introduction

Our colorful world is made up of particles. These particles, such as atoms and molecules, make up different substances like air, water and stones. All these substances could be separated into different states of matter, such as gas, liquid, solid. If the temperature changes, the kinetic energy of the particles and the interactions among the particles could be modified, leading to the transition between two states of matter. As we know, as the temperature decreases, the water vapor (gas) will be condensed to the water (liquid) then solidify into the ice (solid). In addition, another state of matter exists at very low temperatures, the so-called Bose-Einstein condensate. This new state of matter was predicted by Einstein in 1924 [1, 2]. In quantum mechanics, particles can be also regarded as waves whose wavelength is characterized by the temperature. The typical size of an atomic wave packet is determined by the de Broglie wavelength, $\lambda_{\text{dB}} = \sqrt{2\pi\hbar^2/Mk_{\text{B}}T}$ in which M is the atomic mass and T the temperature. Therefore, as the temperature decreases, the de Broglie wavelength becomes larger and larger. When it becomes larger than the inter-particle distance, the wave functions of the particles overlap. At that point, a macroscopic number of atoms will occupy the same quantum state, giving rise to Bose-Einstein condensation. The resulting condensate can be described by a single wave function and its evolution is governed by a nonlinear Schrödinger equation.

This theoretical prediction of the Bose-Einstein condensation was first invoked to explain the behavior of liquid helium. When cooling down liquid helium to a temperature below 2.17 K, Kapitza [3], Allen and Misener [4] observed that the viscosity suddenly dropped to zero, indicating a phase transition from normal liquid to a new state of matter, called "superfluid". One year later, London interpreted this phase transition and noticed that this temperature is very close to the critical temperature for Bose-Einstein condensation of an ideal gas with the same density, which showed that the two phenomena are related. Understanding superfluid helium was helpful to understand later the properties of a Bose-Einstein condensate. A superfluid is a frictionless liquid. It has a critical velocity above which the viscosity of the superfluid is not zero anymore [5]. The wavefunction of a superfluid can be written as $\Psi(\mathbf{r}) = \sqrt{n(\mathbf{r})}e^{i\phi(\mathbf{r})}$ where $n(\mathbf{r})$ is the atomic density and $\phi(\mathbf{r})$ the phase. The velocity of a superfluid depends on the gradient of the phase. The curl of the velocity is zero,

indicating that a superfluid is irrotational. The circulation of such an irrotational fluid must be quantized [6–9] because the phase difference after a closed loop should be an integer times 2π in order to keep the same wavefunction at a given position. As a consequence, setting a superfluid into rotation requires to introduce quantized vortices in the system.

However, the atomic density in the superfluid helium is very large, which leads to strong interactions between the atoms. As a consequence it is difficult to describe the whole system at the microscopic level. On the contrary, in a dilute gas, the density becomes lower and the interaction weaker. In this case, the Gross-Pitaevskii equation well describes the system by taking into account the interactions through a mean field theory. Since the atomic density in a dilute gas is small, the critical temperature of the phase transition is of order 100 nK, much lower than the one for liquid helium. The development of a specific technique to cool down the atoms to such a low temperature was needed.

In the 1980s, the techniques for cooling the atoms were developed rapidly, from realizing the laser cooling on ions [10,11] and neutral atoms [12] to the magnetic, optical and magneto-optical traps which enabled atoms to be both trapped and cooled [13–15]. Because of the achievements that lead to realize and understand laser cooling, magnetic trapping and magneto-optical trapping of atoms, Claude Cohen-Tannoudji, Steven Chu and William D. Phillips won the 1997 Nobel Prize in Physics [16–18]. Several years later, thanks to the evaporative cooling technique, the Bose-Einstein condensation was first carried out by the groups of Eric Cornell and Carl Wieman [19], and Wolfgang Ketterle [20]. They subsequently won the Nobel Prize in 2001 [21,22]. Since then, Bose-Einstein condensates have been produced with many atomic species, as well as condensates of molecules [23], polaritons [24] and photons [25].

Realizing Bose-Einstein condensation opened another door to the quantum world. After the first observation, the field of ultracold atoms physics progressed rapidly. Ultracold atoms system was found to be a fabulous quantum simulator to investigate various models. For example ultracold atoms trapped in an optical lattice [26], created by standing waves formed with far detuned laser beams in one or more directions, is able to mimic electrons in a solid because it can be described by a Bose-Hubbard model whose Hamiltonian is similar to the fundamental model in solid-state physics [27]. Moreover, setting a ring-shaped superfluid into rotation and generating a persistent current to study superfluid flow within wave guides [28–30] leads to the realization of an atomic analogue to a SQUID (Superconducting QUantum Interference Device) [31–33]. A SQUID is a magnetometer used for measuring very weak magnetic fields and made up of Josephson junctions in a superconducting loop. In addition, ultracold atoms were also used to simulate charged particles interacting with a magnetic field. Although neutral particles in a magnetic field do not undergo a force as the Lorentz force perpendicular to the velocity, they undergo the Coriolis force in a rotating frame, which provides a method to apply an artificial magnetic field on the Bose gas. Artificial magnetic fields were first realized by rotating the atomic gas [34,35], later by inducing Berry's phases through the application of Raman lasers [36,37], and recently by using laser-induced tunneling in superlattice potentials [38].

When superfluids are set into rotation in a harmonic potential, as the rotation rate increases, first vortices appear [34, 39], then large vortex lattices [35]. Finally, in a large rotation rate, in analogy with an electron in a strong magnetic field, atoms occupy a Lowest Landau Level [40], which is related to the Quantum Hall Effect [41]. Apart from these quantum simulations, ultracold atoms also give access to the study of supersolids in the presence of dipole-dipole long-range interaction [42, 43]; to apply the concepts of quantum optics with atoms instead of photons [44–46]; to study new quantum systems such as quantum droplets [47–49]; and to investigate the problems of high-energy physics [50].

There are several forms of potential to confine atoms, realized for example with optical traps and magnetic traps, which confine the Bose gas into the regimes of lower dimension [51]. In lower dimension, the Bose-Einstein condensation and superfluidity are not strongly related as in three dimensions. For the one-dimensional and two-dimensional homogeneous Bose gas, under the thermodynamic limit, Bose-Einstein condensation doesn't happen. But in two dimensions, it exists another phase transition between a normal gas to a superfluid which is called the Berezinskii-Kosterlitz-Thouless (BKT) transition [52, 53]. In one dimension, one finds quasi-condensate in weakly-interacting regime and fermionized bosons in strongly-interacting regime. The later is the so-called Tonks-Girardeau gases. [54, 55].

All the remarkable experiments introduced above were realized with gravity. But ultracold atoms in microgravity is also a good platform to investigate fundamental physics, such as dark matter [56], Einstein equivalence principle [57, 58], or improved atom interferometry [59, 60]. In order to achieve a microgravity environment on Earth, gravity can be compensated by a linear optical potential [61] or a magnetic field gradient [62, 63]. With the development of compact experiments, recently the European collaboration QUANTUS produced the first BEC in space in a launched rocket flying in free fall for 6 minutes [64]. In the USA, NASA has launched the Cold Atom Laboratory (CAL) to the International Space Station (ISS) [65], which is designed to produce ultracold degenerate quantum gases to investigate magnetic-lensing techniques [66], few-body dynamics and bubble-shaped gases [67].

The work presented in this thesis concerns superfluidity in annular geometry. The main experimental results can be summarized as three different rings: a levitating ring, a trapped ring and a dynamical ring. The mechanisms for forming these rings are totally different, but rely on a common bubble trap. The levitating ring is obtained in microgravity. The related study shows the full trapping potential on the surface of a bubble trap and provides a new method to compensate gravity on Earth. The trapped ring is related to a superfluid confined in a ring-shaped trap. We use different methods to make the ring-shaped superfluid rotate, which generates a quantized circulation. The dynamical ring is a long-lived supersonic superfluid whose linear velocity can reach Mach 18. It is produced by fast rotating a superfluid in the bubble trap and taking advantage of the centrifugal force. In addition, we also evidence a collective mode of such a rapidly rotating superfluid.

The manuscript is organized as follows.

First of all, in Chapter 1 and Chapter 2, we introduce the physics of Bose-Einstein

condensation and give the principle of the bubble trap which is used for all the experiments. In Chapter 3, we present the experimental setup.

- **Chapter 1:** We start with introducing Bose-Einstein condensate transition for an ideal Bose gas confined in a homogeneous or a harmonic potential. We then give the time-independent and time-dependent Gross-Pitaevskii equation to describe the ground state of the gas. We then show the size and energy of vortices which is a signature of a rotating superfluid. Finally, we present the collective modes of trapped superfluids.
- **Chapter 2:** This chapter introduces adiabatic potentials for atoms dressed by a radiofrequency (rf) field. We first give the coupling between the atomic spin and the magnetic field. Then we write the rf field both in classical and quantum way. After presenting the magnetic resonance via quantum description, we introduce the adiabatic potential and the adiabaticity condition. Finally, we give the principle of the bubble trap as well as the trapping geometry corresponding to various rf polarization.
- **Chapter 3:** The procedures of making a superfluid is described just like a cooking recipe. A recipe normally has two parts, what you need and how to proceed. I introduce the ingredients and utensils to make a superfluid, such as the atoms, the lasers, rf antennas. And then I present the ‘casseroles’ and procedures showing all the steps to obtain a superfluid. Finally, it is the tasting, presenting the way to detect the superfluid.

In the Chapters 4 to 6, we present the main results of this manuscript.

- **Chapter 4:** We introduce a new method to achieve microgravity on Earth using the special trapping geometry of the bubble trap. Realizing a microgravity bubble trap requires a perfectly circularly polarized rf field. Hence, we present a method showing how to adjust the amplitudes and the phases of the surrounding antennas to ensure a pure circular polarization. We then show a numerical simulation that we compare to the experiment results.
- **Chapter 5:** After introducing the theory about ring-shaped superfluids as well as quantized circulations, we show the principle of our ring trap. After that, we present two methods to create a circulation in the annular superfluid and compare their results.
- **Chapter 6:** For these last experiments, we again benefit from the bubble trap, and rotate superfluids at the bottom of the bubble trap. We then present several methods to determine the effective rotation rate of the superfluid. Once the rotation rate is large enough, atoms start climbing the edges of the bubble trap and gradually form a dynamical ring due to the centrifugal force. We then prove that the dynamical ring is a superfluid. After that, we investigate a collective mode of the dynamical ring and give some perspectives for the experiment.

A general conclusion closes the manuscript.

Chapter 1

A Bose-Einstein condensate and its excitations

This chapter aims at recalling some basic concepts about Bose-Einstein condensates (BEC) and superfluids. When needed, other more specific theoretical concepts will also be introduced at the beginning of the experimental chapters to explain the experimental results.

This chapter consists of two parts, the first being dedicated to the description of a BEC at rest and the second to its superfluid dynamics. I will first introduce the ideal Bose gas in the grand canonical ensemble, showing the principle of the BEC transition. I will then describe a weakly-interacting Bose gas, extending the noninteracting case to introduce the famous Gross-Pitaevskii Equation (GPE). As for the elementary excitations of a superfluid, we start by describing the hydrodynamic formulation of a superfluid, obtained from the time-dependent GPE. Finally, based on the hydrodynamic equations, we investigate the Bogoliubov spectrum, quantized vortices and collective modes.

1.1 Bose-Einstein condensation

1.1.1 The ideal Bose gas

1.1.1.1 BEC transition

At first, we consider an ideal Bose gas, meaning there are no interactions among bosons. We have N bosons of atomic mass M , assuming the system is in equilibrium at temperature T and chemical potential μ . The distribution of the particles in the different energy levels can be described by Bose-Einstein statistics. In the grand canonical ensemble, the mean occupation of the state i is written as:

$$N_i = \frac{1}{e^{(E_i - \mu)/k_B T} - 1} \quad (1.1)$$

where E_i is the energy of the state i . The total number of particles in all energy states is then:

$$N = \sum_i N_i = \sum_i \frac{1}{e^{(E_i - \mu)/k_B T} - 1}. \quad (1.2)$$

Since N_i describes the number of particles in the state i , it is supposed to be positive. As a result, the chemical potential μ should be smaller than the energy E_i of all states, including the ground state $i = 0$ of energy E_0 . Defining the zero of energy by the ground state energy such that $E_0 = 0$, we thus have:

$$\mu < E_0 = 0. \quad (1.3)$$

The total number of particles can be written as the sum of two terms, one term being the number of atoms in the ground state N_0 and the other one being the atom number in all excited states N_{exc} , such that $N = N_0 + N_{\text{exc}}$. Moreover, they can be expressed as:

$$N_0 = \frac{Z}{1 - Z}, \quad N_{\text{exc}} = \sum_{i>0} \frac{Z}{e^{E_i/k_B T} - Z}, \quad (1.4)$$

where the fugacity is $Z = \exp(\mu/k_B T)$. Since μ is negative, see (1.3), the value of the fugacity Z is between 0 and 1. Therefore, the population of the excited states has an upper bound,

$$N_{\text{exc}} < N_{\text{exc}}^{(\text{max})}(T) = \sum_{i>0} \frac{1}{e^{E_i/k_B T} - 1} \quad (1.5)$$

as soon as the sum in the right-hand side converges to a finite value $N_{\text{exc}}^{(\text{max})}(T)$. For a given temperature, the number of particles in the excited states will saturate because of this upper bound. It means that if the system at temperature T has N particles and $N > N_{\text{exc}}^{(\text{max})}(T)$, all the additional particles are in the ground state $i = 0$. For a huge number of particles, the ground state population becomes macroscopic. This is the mechanism of Bose-Einstein condensation.

1.1.1.2 The ideal Bose gas in a harmonic trap

In the previous paragraph we have discussed the principle of the BEC transition, which happens both in a box trap or a harmonic trap. In our experiment, almost experimental results are obtained through investigating the quantum gas confined in a harmonic trap, so here we will discuss the situation of an ideal Bose gas confined in a three-dimensional anisotropic harmonic trap. The potential of such a trap reads:

$$V_{\text{tr}}(x, y, z) = \frac{1}{2}M(\omega_x^2 x^2 + \omega_y^2 y^2 + \omega_z^2 z^2) \quad (1.6)$$

where ω_x , ω_y and ω_z are the trapping frequencies in the three directions. The single-particle energy can be written as:

$$E_{n_x, n_y, n_z} = \left(n_x + \frac{1}{2}\right) \hbar\omega_x + \left(n_y + \frac{1}{2}\right) \hbar\omega_y + \left(n_z + \frac{1}{2}\right) \hbar\omega_z. \quad (1.7)$$

in which $n_x, n_y,$ and n_z are three non-negative integers. Thus the lowest single-particle energy is $E_0 = \hbar(\omega_x + \omega_y + \omega_z)/2$ and the corresponding wave function in the ground state is given by [68]:

$$\phi_0(r) = \left(\frac{M\omega_{\text{ho}}}{\pi\hbar}\right)^{3/4} \exp\left[-\frac{M}{2\hbar}(\omega_x x^2 + \omega_y y^2 + \omega_z z^2)\right] \quad (1.8)$$

where $\omega_{\text{ho}} = (\omega_x\omega_y\omega_z)^{1/3}$ is the geometric mean trapping frequency. This wave function is a product of three one-dimensional Gaussian functions whose $1/\sqrt{e}$ -radii are

$$d_j = \sqrt{\hbar/(M\omega_j)}, \quad j = x, y, z \quad (1.9)$$

which is also called the harmonic oscillator length in the direction i . Under the semi-classical approximation that the temperature should be much larger than the level spacing, one can calculate the population in all excited states by using the density of states and the integral over energy instead of adding the populations in all discrete excited states. In the end, we can determine the maximal population in the excited states [69]:

$$N_{\text{exc}}^{(\text{max})}(T) = \zeta(3) \left(\frac{k_{\text{B}}T}{\hbar\omega_{\text{ho}}}\right)^3, \quad (1.10)$$

where ζ is the Riemann function and $\zeta(3) = 1.202$. The equation (1.10) shows that the maximum atom number in the excited states only depends on the temperature. We assume that at a certain temperature T_c the total atom number is the same as the saturated population, $N = N_{\text{exc}}^{\text{max}}(T_c)$. In this situation, since the number of atoms in all excited states is saturated, any additional atom will occupy the ground state. Hence, the critical temperature of an 3D ideal Bose gas trapped in a harmonic potential can be written as:

$$k_{\text{B}}T_c = \hbar\omega_{\text{ho}} \left(\frac{N}{\zeta(3)}\right)^{1/3} = 0.94\hbar\omega_{\text{ho}}N^{1/3}. \quad (1.11)$$

At a temperature T below T_c , the total atom number N is larger than $N_{\text{exc}}^{\text{max}}(T)$ and we can write $N = N_0 + N_{\text{exc}}^{\text{max}}(T)$. Dividing this equality by $N = N_{\text{exc}}^{\text{max}}(T_c)$, we can deduce the fraction of atoms in the ground state from the ratio between the temperature and the critical temperature:

$$\frac{N_0}{N} = 1 - \left(\frac{T}{T_c}\right)^3. \quad (1.12)$$

1.1.2 Weakly interacting BEC

In the previous section, we have shown that below a critical temperature a macroscopic number of particles accumulates in the single-particle ground state. However, in most experiments this picture is not correct because of the presence of interactions between atoms. When considering the interactions, we can not in principle describe the ground state of the N particles as the product of the ones of each particle. For example, taking into account repulsive interactions of a condensate at rest, the true ground state of the whole system is modified in order to reduce the density.

1.1.2.1 Gross-Pitaevskii equation

Now we consider the interactions between particles. In the low temperature regime (~ 1 mK), the kinetic energy in the relative motion of two atoms is below the centrifugal barrier potential. In this case, only isotropic, low energy binary collisions between the particles are important, corresponding to *s-wave* collisions. The interactions can be fully characterized by the scattering length a [68]. The effective interaction potential between two particles can therefore be described by a Dirac potential with only one amplitude parameter [69]:

$$V_{\text{int}}(\mathbf{r}) = g\delta(\mathbf{r}) \quad (1.13)$$

where $\delta(\mathbf{r})$ is the Dirac distribution as a function of \mathbf{r} , the relative coordinate between the two atoms and g is the interaction constant related to the scattering length. In the case of three dimensions, this interaction constant is:

$$g = \frac{4\pi\hbar^2 a}{M}. \quad (1.14)$$

If the mean distance between the particles is larger than the scattering length a , the gas is dilute and the mean field approximation is valid. The many-body problem can be simplified to a particle evolving in an effective potential composed of a trap potential $V_{\text{tr}}(\mathbf{r})$ and a mean field produced by the other $N-1$ bosons. The ground state of a dilute Bose gas thus can be described by the Gross-Pitaevskii equation (GPE). This model explains a large part of the properties observed in experiments on trapped condensed atoms, for instance, the atomic density distribution, the size of the condensate and the dynamical behavior. The time-dependent Gross-Pitaevskii equation reads [69]:

$$i\hbar\frac{\partial\psi}{\partial t}(\mathbf{r}, t) = \left(-\frac{\hbar^2\nabla^2}{2M} + V_{\text{tr}}(\mathbf{r}) + g|\psi(\mathbf{r}, t)|^2 \right) \psi(\mathbf{r}, t), \quad (1.15)$$

where $\psi(\mathbf{r}, t)$ is the single particle wave function with the normalization condition $\int |\psi(\mathbf{r}, t)|^2 d\mathbf{r} = N$. This equation takes the form of the non linear Schrödinger equation. On the right-hand side, the first term describes the kinetic energy of the condensate, the second one corresponds to the external trapping energy and the last term to the interaction energy. To get the stationary solution we can write the wave function separating time and spatial dependence:

$$\psi(\mathbf{r}, t) = \psi(\mathbf{r}) \exp\left(-i\frac{\mu}{\hbar}t\right). \quad (1.16)$$

Replacing the wave function of (1.15) into (1.16), we obtain the stationary Gross-Pitaevskii equation:

$$\mu\psi(\mathbf{r}) = \left(-\frac{\hbar^2\nabla^2}{2M} + V_{\text{tr}}(\mathbf{r}) + g|\psi(\mathbf{r})|^2 \right) \psi(\mathbf{r}). \quad (1.17)$$

This equation is time-independent, specifically describing the ground state of the system at rest.

1.1.2.2 Thomas-Fermi approximation in a harmonic trap

When the number of atoms in the ground state is very large such that $Na \gg d_j$, where d_j is the harmonic oscillator length given by Eq. (1.9), the repulsive interaction term plays a much more important role than the kinetic term in the GP equation. In this case, we can neglect the kinetic term. This is the Thomas-Fermi approximation. The time-independent GPE then becomes:

$$[V_{\text{tr}}(\mathbf{r}) + g|\psi(\mathbf{r})|^2 - \mu] \psi(\mathbf{r}) = 0. \quad (1.18)$$

The wave function is a non-zero component, which leads to the density distribution:

$$n(\mathbf{r}) = |\psi(\mathbf{r})|^2 = \frac{\mu - V_{\text{tr}}(\mathbf{r})}{g}. \quad (1.19)$$

For a gas confined in a harmonic trap, we write the external potential V_{tr} as the equation (1.6). The density distribution can then be rewritten as:

$$n(\mathbf{r}) = n(0) \left(1 - \frac{x^2}{R_x^2} - \frac{y^2}{R_y^2} - \frac{z^2}{R_z^2} \right), \quad (1.20)$$

where $n(0)$ is the density in the trap center which also corresponds to the maximum density $n(0) = \mu/g$. $R_j^2 = 2\mu/M\omega_j^2$ ($j = x, y, z$) are called Thomas-Fermi radii of the trapped condensate in j direction. In this situation, the chemical potential of the Bose gas trapped in a three-dimensional harmonic trap is given by [69]:

$$\mu = \frac{1}{2}M\omega_{\text{ho}}^2 R_{\text{ho}}^2 = \frac{\hbar\omega_{\text{ho}}}{2} \left(\frac{15Na}{d_{\text{ho}}} \right)^{2/5}, \quad (1.21)$$

where $R_{\text{ho}}^2 = 2\mu/M\omega_{\text{ho}}^2$ and $d_{\text{ho}} = \sqrt{\hbar/M\omega_{\text{ho}}}$. The atomic density distribution (1.20) shows that the density decreases to zero on the edges of the condensate. So the interactions become weaker on the edges of condensate and the kinetic term plays a more important role. In this regime, the Thomas-Fermi approximation is not valid anymore. The density profile is smoother on the edges than the simple inverted parabola given by Eq. (1.20). The size over which it happens is the healing length ξ , corresponding to the size such that bending the wave function over ξ costs an energy $\hbar^2/(2m\xi^2)$ equal to the local chemical potential $\mu = gn$. ξ is thus given by:

$$\xi = \sqrt{\frac{\hbar^2}{2M\mu}} = \frac{1}{\sqrt{8\pi an}}. \quad (1.22)$$

1.1.3 Bose gases in the 2D regime or quasi-2D regime

In Chapter 6, we will discuss an experiment in which we set an oblate condensate into rotation. In this experiment, the atomic cloud will be in the quasi-2D regime where the description of the interaction between atoms is different from the 3D case. Therefore, we will discuss the conditions for the 2D and quasi-2D regimes.

There are two criteria to reach the strictly 2D regime. Consider a oblate condensate with temperature T and chemical potential μ , confined in a harmonic trap where $\omega_z \gg \omega_r$. The first criterion is that the atoms occupy the ground state of the vertical harmonic oscillator. In other words, the energy level of the first excited state in the vertical direction should be much larger than the chemical potential and the temperature of the gas, i.e. $\hbar\omega_z > \mu, k_B T$. This prevents the atoms to reach the first excited state. In this situation, we achieve a degeneracy of the ground state in the vertical direction and the gas is in the quasi-2D regime.

The second criterion is that there is no collision occur in the vertical direction and all the collisions occur in the 2D plane. This requires that the vertical harmonic oscillator length characterizing the vertical size of the cloud is smaller than the scattering length, i.e. $d_z < a$. In this case, the atoms all stay in the vertical ground state even during collisions and the cloud is in the strict 2D regime.

In our experiment, we can satisfy the first criterion but not the second one. Our vertical trapping frequency is around 340 Hz and the harmonic oscillator length d_z (~ 600 nm) is typically a hundreds times of the scattering length a (~ 5.3 nm). However the cloud can reach the quasi-2D regime when its temperature gets below 15 nK and its chemical potential below 340 Hz. In this case the vertical motion of the atoms is frozen but the collisions between atoms are still three-dimensional. The interaction coupling constant is then different from the one for a pure 3D condensate, and given by (1.14). The new interaction constant for a quasi-2D cloud depends on the ratio of the harmonic oscillator length and the scattering length, and reads:

$$g_{2D} = \frac{\hbar^2 \sqrt{8\pi} a}{M d_z} = \frac{\hbar^2}{M} \tilde{g}. \quad (1.23)$$

It is remarkable that in two dimensions, the relevant interaction constant \tilde{g} is dimensionless in the sense that there is no characteristic length in the interaction coupling.

1.2 Superfluid dynamics of the condensate

The time-dependent behavior of a Bose–Einstein condensate is an important source of information about its physical nature. We have discussed the properties of the BEC at rest previously. Since in the following experimental chapters we will talk about the dynamics of a superfluid, for example when set into rotation, free expansion and collective modes of the superfluid, we will recall here the essential features of the dynamical behavior of the condensate.

1.2.1 Hydrodynamic formulation

Let us start by describing a condensate with the time-dependent Gross-Pitaevskii equation (1.15), which leads to the hydrodynamic equations of a superfluid. So one can deduce the continuity equation from the time-dependent GPE. If we multiply the time-dependent GPE (1.15) by $\psi^*(\mathbf{r}, t)$ and subtract the complex conjugate of the resulting equation, we find:

$$i\hbar \left(\psi^* \frac{\partial}{\partial t} \psi + \psi \frac{\partial}{\partial t} \psi^* \right) = \frac{\hbar^2}{2M} (\psi \nabla^2 \psi^* - \psi^* \nabla^2 \psi), \quad (1.24)$$

which is equivalent to:

$$\frac{\partial}{\partial t} |\psi|^2 + \nabla \cdot \left[\frac{\hbar}{2Mi} (\psi^* \nabla \psi - \psi \nabla \psi^*) \right] = 0. \quad (1.25)$$

Because $|\psi(\mathbf{r}, t)|^2 = n(\mathbf{r}, t)$, this equation can be written under the form of the continuity equation for a classical compressible fluid:

$$\frac{\partial n}{\partial t} + \nabla \cdot (n\mathbf{v}) = 0, \quad (1.26)$$

where \mathbf{v} is the velocity of the fluid, defined as:

$$\mathbf{v} = \frac{\hbar}{2Mi|\psi|^2} (\psi^* \nabla \psi - \psi \nabla \psi^*). \quad (1.27)$$

If we write the wave function in terms of the density and the phase, which reads:

$$\psi(\mathbf{r}, t) = \sqrt{n(\mathbf{r}, t)} e^{i\phi(\mathbf{r}, t)}, \quad (1.28)$$

and insert this wave function expression into equation (1.27), it leads to the expression of the local velocity of the superfluid:

$$\mathbf{v}(\mathbf{r}, t) = \frac{\hbar}{M} \nabla \phi(\mathbf{r}, t). \quad (1.29)$$

For a superfluid, equation (1.29) shows that the velocity is proportional to the gradient of the phase. Hence, the velocity potential is $-\hbar\phi/M$. We may conclude that the motion of the condensate must be irrotational, supposing the phase has no singularity, since:

$$\nabla \times \mathbf{v} = \frac{\hbar}{M} \nabla \times \nabla \phi = 0. \quad (1.30)$$

Inserting equation (1.28) into the time-dependent GPE (1.15) yields the equation describing the evolution of the phase:

$$\hbar \frac{\partial \phi}{\partial t} = \frac{1}{2} M \mathbf{v}^2 - \frac{\hbar^2}{2M\sqrt{n}} \nabla^2 (\sqrt{n}) + gn + V_{\text{tr}}. \quad (1.31)$$

It can be rewritten as the time derivative of the fluid velocity using the relation (1.29):

$$-M \frac{\partial \mathbf{v}}{\partial t} = \nabla \left(\frac{1}{2} M \mathbf{v}^2 - \frac{\hbar^2}{2M\sqrt{n}} \nabla^2 (\sqrt{n}) + gn + V_{\text{tr}} \right). \quad (1.32)$$

The interaction term ng is equivalent to the chemical potential for a uniform Bose gas, in the absence of the external potential V_{tr} . At zero temperature, changes in the chemical potential for a bulk system are related to changes in the pressure p by the Gibbs–Duhem relation $dp = nd\mu$. It is also valid for the uniform dilute Bose gas since

the equation of state reads $\mu = ng$ and $p = \partial E / \partial V = n^2 g / 2$. Therefore, the equation (1.32) can be written as [70]:

$$\frac{\partial \mathbf{v}}{\partial t} = -\frac{1}{Mn} \nabla p - \nabla \left(\frac{v^2}{2} \right) + \frac{1}{M} \nabla \frac{\hbar^2}{2M\sqrt{n}} \nabla^2(\sqrt{n}) - \frac{1}{M} \nabla V_{\text{tr}}. \quad (1.33)$$

This equation is similar to the classical Euler equation describing an inviscid flow, which reads:

$$\frac{\partial \mathbf{v}}{\partial t} - \mathbf{v} \times (\nabla \times \mathbf{v}) = -\frac{1}{Mn} \nabla p - \nabla \left(\frac{v^2}{2} \right) - \frac{1}{M} \nabla V_{\text{tr}}. \quad (1.34)$$

There are two differences after comparing the classical Euler equation (1.34) and the equation (1.33) describing a superfluid. On the left hand side, the missing part is zero for an irrotational flow, see (1.30). On the right hand side, the additional term involving \hbar corresponds to a “quantum pressure”. The combination of equations (1.26) and (1.32) is equivalent to the time-dependent Gross-Pitaevskii equation, but separating it into amplitude and phase. These hydrodynamic equations allow one to analyse the elementary excitations, compute the collective modes [71] and other dynamics of a superfluid.

1.2.2 Bogoliubov approach for a uniform gas

1.2.2.1 Bogoliubov excitation spectrum

The properties of the elementary excitations can be investigated by considering small deviations of the state of the gas from equilibrium and finding solutions of the time-dependent Gross-Pitaevskii equation. An equivalent approach is to use the hydrodynamic formulation (1.26) and (1.32) introduced above. Here we look for the excitation spectrum of a homogeneous gas, where the external potential V_{tr} is absent. The equilibrium solution corresponds to a uniform density n_0 , with $\mu = gn_0$, and a uniform phase indicating a zero velocity. Therefore, the atomic density n_0 may be taken outside the spatial derivatives. We can write perturbations away from this ground state under the form of a travelling-wave, under the form:

$$n(\mathbf{r}, t) = n_0 + n_1 e^{i(\mathbf{k} \cdot \mathbf{r} - \omega t)}, \quad v(\mathbf{r}, t) = v_1 e^{i(\mathbf{k} \cdot \mathbf{r} - \omega t)} \quad (1.35)$$

where n_1 and v_1 describe very small fluctuations of the density and a very small velocity, \mathbf{k} is the wave vector and ω the frequency of the excitation. Replacing the expressions (1.35) into the hydrodynamic equations, the continuity equation (1.26) becomes:

$$n_1 \omega = n_0 \mathbf{v}_1 \cdot \mathbf{k} \quad (1.36)$$

while the Euler equation describing a superfluid (1.32) becomes, to first order in n_1 , v_1 :

$$v_1 \omega = \frac{k}{M} \left(\frac{\hbar^2 k^2}{4M} + gn_0 \right) \frac{n_1}{n_0}. \quad (1.37)$$

Combining these two equations, we obtain the Bogoliubov dispersion relation:

$$E_k = \sqrt{\frac{\hbar^2 k^2}{2M} \left(\frac{\hbar^2 k^2}{2M} + 2gn_0 \right)} = \frac{\hbar^2 k^2}{2M} \sqrt{1 + \frac{2}{(k\xi)^2}}, \quad (1.38)$$

where E_k is the energy of an elementary excitation of the system. The spectrum is plotted on Fig. 1.1. In the low-energy limit $E_k \ll \mu$, so we have $\hbar^2 k^2/2M \ll \mu$, then

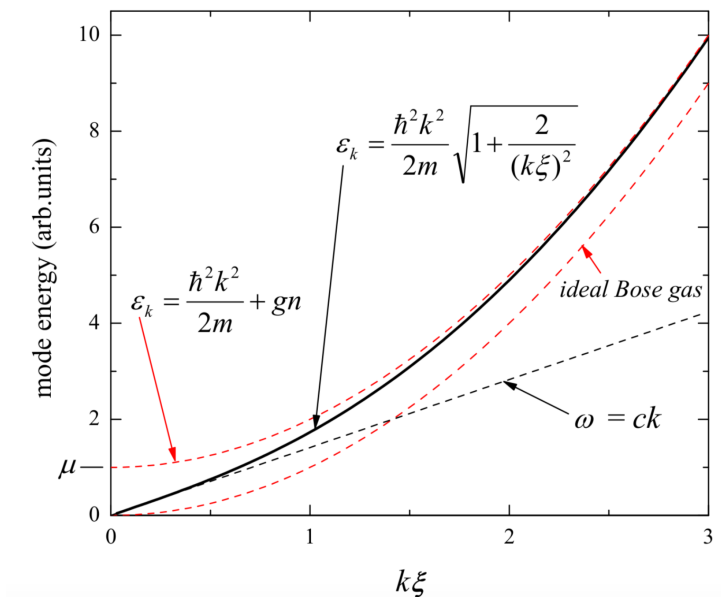


Figure 1.1 – Bogoliubov excitation spectrum plotted as a black solid line, as well as the two excitation limits: phonon regime (black dashed line) and free-particle regime (upper red dashed line). Figure taken from [72].

$k\xi \ll 1$. The dispersion relation becomes:

$$E_k \simeq \sqrt{\frac{\mu}{M}} \hbar k = c \hbar k. \quad (1.39)$$

In this equation, $c = \sqrt{\mu/M}$ is the sound velocity. This is a linear, phonon spectrum and the corresponding regime is the so-called *phonon regime*, plotted with the black dashed line on Fig.1.1.

On the other side, in the high-energy limit, $E_k \gg \mu$, we then have $\hbar^2 k^2/2M \gg \mu$ and $k\xi \gg 1$. This time we find:

$$E_k = \frac{\hbar^2 k^2}{2M} \sqrt{1 + \frac{4M\mu}{\hbar^2 k^2}} \simeq \frac{\hbar^2 k^2}{2M} + \mu. \quad (1.40)$$

This is the spectrum of free particles shifted by the chemical potential and the corresponding regime is the so-called *free-particle regime* plotted with the red dashed line. These two regimes can be also distinguished with a wavelength larger or smaller than the healing length of the condensate.

1.2.2.2 Critical velocity

We have discussed the excitation spectrum of the gas, now we will investigate how to create such an elementary excitation. Let us consider a macroscopic obstacle of a mass m going across a superfluid at rest with a velocity v . The obstacle interacts with the superfluid and may create an excitation by energy and momentum exchange. After writing and solving the conservation of momentum and energy for creating an excitation of energy E_k and momentum $\hbar k$, we find the inequality [68]:

$$v > \frac{E_k}{\hbar k}. \quad (1.41)$$

This inequality implies:

$$v \geq v_c = \min_k \left(\frac{E_k}{\hbar k} \right), \quad (1.42)$$

in which v_c takes the minimum value of the phase velocity $\omega(k)/k$ which is called the critical velocity. Equation (1.42) shows that as soon as v_c is non zero, there is a threshold on the velocity of the obstacle, below which creating this excitation is not allowed. This critical velocity for creating excitations can be deduced from the dispersion relation (1.38). From the Bogoliubov approach shown in Fig. 1.51, the curvature of the dispersion relation curve is always positive, so the minimum phase velocity is found for k close to 0. Then the critical velocity is:

$$v_c = \sqrt{\mu/M}. \quad (1.43)$$

The critical velocity is also the speed of sound c of the superfluid. The critical velocity is non zero which means that an obstacle moving slowly enough will not interact with the superfluid. In other words, it means that the viscosity for the motion of this obstacle is strictly zero, which is also the definition of superfluidity as expressed by Landau [73].

1.2.3 Quantized vortices

In the last section we investigated the elementary excitations by the Bogoliubov approach. However, it is limited since it only considers the excitations with small density fluctuations and small velocities. It misses important excitations such as vortices, which can not be described by Bogoliubov approach because of their large density fluctuations.

In the following experimental chapters, we will deal with a single vortex, a multiply charged vortex and vortex lattice. Here we will introduce the main features of vortices in superfluids. From equation (1.30), one can deduce that the superfluid is irrotational if the phase is not singular. In this case, the circulation of the velocity field around any closed path has to be zero.

Nevertheless, a zero density domain marks a phase singularity where the phase is not defined, around which the velocity field circulation can be nonzero. Vortices are the natural way to realize this situation in a superfluid. The picture of a vortex is like a tornado where the wind rotates around a vortex line of zero density. Around this

domain, to ensure that the wavefunction is uniquely defined, the variation of the phase ϕ has to be an integer times 2π . This leads to a non zero quantized circulation Γ , as noted by Onsager and Feynman [6, 74]:

$$\Gamma = \oint_C \mathbf{v}(\mathbf{r}, t) \cdot d\mathbf{l} = \oint_C \frac{\hbar}{M} \nabla \phi(\mathbf{r}, t) \cdot d\mathbf{l} = \frac{\hbar}{M} (\phi_{\text{end}} - \phi_{\text{start}}) = \ell \times 2\pi \frac{\hbar}{M} = \ell \frac{h}{M}, \ell \in \mathbb{Z}. \quad (1.44)$$

ℓ is the integer called the winding number and h/M is the unit of quantized circulation.

At first, we consider a singly charge vortex with $\ell = 1$ in an uniform disk-shaped 2D gas whose density is n_0 and radius R , assuming the potential is $V_{\text{tr}}(r) = 0$ for $r < R$. Hence, the azimuthal superfluid flow around the vortex is given by:

$$v_r = \frac{\hbar}{M} \nabla \phi = \frac{\hbar}{M} \frac{2\pi}{2\pi r} = \frac{\hbar}{Mr}. \quad (1.45)$$

This equation shows that the superfluid velocity diverges in the center, which is impossible. Therefore, the density in the center of the vortex must vanish. This happens when the local velocity \hbar/Mr reaches $c = \sqrt{\mu/m}$, i.e. for $r = \sqrt{2}\xi$. The numerical solution of the Gross-Pitaevskii equation is shown in Fig 1.2 and confirms this expectation.

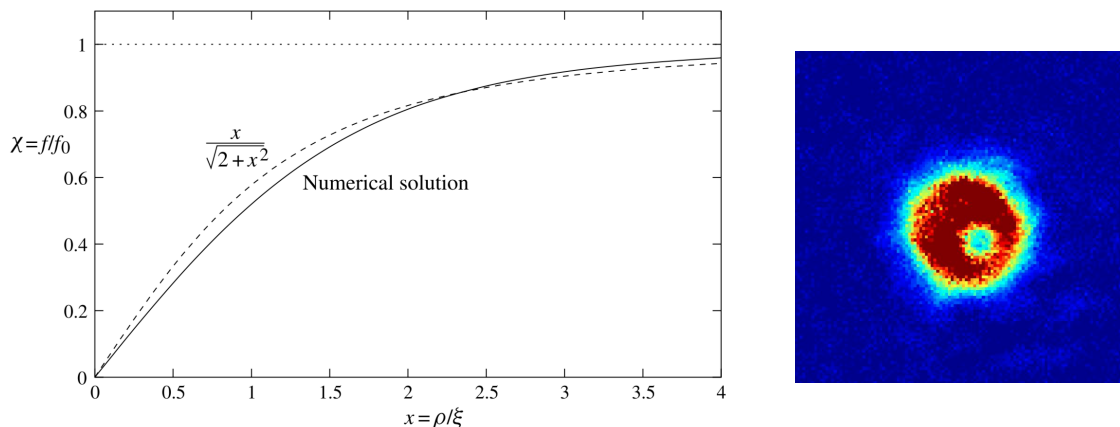


Figure 1.2 – Left: The condensate wave function for a singly quantized vortex as a function of radius. In the picture, the vertical axis represents the modulus f of the wave function with $f^2 = n$ and $f_0^2 = n_0$. The horizontal axis represents the ratio between the radius and the healing length. The numerical solution is given by the full line and the approximate function $x/(2+x^2)^{1/2}$ is plotted by the dashed line [70]. Right: experimental picture of a singly charged vortex in a dilute BEC. The size of the image is $120 \times 120 \mu\text{m}$

The energy of a singly charged vortex in such a condensate of radius R is dominated by the kinetic energy of the superflow. So the energy per unit length of the vortex is

written as:

$$E_1 = \int_{\xi}^R n_0 \frac{1}{2} m \left(\frac{\hbar}{mr} \right)^2 2\pi r dr = \pi n_0 \frac{\hbar^2}{m} \ln \left(\frac{R}{\xi} \right). \quad (1.46)$$

This equation give the energy of a singly charged vortex with $\ell = 1$. Vortices with larger quantum circulation can also exist. Thus for a larger quantized circulation $\ell > 1$, there may be many singly charged vortices or a multiply charged vortex. For the case of a multiply charged vortex, the fluid velocity at large distance from the center of the vortex is $\ell\hbar/Mr$. And the core size for a multiplied charged vortex with ℓ quanta is roughly $|\ell|\xi$ since ℓ could be negative. Therefore, in the absence of the external potential, the kinetic energy for a vortex with charge ℓ associated with the azimuthal motion is given by:

$$E_{\ell} = \ell^2 \pi n_0 \frac{\hbar^2}{m} \ln \left(\frac{R}{|\ell|\xi} \right) = \ell^2 E_1 - \ell^2 \pi n_0 \frac{\hbar^2}{m} \ln |\ell| \simeq \ell^2 E_1. \quad (1.47)$$

The last approximation holds if $R \gg \xi$ and ℓ is a few units. For the same total circulation, equation (1.47) shows that the energy of a single vortex with a multiple charge $\ell^2 E_1$ is larger than the one of a collection of ℓ well separated singly charged vortices ℓE_1 as soon as $|\ell| > 1$. It means that separated singly charged vortices is energetically favorable for excitations. An experimental observation showing that a multiply charged vortex splits into several singly charged vortices will be presented in Chapter 5. Once a superfluid is set into rotation, it forms eventually a vortex lattice, shown in Fig.1.3. As the rotation frequency of a superfluid is increased, the size of the cloud increases due to the centrifugal force.

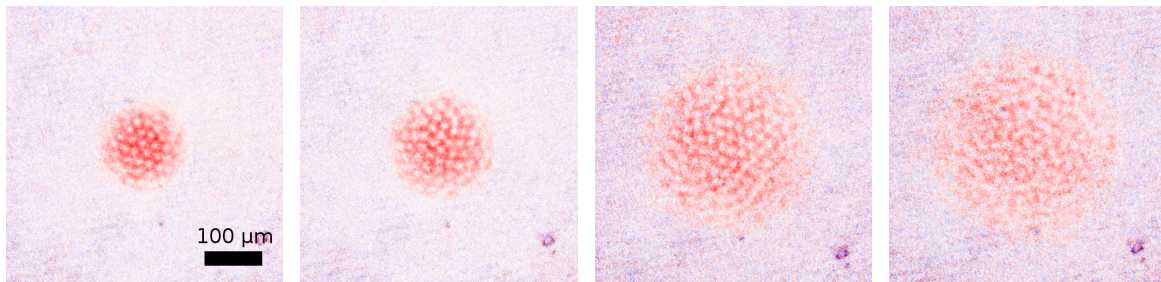


Figure 1.3 — Images of vortex lattices in BECs rotating at different rotation rates Ω . From left to right, the rotation frequency is: 24, 25, 27, 28 Hz while the harmonic trapping frequency is around 34 Hz. Each vortex is singly charged.

1.2.4 Collective modes of a trapped condensate

We consider now the case of a condensate confined in a harmonic trap with cylindrical symmetry, with vertical trapping frequency ω_z and radial frequency ω_r . From the hydrodynamic equations (1.26) and (1.32), one can also deduce the small amplitude oscillations of a trapped condensate, referring to its eigenmodes of oscillation.

Investigating these modes can give a profound insight into the dynamical behavior of the condensate [75–78]. In our experimental conditions, the trapped condensate is highly deformed as a disk shape because the vertical trapping frequency is much larger than the radial trapping frequency, $\omega_z \gg \omega_r$. The condensate can be both 3D or quasi-2D, which depends on the chemical potential.

1.2.4.1 Collective modes of a 3D oblate condensate

Consider a disk-shaped 3D condensate trapped in a cylindrical symmetric trap, under the condition of $\mu \gg \hbar\omega_z \gg \hbar\omega_r$. This system can be described with the hydrodynamic equations which are equivalent to the time-dependent GPE (1.15). For a large number of atoms, the contribution of the kinetic term becomes less important. Consequently, we can neglect the quantum pressure caused from the kinetic energy, which is the hydrodynamic approximation.

In order to determine these in-plane low-energy collective modes, one can linearize the hydrodynamic equations by computing the effect of small variations $\delta n(\mathbf{r}, t)$ of the atomic density around the ground-state solutions $n(\mathbf{r})$ described by the Thomas-Fermi profile. It leads to the dispersion relation of the eigenmodes [79]:

$$\omega^2 = \omega_r^2 \left(\frac{4}{3}n^2 + \frac{4}{3}nm + 2n + m \right) \quad (1.48)$$

in which n and m are two quantum numbers: n gives the number of radial nodes, and m corresponds to the z-axis projection of the angular momentum. A few examples of these modes are shown on figure 1.4.

The surface modes are the modes which have no radial node, such that $n = 0$. The case ($n = 0, m = \pm 1$) corresponds to the two radial dipole excitations with a frequency equal to the trapping frequency $\omega = \omega_r$. The dipole modes also exist in a classical gas, and correspond to the oscillation of the center of mass. Thus, we can not use the dipole mode to distinguish a classical gas from a quantum gas.

The next mode, with ($n = 0, m = 2$), is called the quadrupole mode. This mode is also a surface mode. For a non-rotating superfluid, the quadrupole mode consists in an out-of-phase oscillation of the cloud radii. The mode frequency is given by:

$$\omega_Q^{3D} = \sqrt{2}\omega_r. \quad (1.49)$$

The quadrupole mode exists only for superfluids. Therefore, we can excite such a mode to distinguish if a cloud is a superfluid or a thermal gas. In Chapter 6, we will concentrate on the quadrupole mode of a rotating or non-rotating superfluid in detail.

There is another mode corresponding to ($n = 1, m = 0$), called the monopole mode or breathing mode. This mode is not a surface mode since it has a non zero radial node number. This mode exhibits an oscillation of the cloud radius, hence the denomination of breathing mode. The oscillation frequency of the monopole mode is:

$$\omega_M^{3D} = \sqrt{\frac{10}{3}}\omega_r. \quad (1.50)$$

The mode oscillation modifies the peak atomic density. For this reason, the monopole mode can be used to infer the equation of state $\mu(n)$ [77, 80].

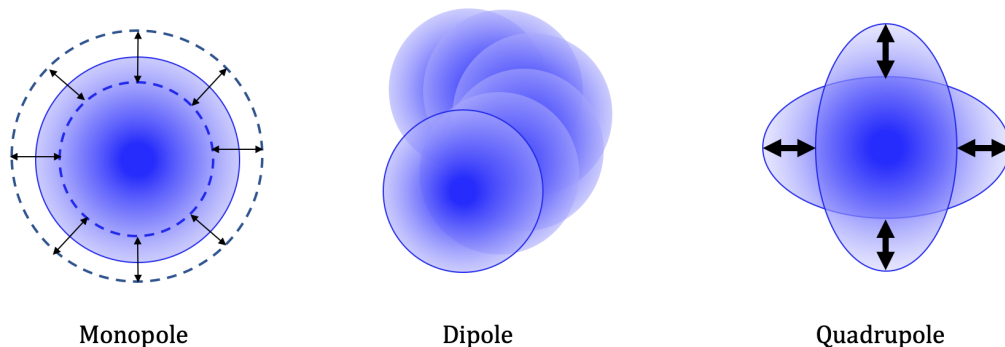


Figure 1.4 – Illustrations of some collective modes in a condensate. From left to right: the monopole mode also called breathing mode ($n = 1, m = 0$), the dipole modes ($n = 0, m = \pm 1$) and the quadrupole modes ($n = 0, m = \pm 2$).

1.2.4.2 Collective modes of a quasi-2D condensate

In the case of the quasi-2D regime, under the condition of $\hbar\omega_z \gg \mu - \frac{1}{2}\hbar\omega_z \gg \hbar\omega_r$, the dispersion relation is different. In the quasi-2D regime, the Thomas-Fermi approximation is not valid in the vertical direction. The in-plane collective modes are similar but their frequencies are not exactly the same [77, 79]. Solving the hydrodynamic equations gives the dispersion relation of a quasi-2D gas:

$$\omega^2 = \omega_r^2 (2n^2 + 2nm + 2n + m). \quad (1.51)$$

The dipole mode frequency is not affected and the frequency of the quadrupole mode in quasi-2D regime is :

$$\omega_Q^{2D} = \sqrt{2}\omega_r. \quad (1.52)$$

In contrast, the monopole frequency in the quasi-2D regime is different from the one in the 3D regime, and reads:

$$\omega_M^{2D} = 2\omega_r. \quad (1.53)$$

This prediction for the monopole frequency is the same as in the strict 2D regime. As a result of the difference between ω_M^{2D} and ω_M^{3D} , exciting the monopole mode and measuring its oscillation frequency can be used to determine if the cloud is in quasi-2D or 3D regime [77].

In this section, we have discussed the collective excitations of a trapped condensate initially at rest. The collective modes of a rotating condensate are also worth studying. In particular, the quadrupole modes of a superfluid can be used as a probe to measure the angular momentum as well as its rotation rate [81, 82]. The details of the collective modes of a rotating condensate will be discussed in Chapter 6.

Chapter 2

RF-dressed adiabatic potential

In our experiment, the most essential tool is the radiofrequency-dressed (rf-dressed) adiabatic potential to trap atoms. Compared to optical potentials, the rf-dressed potential provides a very smooth potential as it avoids the interference and diffraction effects. Using the combination of rf radiation and static magnetic field to produce trapping potentials was firstly investigated in 2001 by O. Zobay and B.M. Garraway [83]. The first experimental realization of rf-dressed trap was achieved in 2003 [84, 85]. In addition, this method was also used to generate a double well potential [86], a ring-shaped trap by combining it with an optical potential [87, 88], lattice potential [89] and time-averaged potentials [90, 91]. In our group it has been used to investigate 2D superfluids [92] and their collective modes [77, 78, 93]. Recently, a supersonic rotating superfluid was achieved and studied in such a trap taking advantage of its specific geometry [94], which will be discussed in detail in Chapter 6.

In this chapter, we will examine the theory of rf-dressed potentials. We start in Sec. 2.1 by describing the interaction of an atomic magnetic dipole moment with an external magnetic field. Then we give the energy level structure of the {rf + atom} quantum system after adding a quantum rf magnetic field, both for the uncoupled states and the dressed states. Having established the theory of dressed states, we discuss in Sec. 2.2 the adiabatic potentials and the adiabaticity condition. We then give the expression of the local Rabi coupling between the atoms and the rf field. In Sec. 2.3, I present the specific case of our experiment, a quadrupole magnetic field dressed by an rf field, resulting in a bubble-shaped trap. I describe the geometry and properties of the bubble trap with different polarisations of the rf-field. Finally, I will introduce the method used to measure the local Rabi coupling experimentally. A significant part of this chapter relies on the Review of H el ene Perrin and Barry Garraway [95], which can provide a more detailed description and discussion.

2.1 An angular momentum coupled to an rf field

An atomic spin can couple to a magnetic field, both static and oscillating, which is the basic principle of the rf-dressed potential. In this section we will examine the magnetic interaction between the atomic spin and the magnetic field.

2.1.1 Magnetic interaction

We start by explaining the way of trapping atoms with an inhomogeneous static magnetic field. We thus consider an atom with an hyperfine structure evolving in such a static magnetic field $\mathbf{B}_0(\mathbf{r})$ whose orientation is position-dependent. Let us consider for the moment that the atomic position is fixed at point \mathbf{r} . We define the direction \mathbf{e}_z as the orientation of the local magnetic field, such that the field writes $\mathbf{B}_0(\mathbf{r}) = B_0(\mathbf{r})\mathbf{e}_z$. The quantisation axis \mathbf{e}_z follows the direction of the magnetic field, which is position-dependent. The total angular momentum is F which is composed of the nuclear spin I , the electronic spin S and the orbital angular momentum L . The total angular momentum operator is noted $\hat{\mathbf{F}}$ and its projection on the quantisation axis \hat{F}_z . $\hat{\mathbf{F}}^2$ and \hat{F}_z commute, so there exists a common basis in which both $\hat{\mathbf{F}}^2$ and \hat{F}_z are diagonal. In such a basis, the spin eigenstates are noted $|F, m_F\rangle$. The eigenvalues are written as:

$$\hat{\mathbf{F}}^2|F, m_F\rangle = F(F+1)\hbar^2|F, m_F\rangle, \quad (2.1)$$

$$\hat{F}_z|F, m_F\rangle = m_F\hbar|F, m_F\rangle, \quad (2.2)$$

in which $m_F\hbar$ is the projection of the spin onto the z axis and $m_F \in \{-F, -F+1, \dots, F-1, F\}$. After introducing these spin operators, the Hamiltonian of the magnetic interaction between the atomic spin and the static field can be described as:

$$\hat{H}_0 = \frac{g_F\mu_B}{\hbar}\mathbf{B}_0 \cdot \hat{\mathbf{F}} = \frac{g_F\mu_B}{\hbar}B_0(\mathbf{r})\hat{F}_z \quad (2.3)$$

where g_F is the Landé factor of the atomic hyperfine state and μ_B the Bohr magneton. Therefore, the eigenenergy of each Zeeman magnetic sub level $|F, m_F\rangle_z$ is found through:

$$\frac{g_F\mu_B}{\hbar}B_0(\mathbf{r})\hat{F}_z|F, m_F\rangle_z = m_Fg_F\mu_B B_0(\mathbf{r})|F, m_F\rangle_z \quad (2.4)$$

which leads to the eigenenergy:

$$E_{m_F} = m_Fg_F\mu_B B_0(\mathbf{r}). \quad (2.5)$$

In this equation, the eigenenergy E_{m_F} could have different sign because m_F and g_F can be both positive or negative. Thus this energy will be positive if $m_Fg_F > 0$, while its absolute value depends on the local magnetic field $B_0(\mathbf{r})$. We note the sign of the Landé factor g_F as s :

$$s = \frac{g_F}{|g_F|} = \pm 1. \quad (2.6)$$

Now let us assume that the atom can move, such that its position \mathbf{r} varies with time. If the atomic velocity is small enough such that the adiabaticity condition is

verified [96], equation (2.5) will still hold as the atom moves and will lead to an effective potential. In the situation where $s = -1$ as it is the case for $F = 1$ ground state of ^{87}Rb , the state $|m_F\rangle$ with $m_F < 0$ making the eigenenergy positive leads to a force attracting the atom towards the regions of weaker field. In this situation, the state $|m_F\rangle$ is called a low-field seeking state. Meanwhile, the m_F state making the eigenenergy negative is high-field seeking states.

The discussion above is the basic principle of trapping an atom in a inhomogenous magnetic field. Trapping the atom in the minimum or maximum of the magnetic field depends on the sign of $m_F g_F$. However, Wing's theorem shows that a static magnetic field cannot have a maximum in free space [97]. Hence it is necessary to trap atoms in a low-field seeking state around a minimum of magnetic field. The eigenenergy can also be written as $E_{m_F} = sm_F \hbar \omega_0$, describing the energy of the trappable Zeeman sublevels with $sm_F > 0$. ω_0 is the Larmor frequency, given by:

$$\omega_0 = \frac{|g_F| \mu_B B_0}{\hbar}, \quad (2.7)$$

which describes the frequency spacing between Zeeman sublevels.

2.1.2 Description of the rf field mode

Before introducing the interaction between the atoms and the quantized rf field, we need to properly define the classical modes of the rf field that will be populated with photons. The atoms are placed in a static magnetic field, taken uniform in this section, and an oscillating rf field. The orientation of the static magnetic field defines the z axis, it is written as $\mathbf{B}_0 = B_0 \mathbf{e}_z$. The arbitrary rf magnetic field is given in the classical limit by:

$$\mathbf{B}(t) = B_x \cos(\omega t + \phi_x) \mathbf{e}_x + B_y \cos(\omega t + \phi_y) \mathbf{e}_y + B_z \cos(\omega t + \phi_z) \mathbf{e}_z \quad (2.8)$$

in which ω is the rf frequency. Since describing the rf field and the polarization with the complex notation is more convenient, the rf field can be written as $\mathbf{B}_1(t) = \mathcal{B}_1 e^{-i\omega t} + c.c$ where \mathcal{B}_1 is the complex amplitude, written as:

$$\mathcal{B}_1 = \frac{B_x}{2} e^{-i\phi_x} \mathbf{e}_x + \frac{B_y}{2} e^{-i\phi_y} \mathbf{e}_y + \frac{B_z}{2} e^{-i\phi_z} \mathbf{e}_z. \quad (2.9)$$

This defines the mode in which photons are created when we use a quantum description of the rf field. The complex amplitude can also be described with the complex polarization of the field $\boldsymbol{\epsilon}$ whose norm is 1, which reads $\mathcal{B}_1 = B_1 \boldsymbol{\epsilon}$. Instead of decomposing the rf polarization in the orthogonal basis $(\mathbf{e}_x, \mathbf{e}_y, \mathbf{e}_z)$, we write it in the spherical basis $(\mathbf{e}_+, \mathbf{e}_-, \mathbf{e}_0)$. The change between these two bases uses:

$$\mathbf{e}_+ = -\frac{1}{\sqrt{2}}(\mathbf{e}_x + i\mathbf{e}_y), \quad \mathbf{e}_- = \frac{1}{\sqrt{2}}(\mathbf{e}_x - i\mathbf{e}_y), \quad \mathbf{e}_0 = \mathbf{e}_z. \quad (2.10)$$

Since the component along the z direction of the rf field B_z is aligned with the static magnetic field $B_0 \mathbf{e}_z$ with $B_z \ll B_0$, we can neglect the effect of this component [98, 99].

So we only consider the components in the $x - y$ plane and the complex amplitude of the rf field reads $\mathcal{B}_{1\perp} = B_+ \mathbf{e}_+ + B_- \mathbf{e}_-$. Therefore, in the spherical basis, the rf magnetic field can be rewritten as

$$\mathbf{B}_{1\perp}(t) = (B_+ \mathbf{e}_+ + B_- \mathbf{e}_-) e^{-i\omega t} + c.c., \quad (2.11)$$

where B_+ and B_- are the complex projections, given by:

$$B_{\pm} = \mathbf{e}_{\pm}^* \cdot \boldsymbol{\epsilon} B_1 = \frac{1}{2\sqrt{2}} (\mp B_x e^{-i\phi_x} + i B_y e^{-i\phi_y}). \quad (2.12)$$

The projections of the spin operator in the spherical basis are:

$$\hat{\mathbf{F}} \cdot \mathbf{e}_{\pm} = \mp \frac{1}{\sqrt{2}} \hat{F}_{\pm}, \quad (2.13)$$

where \hat{F}_+ and \hat{F}_- are the raising and lowering operators defined as $\hat{F}_{\pm} = \hat{F}_x \pm i\hat{F}_y$. The classical amplitudes B_{\pm} of the rf field in the spherical basis will be used to determine the local Rabi coupling in the following of this chapter.

2.1.3 Quantum description of the rf field and magnetic resonance

Let us consider now the interaction of an atom with the rf field introduced in the last section. In order to understand this interaction better, we describe the rf field in a quantum way with the field operator $\hat{\mathbf{B}}_1$ and give the energy level of the {rf+atom} quantum system, thus introducing the dressed atom picture. During the process of the interaction, the spontaneous emission is absent since the relevant states are the ground state Zeeman sublevels. In this section, we assume that the static magnetic field is uniform $\mathbf{B}_0(\mathbf{r}) = B_0 \mathbf{e}_z$, such that we will not consider the atomic external motion for now. The Hamiltonian then is given by:

$$\hat{H} = \hat{H}_0 + \hat{H}_{\text{rf}} + \hat{V}_1, \quad (2.14)$$

which is composed of three terms. From left to right, the first term \hat{H}_0 , already mentioned at equation (2.3), corresponds to the energy of the atom without the rf field; the second term \hat{H}_{rf} is the Hamiltonian of the quantum rf field; and the third term $\hat{V}_1 = (g_F \mu_B / \hbar) \hat{\mathbf{B}}_1 \cdot \hat{\mathbf{F}}$ is the atom-field coupling.

In our experiment, we use ^{87}Rb as atomic source. For a ^{87}Rb atom evolving in a magnetic field, its ground state is defined as the lowest hyperfine state $F = 1$ with $g_F = -1/2$ (see Chapter 3). So in the following discussion, we take the sign to be negative $s = -1$ and the low-field seeking state is $|m_F = -1\rangle$.

The eigenstates of \hat{H}_0 are the Zeeman states $|m_F\rangle$ with associated eigenenergies $E_{m_F} = -m_F \hbar \omega_0$. The Hamiltonian can be also written as:

$$\hat{H}_0 = -\omega_0 \hat{F}_z. \quad (2.15)$$

The second term describes the energy of the quantized rf field of frequency ω , the corresponding Hamiltonian is written as:

$$\hat{H}_{\text{rf}} = \hbar\omega(\hat{a}^\dagger\hat{a} + \frac{1}{2}) \quad (2.16)$$

in which \hat{a}^\dagger and \hat{a} are the creation and annihilation operators for the rf photons in the field mode. The rf frequency ω is chosen close to the Larmor frequency ω_0 , such that $|\delta| \ll \omega$ where $\delta = \omega - \omega_0$ is the detuning. The eigenstates of the Hamiltonian \hat{H}_{rf} are the Fock states $|N\rangle$ indexed by the number of photons N :

$$\hat{H}_{\text{rf}}|N\rangle = \hbar\omega(N + \frac{1}{2})|N\rangle. \quad (2.17)$$

We assume that the rf field is in a coherent state of large amplitude, in a mode polarized in the x-y plane orthogonal to the static field $\hat{\mathbf{B}}_0$ and with an average amplitude $\langle\hat{\mathbf{B}}_1\rangle = B_+\mathbf{e}_+ + B_-\mathbf{e}_-$ where $(\mathbf{e}_+, \mathbf{e}_-, \mathbf{e}_0)$ is the spherical basis for the rf polarization, presented in equation (2.10). Since the mean photon number $\langle N\rangle$ in this large coherent state is much larger than 1, $N \pm 1 \simeq N \simeq \langle N\rangle$ and the effect of \hat{a}^\dagger and \hat{a} on the state $|N\rangle$ can be approximately written as:

$$\hat{a}|N\rangle \simeq \sqrt{\langle N\rangle}|N-1\rangle \quad (2.18)$$

$$\hat{a}^\dagger|N\rangle \simeq \sqrt{\langle N\rangle}|N+1\rangle. \quad (2.19)$$

The third term in the Hamiltonian (2.14) is the interaction between the atom and rf field. The rf magnetic field operator can be written as:

$$\hat{\mathbf{B}}_1 = \left(\frac{B_+\mathbf{e}_+}{\sqrt{\langle N\rangle}} + \frac{B_-\mathbf{e}_-}{\sqrt{\langle N\rangle}} \right) \hat{a} + h.c. \quad (2.20)$$

Thus the coupling operator can be described as:

$$\hat{V}_1 = \frac{g_F\mu_B}{\hbar}\hat{\mathbf{B}}_1 \cdot \hat{\mathbf{F}} = \frac{g_F\mu_B}{\hbar\sqrt{\langle 2N\rangle}}(-B_+\hat{a}\hat{F}_+ + B_-\hat{a}^\dagger\hat{F}_-) + h.c. \quad (2.21)$$

In the end, this operator is given by [95]:

$$\hat{V}_1 = \frac{-1}{2\sqrt{\langle N\rangle}} \left[\Omega_-\hat{a}\hat{F}_- + \Omega_-^*\hat{a}^\dagger\hat{F}_+ + \Omega_+\hat{a}\hat{F}_+ + \Omega_+^*\hat{a}^\dagger\hat{F}_- \right], \quad (2.22)$$

where Ω_\pm is the coupling amplitude defined as:

$$\Omega_\pm = \pm\sqrt{2}\frac{g_F\mu_B}{\hbar}B_\pm. \quad (2.23)$$

2.1.3.1 Uncoupled states

Now let us consider the situation of no interaction, which means that the coupling between the atomic spin and the rf field is zero, namely $\Omega_\pm = 0$. Therefore, in the

absence of coupling, the eigenstates of the system can be described as the tensor products of the Zeeman substates $|F = 1, m_F\rangle$ of the atom and the Fock states $|N\rangle$ of the rf field, also noted as $|m_F, N\rangle$. The eigenenergies are then given by:

$$(\hat{H}_0 + \hat{H}_{\text{rf}})|m_F, N\rangle = (-m_F\hbar\omega_0 + N\hbar\omega)|m_F, N\rangle. \quad (2.24)$$

The eigenenergy can also be written in terms of the detuning $\delta = \omega - \omega_0$,

$$E_{m_F, N} = m_F\hbar\delta + (N - m_F)\hbar\omega. \quad (2.25)$$

From the last equation, one finds that for each given N there are three eigenstates $|m_F, N + m_F\rangle, m_F \in \{-1, 0, +1\}$ separated by a small energy of $\hbar\delta$. The ensemble of these three energy levels defines the manifold $\mathcal{E}_N = \{|-1, N-1\rangle, |0, N\rangle, |1, N+1\rangle\}$. In the manifold \mathcal{E}_N , the associated eigenenergies are:

$$E_{m_F, N} = m_F\hbar\delta + N\hbar\omega. \quad (2.26)$$

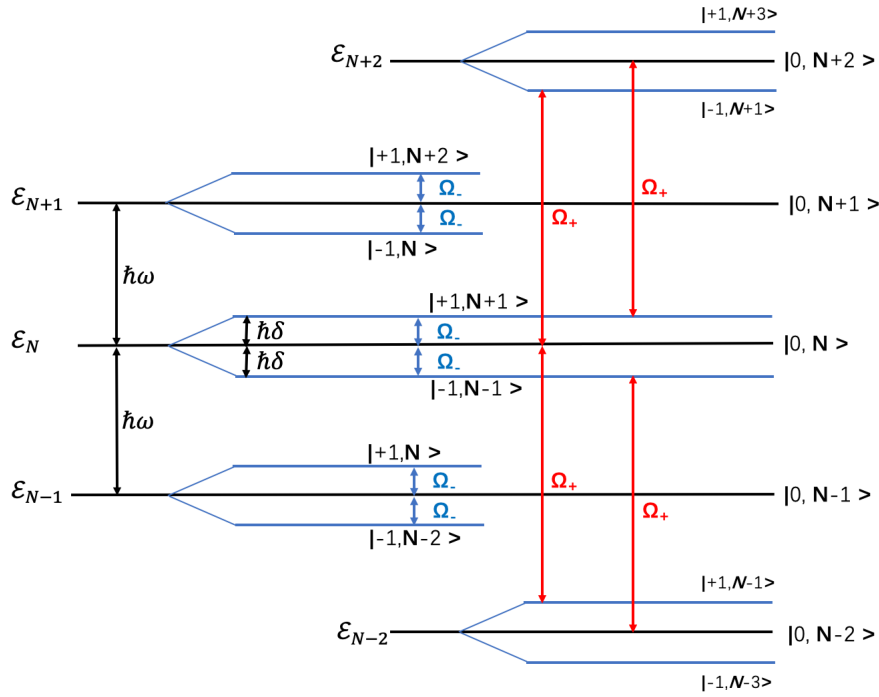


Figure 2.1 – The uncoupled states of the {atom + photon} system. For a fixed N , there are three states in the manifold \mathcal{E}_N , corresponding to m_F equal to $-1, 0, +1$. They are separated with a small energy difference $\hbar\delta$ compared to the energy spacing between manifolds $\hbar\omega$. Ω_- represents the coupling within a certain manifold between levels split by $\hbar\delta$ while Ω_+ indicates the coupling between the states in two different manifolds, split by $\hbar(\omega + \omega_0)$. The sketch corresponds to the case $\delta > 0$.

The picture of uncoupled states is shown in Fig. 2.1 which is plotted under the assumption of $\delta > 0$. The energy splitting between manifolds is $\hbar\omega$, much larger than the splitting between levels inside a manifold.

2.1.3.2 Dressed states in the rotating wave approximation

Now let us consider the case of a non zero coupling term. We remind $s = -1$ and the effects of the lowering and raising operators are:

$$\hat{F}_{\pm}|m_F\rangle = \hbar\sqrt{F(F+1) - m_F(m_F \pm 1)}|m_F \pm 1\rangle. \quad (2.27)$$

We then examine the effect of the rf field coupling. For the four components of the coupling operator (2.22), the first two terms proportional to Ω_- describe the coupling between the two states separated with a small energy $\pm\hbar\delta$ inside a given manifold \mathcal{E}_N if the coupling is nonzero, which is illustrated in the Fig. 2.1. Assuming the coupling amplitudes Ω_{\pm} are real, these two coupling terms can be written as:

$$\langle m_F \pm 1, N + m_F \pm 1 | \frac{\Omega_-}{2\sqrt{\langle N \rangle}} (\hat{a}\hat{F}_- + \hat{a}^\dagger\hat{F}_+) | m_F, N + m_F \rangle \simeq \frac{\Omega_-}{2} \langle m_F \pm 1 | \hat{F}_{\pm} | m_F \rangle \quad (2.28)$$

where we assume $N + m_F \simeq \langle N \rangle$ since $\langle N \rangle \gg 1$. The last two coupling components related to Ω_+ describe the coupling between the states of the \mathcal{E}_N manifold and the states of the $\mathcal{E}_{N\pm 2}$ manifold, which are separated with a large energy of $\hbar(2\omega - \delta)$. The matrix elements read:

$$\langle m_F \pm 1, N + m_F \mp 1 | \frac{\Omega_+}{2\sqrt{\langle N \rangle}} (\hat{a}\hat{F}_+ + \hat{a}^\dagger\hat{F}_-) | m_F, N + m_F \rangle \simeq \frac{\Omega_+}{2} \langle m_F \pm 1 | \hat{F}_{\pm} | m_F \rangle. \quad (2.29)$$

This kind of coupling is also shown in Fig. 2.1, noted in red. Let us note that if s is positive the states of the \mathcal{E}_N manifold become $|m_F, N - m_F\rangle$. In this case, Ω_+ describes the coupling between the states inside a given \mathcal{E}_N manifold, and the Ω_- terms couple the states separated by a large energy.

When $|\delta| \ll \omega$ and $|\Omega_{\pm}| \ll \omega$, the effect of the coupling will stay small with respect to the separation between manifolds, and we can take the rotating wave approximation (RWA): we neglect the Ω_+ terms coupling the states far away in energy. In this approximation, N is a quantum number describing different energy manifolds. Each eigenstate is supposed to be a superposition of uncoupled states $|m_F, N + m_F\rangle$ within the same manifold. Therefore, the total Hamiltonian composed by the three terms can be written as:

$$\hat{H} = -\omega_0\hat{F}_z + \hbar\omega\hat{a}^\dagger\hat{a} - \frac{\Omega_-}{2\sqrt{\langle N \rangle}}(\hat{a}\hat{F}_- + \hat{a}^\dagger\hat{F}_+). \quad (2.30)$$

It acts inside a given manifold \mathcal{E}_N . The effect of the spin operators \hat{F}_z and \hat{F}_{\pm} in (2.2) and (2.27) can be written under matrix form in the basis $\{|m_F = 1\rangle, |m_F = 0\rangle, |m_F = -1\rangle\}$:

$$\hat{F}_z = \hbar \begin{pmatrix} 1 & 0 & 0 \\ 0 & 0 & 0 \\ 0 & 0 & -1 \end{pmatrix}, \quad \hat{F}_+ = \hbar \begin{pmatrix} 0 & \sqrt{2} & 0 \\ 0 & 0 & \sqrt{2} \\ 0 & 0 & 0 \end{pmatrix}, \quad \hat{F}_- = \hbar \begin{pmatrix} 0 & 0 & 0 \\ \sqrt{2} & 0 & 0 \\ 0 & \sqrt{2} & 0 \end{pmatrix}. \quad (2.31)$$

Assuming that $N + m \simeq N$, the total Hamiltonian (2.30) can also be written in matrix form in the basis $\{|+1, N+1\rangle, |0, N\rangle, |-1, N-1\rangle\}$, which reads:

$$\hat{H} = \hbar \begin{pmatrix} \delta & -\frac{\Omega_-}{\sqrt{2}} & 0 \\ -\frac{\Omega_-}{\sqrt{2}} & 0 & -\frac{\Omega_-}{\sqrt{2}} \\ 0 & -\frac{\Omega_-}{\sqrt{2}} & -\delta \end{pmatrix} + N\hbar\omega. \quad (2.32)$$

After diagonalising this 3×3 matrix, one can obtain the eigenvalues:

$$\left\{ +\hbar\sqrt{\delta^2 + \Omega_-^2}, 0, -\hbar\sqrt{\delta^2 + \Omega_-^2} \right\}.$$

The corresponding eigenstates are the superposition of the three Zeeman states. The eigenstates are the dressed states, noted as $|m, N\rangle$, where m describes different dressed states in manifold \mathcal{E}_N and it can take the same value as m_F . So the eigenenergies of the dressed states $|m, N\rangle$ can be written as a function of m , which is

$$E_{m,N} = m\hbar\sqrt{\delta^2 + |\Omega_-|^2} + N\hbar\omega. \quad (2.33)$$

The interaction between the atom and the rf field generates an avoided crossing on resonance $\delta = 0$ where the states are split by $|\Omega_-|$. Note that we have taken the convention that the states with $m > 0$ have a positive energy, in contrast to the bare states $|m_F\rangle$. The states $|m\rangle$ with $m > 0$ exhibit a potential minimum on resonance, which provides a mechanism to trap atoms in the dressed state when the detuning varies with position (see next section).

However, in the real case of our experiment, the typical values of the coupling amplitude and the rf frequency are around $\Omega_{\pm}/(2\pi) \approx 50$ to 100 kHz and $\omega \approx 2\pi \times 300$ kHz, which in fact can not perfectly satisfy the condition of the rotating wave approximation: $\Omega_{\pm} \ll \omega$. Therefore, sometimes we will have to consider the coupling terms with Ω_+ which couple the states well separated with an energy of $\hbar(\omega + \omega_0)$. The details about the coupling beyond the RWA terms will be discussed in Chapter 4.

2.2 Adiabatic potentials for rf dressed atoms

2.2.1 Adiabatic potential

In the previous section, we have introduced the dressed states in an rf field and a uniform static magnetic field. In this case, the Larmor frequency is position independent. To trap atoms, the static magnetic field has to be inhomogeneous, which results in a position-dependent detuning $\delta(\mathbf{r})$ as well as local Rabi coupling $\Omega_-(\mathbf{r})$. If we assume that the variations of the eigenstates are slow enough as the atom moves in this position-dependent coupling, the state will follow adiabatically the variations of the Hamiltonian and its position-dependent eigenenergy $E_{m,N}(\mathbf{r})$ will appear as a potential energy for the atom. Through the energies of the dressed states in (2.33), one can deduce the effective potential:

$$V_m(\mathbf{r}) = m\hbar\Omega(\mathbf{r}) = m\hbar\sqrt{\delta^2(\mathbf{r}) + |\Omega_-(\mathbf{r})|^2}, \quad (2.34)$$

where the position dependent detuning can be written as:

$$\delta(\mathbf{r}) = \omega - \omega_0(\mathbf{r}) \quad (2.35)$$

where $\omega_0(\mathbf{r})$ is the Larmor frequency at position \mathbf{r} , see equation (2.7). $V_m(\mathbf{r})$ describes the eigenenergy of the adiabatic state $|m\rangle$ where we have dropped the index N of the manifold \mathcal{E}_N . In our case, only the state $|m = 1\rangle$ has a positive energy all the time.

In order to illustrate what happens when the static magnetic field depends on position and introduce the concept of adiabatic states, we consider the case where the magnitude of the static magnetic field is linearly proportional to the position r while the Rabi coupling is position independent, $\Omega_-(\mathbf{r}) = \Omega_-$. Then the Larmor frequency can be described as a constant gradient times a position coordinate, i.e. $\omega_0(r) = |\nabla\omega_0|r = \alpha r$ where $\alpha = |\nabla\omega_0|$ is the local gradient of the Larmor frequency. We can plot at each position the energies of the uncoupled states through the equation (2.5), shown in Fig. 2.2. We call r_0 the position where the resonance $\omega_0(r_0) = \omega$ occurs, see Fig. 2.2. So the atoms following the upper adiabatic states with $m > 0$ undergo a force that push them to the resonant position r_0 where the energy is minimized. For the atoms trapped in such a potential, their spin will flip when they pass across this resonant position slow enough while the detuning δ changes sign. The adiabaticity condition describing how slow is "slow enough" will be explained in the next section.

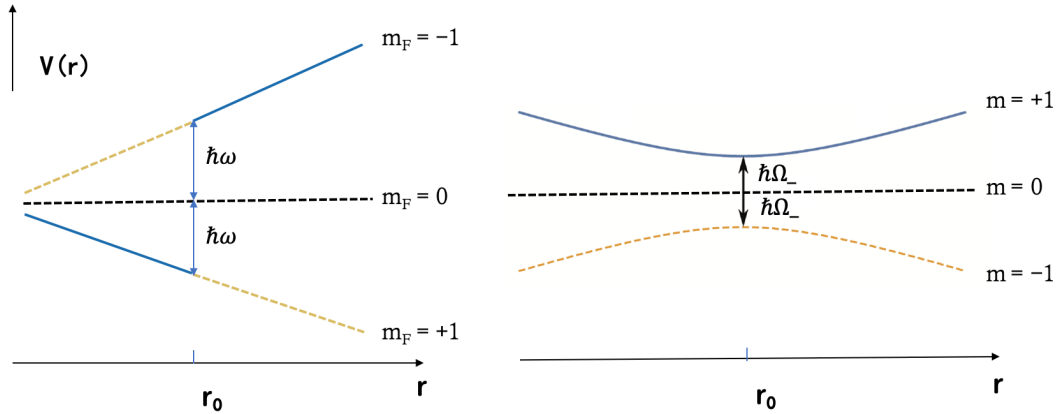


Figure 2.2 – Left: Magnetic potential of the uncoupled states with a total spin $F = 1$. The resonance of the rf frequency and the Larmor frequency occurs at r_0 . Right Adiabatic potentials corresponding to the dressed states with a position independent Rabi coupling Ω_- . At the resonance position $\delta(r_0) = 0$, the nearby two states are split by an energy $\hbar\Omega_-$. Figure adapted from [95].

If the adiabaticity condition is met, we can estimate the trapping frequency of such an adiabatic potential. Since the static magnetic field is inhomogeneous, there exists an isomagnetic surface on which the rf is resonant with the Larmor frequency.

Since the atoms are confined around the resonant surface, the adiabatic potential in the direction normal to this surface can be locally regarded as a harmonic trap with trapping frequency ω_t . For a small displacement dr away from the resonant position r_0 in the direction normal to the isomagnetic surface, we have

$$\frac{1}{2}M\omega_t^2(dr)^2 = V(r_0 + dr) - V(r_0), \quad (2.36)$$

where M is the atomic mass and V the adiabatic potential given by (2.34). The second order expansion of equation (2.34) gives:

$$\omega_t = \alpha \sqrt{\frac{m\hbar}{M\Omega_-}}. \quad (2.37)$$

2.2.2 Adiabaticity condition

In this section we will discuss the adiabaticity condition by using a simple model of a two level system, i.e. an angular momentum $F = 1/2$. The energies of the two uncoupled levels are $\pm\hbar\delta/2$ while the coupling between these two levels is Ω_- . So the two eigenenergies are $\mathcal{E}_{\pm}(\mathbf{r}) = \pm\frac{\hbar}{2}\sqrt{\delta^2(\mathbf{r}) + |\Omega_-(\mathbf{r})|^2}$, as presented in the last section. The total Hamiltonian of the system can be written under the form of a 2×2 matrix, which reads:

$$\hat{H} = \frac{\hbar}{2} \begin{pmatrix} -\delta(\mathbf{r}) & \Omega_-(\mathbf{r}) \\ \Omega_-(\mathbf{r}) & \delta(\mathbf{r}) \end{pmatrix}. \quad (2.38)$$

The detuning $\delta(\mathbf{r})$ and the Rabi coupling $\Omega_-(\mathbf{r})$ are position-dependent. Because the position operator $\hat{\mathbf{R}}$ and the momentum operator $\hat{\mathbf{P}}$ do not commute, we cannot diagonalize the Hamiltonian point by point as soon as the kinetic term $\hat{\mathbf{P}}^2/(2M)$ is taken into account. To gain insight of what happens, we will assume that the atom moves at constant velocity v and we will rewrite this Hamiltonian as time-dependent using $\mathbf{r} = \mathbf{v}t$. Since the velocity is a constant, the detuning and the coupling now become time-dependent, written as $\delta(t)$ and $\Omega_-(t)$. So the Hamiltonian reads:

$$\hat{H} = \frac{\hbar}{2} \begin{pmatrix} -\delta(t) & \Omega_-(t) \\ \Omega_-(t) & \delta(t) \end{pmatrix}. \quad (2.39)$$

For a given t , after diagonalizing the Hamiltonian with a unitary operator $\hat{U}(t)$, it becomes:

$$\hat{H}_A = \frac{\hbar}{2} \begin{pmatrix} \Omega(t) & 0 \\ 0 & -\Omega(t) \end{pmatrix} = \hat{U}^\dagger(t)\hat{H}\hat{U}(t) \quad (2.40)$$

where the time-dependent eigenenergies are $\pm\hbar\Omega(t)/2$ with $\Omega(t) = \sqrt{\delta^2(t) + |\Omega_-(t)|^2}$. The Schrödinger equation reads:

$$i\hbar\frac{\partial}{\partial t}\Psi(t) = \hat{H}\Psi(t) \quad (2.41)$$

where $\Psi(t)$ is the atomic state. In order to describe it in the adiabatic basis, we write the Hamiltonian and the atomic state in the adiabatic basis with $\Psi(t) = \hat{U}(t)\Psi_A(t)$ and $\hat{H} = \hat{U}(t)\hat{H}_A\hat{U}^\dagger(t)$. After transforming to the new basis, the Schrödinger equation becomes:

$$i\hbar\frac{\partial}{\partial t}\Psi(t) = \hat{H}_A\Psi_A(t) - i\hbar\hat{U}^\dagger\frac{\partial}{\partial t}\hat{U}\Psi_A(t) \quad (2.42)$$

where $\hat{H}_A - i\hbar\hat{U}^\dagger\frac{\partial}{\partial t}\hat{U}$ is the effective Hamiltonian whose first term is diagonalized and the second term can be regarded as a correction of the non-adiabatic coupling. The second term takes the form [95]:

$$\frac{\hbar}{2} \begin{pmatrix} 0 & \gamma(t) \\ \gamma^*(t) & 0 \end{pmatrix}, \quad (2.43)$$

where the correction $\gamma(t)$ indicating the non-adiabatic coupling between the adiabatic eigenstates is given by:

$$\gamma(t) = i\frac{\dot{\delta}(t)\Omega_-(t) - \delta(t)\dot{\Omega}_-(t)}{\Omega(t)^2}. \quad (2.44)$$

In the adiabatic basis, the effective Hamiltonian has the eigenenergies $\pm\hbar\Omega/2$ on the diagonal as well as the non-adiabatic coupling terms $\hbar\gamma(t)/2$ and $\hbar\gamma^*(t)/2$ on the off-diagonal. Therefore, the adiabaticity condition is [96]:

$$|\gamma(t)| \ll \Omega(t) \quad \text{or} \quad \left| \dot{\delta}(t)\Omega_-(t) - \delta(t)\dot{\Omega}_-(t) \right| \ll (\delta^2(t) + |\Omega_-(t)|)^{3/2}. \quad (2.45)$$

Returning to the position-dependent description, this means that the velocity should satisfy

$$|\mathbf{v} \cdot (\Omega_-(\mathbf{r})\nabla\delta - \delta(\mathbf{r})\nabla\Omega_-)| \ll (\delta^2(\mathbf{r}) + |\Omega_-(\mathbf{r})|)^{3/2}. \quad (2.46)$$

If the Rabi coupling is zero, the splitting between the eigenenergies $\hbar\Omega$ on the resonant position where $\delta(\mathbf{r}) = 0$ vanishes. In this case, the adiabaticity condition can not be satisfied, which leads to atom losses due to the spin flip.

2.2.3 Local Rabi coupling

In the last section, we have examined the properties of the adiabatic potential treating the Rabi coupling Ω_- as a position independent parameter. However, this coupling term depends on the orientation of the static magnetic field, the amplitude and the polarization of the rf field. In order to determine the local Rabi coupling, here we describe the static field and the rf field in a classical way:

$$\mathbf{B}_0(\mathbf{r}) = B_0(\mathbf{r})\mathbf{u}(\mathbf{r}), \quad (2.47)$$

$$\mathbf{B}_1(\mathbf{r}, t) = B_1(\mathbf{r})\boldsymbol{\epsilon}(\mathbf{r})e^{-i\omega t} + c.c \quad (2.48)$$

where $\mathbf{u}(\mathbf{r})$ gives the orientation of the local static magnetic field and $\boldsymbol{\epsilon}(\mathbf{r})$ is the complex polarisation of the rf field with $|\boldsymbol{\epsilon}(\mathbf{r})| = 1$. In the RWA, we have explained that the

terms with Ω_- are the only efficient terms to couple the spin states for a negative g_F . The corresponding polarisation σ^- is defined with respect to the orientation of the local magnetic field $\mathbf{u}(\mathbf{r})$. The components of the rf field amplitudes can be described in the local spherical basis $\{\mathbf{e}_+(\mathbf{r}), \mathbf{e}_-(\mathbf{r}), \mathbf{u}(\mathbf{r})\}$, which reads:

$$B_{\pm} = \mathbf{e}_{\pm}^* \cdot \boldsymbol{\epsilon}(\mathbf{r}) B_1(\mathbf{r}). \quad (2.49)$$

In the same basis, through the definition of Ω_- in (2.23), the position dependent Rabi coupling can be written as:

$$\Omega_-(\mathbf{r}) = -\sqrt{2} \frac{g_F \mu_B}{\hbar} B_-(\mathbf{r}) \quad (2.50)$$

$$= -\sqrt{2} \frac{g_F \mu_B}{\hbar} B_1(\mathbf{r}) \mathbf{e}_-(\mathbf{r}) \cdot \boldsymbol{\epsilon}(\mathbf{r}) \quad (2.51)$$

$$= \Omega_{\text{rf}}(\mathbf{r}) \mathbf{e}_-(\mathbf{r}) \cdot \boldsymbol{\epsilon}(\mathbf{r}), \quad (2.52)$$

where $\Omega_{\text{rf}}(\mathbf{r}) = -\sqrt{2} g_F \mu_B B_1(\mathbf{r}) / \hbar$ is the maximum achievable Rabi coupling. From the last expression we find that the Rabi coupling is position-dependent, because \mathbf{e}_- is defined with respect to the local quantized axis $\mathbf{u}(\mathbf{r})$ which could be position-dependent. By using the properties in the spherical basis, in the end, $\Omega_-(\mathbf{r})$ can also be written as [95]:

$$|\Omega_-(\mathbf{r})| = \frac{\Omega_{\text{rf}}(\mathbf{r})}{2} |\boldsymbol{\epsilon} \times \mathbf{u} - i \mathbf{u} \times (\boldsymbol{\epsilon} \times \mathbf{u})|. \quad (2.53)$$

Now we have the general expression of the Rabi coupling, let us consider two particular cases where the polarisation of the rf field is uniform in space, linear or circular. If it is linearly polarised along the axis x , then the polarisation is $\boldsymbol{\epsilon} = \mathbf{e}_x$ and the Rabi coupling becomes:

$$|\Omega_-(\mathbf{r})| = \Omega_{\text{rf}}(\mathbf{r}) \sqrt{\frac{1 - u_x(\mathbf{r})^2}{2}} \quad (2.54)$$

in which $u_x = \mathbf{u}(\mathbf{r}) \cdot \mathbf{e}_x$. From the equation one can find that the coupling reaches a maximum $\Omega_{\text{rf}}(\mathbf{r}) / \sqrt{2}$ if \mathbf{u} is orthogonal to the axis x of the polarization, and that it vanishes at the positions where the orientation of the local magnetic field is aligned with the direction of the rf polarisation. The zero coupling leads to the losses of atoms.

In the case of a circular polarisation σ^- with respect to the z axis, it is described as $\boldsymbol{\epsilon} = \mathbf{e}_-$ in the spherical basis of axis z . In this situation, the Rabi coupling becomes:

$$|\Omega_-(\mathbf{r})| = \frac{\Omega_{\text{rf}}(\mathbf{r})}{2} [1 + u_z(\mathbf{r})], \quad (2.55)$$

where $u_z(\mathbf{r}) = \mathbf{u}(\mathbf{r}) \cdot \mathbf{e}_z$. The Rabi coupling reaches its maximum value $\Omega_{\text{rf}}(\mathbf{r})$ when $\mathbf{u}(\mathbf{r})$ has the same direction than \mathbf{e}_z . It vanishes when the direction of the quantisation axis is $-\mathbf{e}_z$.

Since \mathbf{u} is the unit vector pointing the direction of the local magnetic field, both u_x and u_z belong to $[-1, 1]$. From the results in (2.54) and (2.55) we remark that, for the same rf complex amplitude B_1 , the maximum achievable Rabi coupling for a circular polarisation is $\sqrt{2}$ times the one for a linear polarisation.

2.3 A dressed quadrupole trap

We have seen the general properties of the adiabatic potentials and Rabi coupling, here we will examine the particular case of our experiment where atoms evolve in the combination of a quadrupole magnetic field and an rf field. The resulting potential is a dressed quadrupole trap whose minimum lays on an ellipsoid. For this reason we also call it a bubble trap. Again, the results presented here are taken from Refs. [95, 100], they are recalled for the sake of completeness.

2.3.1 Principle of the bubble trap

The quadrupole magnetic field is easily generated by a pair of coils in anti-Helmholtz configuration. Such a magnetic field is described as:

$$\mathbf{B}_0(\mathbf{r}) = b'(x\mathbf{e}_x + y\mathbf{e}_y - 2z\mathbf{e}_z), \quad (2.56)$$

which linearly increases from the center along x , y and z . So its magnitude at $\mathbf{r} = x\mathbf{e}_x + y\mathbf{e}_y + z\mathbf{e}_z$ is written as:

$$B_0(\mathbf{r}) = b'\sqrt{x^2 + y^2 + 4z^2}. \quad (2.57)$$

The corresponding Larmor frequency is given by:

$$\omega_0(\mathbf{r}) = \frac{|g_F|\mu_B b'}{\hbar} \sqrt{x^2 + y^2 + 4z^2}. \quad (2.58)$$

We define α as the magnetic gradient in the xy plane, given by:

$$\alpha = \frac{|g_F|\mu_B b'}{\hbar}. \quad (2.59)$$

For a given rf frequency ω , the atoms can be confined on the isomagnetic surface where the resonance occurs $\omega = \omega_0(\mathbf{r})$. Since the magnitude of the local field is constant on such a surface, $x^2 + y^2 + 4z^2$ is also supposed to be a constant, as:

$$x^2 + y^2 + 4z^2 = r_b^2. \quad (2.60)$$

This equation describes an ellipsoid with a semi-major axis r_b and a semi-minor axis $r_b/2$. This radius r_b of the bubble trap is given by:

$$r_b = \frac{\omega}{\alpha}. \quad (2.61)$$

The orientation of the local magnetic field on the resonant surface \mathbf{u} can be written as:

$$\mathbf{u} = \frac{b'(x\mathbf{e}_x + y\mathbf{e}_y - 2z\mathbf{e}_z)}{b'\sqrt{x^2 + y^2 + 4z^2}} = \frac{x\mathbf{e}_x + y\mathbf{e}_y - 2z\mathbf{e}_z}{r_b}. \quad (2.62)$$

2.3.2 Circular polarization

The choice of a circularly polarised rf field around the vertical z axis can make a rotational symmetrical trap. It can be simply produced by a pair of orthogonal antennas of axis x and y generating two fields with the same amplitude and a phase difference $\pi/2$. The polarisation of the rf field σ^- can be written as:

$$\boldsymbol{\epsilon} = \frac{1}{\sqrt{2}}(\mathbf{e}_x - i\mathbf{e}_y). \quad (2.63)$$

Using the same description as in (2.48), we can write the rf field as:

$$\mathbf{B}_1(\mathbf{r}, t) = B_1\boldsymbol{\epsilon}(\mathbf{r})e^{-i\omega t} + c.c \quad (2.64)$$

$$= \sqrt{2}B_1[\cos(\omega t)\mathbf{e}_x + \sin(\omega t)\mathbf{e}_y]. \quad (2.65)$$

We have determined the local Rabi coupling for a circular polarised rf field, given by (2.55). In this case, the term $u_z(\mathbf{r})$ becomes:

$$u_z = \mathbf{u} \cdot \mathbf{e}_z = \frac{(x\mathbf{e}_x + y\mathbf{e}_y - 2z\mathbf{e}_z) \cdot \mathbf{e}_z}{r_b} = -\frac{2z}{r_b}. \quad (2.66)$$

Therefore, the local Rabi coupling on the resonant surface is written as:

$$\Omega_-(z) = \frac{\Omega_0}{2} \left(1 - \frac{2z}{r_b}\right) \quad (2.67)$$

with the maximum achievable Rabi coupling Ω_0 :

$$\Omega_0 = \sqrt{2} \frac{|g_F \mu_B B_1|}{\hbar}. \quad (2.68)$$

For any point belonging to the isomagnetic surface, we have $-r_b \leq 2z \leq r_b$. Equation (2.67) shows that the maximum Ω_0 is located at the bottom of the bubble. The coupling term vanishes for $z = r_b/2$, which means that the Rabi coupling is zero at the top of the bubble, which is shown in Fig. 2.3 (if the polarisation is σ^+ , the zero coupling position is located at the bottom). The potential on the resonant surface of the bubble consists of two parts, the dressed adiabatic potential $V_m(\mathbf{r})$ and the gravitational potential Mgz . After inserting the Rabi coupling $\Omega_-(z)$ expressed in (2.67) and taking $\delta(\mathbf{r}) = 0$, the potential on the bubble surface can be written as:

$$V_{\text{bub}}(z) = \hbar\Omega_-(z) + Mgz \quad (2.69)$$

$$= \frac{\hbar\Omega_0}{2} \left(1 - \frac{2z}{r_b}\right) + Mgz \quad (2.70)$$

$$= \frac{\hbar\Omega_0}{2} + \left(Mg - \frac{\hbar\Omega_0}{r_b}\right) z. \quad (2.71)$$

If the coefficient in front of z is negative, meaning that $\hbar\Omega_0 > Mgr_b$, the potential minimum occurs at the top of the bubble where z gets largest. In this case, atoms

undergo a force pushing them to the top where the potential minimum occurs. But atoms can not be confined in such a minimum potential, because when the rf coupling vanishes there, they can not follow a dressed state and make spin flip. Consequently, atoms escape from the non-coupling position which acts as a hole. In order to avoid this effect and keep the potential minimum at the bottom of the bubble, the coefficient in front of z should be positive, which means that:

$$\hbar\Omega_0 < Mgr_b. \quad (2.72)$$

In the case where these two quantities are equal, the rf coupling gradient can compensate gravity. This situation is investigated specifically in Chapter 4.

The last condition is still not enough to trap the atoms at the bottom of the bubble. If the effect of gravity is greater than the magnetic gradient, atoms won't be trapped and will fall down. So it also has to satisfy the condition:

$$\frac{Mg}{2\hbar\alpha} = \varepsilon < 1. \quad (2.73)$$

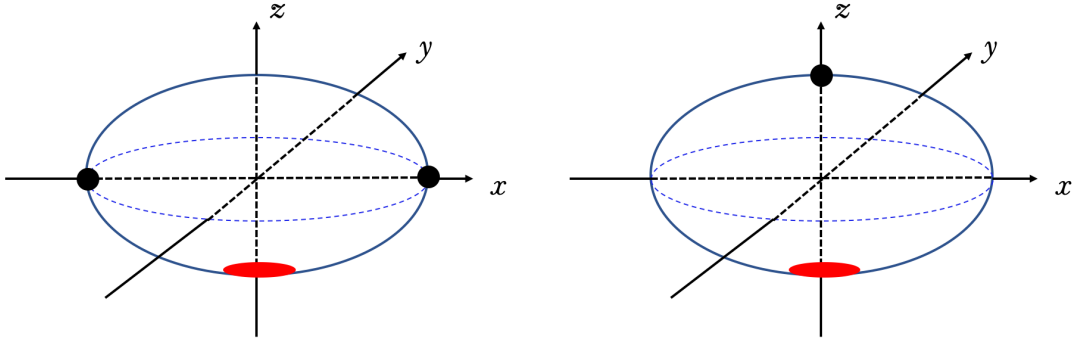


Figure 2.3 – Sketch of the bubble trap in three dimensions. The semi-major axis and the semi-minor axis are r_b and $r_b/2$. Atoms plotted in red are located at the bottom of the bubble. The black solid dots on the surface describe the points where the Rabi coupling vanishes, leading to atom losses. Left: A quadrupole trap dressed by a linear polarised rf field along x . There are two holes on the equator of the bubble along x axis. Right: The case of a circular polarisation configuration, in which one hole is located at the top of the bubble.

Because of gravity, the potential minimum is slightly shifted down from the resonant surface. It is located at position $(x = 0, y = 0, z = -R)$, where R can be written as [92]:

$$R = \frac{r_b}{2} \left(1 + \frac{\varepsilon}{\sqrt{1 - \varepsilon^2}} \frac{\Omega_0}{\omega} \right). \quad (2.74)$$

Since the trap is cylindrically symmetric, it is characterized in the harmonic approximation close to its minimum by a radial frequency ω_r and a vertical frequency ω_z .

Through a second order development of the potential around the minimum, one can obtain these two oscillation frequencies at the bottom [92]:

$$\omega_r = \sqrt{\frac{g}{4R}} \left[1 - \frac{\hbar\Omega_0}{2MgR} \sqrt{1 - \varepsilon^2} \right]^{1/2}, \quad (2.75)$$

$$\omega_z = 2\alpha \sqrt{\frac{\hbar}{M\Omega_0}} (1 - \varepsilon^2)^{3/4}. \quad (2.76)$$

2.3.3 Linear polarization

Now we consider the case of a linearly polarised rf field, which can be generated by a single antenna. We assume that the linear polarisation is along x axis, which reads:

$$\boldsymbol{\epsilon} = \mathbf{e}_x. \quad (2.77)$$

The rf magnetic field thus reads:

$$\mathbf{B}_1(\mathbf{r}, t) = B_1 \boldsymbol{\epsilon}(\mathbf{r}) e^{-i\omega t} + c.c. \quad (2.78)$$

$$= 2B_1 \cos(\omega t) \mathbf{e}_x. \quad (2.79)$$

We have determined the corresponding local Rabi coupling in (2.54), in the case of a bubble trap, we have $u_x = x/r_b$. So from the equation (2.54), the local Rabi coupling for a linearly polarised rf field is:

$$\Omega_-(\mathbf{r}) = \Omega_0 \sqrt{1 - \frac{x^2}{r_b^2}}. \quad (2.80)$$

where the maximum coupling is now $\Omega_0 = |g_F \mu_B B_1|/\hbar$, a factor $\sqrt{2}$ smaller as in (2.68) as already pointed out previously. The equation shows that the maximum Rabi coupling occurs for $x = 0$, corresponding to the $y - z$ plan. Moreover, the coupling vanishes at the two extreme points along x axis, located at $(\pm r_b, 0, 0)$, where the local magnetic field is parallel to the rf field.

Considering the effect of gravity, the equilibrium position at the bottom is given by (2.74), which is the same as for circular polarisation. In this situation, the coupling is no longer rotationally invariant, so the trapping frequencies along x and y axis are different. The oscillation frequencies along the 3 directions are [92]:

$$\omega_x = \sqrt{\frac{g}{4R}} \left[1 - \frac{\hbar\Omega_0}{MgR} \sqrt{1 - \varepsilon^2} \right]^{1/2}, \quad (2.81)$$

$$\omega_y = \sqrt{\frac{g}{4R}}, \quad (2.82)$$

$$\omega_z = 2\alpha \sqrt{\frac{\hbar}{M\Omega_0}} (1 - \varepsilon^2)^{3/4}. \quad (2.83)$$

2.3.4 Elliptical polarization

We have discussed the cases of a circularly polarised and a linearly polarised rf field. Realizing a circularly polarised rf field requires a pair of orthogonal linearly polarised rf field with the same amplitude and a phase difference of $\pi/2$. In the experiment, it is difficult to make their amplitude and the phase difference exactly in such a condition, which sometimes results in an elliptical polarization. In addition, in order to excite the trapped gas, for example creating a quadrupole mode excitation, we have to make the rf field elliptically polarised on purpose. So here I will recall the results presented in [100] on the elliptical polarisation in the horizontal plane perpendicular to the z axis.

Previously we have seen that for a linear rf polarisation, there are two holes at the equator where the static field is aligned with the rf field. But for a σ^- or a σ^+ polarisation, these two holes coincide at the top or the bottom of the bubble. For an elliptical polarisation in the $x - y$ plane, there are two holes well separated. They belong to a vertical plane and are symmetric with respect to the z axis. Investigating the positions of the two non-coupling points is helpful to understand the effects of the amplitude difference or the phase difference of the orthogonal linearly polarised magnetic fields. The elliptical polarization in the $x - y$ plane can be described as:

$$\boldsymbol{\epsilon} = \cos(\Theta) \mathbf{e}_x + e^{i\Phi} \sin(\Theta) \mathbf{e}_y. \quad (2.84)$$

In this equation, Θ and Φ control the amplitude difference and the phase difference, respectively. For example, the case of $\Theta = \pi/4$, $\Phi = \pi/2$ describes a circular polarisation. In order to locate the positions of the two holes, we translate the Cartesian coordinate to the spherical coordinate (r, θ, ϕ) . The condition for belonging to the ellipsoid writes:

$$r = \frac{r_b}{\sqrt{1 + 3 \cos^2 \theta}}. \quad (2.85)$$

As a consequence, the Cartesian coordinates of one of the holes on the bubble surface are related to these spherical coordinates (θ, ϕ) by:

$$x = \frac{r_b}{\sqrt{1 + 3 \cos^2 \theta}} \sin \theta \cos \phi \quad (2.86)$$

$$y = \frac{r_b}{\sqrt{1 + 3 \cos^2 \theta}} \sin \theta \sin \phi \quad (2.87)$$

$$z = \frac{r_b}{\sqrt{1 + 3 \cos^2 \theta}} \cos \theta \quad (2.88)$$

which is shown in Fig. 2.4. The other hole is obtained by replacing ϕ by $\phi + \pi$. The spherical coordinates (θ, ϕ) locating the holes on the ellipsoid can be computed from the condition of vanishing coupling, one finds:

$$\cos \theta = \frac{\sin(2\Theta \sin \Phi)}{1 + \sqrt{1 - \sin^2(2\Theta) \sin^2 \Phi}}, \quad (2.89)$$

$$\tan(2\phi) = \tan(2\Theta) \cos \Phi, \quad (2.90)$$

The equation (2.90) has two solutions both ϕ and $\phi + \pi$, which means that the two holes are symmetric with respect to z axis. If the phase difference Φ is always $\pi/2$ while Θ is ramped from 0 to $\pi/4$, the holes will climb from the equator to the top of the bubble. Meanwhile, ϕ is always 0, which means these two holes don't rotate along z axis. When we scan the phase difference Φ they start to rotate. The behavior of the hole positions as a function of the Φ and Θ provide a way of performing the fine tuning for the circularly polarised rf field, which will be discussed particularly in Chapter 4.

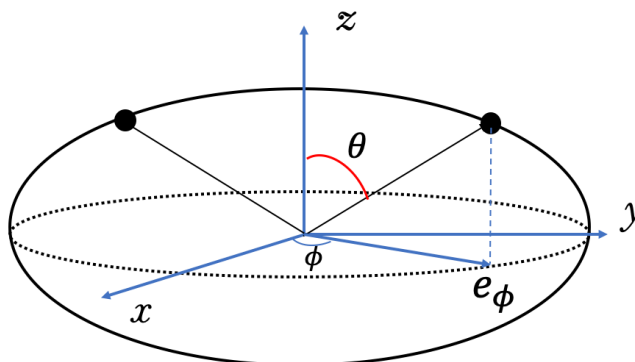


Figure 2.4 — Sketch of the hole positions in spherical coordinates. The two black solid dots indicates the two holes on the surface of the bubble.

For the detailed calculation of an arbitrarily polarised rf field including outside the $x - y$ plane, one can go into [100].

2.3.5 Determining the local Rabi coupling experimentally

In the experiment, we can measure the local Rabi coupling in which atoms are trapped by performing a spectroscopy in the trap. Apart from the antennas serving to dress the magnetic trap to obtain the adiabatic potential, another antenna generates a weak rf field that couples the two dressed states $|F = 1, m = 1\rangle$ and $|F = 1, m = 0\rangle$, shown in Fig. 2.2. Since only $|F = 1, m = 1\rangle$ can trap atoms, once the spectroscopy frequency is resonant with the Rabi coupling the trapped atoms will change the state and escape from the trap, which leads to atom losses. So scanning the spectroscopy rf frequency with a weak amplitude and plotting the number of atoms gives the Rabi coupling at the position of atoms. An example of the rf spectroscopy with atoms trapped at the bottom of the bubble trap is shown in Fig. 2.5, which indicates that the Rabi coupling at the bottom is around $\Omega_- = 2\pi \times 98$ kHz, with a circular polarization.

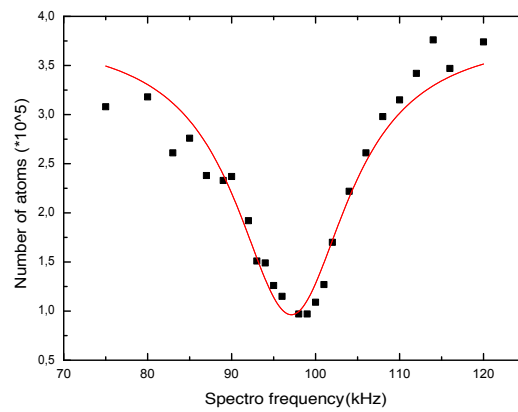


Figure 2.5 — A spectroscopy curve measured at the bottom of the bubble trap. The red line is a Lorentzian distribution fitting the data.

Chapter 3

The superfluid recipe

Making a superfluid is just like cooking with the difference that we cool instead. In order to produce a superfluid, we have to prepare atoms and lasers, which play the role of ingredients, put atoms in different traps that play the role of casseroles and follow the procedures just as we follow a recipe. This chapter aims at introducing the procedures for obtaining a superfluid in our experiment.

A recipe usually has two parts, what you need and how to proceed. So here I will first introduce the ingredients, which are the rubidium atoms and the lasers with different functionalities. Then I will present the casseroles to hold the superfluid, mainly the 2D and the 3D magneto optical trap (MOT), an optical plugged quadrupole trap and a rf dressed quadrupole trap. I will also introduce the experimental time sequence which is the cooking recipe of the superfluid. Finally, we will see how to taste, namely the method to detect the superfluid.

The experimental set up has given its first experimental results in 2012. Meanwhile four PhD students have contributed to it. More details about the set up were written in their theses. [100–103]

3.1 The ingredients and utensils

3.1.1 The cold Atom source: Rubidium 87

In the previous chapter we have mentioned that we chose ^{87}Rb to produce the superfluid. Rubidium is a soft silvery-white metal in the alkali metal group that has a simple electronic structure, one single s electron in its outermost principal energy. One of the first Bose-Einstein condensate was realized with rubidium [19], because the scattering length of rubidium (~ 5.4 nm) allows a good collision rate for evaporation. In the previous chapter we have introduced its lowest hyperfine states and its complete D_2 transition ($5^2S_{1/2} \rightarrow 5^2P_{3/2}$) hyperfine states are shown in Fig. 3.1.

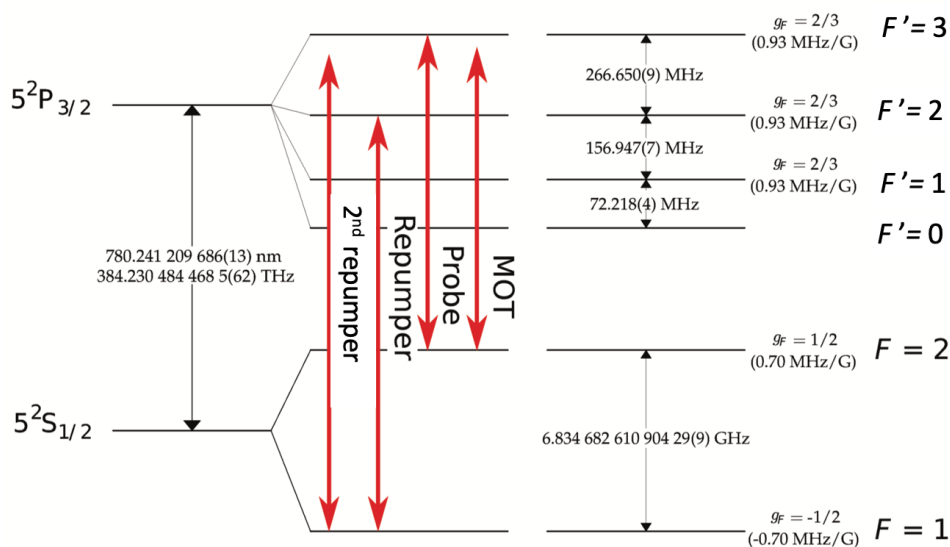


Figure 3.1 — ^{87}Rb D_2 transition hyperfine structure and the frequency of the different lasers with wavelength 780 nm: cooling beam (MOT), repump beam (2^{nd} repump and Repumper) and probing beam (Probe). In the experiment, the imaging state and the trapping state are $|F = 2\rangle$ and $|F = 1\rangle$ respectively. Figure is adapted from [104]

3.1.2 Laser system

In our experiment, we use lasers with two different wavelengths, 780 nm and 532 nm. The 780 nm lasers are used to cool, repump and probe the atoms. The 532 nm lasers are used to create dipolar potentials, for confining the atoms in the vertical direction, plugging the magnetic trap and stirring the atoms.

3.1.2.1 780nm lasers

An extended cavity diode laser: For imaging, if the linewidth of the laser is too large, the Beer-Lambert law is modified and it is more complicated to find the atom number. So an extended cavity laser is needed because of its narrow linewidth. The extended cavity laser (NarrowDiode, from Radiant Dyes) is locked on the transition of $|5S_{1/2}, F = 2\rangle \rightarrow |5P_{3/2}, F = 3\rangle$ by saturated absorption means. It provides the two imaging beams (horizontal and vertical) and a beam that serves as the frequency reference for the beat note with the doubled laser.

Doubled frequency laser: It is based on a telecom 1560 nm 10 W laser whose frequency is doubled in a single pass PPLN crystal. In the end, we obtain a 780 nm laser with 1 W of useful power. Its frequency, close to the transition $|5S_{1/2}, F = 2\rangle \rightarrow |5P_{3/2}, F = 3\rangle$, is locked via a beat note to the reference laser. The laser can be easily detuned for the Sisyphus cooling part. This laser (called MOT in Fig.3.1) is used not

only to cool down the atoms in 2D and 3D MOT but also to push the atoms from 2D MOT to the 3D MOT. It was developed in our group and one can find more details on this laser in [101].

Two mid-range power 780nm diode lasers :

These two 780 nm laser diodes are independent. Both of them are used to repump the atoms from the ground state $|5S_{1/2}, F = 1\rangle$ to the state $|5S_{1/2}, F = 2\rangle$ so that the atoms can be absorbed by the probe beams or recycled in the MOT. One is resonant with the transition $|5S_{1/2}, F = 1\rangle \rightarrow |5P_{3/2}, F = 2\rangle$ and it repumps the atoms in the MOTs and before the imaging process along the horizontal axis. The other one can be detuned from the transition frequency (see Fig. 3.1). Increasing the detuning leads to reduce the effective absorption section, which helps to uniformly repump the high-density atomic cloud. The detailed discussion is found in section 3.3.

3.1.2.2 532nm lasers

10W laser :

This laser delivers 10 W at 532 nm which is blue detuned compared to the D_2 line. It can act a repulsive force on atoms. It serves as an optical plug at the center of the quadrupole trap to avoid Majorana losses during the production of condensate [105], see section 3.2.3. A small fraction of its power is taken and sent to the optical path of a stirrer beam which can rotate atoms around the vertical axis (see Chapter 5).

5W laser :

This laser has a maximum power of 5 W at 532 nm. It is sent to a $0 - \pi$ phase plate and generates a pair of sheet-shaped beams between which the atoms are strongly confined in the vertical direction. Combined with the dressed quadrupole potential, it allows us to create a ring-shaped trap, which is investigated in Chapter 5.

3.2 The casseroles and the recipe: experimental sequence

After introducing the ingredients, I will present the casseroles and the recipe to make a superfluid, which includes all the traps holding atoms from the oven to the bubble trap and the main experimental time sequence. Following the trajectory of the atoms, they come out of the oven to a 2D MOT, 3D MOT and then they are driven to the science cell by the displacement of the MOT coils. In the science cell, the atoms are confined in a optically plugged quadrupole trap. In the end, they are loaded to a rf dressed quadrupole trap. The sketch of the Rb source, 2D, 3D MOT and the science cell is presented in Fig. 3.2.

All these steps of production and detection of the gas are controlled by the computer. Two National Instruments PCI cards provide the interface with the experiment. One is a PCI-DIO-32HS card providing 32 digital outputs (TTL levels, 0 – 5 V), while

another one is a PCI-6733 card providing 8 digital outputs and 8 analog outputs (variable voltage between -10 V and $+10\text{ V}$, 16-bit resolution). Our experimental sequence defined by a program coded in C++, which is based on a program previously written by the group of Jakob Reichel. The time resolution to control the experiment is of the order of the millisecond. More details can be found in the thesis of T. Liennard [101].

3.2.1 2D+3D MOT

We load a 3D MOT with a collimated flux of atoms from a 2D MOT in order to have a short loading time and have a good residual vacuum in the 3D MOT chamber.

In the 2D MOT, rubidium atoms are heated in an oven around 70°C , in connection with the 2D MOT chamber which is designed by the SYRTE laboratory. In this chamber, two pair of coils in an anti-Helmholtz configuration create a magnetic gradient along the two transverse axes and two elongated orthogonal beams retroreflected in the transverse plane cross. These two beams are circularly polarized and red detuned with respect to the transition $|5S_{1/2}, F = 2\rangle \rightarrow |5P_{3/2}, F = 3\rangle$, which cools down the atoms transversely. The transverse cooling chamber is connected to the 3D MOT chamber by a tube of diameter 16 mm and length 18 cm, shown in Fig. 3.2 and ends up with a 1.5 mm diameter hole in the octagonal 3D MOT chamber. To enhance the flux, a third beam in the longitudinal direction pushes the atoms towards this hole. In the end, the atoms are primarily cooled in the 2D MOT and pushed towards the 3D MOT chamber.

The 3D MOT is composed of three pairs of orthogonal, counter-propagating beams and a pair of coils in anti-Helmholtz configuration. The six beams are a mixture of the repumping laser and the cooling laser. In the end, there are nearly 10^9 atoms further cooled down and trapped in the center of the 3D MOT chamber, with a rubidium vapor pressure in the octogon around 10^{-9}mbar . More details of the 3D MOT can be found in [101, 102].

3.2.2 Magnetic transport

Since we want to investigate the atoms within a high vacuum quality environment of $\sim 10^{-11}\text{ mbar}$, we have to transfer the atoms from the 3D MOT to what we will refer to as the science cell. The 3D MOT coils are tied to a Parker translation stage 404XR. Therefore, they are able to slide from the position of the 3D MOT chamber to the science cell, allowing to transport the atoms. Its maximum speed is $1.2\text{ m}\cdot\text{s}^{-1}$ and maximum acceleration 20 m/s^2 with a $1.3\text{ }\mu\text{m}$ accuracy. The steps of the transport procedure are the following. At first, we increase the magnetic gradient from $5.5\text{ G}\cdot\text{cm}^{-1}$ (22 A) to $20\text{ G}\cdot\text{cm}^{-1}$ (80 A) in the 3D MOT and increase the detuning of the MOT beams in order to compress the atomic cloud and reduce the repulsive force between the atoms due to the multiple scattering. Once they are compressed, we abruptly turn off the current in the coils and increase again the detuning to further cool down the atoms in a molasses+Sisyphus phase. After 150 ms, the current is switched on and the gradient ramped to $87.5\text{ G}\cdot\text{cm}^{-1}$ (350 A) while the beams are turned off, confining the atoms in the low-field seeking state $|F = 1, m_F = -1\rangle$ in a pure magnetic quadrupole

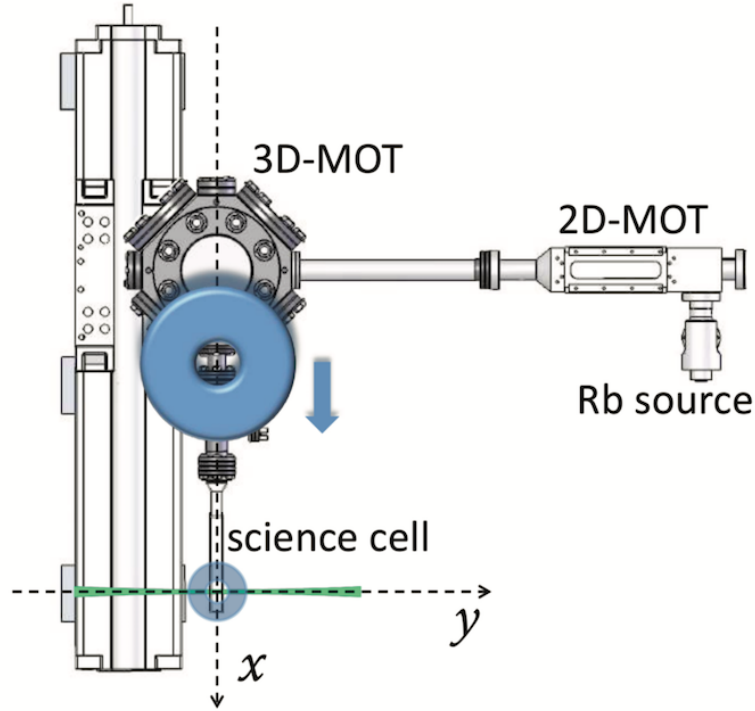


Figure 3.2 — Simplified view of the set up from above. Atoms are pushed from the 2D MOT chamber to the 3D MOT chamber. The atoms are magnetically transported to the science cell by a pair of transport coils drawn in thick blue. The small coil in light blue describes a pair of conic coils over and below the science cell generating a quadrupole trap (see Fig 3.3). The line in green along y axis is the plug beam, which optically plug the quadrupole trap. Figure is taken from [105].

trap. We then displace the coils mechanically to the science cell position at a distance of 28 cm in 1.08 s. Finally, the currents in the MOT coils are ramped down at a constant gradient while ramping the current up in the quadrupole coils of the science cell (see Fig 3.3), transferring the atoms to a new magnetic trap. Once the transport procedure is finished, the MOT coils go back to their initial position and are in place for the next sequence. By this way, we succeed to transport $\sim 5 \times 10^6$ atoms in the science cell. The science cell conical coils gradient has been measured at $2.071 \pm 0.16 \text{ G} \cdot \text{cm}^{-1} \cdot \text{A}^{-1}$, see Appendix A.

3.2.3 Plugged quadrupole trap

Once the atoms are loaded in the science cell in the static science quadrupole trap, we need to cool them down by evaporative means in order to reach condensation. But let us consider an atom in $|m_F = -1\rangle$ state, experiencing an attractive force towards the trap center. In the quadrupole trap, the magnetic field vanishes at the trap center where atoms could spin flip and escape from the trap due to the Majorana losses [106]. During the evaporation stage, we ramp the gradient up to $225.9 \text{ G} \cdot \text{cm}^{-1}$ (110 A) to

compress the cloud in order to have a good collision rate for evaporation. While the sample temperature decreases, the atomic density increases at the trap center position and the coldest atoms spin-flip, resulting in atoms losses and heating. In order to avoid the Majorana losses, our solution is to focus a 10 W, 532 nm blue detuned laser to plug the center of the quadrupole trap. By doing so, the atoms are prevented from accessing the region with zero magnetic field leading to Majorana losses. To increase the plug barrier potential, we decompress mid-way the trap by ramping down the magnetic gradient at $57.5 \text{ G} \cdot \text{cm}^{-1}$ (28.5 A). The potential minimum of this plugged quadrupole trap is slightly off centered, where it can trap about 5×10^5 atoms around 200 nK.

Evaporation is performed with two distinct rf sources, and is made with linear frequency sweeps ranging from 50 MHz to 300 kHz during approximately 18 s.

3.2.4 Dressed quadrupole trap: the bubble trap

3.2.4.1 The rf antennas for dressing

As explained in Chapter 2, our bubble trap is obtained by dressing a quadrupole trap with a circularly polarized rf field. Therefore, besides the coils generating the quadrupole trap, three rf antennas are required to generate a rf field with arbitrary polarization. These antennas are placed orthogonally surrounding the science cell, shown in Fig. 3.3.

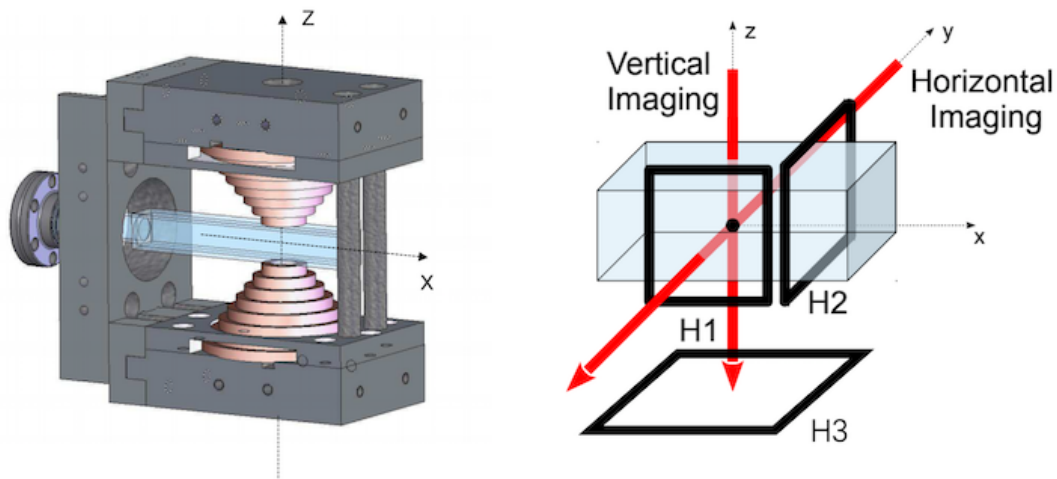


Figure 3.3 — Left: Sketch of the science cell between a pair of conic coils generating a quadrupole trap, taken from [102]. Right: View of the science cell surrounded by three orthogonal antennas producing rf field.

In our experiment, a circularly polarized rf field with respect to the z axis is needed to create a rotationally symmetric bubble trap, as mentioned in the previous chapter. Theoretically, only two horizontal antennas (H2 and H1) along x and y axis and

dephased by $\pi/2$ are enough to produce a rf field with a circular polarization of axis z . But it has proven not possible to achieve perfect circular polarization with only the horizontal antennas (see [100]). For example, due to a slight tilt of the horizontal antennas with respect to the vertical plane, the polarization is no longer orthogonal to the z axis, resulting in an elliptical polarization. Adding a third antenna (H3) below the science cell allows to compensate the vertical component of the rf field to ensure a circular polarization in the $x - y$ plane.

These three antennas are controlled by a home-made DDS (Direct Digital Synthesizer). It has a 10-bit amplitude resolution, 14-bit phase resolution and 32-bit frequency resolution. It converts a 10 MHz clock signal provided by an external Stanford DS345 synthesizer into 8 analog periodic signals, amplitude and frequency. The DDS is controlled by a program written in Octave by Romain Dubessy. The important parameters of the antennas, such as the amplitudes, the phases and the frequencies, are all controlled by this program, and allow an accurate control of the dressed trap parameters. The details of the DDS control are written in [100].

3.2.4.2 The other rf antennas

In addition to the three main antennas to generate the rf field for dressing the atoms in the quadrupole trap and the one for evaporative cooling in the plugged trap, there are still two other rf antenna sources installed besides the science cell along y axis.

One rf source is controlled by a synthesizer Stanford DS345, which is used for trap spectroscopy to know the real Rabi coupling experienced by the atoms. The details of this measurement was presented in section 2.3.5. The last rf antenna is used to produce a rf knife, using a synthesizer Tabor WW2571A. It realizes evaporative cooling on the atoms trapped in the bubble trap. The principle of the cooling is that the weak rf field leads to a double dressing [107], which is explained in detail in Chapter 6.

3.2.4.3 Loading the bubble trap

In order to transfer the atoms from the plugged trap to the bubble trap, we need to be careful about fulfilling adiabaticity requirements as described in section 2.2.2. We also need to avoid to impart too much a dipolar excitation in the dressed trap, since the atoms undergo a repulsive force from the blue detuned plug beam. Due to the plug beam, the atoms are trapped off-center where the expected resonant surface at the plugged trap corresponds approximately to a rf frequency of 250 kHz. We switch on the dressing rf antennas with a fixed frequency of 175 kHz and then ramp the amplitude in 5 ms. The corresponding resonant surface is far from the atoms ($\sim 20 \mu\text{m}$) as well as the resonant surface for the second harmonic at 350 kHz, ensuring adiabaticity at the switching on, and no change in the trap geometry at first. After that, we ramp the rf frequency up. During this process, the resonant bubble grows up and reaches the atoms position, catching them on the resonant surface, shown in Fig. 3.4. The bubble is quickly expanded to bring the atoms away from the plugged influence to the bottom of a bubble trap whose semi-major radius is $200.2 \mu\text{m}$ (at 770 kHz). We have improved the minimization of the dipolar excitation by decreasing the plug intensity linearly to 0

in 300 ms once the atoms have reached this position. In the experiment, we decided to study a smaller bubble trap of $78\ \mu\text{m}$, corresponding to a rf frequency of 300 kHz. We compress the bubble by ramping down the rf dressing frequency to 300 kHz. Because when we remove the plug the bubble is very large and the atoms are located far from the plug, the atoms are not affected too much. After doing so, the dipolar oscillation amplitude is minimized to $\sim 3\ \mu\text{m}$ (see Fig. 3.4).

An rf knife is always on at a frequency above the dressing frequency during the whole transfer, in order to avoid heating during the transfer itself, and also to be used as an evaporative cooling tool once the atoms are loaded in the dressed trap.

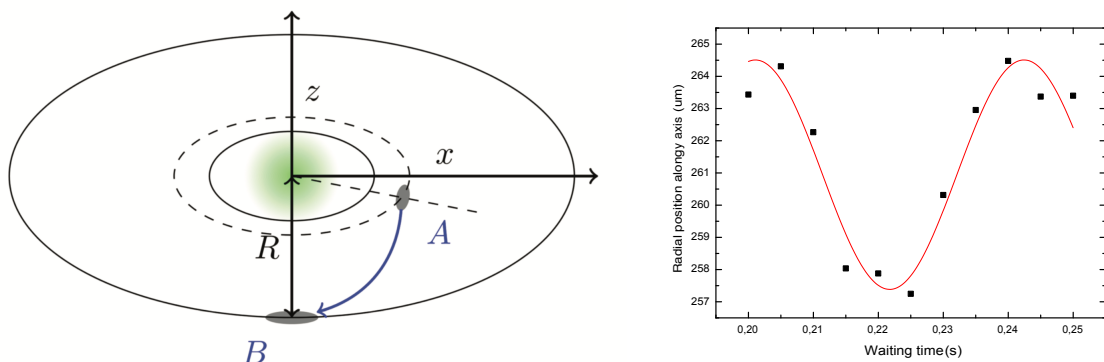


Figure 3.4 — Left: Sketch of the procedure from the plugged trap to the dressed quadrupole trap. During this process, the atoms are transferred from position A to B. The solid small and large ellipses describe the resonant surface with dressing frequency of 175 kHz and 770 kHz respectively. The dashed ellipse describes the resonant surface in which the atoms are caught by the growing bubble trap. Image taken from [92]. Right: Dipolar oscillation at the bottom of the bubble after ramping down the rf frequency to 300 kHz, which is minimized by separating the step of removing the plug beam and compressing the bubble.

3.3 Degustation: Imaging system

After preparing a dish, the most important is how to taste it. So here I will introduce the ways to detect the superfluid, which are our imaging systems. Fig. 3.3 presented the geometry of the science cell, for which there are two independent imaging systems, one horizontal with a probe beam from the side and the other one vertical with a probe beam along the z axis. By using these imaging systems, one can detect the atoms in the trap (in situ picture) or after free expansion when the trap is switched off (time-of-flight, or TOF, picture). The in situ images give the spatial distribution of the cloud, which allow to observe low atomic densities, the atomic density profile and the anisotropy of the cloud. The TOF images display the momentum distribution, which

magnify the images and make it possible to observe vortex lattices and measure the atom number accurately. In our experiment, the method used for imaging the atoms is absorption imaging.

3.3.1 Absorption imaging

3.3.1.1 Principle

The principle is to shine a resonant beam onto the atoms and measure the remaining intensity with a CCD camera. This absorption picture is then compared with the situation where we shine the same beam but in the absence of the atoms. The shadow generated by the absorption of photons is linked to the shape of the atomic cloud. The resonant transition that we use corresponds to the cycling atomic transition of $|5S_{1/2}, F = 2\rangle \rightarrow |5P_{3/2}, F = 3\rangle$. Now we consider a probe beam propagating along z axis detuned by δ with respect to this atomic transition frequency of width Γ . We note $I_i(x, y)$ and $I_t(x, y)$ the intensity of the probe beam before and after going across the atomic cloud at the position (x, y) . From the Beer-Lambert law, the optical density $D_z(x, y)$ along the z direction is given by:

$$D_z(x, y) = -\ln \frac{I_t(x, y)}{I_i(x, y)}. \quad (3.1)$$

Now we assume that the intensity of the incident beam is much weaker than the saturation intensity:

$$I_i \ll I_{\text{sat}} = \frac{\hbar\omega_p\Gamma}{2\sigma_0} \quad (3.2)$$

where $\sigma_0 = 3\lambda^2/2\pi$ is the resonant absorption cross section and ω_p is the pulsation of the transition. It corresponds to the situation where the interaction between an atom and the light is independent from the other atoms. In this case, the Beer-Lambert law is valid and the relation linking the optical density $D_z(x, y)$ and the atomic density $n_0(x, y, z)$ can be written as:

$$D_z(x, y) = \sigma \int n_0(x, y, z) dz \quad (3.3)$$

where σ is the effective absorption cross section. In the low atomic density situation, this cross section is independent on the intensity of incident beam, and reads:

$$\sigma = \frac{\sigma_0}{1 + \frac{4\delta^2}{\Gamma^2}}. \quad (3.4)$$

So if we know the ratio between the intensity of the incident beam and the one after going through the cloud, as well as the effective cross section $\sigma(\delta)$, we can obtain the atomic density distribution integrated along the z direction. The integrated atomic density thus writes:

$$n(x, y) = -\frac{1}{\sigma} \ln \frac{I_t(x, y)}{I_i(x, y)}. \quad (3.5)$$

3.3.1.2 Experimental situation

For the high density atomic cloud, such as a BEC in the trap, we can not anymore use the low intensity probe beam to absorb the atoms because all the intensity would be absorbed and there are collective effects for a 2D cloud [108]. We need to use a saturating beam, with intensity I larger than I_{sat} . In this regime, the effective absorption cross section depends on the intensity of the beam, and reads:

$$\sigma(I_i) = \frac{\sigma_0}{c^* + \frac{I_i}{I_{\text{sat}}}}. \quad (3.6)$$

where c^* is a dimensionless parameter that can be measured experimentally [109, 110]. In the end, the optical density becomes:

$$\sigma_0 n(x, y) = -c^* \ln \frac{I_t(x, y)}{I_i(x, y)} + \frac{I_t(x, y) - I_i(x, y)}{I_{\text{sat}}}. \quad (3.7)$$

Now it depends explicitly on the probe beam intensity with and without atoms, not only on their ratio. For imaging high density clouds, we can either repump a fraction of the atoms or increase the intensity of the probe beam. A detailed discussion of the high density absorption imaging in the group can be found in [100, 103].

For repumping the high density clouds, a resonant repumping beam will be only absorbed by the front side of the atomic cloud not by the back, which can not draw an accurate density profile of the cloud. Equation (3.5) shows that the transmission of the repumping beam will increase if the effective cross section decreases. As the equation (3.4) shows, we can decrease the effective cross section by increasing the detuning of the beam. Therefore, we use a far detuned repumping beam which is 250 MHz detuned to the blue of the $|5S_{1/2}, F = 2\rangle \rightarrow |5P_{3/2}, F = 3\rangle$ transition. By using this second repumper, one can repump the high-density cloud uniformly. Moreover, the far detuned beam can repump a fraction of the atoms, which also allows high density absorption imaging of 3D in situ clouds.

3.3.1.3 Stern-Gerlach procedure

If we want to take a TOF picture, we have to abruptly release the trap. However, there is a residual magnetic gradient we do not control, leading to a force applying on the atoms in the $|m_F = -1\rangle$ and $|m_F = 1\rangle$ states. It results in an imperfect overlap of the three clouds when taking the pictures after TOF. It may blur some structures in the cloud, for example the vortex lattice.

The Stern-Gerlach procedure during the imaging process helps to separate the clouds with different states and to avoid the overlap. In Chapter 2 we have explained that the atoms confined in a dressed state $|m = 1\rangle$ are in a mixture of Zeeman substates of $|m_F = -1\rangle$, $|m_F = 0\rangle$ and $|m_F = 1\rangle$ of the bare trap. If the rf field is turned off but the quadrupole field is kept on during a few milliseconds, the initial atomic cloud will be separated into three parts with different Zeeman substates: the atoms in the state $|m_F = -1\rangle$ or $|m_F = 1\rangle$ experience opposite forces while the atoms in $|m_F = 0\rangle$

do not feel any magnetic force. The $|m_F = 0\rangle$ cloud simply falls due to gravity, and we image only this cloud. In our experiment, we switch off all the antennas and beams but keep the quadrupole magnetic field on for another ~ 2 ms, which is able to separate these three clouds with different spin states. As shown in Fig. 3.5, the $|m_F = 1\rangle$ cloud is expelled from the trap center which is why it expands radially. Inversely, the $|m_F = -1\rangle$ cloud undergoes a force towards low fields which makes it closer to the previous trap center and compressed. The atomic cloud in middle with $|m_F = 0\rangle$ does not undergo any force from the magnetic field, so its shape is preserved and this is the cloud we detect.

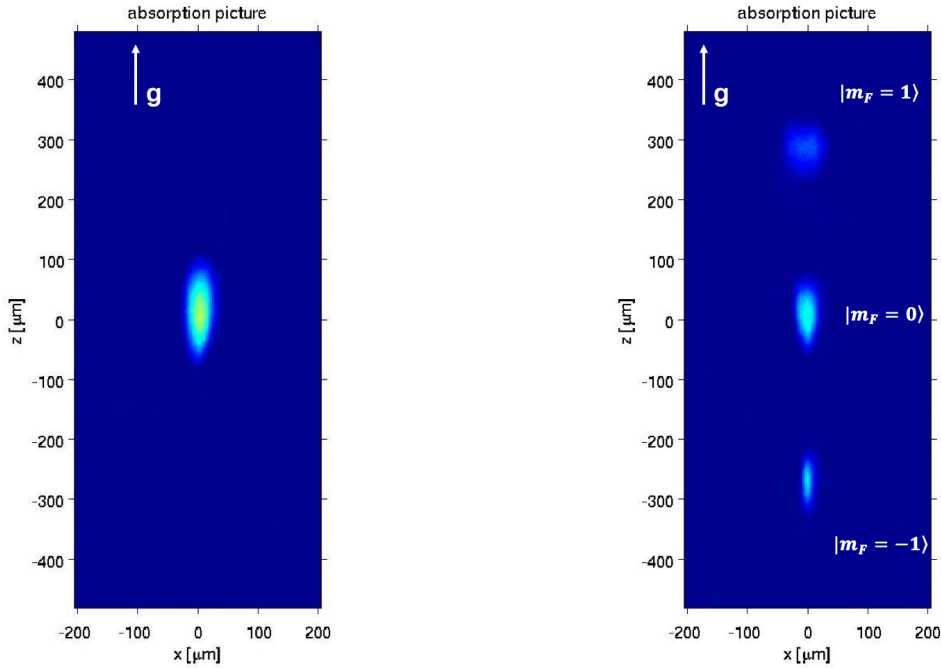


Figure 3.5 — Left: Image of an atomic cloud initially confined at the bottom of the bubble trap after 23 ms TOF without the Stern-Gerlach procedure. Right: TOF image in the same conditions of the figure on the left but with a 0.3 ms Stern-Gerlach procedure. The z direction is aligned with the direction of the gravity, gravity is oriented upwards.

3.3.2 Horizontal imaging system

The horizontal images are used to record TOF pictures. First, a repump beam resonant with the $|5S_{1/2}, F = 1\rangle \rightarrow |5P_{3/2}, F = 2\rangle$ transition is shined onto the atoms to prepare them in the state of $|5S_{1/2}, F = 2\rangle$. Then an horizontal 780 nm 17 μ s long pulse of probe beam with waist 2.7 mm is sent from the side of the science cell, along the y axis (sketch shown in Fig.3.3). This probe beam is circularly polarized and a bias magnetic field of 1.9 G aligned with it defines a quantization axis for the atoms.

Along this direction, there is also the high power 532 nm plug beam going through the trap center, so we installed a 532 nm polarizing beam splitter just after the cell to reflect the plug beam and transmit the probe beam. In addition, an 532 nm interferential filter located before the camera prevents photons coming from the plug to enter.

A two lenses imaging system shown in Fig. 3.6 achieves a magnification of $G = 2.17$. We use a iXon 885D EMCCD camera from Andor. It has a 1004×1002 pixel matrix with a pixel size of $8 \times 8 \mu\text{m}^2$.

By investigating horizontal pictures after TOF, one can deduce the temperature of the cloud from its free fall expansion or observe the rotation of the cloud through its anisotropy. It is also very useful to tune the horizontal light sheet relative position with the atoms.

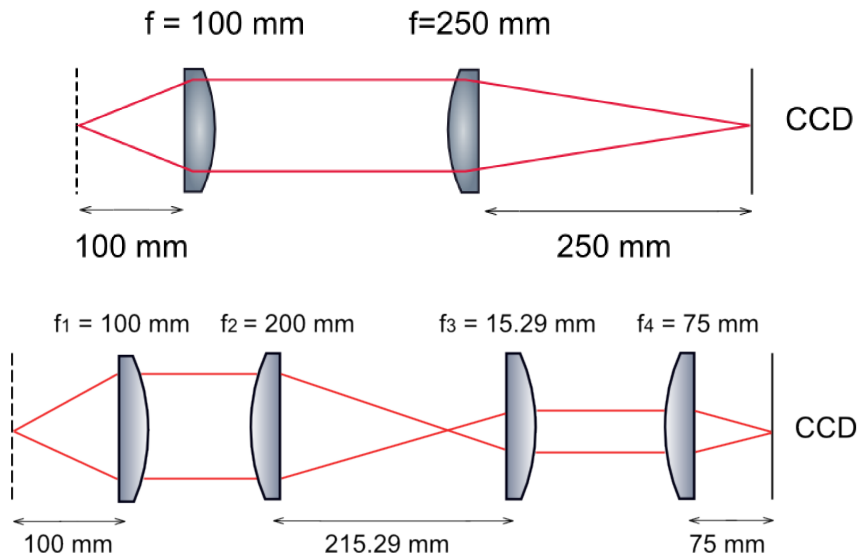


Figure 3.6 — Top: Lenses of the horizontal imaging system with a magnification of 2.17. The vertical dashed line and the solid line indicate the atomic plan and the camera respectively. Bottom: Lenses of the vertical imaging system with a magnification of 8.4. Images taken from [103]

3.3.3 Vertical imaging system

Since we examine the atomic clouds confined at the bottom of the bubble with a disk shape, a probe beam shining from top to bottom to observe the density profile from above is necessary. Such a vertical imaging system also allows to see vortices after TOF and annular clouds.

The imaging system is composed of 4 lenses and reaches a magnification of $G = 8.4$ with a resolution of $4 \mu\text{m}$, as shown in Fig. 3.6. The depth of field of the system is around $70 \mu\text{m}$ which is comparable with the vertical radius of the bubble in the usual

condition of a rf frequency of 300 kHz and a magnetic gradient of $59.0 \text{ G} \cdot \text{cm}^{-1}$ (28.5 A).

For vertical imaging, the atoms position is different depending whether one performs *in situ* imaging or TOF imaging. The imaging plane has to be shifted from the free fall distance during usually from 23 ms to 30 ms, corresponding to 2.6 mm to 4.4 mm. Therefore, the vertical imaging system is installed on a 3 axes micrometric translation and can be displaced vertically to ensure an optimal focus for the images.

The probe beam pulse is 20 μs long and is circularly polarized, with a waist of 0.7 mm. A vertical bias magnetic field of 1.9 G is also present to polarize the atoms. Before the absorption on the $|5S_{1/2}, F = 2\rangle \rightarrow |5P_{3/2}, F = 3\rangle$ transition, the atoms have to be repumped to the $|5S_{1/2}, F = 2\rangle$ state. For the TOF pictures, we use a repumping beam resonant with the $|5S_{1/2}, F = 1\rangle \rightarrow |5P_{3/2}, F = 2\rangle$ transition because the atomic density is low and there are no problems of total absorption of the repumping beam.

For *in situ* imaging, because of the high atomic density, we use another repumper far detuned compared with the above transition. With the reduced cross section the atoms can be uniformly repumped, and in addition we can control the fraction of repumped atoms, as explained in section 3.3.1.

The camera for the vertical imaging is a Luca-R EMCCD from Andor, with a 1004×1002 pixel matrix and a $8 \times 8 \mu\text{m}^2$ pixel size. An interferential filter located just before the lens prevents the 532 nm stirrer beam to enter the camera (see Chapter 5).

Through the TOF images we can observe structures in the clouds, as the vortex lattice or the specific shape of a rotating ring of superfluid (see Chapter 5). With *in situ* pictures, we can observe the profile of the trapped clouds, and also the shape of specific excitations.

We have now prepared a Bose-Einstein condensate at the bottom of a bubble-shaped trap. This superfluid degenerate gas is the starting point for the three experiments I am going to describe in the following chapters.

Chapter 4

Ultracold atoms trapped in a gravity compensated bubble trap

The physics of ultracold atoms in a microgravity environment has always attracted a lot of interest. Ultracold atoms in microgravity is a good platform to investigate fundamental physics, for instance, studying dark matter [56], testing the Einstein equivalence principle [57, 58], investigating the improved atom interferometry [59, 60]. In order to study cold atoms in a microgravity environment, the European collaboration QUANTUS performed laser cooling and trapping of atoms to produce the first BEC in space in a launched rocket flying in free fall for 6 minutes [64]. In addition, NASA has launched the Cold Atom Laboratory (CAL) to the International Space Station (ISS) [65], which is designed to produce ultracold degenerate quantum gases of rubidium and potassium [111]. The desired investigation topics are about magnetic-lensing techniques [66], few-body dynamics and bubble-shaped gases [67]. Among these topics, ultracold degenerated gases confined on the surface of a bubble trap is expected to exhibit interesting behaviors due to the special topological geometry. In microgravity, a hollow-shaped BEC can form, which shows different properties compared with a bulk BEC, such as the collective modes of a hollow BEC [112], the critical temperature [113] and the BKT phase transition [114] of a bubble-shaped BEC. In addition, the distribution of the vortices on the bubble surface is also interesting. The total number of vortices is always an even number because a vortex always has a corresponding antivortex. For a two-dimensional thin hollow BEC, the vortex-antivortex pair exhibits a long-range attraction [115].

On Earth, many groups try to investigate cold atoms physics in microgravity through their specially designed experimental setups, for example, realizing microgravity in a drop tower [59], compensating gravity by a linear optical potential [61] or cancelling the gravity by a magnetic field gradient [62, 63]. In our experiment, due to the inhomogeneous distribution of the Rabi coupling on the resonant surface of the bubble trap, the atoms actually undergo a force pushing them upwards. Therefore, we can achieve a microgravity environment as long as this upward force exactly equals to the force of gravity.

In this chapter, we will first introduce the principle of compensating gravity in the bubble trap and give a theoretical prediction of the microgravity condition. If the upward force is larger than the force of gravity, atoms are pulled to the top of the bubble and escape from the hole where the Rabi coupling vanishes. Therefore, we can roughly check this predicted microgravity condition experimentally by measuring the atom number as a function of the upward force. In order to obtain a perfect gravity compensated bubble trap, it is necessary to generate a perfectly circularly polarized rf field in the horizontal plane, which requires a fine alignment of the amplitudes and the phases of three rf antennas. Thus we will present the way of performing these fine alignments. However, once gravity is compensated, atoms do not distribute over the whole surface of the bubble as expected. Surprisingly, they form a levitating ring-shaped gas near the equator. To understand this behavior, we will improve the analytical model that takes into account the inhomogeneous transverse confinement. The improved model is in qualitative agreement with the experimental results. Finally, we will use this model to show how the atoms spread in the bubble trap when we increase the upward force by changing the Rabi coupling.

4.1 Gravity compensation mechanism

4.1.1 Analytical predictions

In Chapter 2, we have presented the principle of the bubble trap as well as the distribution of the local Rabi coupling on the resonant surface with a circularly polarized rf field. If we assume that all the atoms are exactly trapped on the resonant surface of the bubble and we make the rotating wave approximation (RWA), the Rabi coupling on the resonant surface is given by:

$$\Omega_-(z) = \frac{\Omega_0}{2} \left(1 - \frac{2z}{r_b} \right) \quad (4.1)$$

where $r_b = \omega_{\text{rf}}/\alpha$ is the semi-major radius of the bubble. The on-bubble potential is composed of the resonantly dressed adiabatic potential (2.34) and the gravitational potential energy, and reads:

$$V_{\text{bub}}(z) = \hbar\Omega_-(z) + Mgz \quad (4.2)$$

$$= \frac{\hbar\Omega_0}{2} \left(1 - \frac{2z}{r_b} \right) + Mgz \quad (4.3)$$

$$= \frac{\hbar\Omega_0}{2} + \left(Mg - \frac{\hbar\Omega_0}{r_b} \right) z. \quad (4.4)$$

This means that an upward force due to the inhomogeneous Rabi coupling $\hbar\Omega_0/r_b$ opposes gravity and attracts the atoms towards the hole at the top. Thus, the microgravity condition can be written:

$$Mg = \frac{\hbar\Omega_0}{r_b} \quad (4.5)$$

which can be also written as the condition on the maximum Rabi coupling Ω_0 for a given bubble geometry with a radius r_b , under the form:

$$\Omega_0 = \frac{Mg}{\hbar} r_b. \quad (4.6)$$

This condition can be easily understood: when the accumulation of the gravitational potential energy from the bottom to the top (Mgr_b) is equal to the decrease of the Rabi coupling energy from the bottom to the top ($\hbar\Omega_0$), gravity will be exactly compensated. Because r_b depends on the magnetic gradient and the rf dressing frequency, for a fixed rf frequency, we can achieve a microgravity environment by adjusting the magnetic gradient or the maximum Rabi coupling.

4.1.2 Experimental verification of the threshold

We have given the analytical prediction for the condition to achieve microgravity, described in equation (4.6). Here I will present an experiment designed to roughly verify the predicted condition. If the magnetic gradient is increased, the minor axis of the bubble will be reduced. So for a given Rabi coupling Ω_0 , increasing the magnetic gradient leads to an increase of the upwards force. Therefore, when we fix the Rabi coupling and increase the magnetic gradient, atoms will first undergo a force downwards when gravity dominates, then gradually go into a microgravity environment as gravity is compensated, and finally undergo a force pushing them upwards to the top hole where atoms can escape from the trap. So we can measure the atom number while increasing the gradient and upward force in order to verify if gravity is compensated.

As usual, we first prepare the atoms confined at the bottom of the bubble with a quadrupole current 28.5 A, an rf dressing frequency 300 kHz and a fixed Rabi coupling. After that, we increase the quadrupole current to a final value in 300 ms to compress the bubble. Finally, after waiting another 200 ms in the compressed bubble, we take a (23 ms) TOF absorption image and measure the atom number. We took three series of experiments with different maximum Rabi coupling: $2\pi \times 93.8$ kHz, $2\pi \times 79.0$ kHz and $2\pi \times 65.8$ kHz, which are plotted in Fig. 4.1. The three experimental series show a clear threshold after which the atom number drops dramatically, which indicates that the atoms start to escape from the top hole once the upward force overcompensates gravity. During these experiments, an rf knife at $2\pi \times 365$ kHz is always applied to evaporatively cool down the atoms. After fitting the decay by a linear slope, we also obtain the critical current I_c where the atom number is the half of the average atom number in the constant plateau at low current. The critical currents for the cases of the three different maximum Rabi couplings are 47.3 A, 54.1 A and 63.5 A respectively, shown in Fig. 4.1. Through the equation (4.6), the corresponding predicted currents compensating gravity should be 47.0 A, 55.8 A and 63.5 A. Comparing the critical current determined experimentally and the predicted current compensating gravity, they are very close especially for the $2\pi \times 93.8$ kHz Rabi coupling. Therefore, the sharp decrease of the atom number shows that the atoms indeed undergo a upward force to push them to the top. The predicted microgravity condition and the measured critical

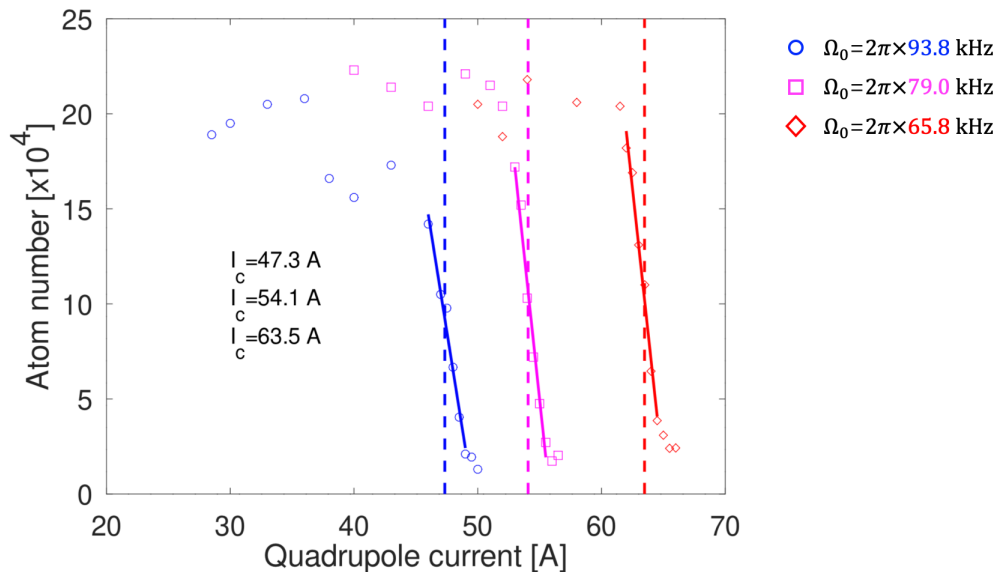


Figure 4.1 — Atom losses as a function of the quadrupole current for three different setting Rabi coupling: $\Omega_0 = 2\pi \times (93.8, 79.0, 65.8)$ kHz, respectively corresponding to blue circles, magenta squares and red diamonds. The solid curves are linear fit of the decay. The critical current is defined by the current for which the atom number is half of the average atom number in the constant plateau at low current.

currents are in fair agreement, indicating that the gravity compensation mechanism is verified experimentally.

The Rabi coupling depends on the rf magnetic field amplitude which is linked to the current in the antennas. It is controlled by our DDS. The calibration of the Rabi coupling with an rf spectroscopy, see Sec. 2.3.5, was done at $2\pi \times 93.8$ kHz. For other values of the Rabi coupling, they are assumed to depend linearly on the current as we did not perform a spectroscopy to measure the real Rabi coupling for other values to check if they are in agreement. It means that in the two experiments at lower rf amplitude, the true Rabi coupling could be slightly different from $2\pi \times 79.0$ kHz and $2\pi \times 65.8$ kHz.

4.2 Detailed study of the bubble trap in microgravity

In the previous section, we have estimated the condition for ensuring gravity compensation and presented its experimental verification as measured on the apparition of atom losses as the atoms are pushed towards the hole at the top. In this section, we will present the in situ images of the clouds taken from above and analyze the atomic distribution on the surface of the bubble when gravity compensation is realized. In order to reach the situation for gravity compensation, at first, a rotationally symmetrical bubble trap is necessary. Any inclination of the horizontal antennas may leads to an elliptically polarized rf field. For this reason we place an antenna of vertical axis below

the science cell in order to cancel the vertical component of the rf field and make the rf polarization belong to the horizontal plane. Each antenna has two parameters, the phase and the amplitude, such that three antennas have six independent parameters. In this section, I will also present a method to finely adjust the parameters of the antennas to obtain a circularly polarized rf field. Finally, I will show what the atomic cloud becomes when the atoms are confined in the bubble trap in microgravity.

4.2.1 Experimental sequence

The experimental sequence for realizing the conditions for microgravity is the same as the one designed to detect the atom losses, described in the previous section. Previously, we have shown that the microgravity condition can be regarded as the competition between an upward force $\hbar\Omega_0/r_b$ and the force of gravity Mg . Since Mg is constant, the microgravity condition in fact depends on the ratio between the maximum Rabi coupling potential $\hbar\Omega_0$ and the bubble vertical diameter r_b . Once one is fixed, the other one will be also determined by the analytical prediction, shown in equation (4.6). We would like to have a large bubble that will make the observation of the atomic density easier. However, considering that in microgravity the atoms will be distributed on the whole surface of the bubble, the vertical extension of the bubble should be smaller than the depth of field of the vertical imaging system in order to have the atoms always in the focal plane of the camera. Finally we set the minor axis of the bubble to a value of $46\ \mu\text{m}$ corresponding to a quadrupole current 45 A, which is smaller than the depth of field of $70\ \mu\text{m}$. For such a radius, the maximum Rabi coupling should be $2\pi \times 93.8\ \text{kHz}$ to achieve microgravity, see Fig. 4.1. Therefore, after ramping the quadrupole current from 28.5 A to 45 A in 400 ms and waiting for 1200 ms to damp any residual excitation, we take an in situ absorption image, shown in Fig. 4.2. While loading atoms at the bottom of the bubble, evaporation is performed with an antenna of horizontal axis. Since the field of this rf-knife is linearly polarized, it may break the rotational symmetry of the bubble trap. Therefore, when we start to increase the current and compress the bubble, the rf knife is switched off for the subsequent steps.

Surprisingly, we obtain two spots located on a diameter instead of a rotationally symmetric cloud. In order to figure out the relative position of these two spots on the bubble, we realise an rf spectroscopy on the cloud, as explained in Sec. 2.3.5: we measure the remaining atom number locally, in two regions around the two spots, as a function of the applied rf frequency of the probe. The spot labelled "A" in Fig. 4.2 is resonant around $2\pi \times 47\ \text{kHz}$ while the spot labelled "B" is resonant around $2\pi \times 44\ \text{kHz}$. Compared to the maximum Rabi coupling at the bottom $2\pi \times 93.8\ \text{kHz}$, it indicates that this spot A is situated $0.46\ \mu\text{m}$ below the equator while the spot B is located $1.4\ \mu\text{m}$ above the equator.

Let us figure out why we have two spots when compensating gravity. In Chapter 2, we have shown that if the rf field is perfectly circularly polarized, there is only one hole appearing at the top of the bubble. If the rf field polarisation is elliptical or linear in the horizontal plane, there are two holes located symmetrically with respect to the z axis. In this case, the potential minima on the bubble surface are located at the position of these two holes, and the atoms undergo a force attracting them to

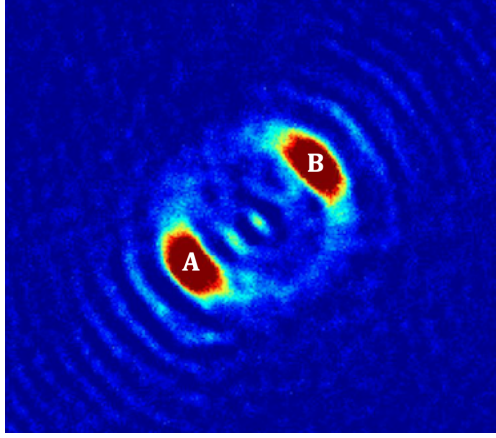


Figure 4.2 – In situ image of the atomic cloud confined on the surface of the bubble trap when the condition for microgravity is met.

the holes' position. It results in two clouds located symmetrically with respect to the z axis. The top view of these two clouds should verify this symmetry, as the clouds shown in Fig. 4.2. Therefore, this unexpected experimental result could be caused by a non perfectly horizontal circular polarization of the rf field. Since the microgravity experiment requires a strict circular polarization, I will present the fine alignment procedure of the rf polarization next paragraph.

4.2.2 Fine alignment of the rf field parameters

Let us recall the expression for the rf field from Chapter 2:

$$\mathbf{B}(t) = B_x \cos(\omega t + \phi_x) \mathbf{e}_x + B_y \cos(\omega t + \phi_y) \mathbf{e}_y + B_z \cos(\omega t + \phi_z) \mathbf{e}_z. \quad (4.7)$$

A perfectly σ^- circularly polarized rf field requires that $B_x = B_y$, $B_z = 0$ and $\phi_y - \phi_x = -\pi/2$. The third antenna placed below the science cell with a vertical axis allows us to cancel the vertical component of the rf field generated by the two antennas with nearly horizontal axis. After the vertical component is cancelled, the rf polarization is in the horizontal plane. Therefore, in order cancel the vertical component, the magnetic field produced by the third antenna should be: $-B_z \cos(\omega t + \phi_z) \mathbf{e}_z$. Although the rf polarization now is in the horizontal plane, due to the inclination of the antennas, if we set the same amplitude and a phase difference $\pi/2$ for the two horizontal antennas, the real polarization is also a little bit elliptical and it still requires small corrections on the amplitude and the phase. To obtain a perfect circular polarisation in the experiment, here we introduce a relative amplitude correction δ_B and a phase correction δ_ϕ between the two horizontal antennas. So the rf magnetic field writes:

$$\mathbf{B}(t) = (1 + \delta_B) B_x \cos(\omega t + \phi_x) \mathbf{e}_x + (1 - \delta_B) B_y \cos(\omega t + \phi_y + \delta_\phi) \mathbf{e}_y. \quad (4.8)$$

Experimentally, our objective is to optimize δ_B to make the amplitude along x axis and y axis equivalent: $(1 + \delta_B) B_x = (1 - \delta_B) B_y$, and modify δ_ϕ to make the phase difference equal to $-\pi/2$: $\phi_y + \delta_\phi - \phi_x = -\pi/2$.

Therefore, there are four crucial parameters to make the rf field polarization circular, which are the amplitude B_z and the phase ϕ_z of the third antenna as well as the amplitude correction δ_B and the phase correction δ_ϕ between the two horizontal antennas. At first, we should align the parameters of the vertical antenna to make the rf polarisation in the horizontal plane. Optimizing the phase allows us to displace the atoms at different angular position on the bubble. Once the third antenna cancels the vertical component of the rf field following the procedure described in Sec. 4.2.2.1, the rf field polarization is in the horizontal plan. To generate a circularly polarized rf field, we then tune the amplitude correction δ_B and the phase correction δ_ϕ of the horizontal antennas, as detailed in Sec. 4.2.2.2.

4.2.2.1 Phase and amplitude of the third antenna

During the alignment procedures, we first adjust the amplitude and the phase of the third antenna. Since its parameters are independent from the parameters of the horizontal antennas, we first make the amplitudes of the latter imbalanced to generate an elliptically polarized rf field on purpose. In this way we get two clouds after compensating gravity, as shown in Fig. 4.2. From the top view of the clouds, these two clouds are located on an annular trajectory, shown in Fig. 4.3. The precise position and the atom number in the two clouds depend on the parameters of the vertical antenna. We then tune the phase and the amplitude of the vertical antenna. If the third antenna's phase is not well adjusted, the two clouds are not located symmetrically with respect to the center. As Fig. 4.3(a) shows, in the top view, the two clouds are located in the same half-circle. We then tune the phase ϕ_z to make the position of the two clouds symmetric with respect to the center, as shown in Fig. 4.3(b).

From the picture we can see that the two clouds do not have the same atom number. This can be solved by adjusting the amplitude B_z of the third antenna. When the amplitude of the third antenna is not large enough to compensate the vertical component of the rf field, the cloud on the left has much more atoms than the right one, shown as Fig. 4.3(b). After adjusting the amplitude of the third antenna, when these two clouds are almost balanced, the amplitude B_z should be well adjusted. As Fig. 4.3(c) shows, from the top view, the two clouds on the annular trajectory are centrosymmetric and balanced. This is the signature of good parameters of the third antenna. Therefore, by this way we align the phase and the amplitude of the third antenna.

4.2.2.2 Phase difference and amplitude difference of the first two antennas

After adjusting the third antenna to compensate the vertical component of the rf field, the rf field polarization is in the horizontal plane. In order to obtain a perfect circularly polarized rf field, we use an amplitude correction parameter δ_B and a phase correction parameter δ_ϕ to adjust it. In the following, I will show the procedures for getting a circularly polarized rf field experimentally by adjusting δ_B and δ_ϕ .

As seen in Chapter 2, the rf polarization in the horizontal plane writes:

$$\epsilon = \cos(\Theta) \mathbf{e}_x + e^{i\Phi} \sin(\Theta) \mathbf{e}_y, \quad (4.9)$$

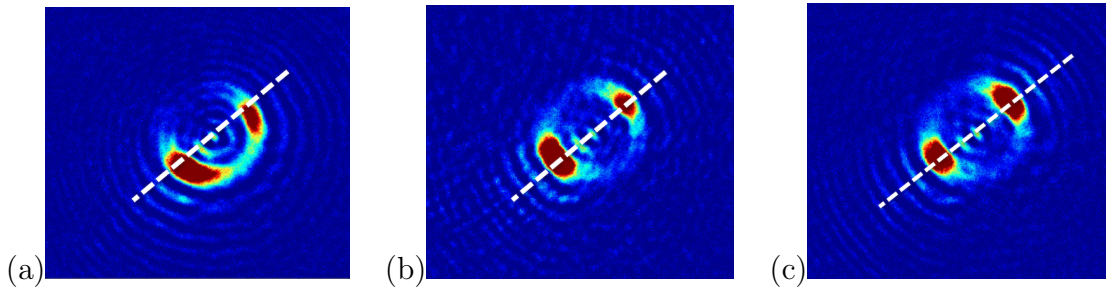


Figure 4.3 – In situ images of the atoms in microgravity, taken from above. (a): The phase and the amplitude of the third antenna are not adjusted because the two clouds are neither located symmetrically with respect to the center of the annular trajectory, nor balanced in terms of atom number. The white dashed line represents a diameter. (b): The phase of the third antenna is well adjusted but the amplitude does not exactly cancel the vertical component of the rf field because the atom number in the two clouds are imbalanced. (c) Both phase and amplitude of the third antenna are well adjusted because the two clouds are symmetric in the in situ image taken from the top.

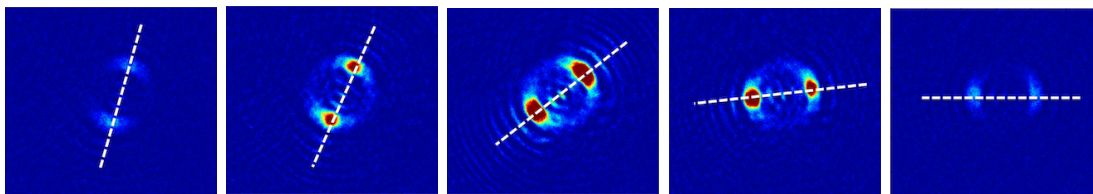


Figure 4.4 – In situ images of the atoms in microgravity, taken from above. The rf field polarization is elliptical in the horizontal plane. The maximum Rabi coupling at the bottom is $2\pi \times 93.8$ kHz. The small amplitude correction is $\delta_B = 0.024$. From left to right, the phase correction δ_ϕ is $0.05\pi/2$, 0 , $-0.025\pi/2$, $-0.05\pi/2$ and $-0.15\pi/2$.

where Φ is the phase difference between the two antennas and the $\cos \Theta$ and $\sin \Theta$ terms indicate the amplitudes of two antennas with a total amplitude normalized to 1. Thus, our aim is to make $\cos \Theta = \sin \Theta$ and $\Phi = \pi/2$. If the rf polarization is elliptical in the horizontal plane, the two holes with zero Rabi coupling are located symmetrically with respect to the z axis. We thus expect to observe two symmetric atomic clouds from the top. Their angular position is described by the polar angle θ and the azimuthal angle ϕ shown in Fig. 2.4. In the top view picture, although changing the polar angle θ should modify the distances between the two holes, in the experiment the distance between the two atomic clouds is not very sensitive to this parameter. Instead, we use the azimuthal angle ϕ to get information about both the amplitude and the phase. Through equation (2.90), the angular position of these two holes are ϕ and $\phi + \pi$ where:

$$\phi = \frac{1}{2} \arctan[\tan(2\Theta) \cos \Phi]. \quad (4.10)$$

Since we are not far from circular polarisation, $\Theta \simeq \pi/4$ and $\Phi \simeq \pi/2$. So these two

parameters can be written as: $\Theta = \pi/4 + \delta\Theta$ and $\Phi = \pi/2 + \delta\Phi$ where $\delta\Theta$ and $\delta\Phi$ are very small. Injecting these expressions into equation (4.10), we get:

$$\phi = \frac{1}{2} \arctan \left[\frac{\sin(\delta\Phi)}{\tan(2\delta\Theta)} \right] \simeq \frac{1}{2} \arctan \left(\frac{\delta\Phi}{2\delta\Theta} \right). \quad (4.11)$$

This equation shows that for a given $\delta\Theta$ the angular position angle ϕ depends on $\delta\Phi$ with an arctan shape. Experimentally, it indicates that for a given amplitude difference of the horizontal antennas the two atomic clouds in the vertical image rotate as a function of the phase difference between them. If $\delta\Theta$ is positive and almost equal to zero, the rf amplitude along x is slightly smaller than the amplitude along y . In this case, during scanning $\delta\Phi$ from negative to positive values, in the beginning the angular angle ϕ is $-\pi/4$, and then it jumps to $\pi/4$ when $\delta\Phi$ crosses 0. If we define the width of the transition as the width of the region for which ϕ goes from $-\pi/8$ to $\pi/8$, this width is $4\delta\Theta$. The goal is then to adjust the relative amplitude such that we minimize this width. If the amplitude along x is slightly larger than the amplitude along y , the same behavior occurs with the limits $-\pi/4$ and $\pi/4$ reversed, as shown in Fig. 4.5.

Experimentally, we proceed as follows to determine the optimal value for δ_B and δ_ϕ . We scan the phase correction parameter δ_ϕ for different given values of δ_B see Fig. 4.5, and we fit the data with Eq. (4.11). The function (4.11) shows that when the width of the transition becomes the thinnest, Θ is $\pi/4$ and the amplitudes of the horizontal antennas are well balanced. In addition, the good parameter δ_ϕ , corresponding to the phase difference between the horizontal antennas equal to $\pi/2$, can be determined by averaging over the centers of the arctan fits δ_ϕ satisfying $\phi = 0$ for different values of δ_B .

Fig. 4.5(a) shows that the symmetry axis of the two clouds rotates as the phase correction parameter δ_ϕ between the horizontal antennas is varied around $\pi/2$. As we have explained ϕ is either an increasing or a decreasing function of δ_ϕ , depending on the sign of $\delta\Theta$. Fig. 4.5(a) obviously shows that the variations of ϕ change sign when the amplitude correction δ_B is modified from -0.02 to -0.04. It means that the optimal value of δ_B making the horizontal antennas' amplitudes balanced should be between -0.02 and -0.04. We determine precisely the optimal value by plotting the transition widths as a function of the amplitude correction δ_B , as shown in Fig. 4.5(b), and finding the minimum width with a quadratic fit.

In principle, the optimal value of the phase correction δ_ϕ could be determined through each curve in Fig. 4.5(a). For a given amplitude correction δ_B , the phase correction δ_ϕ making $\phi = 0$, corresponding to $\delta\Phi = 0$, should be the good value for which the phase difference of the horizontal antennas is exact $\pi/2$. In order to be more precise, we determine the good value of δ_ϕ for the five cases in Fig. 4.5(a) and average them to obtain the optimal value for δ_ϕ , shown in Fig. 4.5(d). Finally, we obtain the following optimal values for the amplitude and phase corrections: $\delta_B = -0.0334$ and $\delta_\phi = -0.003257 \times \pi/2$. These values allow us to realize a perfectly circularly polarized rf field.

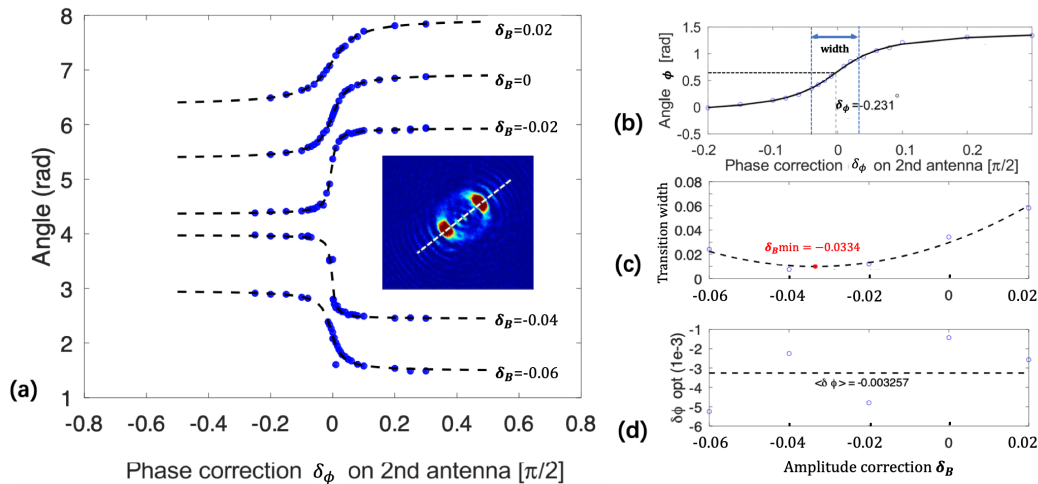


Figure 4.5 — (a): Azimuthal angle ϕ of the two atomic clouds as a function of the phase correction δ_ϕ for different amplitude corrections δ_B . The blue solid circles are the experimental results and the black dashed lines are the fits with the arctan function. The different data sets for different δ_B are shifted by 1 rad for clarity. Inset: in situ image with two clouds whose azimuthal angle is $\phi \simeq 0$, corresponding to the amplitude and phase correction of $\delta_B = -0.02$ $\delta_\phi = -0.003$. (b): Data corresponding to $\delta_B = 0.02$ in figure (a). The width of the transition is indicated. (c): Plot of the transition width for the values of δ_B presented in figure (a). We obtain the optimal value for δ_B from a quadratic fit. (d): Phase corrections δ_ϕ corresponding to $\phi = 0$ and their average value.

4.2.3 Experimental results with a pure circular polarization

4.2.3.1 A levitating ring

In the previous section I have presented the method to determine the optimal parameters to achieve a perfectly circularly polarized rf field. After setting these values, we have a rotationally invariant bubble trap which is prepared to test the condition of microgravity presented in equation (4.6). We set the maximum Rabi coupling $2\pi \times 93.8$ kHz at the bottom and the final quadrupole current after the ramp is 45 A. The sequence is the same as for the experiments of the alignments mentioned before. Surprisingly, we finally observed a levitating ring-shaped cloud instead of an expected bubble-shaped cloud with a hole at the top, as shown in Fig. 4.6. The atomic density along the ring presents variations of order $\sim 17\%$, see Fig. 4.6. In addition, the radius of the ring is around $43 \mu\text{m}$ which is smaller than the semi-major axis of the bubble $r_b = 46 \mu\text{m}$, indicating that the ring is located slightly above the equator. We wonder if this unexpected result is caused by insufficiently or over compensating gravity, so we will fix the current to keep the bubble size and scan the maximum Rabi coupling.

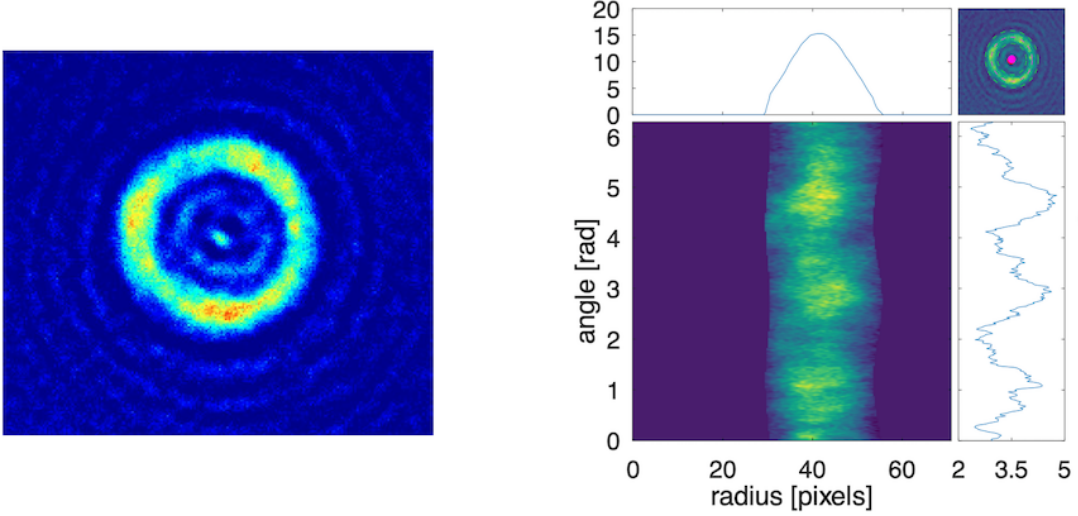


Figure 4.6 – Left: In situ image of a levitating ring-shaped cloud in microgravity after the optimization of the circularly polarized rf field. (b): Density profile of the unfolded levitating ring as a function of the radius and the azimuthal angle.

4.2.3.2 Evolution of the atomic density across the microgravity threshold

In order to figure out how does a connected cloud at the bottom of the bubble evolve into a levitating annular gas located around the equator, we will fix the final quadrupole current at 45 A and ramp the maximum Rabi coupling to different final values. More precisely, as shown in Fig. 4.7: at $t = 0.6$ s we obtain a BEC at the bottom with the maximum Rabi coupling $2\pi \times 79.0$ kHz and a current 28.5 A in the quadrupole coils; then we ramp the quadrupole current to 45 A in 0.6 s to compress the bubble while the atoms are still trapped at the bottom because such a maximum Rabi coupling is not large enough to compensate gravity; after that we remove the rf knife and hold the atoms in the compressed bubble trap for another 0.2 s; we then gradually ramp the maximum Rabi coupling from $2\pi \times 79.0$ kHz to a final target value in 1 s; after waiting for 0.1 s, we take an in situ absorption image. Scanning the ramped value of the maximum Rabi coupling from $2\pi \times 79.0$ kHz to $2\pi \times 112.6$ kHz, we observe the process of the formation of a levitating ring. Fig. 4.7 shows absorption images taken for different final values of the Rabi coupling.

As the maximum Rabi coupling increases, the force pushing the atoms upwards becomes larger and more and more atoms escape from the top hole. As shown in Fig. 4.1, when the upward force is larger and larger as compared to the force of gravity, more and more atoms escape from the hole located at the top of the bubble, leading to atom losses. We quantify this effect by measuring the remaining atom number for the sequence illustrated in Fig. 4.7 as a function of the maximum Rabi coupling. Fig. 4.8 shows that the atom number of the levitating ring decreases as a function of the maximum Rabi coupling.

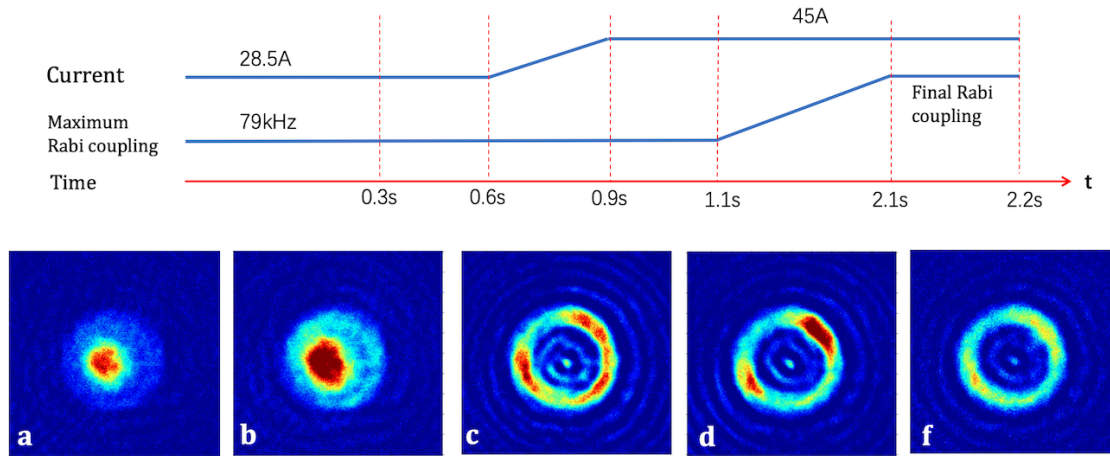


Figure 4.7 — Top: Experimental sequence used to scan the maximum Rabi coupling. Bottom: In situ images of the atomic cloud with different Rabi couplings. From figure (a) to (f), the maximum Rabi coupling is respectively: $2\pi \times (79, 82.7, 93.8, 97.8, 103.4)$ kHz.

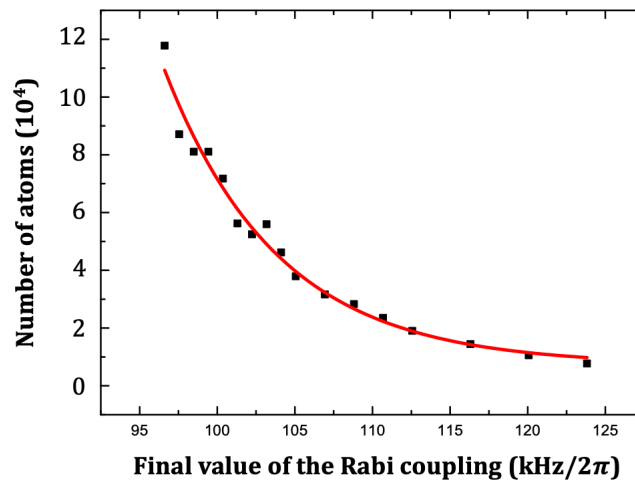


Figure 4.8 — Atom number in the levitating ring as a function of the maximum Rabi coupling in the range from $2\pi \times 95.7$ kHz to $2\pi \times 123.8$ kHz. The red solid curve is as fit with an exponential function.

The in situ images with different Rabi couplings show the process through which a connected cloud becomes an annular gas when gravity is compensated. The cloud stays ring-shaped when gravity is over-compensated. However, the on-shell potential written in equation (4.4) describing the previous analytical model shows that if gravity is exactly compensated the potential on the bubble surface should be homogeneous and equal to $\hbar\Omega_0/2$. This means that some essential factor is missing in our simple theoretical description. This essential factor is that the transverse confinement strength is not uniform on the surface of the bubble trap. We are explaining it in the next

paragraph.

4.3 Interpretation of the results

4.3.1 Improved analytical model

In the previous section, we have shown the experimental result in microgravity which is an unexpected levitating ring instead of a hollow cloud distributed on the whole surface of the bubble trap. In fact, the previous simple analytical model only considers the effect of the inhomogeneous Rabi coupling on the bubble surface and gravity but we neglected a crucial effect: the strength of the transverse confinement is not uniform on the bubble which results in a contribution to the on-shell potential. On the resonant surface of the bubble trap, the tangential trapping frequency ideally vanishes when gravity is compensated, whereas the transverse trapping frequency is large. We will thus model the tangential motion by assuming that the atoms stay in the ground state of the transverse direction and add to the longitudinal on-shell potential a contribution $\hbar\omega_{\text{trans}}(z)/2$ which takes into account the transverse ground-state energy. Therefore, based on the potential in equation (4.6), we should add another term $\hbar\omega_{\text{trans}}(z)/2$ to the complete expression of the on-shell potential due to the inhomogeneous transverse trapping frequency on the bubble. We have given the transverse trapping frequency at the bottom of the bubble in equation (2.37) of Chapter 2. The altitude-dependent transverse trapping frequency is given by:

$$\omega_{\text{trans}}(z) = \alpha(z) \sqrt{\frac{\hbar}{M\Omega(z)}}, \quad \alpha(z) = \alpha \sqrt{1 + \frac{12z^2}{r_b^2}} \quad (4.12)$$

where $\alpha(z)$ is the magnetic gradient in the direction normal to the ellipsoid, $\alpha = \alpha(0)$ corresponds to the magnetic gradient in the $x - y$ plane and $\Omega(z)$ is the local Rabi coupling (2.67). From this expression we have an idea why the atoms form a levitating ring. We could compare the transverse trapping frequency $\omega_{\text{trans}}(z)$ at three positions: the top, the equator and the bottom of the bubble. From the bottom to the equator, the value of the magnetic gradient reduces to its half $\alpha(-r_b/2) = 2\alpha(0)$ while the value of the local Rabi coupling also decreases to its half according to the equation (2.67). So the transverse frequency is decreased from the bottom to the equator, $\omega_{\text{trans}}(0) = \omega_{\text{trans}}(-r_b/2)/\sqrt{2}$. However, from the equator to the top of the bubble, the transverse frequency increases because the gradient increases and the Rabi coupling decreases. The trapping frequency should even diverge at the top where the Rabi coupling vanishes. So there must be a global minimum of the transverse frequency located around the equator of the bubble.

Let us change the variable from z to φ to describe the position on the bubble, where φ is the angle with respect to the z axis in the stretched bubble, see in Fig. 4.9. The angle φ is defined by $\cos \varphi = 2z/r_b$ or $\tan \varphi = r/(2z)$ with $\varphi \in [0, \pi]$. We can write the on-shell potential including the contribution of the inhomogeneous transverse

confinement, which reads:

$$V_{\text{shell}}(\varphi) = V_{\text{bub}}(\varphi) + \frac{\hbar\omega_{\text{trans}}(\varphi)}{2} \quad (4.13)$$

$$= \frac{\hbar\Omega_0}{2} + \left(\frac{\omega_{\text{rf}}Mg}{\alpha} - \hbar\Omega_0 \right) \frac{\cos\varphi}{2} + \hbar\alpha\sqrt{\frac{\hbar}{M\Omega_0}} \frac{\sqrt{5+3\cos(2\varphi)}}{\sqrt{8}\sin(\varphi/2)}, \quad (4.14)$$

where the first two terms are just $V_{\text{bub}}(z)$ in equation (4.4) but being described by φ and α is the magnetic gradient at the equator of the bubble. When the microgravity condition is met, the second term vanishes and the on-shell potential is determined by the third term due to the transverse confinement. We plot the transverse trapping frequency as a function of φ in Fig. 4.9. The potential minimum occurs at $\varphi = 0.55\pi$, corresponding to the altitude of $1.8\ \mu\text{m}$ below the equator in the real bubble. Therefore, after taking into account the inhomogeneous transverse confinement, in microgravity environment the potential on the bubble surface has a minimum around bubble equator instead of being uniform, which explains qualitatively the observed levitating ring.

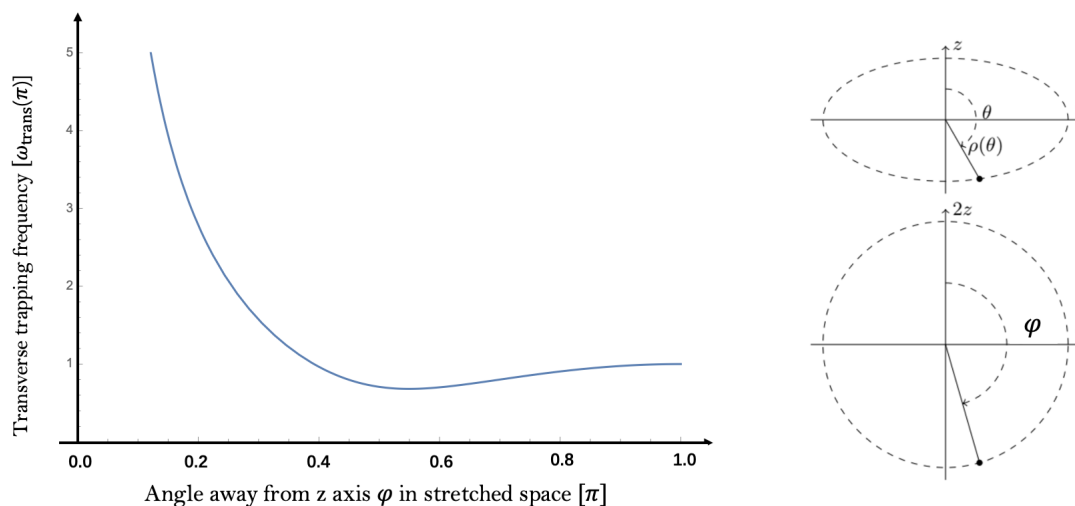


Figure 4.9 – Left: Plot of the transverse trapping frequency as a function of the angle φ/π away from the z axis in the stretched bubble illustrated on the right. Right: The bubble trap in real space (top) and the stretched bubble trap (bottom). We have discussed the spherical coordinates in the real bubble in Chapter 2 where $\rho(\theta) = r_b/\sqrt{1+3\cos^2\theta}$.

4.3.2 Numerical simulation of the experiment

In order to understand better the evolution of the atomic cloud in the process of compensating gravity, it is better to numerically simulate the atoms confined in a fixed bubble trap with different Rabi coupling. The work of the numerical simulation was

done by Romain Dubessy. In Chapter 2, we use the rotating wave approximation (RWA) under which we only consider the coupling Ω_- within a manifold. In fact, this approximation is valid for $\Omega_0 \ll \omega$. But in our experiment, the maximum Rabi coupling is around 100 kHz while the rf dressing frequency is 300 kHz, which does not satisfy the RWA condition. Therefore, we should consider the coupling between the manifolds, for instance, the coupling term Ω_+ that couples the manifold \mathcal{E}_N to the manifolds $\mathcal{E}_{N\pm 2}$ with a resonant frequency $\omega_0 + \omega$ where ω_0 is the Larmor frequency.

Under the RWA approximation, the adiabatic trapping potential can be written as equation (2.34). If Ω_+/ω is not very large, after considering the coupling terms with Ω_+ , we can follow the approach of [95] and take into account the ‘light shift’ of the main transition due to the weak coupling Ω_+ of the two main levels to levels in other multiplicities. With this perturbative approach we get:

$$V_{\text{eff}}(r, z) = \hbar \sqrt{\left[\omega_0(r, z) - \omega + \frac{\Omega_+^2}{2(\omega + \omega_0(r, z))} \right] + \Omega_-^2}. \quad (4.15)$$

However, putting this effective potential into the GPE equation and getting the atomic density fails to fit the experimental results. Consequently, a more precise trapping potential should be computed with Floquet expansion [116]. For example, the second order Floquet expansion has to consider the coupling within a manifold \mathcal{E}_N , the coupling between the manifold \mathcal{E}_N and $\mathcal{E}_{N\pm 1}$ and the coupling between the manifold \mathcal{E}_N and $\mathcal{E}_{N\pm 2}$. A given manifold \mathcal{E}_N couples with 4 other manifolds and each manifold has three substates, $m = 0, \pm 1$. So the effective Hamiltonian in the rotating frame can be described as a 15×15 matrix since there are 15 substates in the related 5 manifolds. After diagonalizing the Hamiltonian, one can deduce the eigenenergies of these substates, leading to a new trapping potential with the second order Floquet expansion. Romain Dubessy computed the on-shell equilibrium position φ for different maximum Rabi couplings with the quadrupole current 45 A for different approximations: RWA, effective potential in equation (4.15), first, second and third order Floquet expansion. After comparing these data, he found that a second order Floquet expansion is sufficiently accurate to model the trapping potential.

Injecting the trapping potential, determined through diagonalization of the Hamiltonian in the rotating frame within the second order Floquet expansion, into the Gross-Pitaevskii equation and solving it in imaginary time gives the atomic density distribution at zero temperature. In order to illustrate the formation of the levitating ring, he used the GP equation to simulate the atomic distribution on the bubble surface with various Rabi coupling Ω_0 . Fig. 4.10 presents the ground states of 10^5 atoms confined on the bubble surface with different Rabi coupling with an rf frequency $\omega_{\text{rf}} = 2\pi \times 300$ kHz and a magnetic gradient in units of frequency $\alpha = 2\pi \times 6523$ Hz $\cdot \mu\text{m}^{-1}$ corresponding to a quadrupole current 45 A. The simulation in Fig. 4.10 does not consider the Majorana losses due to the spin-flip near the hole at the top. It shows that as the Rabi coupling increases, the atomic cloud evolves from a connected cloud to an annular cloud and then this annular cloud climbs on the edges of the bubble.

Comparing with the experimental result presented in Fig. 4.7, the process of the levitating ring formation is similar but the radius and the thickness of the levitating ring

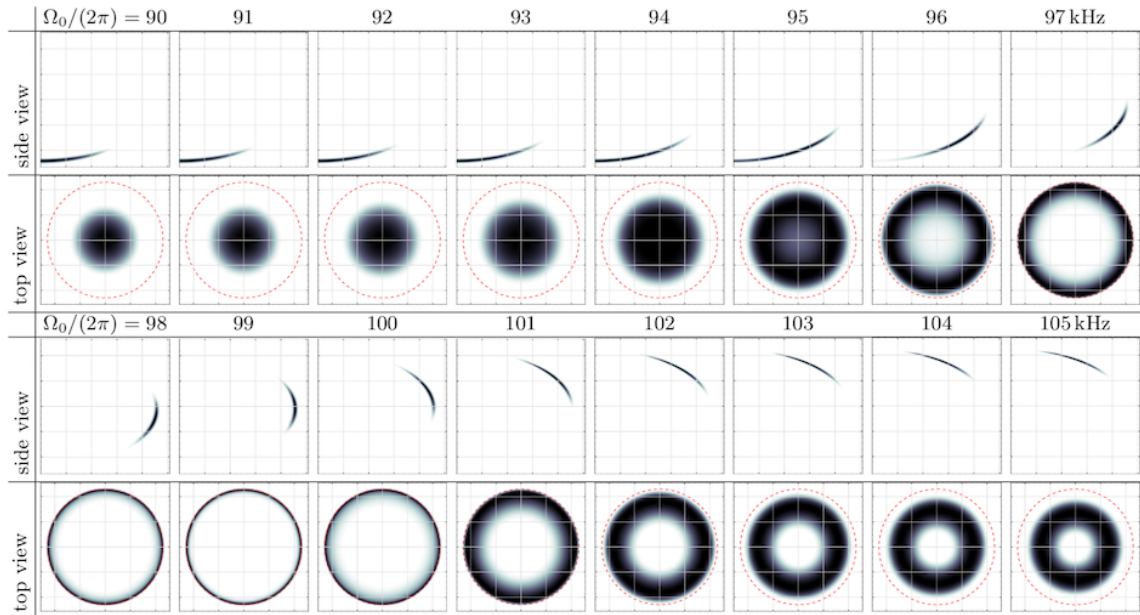


Figure 4.10 – Numerical simulation of the formation of the levitating ring with 10^5 rubidium atoms in the ground state in the full shell potential, including gravity and the ± 1 and ± 2 Floquet manifolds for different Rabi couplings. The first line is the side view of the atoms confined on the surface of the right side of the bubble and the second line shows the top view of the atoms. The red dashed circle in the top view images indicates the radius at equator. In addition, the grid lines are spaced by $10 \mu\text{m}$ for the side view and $20 \mu\text{m}$ for the top view. Pictures provided by Romain Dubessy.

for a given Rabi coupling does not agree very well quantitatively. It could be caused by three reasons: (i) The amplitude correction δ_B and phase correction δ_ϕ making the rf field circularly polarized was adjusted with the Rabi coupling 93.8 kHz , it could not be always valid for other Rabi couplings. (ii) The Rabi coupling is controlled by rf amplitude, the rf amplitude could be saturated when we ask for a large current from the amplifier. So the real Rabi coupling, especially for the large Rabi couplings, could be smaller than the expected value. (iii) The simulated atomic density distribution in Fig. 4.10 did not consider the Majorana losses. Fig. 4.8 shows that the atom losses increase as the maximum Rabi coupling increases. In the experiment there could exist an area centered around the top of the bubble in which the Rabi coupling is too small to satisfy the adiabatic condition, resulting in atom losses. For instance, as for the large Rabi couplings in Fig. 4.10, if we take the Majorana losses into account, the thickness the levitating ring could be thinner and the average radius becomes larger.

In conclusion, we succeeded in compensating gravity taking advantage of the inhomogeneous Rabi coupling on the resonant surface of the bubble trap. After finely adjusting the amplitude and the phase of the three antennas, we obtained a perfectly circularly polarized rf field. Finally, we observed a levitating annular gas located around the equator of the bubble instead of a bubble-shaped hollow cloud. We found that it

is due to the inhomogeneous transverse confinement on the bubble surface. It can be explained through the equilibrium position on the bubble surface with the trapping potential determined by the second order Floquet expansion. Our study provides a new method to achieve microgravity environment on Earth and generates a levitating ring. In future work, we will evaporatively cool down the levitating ring without breaking the rotational symmetry, by using the vertical antenna to cool the dynamical ring presented in Chapter 6. Given the low energies accessible once gravity is compensated, we demonstrated the crucial importance of describing accurately the adiabatic potential, taking into account beyond-RWA effects. Therefore, our study of the levitating ring, formed in the microgravity bubble trap, could be helpful for the study of cold atoms in microgravity environment, especially for the experiment carried out in the ISS.

Chapter 5

Superfluid flow in a ring trap

A superfluid is an irrotational fluid since its velocity is defined by the gradient of the phase. For a superfluid trapped in a connected potential, rotating a superfluid leads to the apparition of vortices, which was discussed in Chapter 1. However, for a superfluid confined in a ring trap, the presence of the vortices in the bulk of the fluid is not necessary to set the superfluid into rotation. The quantum gas confined in a ring trap has applications to quantum sensing and quantum simulation, such as: realizing atom interferometry based on the Sagnac effect [117–119], investigating the universe expansion through the analogy with a supersonic expansion of a quantum gas [120], studying the Kibble-Zurek mechanism with matter-wave interferometry [121, 122], investigating a quantized superfluid flow [29, 123] and realizing an atomtronic circuit to study electronic transport in electric circuit and to mimic a SQUID (Superconducting QUantum Interference Device) [32, 124].

The first group who achieved a ring-shaped BEC and observed a persistent atomic flow inside the trap was the group of W. D. Phillips in 2007 [28]. A ring trap can be generated in different ways: plugging a connected magnetic trap with a blue-detuned laser beam [28]; the combination of a red detuned horizontal sheet beam and a red detuned vertical annular beam in a Laguerre-Gauss mode [125]; a red detuned horizontal sheet beam and a blue detuned vertical beam with a ring-shaped mask [123]; the combination of a bubble trap generated by dressing a quadrupole trap (see Chapter 2) and a vertical standing wave [87] or a blue detuned double light sheet [88], which is the setup we use in our experiment. The ring geometry gives access to the preparation and observation of a quantized persistent flow. A persistent flow of the ring-shaped superfluid is usually generated by a stirring blue detuned laser beam [126] or by using laser beams to impart angular momentum directly onto the atoms [28, 29, 127].

In this chapter, I will first introduce the theory and the motivations for setting a ring-shaped superfluid into rotation, which is relevant to many interesting phenomena such as quantized circulation, quantum and classical phase jumps, and hysteretic behaviour of the phase transition. Then I will present the principle of the ring trap, including the construction and the procedures for loading the atoms into the ring trap. After getting a ring, I will show two independent methods to rotate the superfluid and

create the current: the stirring method already mentioned, with a blue-detuned laser beam, and a new method to set the atoms into rotation by rotating a quadrupolar trap deformation which breaks the rotational symmetry. In addition, I will also explain the way we detect the circulation by performing a time-of-flight expansion and observing the central hole due to destructive phase interference. I will then present an improved detection method for making the central hole more visible by reconnecting the annular gas at the bottom of the bubble. Finally, I will show evidences of a quantized circulation.

The construction of the setup was almost done by the two previous PhD students, Mathieu de Goër de Herve [100] and Camilla De Rossi [103]. More details on the construction and optimization of the ring trap will be found in their theses. The significant part of my work was to prepare and detect the circulation of the superfluid.

5.1 Theory of rotating annular superfluids

5.1.1 A single atom rotating in a ring trap

Let us start by examining a one-dimensional single atom model. In this section I will follow the path taken in J. Dalibard's course at Collège de France [128]. Considering an atom with mass M rotating in a ring trap with a radius r , the wavefunction ψ of the atom is described by the azimuthal angle φ . Since the ring is closed, the wavefunction satisfies periodic boundary conditions. ψ is thus periodic with a period of 2π and we have $\psi(\varphi) = \psi(\varphi + 2\pi)$. Because the potential along the ring is constant and there is no interaction, the Hamiltonian only has the kinetic term, which reads:

$$\hat{H} = -\frac{\hbar^2}{2M}\nabla^2 = -\frac{\hbar^2}{2Mr^2}\frac{d^2}{d\varphi^2}. \quad (5.1)$$

The corresponding eigenstates and eigenenergies are:

$$\psi_\ell(\varphi) = \frac{1}{\sqrt{2\pi r}}e^{i\ell\varphi}, \quad E_\ell = \frac{\hbar^2}{2Mr^2}\ell^2, \quad (5.2)$$

where ℓ is the winding number describing the phase winding of $\ell \times 2\pi$ for one period along the ring. It also indicates the circulation of a superfluid in units of h/m , which was explained in equation (1.44). The velocity of the superfluid is defined as the gradient of the phase, through the eigenstate presented above, the local velocity and the angular velocity with a winding number ℓ write:

$$\mathbf{v}(\varphi) = \frac{\hbar}{Mr}\ell\mathbf{e}_\varphi, \quad \Omega_\ell = \ell \times \frac{\hbar}{Mr^2} = \ell \times \Omega_0 \quad (5.3)$$

where Ω_0 is the circulation quantum corresponding to the angular velocity with $\ell = 1$.

Describing the motion in the frame rotating at an angular velocity of Ω allows us to make the Hamiltonian time-independent. The Hamiltonian in the rotating frame

reads:

$$\hat{H}_{\text{rot}} = \hat{H} - \Omega \hat{L}_z = -\frac{\hbar^2}{2Mr^2} \frac{d^2}{d\varphi^2} + i\hbar\Omega \frac{d}{d\varphi} \quad (5.4)$$

$$= \frac{\hbar^2}{2Mr^2} \left(-i \frac{d}{d\varphi} - \frac{\Omega}{\Omega_0} \right)^2 - \frac{1}{2} M \Omega^2 r^2. \quad (5.5)$$

The eigenstates in the rotating frame are the same than the ones in the laboratory frame (5.2), but the eigenenergies then become:

$$E_\ell(\Omega) = \frac{\hbar^2}{2Mr^2} \left(\ell - \frac{\Omega}{\Omega_0} \right)^2 - \frac{1}{2} M \Omega^2 r^2. \quad (5.6)$$

The last term is the centrifugal energy, which is uniform along the ring and it doesn't depend on the azimuthal position nor on the winding number. We can thus remove the centrifugal term by changing the origin of energies for different Ω . Therefore, the energy of the state corresponding to a winding number of ℓ becomes:

$$E_\ell(\Omega) = \frac{\hbar^2}{2Mr^2} \left(\ell - \frac{\Omega}{\Omega_0} \right)^2. \quad (5.7)$$

The energy spectrum with different ℓ is plotted in Fig. 5.1. For a given ℓ , the energy as a function of the angular velocity is a parabola which is symmetric about $\Omega = \ell\Omega_0$. The spectrum is periodic with a period of Ω_0 , we then have: $E_\ell(\Omega) = E_{\ell+n}(\Omega + n\Omega_0)$. For a potential rotating at Ω , the corresponding ground state is ψ_ℓ where $\ell\Omega_0$ is the closest to Ω . Therefore, the ground state changes as a function of the angular velocity of the rotating potential. When $|\Omega| < \Omega_0/2$, the ground state corresponds to $\ell = 0$ and is a non-rotating state.

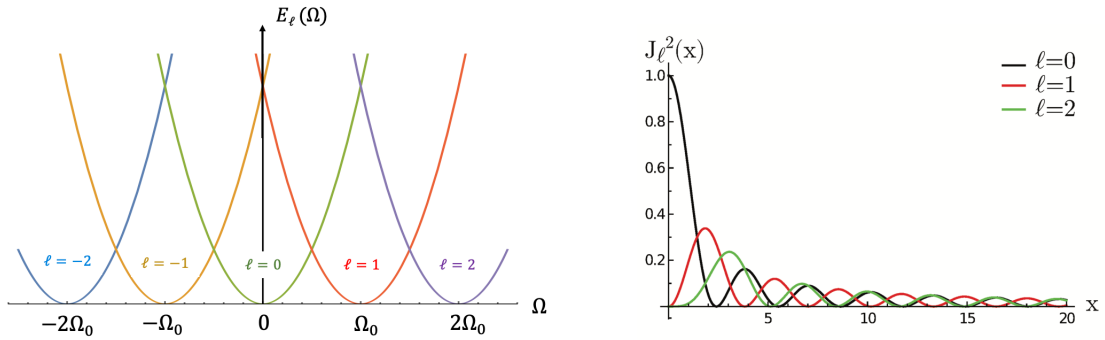


Figure 5.1 — Left: Energy spectrum of the different ℓ states as a function of the angular velocity Ω . Right: The square of the first kind Bessel function of order 0 (black line), 1 (red line) and 2 (green line).

The detection of the superfluid flow relies on the atomic density distribution after a TOF by using the method of "self interference", as first observed by the group of W. D.

Phillips [28]. When the atoms in the ring are at rest, the phase is uniform at different positions. In this case, after switching off the trap and letting the atoms expand freely during a TOF, the atoms at different places of the ring overlap and constructively interfere at the center forming a density peak. When the atoms rotate with a winding number $\ell \neq 0$, after TOF the atoms with all possible phases overlap at the center and interfere destructively, forming a density zero at the center in a region which is broader for a larger $|\ell|$. By this way, we can determine if there is a flow in the ring trap.

More precisely, the distribution after a TOF, in the absence of interactions, is simply related to the momentum distribution in the trap. In order to distinguish different winding number ℓ , we go to the simple 1D model and investigate the atomic density distribution after the TOF with different winding number. The density distribution after TOF describes the momentum space of the atoms, which can be deduced by the square of the Fourier transform of the wavefunction. The wavefunction in momentum space for a given momentum p is proportional to the Bessel function $J_\ell(rp)$. The momentum distribution of the atoms as a function of $x = rp$ is plotted in Fig. 5.1 (right). The figure shows that the maximum in momentum increases as a function of the winding number ℓ . Therefore, for a non zero winding number, the larger the circulation, the larger the hole at the center. It provides a method to determine the modulus of the circulation $|\ell|$ of a superfluid flow in the ring trap.

5.1.2 Phase jump and persistent flow

In the previous section, we have derived the energy spectrum with discrete circulation states in a one-dimensional ring trap and we have seen that the ground state is a given ℓ state which depends on the rotation frequency of the potential. The increase or decrease of the rotation may thus trigger the transition between the states through a change in the phase winding [29, 129].

If the ground state changes from ℓ to $\ell - 1$ due to the decrease of the rotation rate, this transition presents an hysteretic behavior instead of a continuous transition. The transition from the state ℓ to $\ell - 1$ occurs with a phase slip as the phase winding jumps from $\ell 2\pi$ to $(\ell - 1)2\pi$. The phase jump happens for a rotation rate Ω such that $(\ell - 1)\Omega_0 < \Omega < (\ell - 1/2)\Omega_0$, which explains the hysteretic behavior.

Fig. 5.2(a-b) presents the hysteresis loops realized in the group of G. K. Campbell. A circulation was created in the annular gas by a rotating a blue-detuned laser which could produce a potential barrier and reduce the local atomic density. After preparing either a non rotating ring or a rotating ring with $\ell = 1$, they rotated the barrier at various frequencies with two different barrier heights in order to measure when the phase jump occurs. In both cases, an hysteresis loop is present, indicating that the phase slip happens beyond $\Omega_0/2$. Moreover the hysteresis loop becomes wider if the repulsive potential decrease. The hysteresis displaces the threshold frequency of the transition between the states, leading to a metastable superfluid flow.

Up to now, we considered the energy spectrum and the momentum distribution of the atoms by analyzing the simple 1D model. In interacting gases, the phase jump in 1D ring is due to the creation of a soliton which is determined by the interaction strength, rotation frequency and the barrier height [129]. However, in the experiments

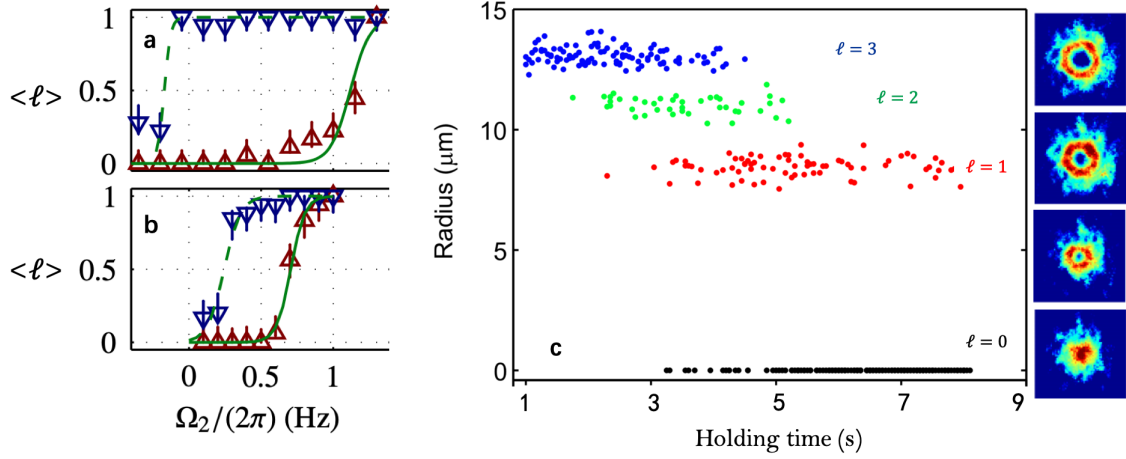


Figure 5.2 – (a-b): Hysteresis loop of the states transition with a small (a) or large (b) barrier potential. The red and blue triangles show the average winding number corresponding to a initial state of $\ell = 0$ and $\ell = 1$, respectively. Taken from [30]. (c): Time evolution of the hole radius after TOF evidencing the discrete values it takes, corresponding to $\ell = 3, 2, 1, 0$. Right: four TOF pictures showing the typical size of the hole or a density peak in the center. Figure is taken from [29].

until now, the realized ring trap is still in 2D or 3D regime.

In 2D or 3D regime, the ring has a radial thickness that allows the presence of vortices in the bulk of the ring. Instead of introducing a soliton to trigger the phase jump as in a 1D ring, in this case a vortex can cross the annulus and enter inside the ring to generate a phase jump of 2π [130]. It can happen, for example, when a blue-detuned laser creates a barrier in the ring and excites the ring. In the 2D regime, measuring the size of the hole after TOF also enables to identify the different circulations, as shown in Fig. 5.2(c) realized by the group of Z. Hadzibabic. This experiment started by preparing a circulation of $\ell = 3$, then waiting for a given time and finally measuring the hole radius after TOF. The radius, or the size, takes discrete values for different circulations.

5.2 Experimental realization of an annular trap

5.2.1 Principle of the ring trap

In our experiment, benefiting from the smooth surface of the bubble trap, our ring trap is constructed by adding a horizontal blue-detuned double light sheet beam intersecting the bubble, which confines the atoms at the equator of the ellipsoid [87]. The principle of the ring trap is shown in Fig. 5.3.

The blue-detuned light sheet beam of wavelength 532 nm had been installed by the previous two PhD students in the group, the details of the installation and the alignment were written in their theses [100, 103]. The double light sheet is shined along

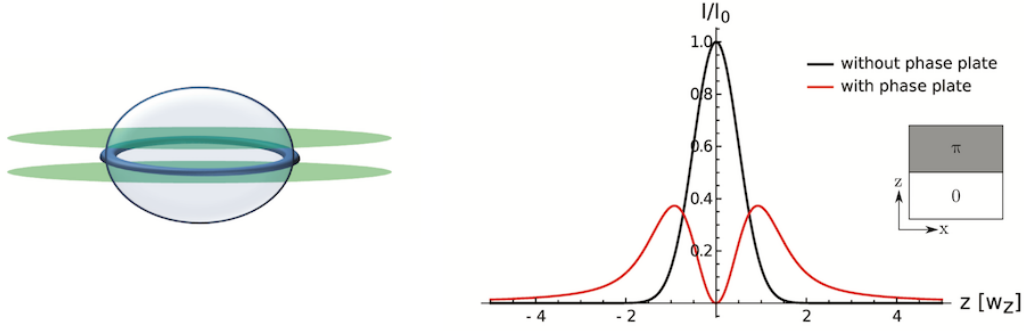


Figure 5.3 – Left: Principle of the ring trap. The light blue ellipsoid shows the isomagnetic surface of the bubble trap and the green sheets indicate the blue-detuned light sheets. Their intersection generates a ring trap plotted in dark blue. Right: Intensity profile of the double light sheet beam (in red) going through the phase plate and the Gaussian beam profile without crossing the phase plate (in black). Inset: scheme of the $0 - \pi$ phase plate. Figure taken from [100]

the y axis which is aligned with the horizontal probe beam. It is generated by placing a $0 - \pi$ phase plate on the path of a blue-detuned very anisotropic Gaussian beam. When the beam passes this phase plate, the phase of the upper half beam is shifted by π with respect to the lower half beam. This phase difference generates a horizontal plane where the light intensity vanishes due to the destructive interference, shown in Fig. 5.3. The atoms thus undergo a repulsive force which pushes them towards the center of the light sheet. In the horizontal plane where they are confined, the vertical trapping frequency reads [88]:

$$\omega_z(x) = \frac{4}{\pi} \sqrt{\frac{\eta_L P_0}{M w_z^3 w_x}} e^{-\frac{x^2}{w_x^2}}, \quad (5.8)$$

where $\eta_L = 1.22 \times 10^9 \text{ Hz} \cdot \text{W}^{-1} \cdot \mu\text{m}^2$ and P_0 is the total power in the light sheet beam. The light sheet beam has a focused waist of $w_z = 6 \mu\text{m}$ in the vertical direction and is collimated to $w_x = 200 \mu\text{m}$ in the horizontal direction. This produces an optical potential with a maximum oscillation frequency in the harmonic approximation of $2.72(2) \text{ kHz}$ measured with a laser power of 3 W . In the experiment we typically use a reduced laser power of 300 mW , leading to a calculated vertical oscillation frequency of 850 Hz .

Since the ring is at the equator of the bubble, the radius of the ring is the same as the semi-major axis of the ellipsoid, which reads $r = \alpha/\omega_{\text{rf}}$. The radial confinement is independent of the dipole trap and can be deduced from the equation (2.37):

$$\omega_r = \alpha \sqrt{\frac{2\hbar}{M\Omega_-}} \quad (5.9)$$

in which Ω_- is the maximum Rabi coupling at the bottom of the bubble and the one at the equator is half of the maximum value. For our ring trap, the current in the

coils is 90 A and we work with a dressing frequency of 300 kHz resulting in a radius of 23 μm . With such a gradient and with the maximum Rabi coupling of 93.8 kHz, the theoretical radial trapping frequency is 647.2 Hz, which is comparable with the measured oscillation frequency 643(1) Hz [100].

Once we have the radius and the confining frequencies of the ring trap, we can deduce the chemical potential. For the ring trap with oscillation frequencies ω_r, ω_z and assuming a uniform azimuthal confinement, the chemical potential for a 3D gas in the Thomas-Fermi regime can be written as [87]:

$$\mu_{3D} = \hbar\bar{\omega}\sqrt{\frac{2Na}{\pi r}}, \quad (5.10)$$

where $\bar{\omega} = \sqrt{\omega_r\omega_z}$ is the geometrical average of the oscillation frequencies. The chemical potential is estimated to be $\mu = \hbar \times 3 \text{ kHz}$ for $\omega_r = 2\pi \times 650 \text{ Hz}$, $\omega_z = 2\pi \times 850 \text{ Hz}$ and $N = 10^5$. Since in this case $\mu_{3D}/\hbar > \omega_r, \omega_z$, the quantum gas studied in this work is well inside the 3D regime.

5.2.2 Loading atoms into the ring trap

Now that I have given the principle of the ring trap and I will detail the procedure for loading the atoms into the trap. The overall loading procedure consists of four steps: (i) confining atoms at the bottom of the bubble trap; (ii) shifting the bubble vertically to match the altitude of the atoms with the intensity minimum of the double light sheet; (iii) switching on the double light sheet to compress the atoms inside; (iv) compressing the bubble by ramping the magnetic gradient while displacing the magnetic zero to bring the atoms at the equator. During the first three steps, the current in the quadrupole coils stays at 28.5 A and the rf dressing frequency at 300 kHz. In the last step, the current in the coils is ramped to 90 A, which results in a compressed bubble whose radius is 23 μm . In Chapter 3 we have seen how to confine the atoms at the bottom of the bubble. For the fine alignment for matching the atoms into the potential minimum of the double light sheet and the precise procedure for compressing the bubble and forming the final ring trap I refer to Appendix B.

In addition, while the atoms are loaded into the light sheet, the rf knife is applied to cool down the atoms, at a frequency 15 kHz higher than the minimum trapping potential. When the bubble is shifted to displace the atoms from the bottom to the equator of the bubble, the Rabi coupling at which the atoms are trapped decreases by half of the initial value. Therefore, during this phase, the rf-knife kept at fixed frequency is at a much higher height from the trap bottom, namely the Rabi frequency plus 15 kHz. After the atoms have been loaded in the final ring trap, the knife is thus decreased again to bring the relative depth of the trap back to 15 kHz.

5.2.3 Imaging the annular gas

5.2.3.1 In situ image

After following the steps presented above, atoms are confined at the equator of the bubble. We then wait for another 500 ms to cool down the cloud, and take an in situ image of the atoms in the ring trap, shown in Fig. 5.4. The method of optimizing the circularly polarized rf field is similar to the one presented in Chapter 4. The most crucial parameters are the amplitudes of the third antenna and the amplitude difference between the two horizontal antennas. By optimizing the third antenna we obtain a double-moon shaped symmetrical cloud, which is a signature of an elliptically polarized rf field in the horizontal plane. Optimizing the amplitude difference between the horizontal antennas finally leads to a circular polarization. The measured radius of the resulting ring is $23\ \mu\text{m}$ corresponding to the rf dressing frequency 300 kHz and the quadrupole current 90 A. Its vertical oscillation frequency is estimated to be 850 Hz from the frequency measured at different light powers in the double light sheet but without the bubble trap. The measured radial oscillation frequency is $643(1)\ \text{Hz}$, as described in [100].

Equation (B.3) in Appendix B presents the theoretically computed current in the bias coils needed to put the atoms at the equator of the bubble. This calculation should be checked experimentally. The way to verify if the cloud is indeed at the equator is to measure the Rabi coupling at the atomic position. The distribution of the Rabi coupling is described in equation (2.67), and is determined by the relative altitude on the bubble. Since the maximum Rabi coupling occurring at the bottom of the bubble doesn't depend on the magnetic gradient¹, the maximum Rabi coupling $\Omega_- = 2\pi \times 93.8\ \text{Hz}$ is measured with a quadrupole current 28.5 A. It should thus be $2\pi \times 46.9\ \text{kHz}$ if the atoms are at the equator. We then realize a spectroscopy to measure the Rabi coupling at the atomic position after the loading procedure and waiting time 500 ms. The resulting curve is shown in Fig. 5.4. The measured Rabi coupling is $47.9(2)\ \text{kHz}$, which indicates that the ring is $\sim 0.3\ \mu\text{m}$ below the equator.

5.2.3.2 After time-of-flight

If the ring is not rotating, the phase of the wavefunction at different angular position of the ring is identical. Thus it is supposed to generate a density peak in the center after a TOF which is long enough to let the ring expand radially and get a constructive interference. In order to estimate the typical TOF duration for which we can observe this self interference pattern, we can first investigate the expansion rate of a cigar shaped cloud which can be regarded as an open ring. For a very elongated trap, the radial trapping frequency ω_{cr} and the trapping frequency along the elongation axis ω_{cz} verify $\omega_{cr} \gg \omega_{cz}$. For this model, after expansion during the TOF, the radial Thomas-Fermi radius writes [131]:

$$R(t_{\text{TOF}}) = R(0) \sqrt{1 + \omega_{cr}^2 t_{\text{TOF}}^2}. \quad (5.11)$$

1. The Rabi frequency measured at the bottom of the ellipsoid is corrected for the gravitational sag, which puts the atoms slightly below the resonant surface.

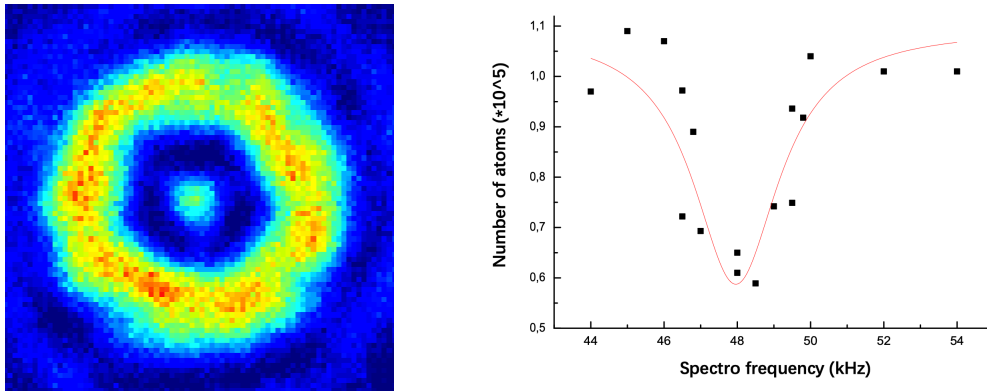


Figure 5.4 – Left: Optimized ring with $\sim 10^5$ atoms, situated around the equator of the bubble. The central dot is due to the diffraction of the imaging system and not to real atoms. Right: Spectroscopic curve fitted with a Lorentzian distribution, showing that the resonance is at 47.9(2) kHz.

The radial expansion of the ring-shaped cloud is comparable with the radial expansion of a cigar-shaped cloud. If ω_{cr} takes the value of the radial oscillation frequency of the ring, the transverse Thomas-Fermi radius after expansion becomes larger than $23\mu\text{m}$ when the TOF duration is longer than 5 ms. So for such a TOF duration, the constructive interference is achievable in the case of the ring trap. Fig. 5.5 shows the cloud after 23 ms TOF including the Stern-Gerlach procedure aiming at well separating the clouds with different Zeeman sublevels. Both horizontal and vertical images in Fig. 5.5 present a density peak in the center, which proves that the phase is uniform all along the ring.

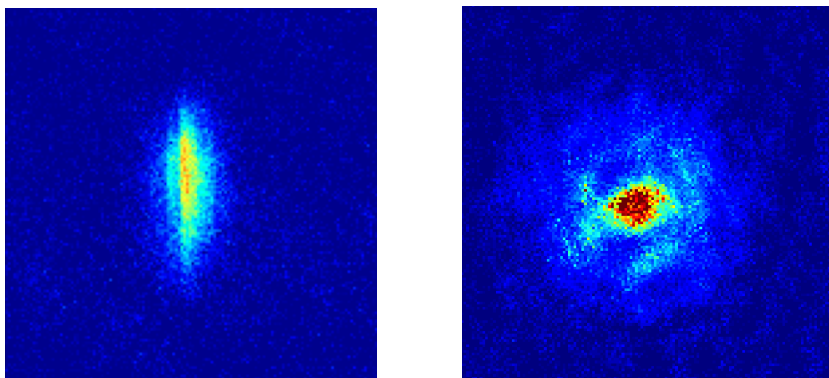


Figure 5.5 – Left: Side image of the expanding annular gas after 23 ms TOF with 0.5 ms of Stern-Gerlach delay, observed from the side. Right: Top image of the expanding ring after 10 ms TOF with a 0.7 ms Stern-Gerlach delay, observed from above.

5.3 Preparation and detection of a quantized flow

In order to investigate persistent flows and phase slips after confining atoms in the ring trap, we have to set them into rotation. Let us first estimate the elementary rotation rate Ω_0 corresponding to $\ell = 1$ in our case. The elementary rotation rate only depends on the radius of the ring, $\Omega_0 = \hbar/(Mr^2)$. The radius of our ring is $23 \mu\text{m}$, so the elementary rotation rate is 0.22 Hz . The critical rotation rate will depend in particular on the geometry of the annular gas [132]. The chemical potential for the 3D ring, computed with 10^5 atoms, is $h \times 3 \text{ kHz}$. So the thickness of the ring, equivalent to twice the Thomas Fermi radius, is $2.46 \mu\text{m}$ which is much smaller than the radius. In this very thin annulus, we expect that the critical excitation frequency, for a very weak perturbation, will be close to the speed of sound. The speed of sound in our ring is comparable with the one in an elongated cigar-shaped cloud which is $v_c = \sqrt{\mu/(2M)} = 2.6 \text{ mm} \cdot \text{s}^{-1}$ [79]. Consequently, the critical rotation rate of our ring is at most $\Omega_c = v_c/r = 2\pi \times 17.9 \text{ Hz}$. On the other hand, for a strong perturbation such as a focused beam fully depleting the density at some point, the critical velocity should be close to $\Omega_0/2$, as already shown in the Campbell group [30].

Here, I will present two experimental methods for rotating the atoms. One consists in deforming the trap and rotating the deformation. The other one consists in using a blue-detuned laser to stir the atoms in the ring trap. Both of them create at least one density dip where the vortices can enter and exit, leading to phase slips [130]. We will compare the atomic density profiles after TOF with different circulations generated by these two methods.

5.3.1 Rotating the deformed bubble

5.3.1.1 Principle

The first method to rotate the atoms is deforming and rotating the trap, in the spirit of the "rotating bucket" experiment. We change the polarization of the rf field from circular to elliptical by increasing the amplitude of one horizontal antenna while decreasing the amplitude of the other one, leading to modify the Rabi coupling distribution along the ring. It is realized by our DDS through changing $\eta = 1$ to $\eta = 1 - \delta\eta$, where η is defined as:

$$\eta = |\boldsymbol{\epsilon} \cdot \mathbf{e}_+^*|^2 = \frac{1 + \sin 2\Theta \sin \Phi}{2}. \quad (5.12)$$

Through equation (2.84), it implies that $\eta = 1$ corresponds to a circular polarized rf field as well as a uniform ring at the equator whose trap bottom potential is $\hbar\Omega_0/2$ in which Ω_0 is the Rabi coupling at the bottom of the bubble. A non zero deformation $\delta\eta$ leads to a modulation of the trap bottom in the horizontal plane, which becomes:

$$V(\phi) = \frac{\hbar\Omega_0}{2}(1 + \sqrt{\delta\eta} \cos 2\phi) \quad (5.13)$$

where ϕ is the azimuthal angle along the ring. The density is then inhomogeneous around the ring, with a characteristic double-moon shape, shown in Fig. 5.6. By

rotating the axis of the deformation, the atoms are able to be set into rotation. In the experiment, the steps taken for rotating the atoms and detecting the flow are as follows. After loading the atoms into the ring trap, we wait for a duration t_1 while evaporative cooling is applied. We then deform the trap by changing η from 1 to $1 - \delta\eta$ in 0.4 ms. After that, we rotate the deformation for t_{rot} which depends on the rotating frequency and the number of rotation turns. The trap returns to uniform in 0.4 ms and then we wait for a time t_2 while the atoms are rotating inside. In the end, we take an absorption image of the expanded cloud after TOF with a Stern-Gerlach delay.

This method is easy to implement and doesn't require further fine alignments with respect to the ones implemented to balance the density of the ring trap. It creates two potential minima where vortices can enter and exit, generating a 2π phase jump. However, a shortcoming of this method is that the amplitude of the perturbation cannot be very small because of the amplitude resolution of the DDS. The minimum achievable $\delta\eta$ is 10^{-4} , corresponding to a minimum perturbation of the deformation on the Rabi coupling around $2\pi \times 500$ Hz. Compared to the chemical potential $\sim h \times 3$ kHz, this perturbation is not small. For a larger perturbation strength, the local minimum of the chemical potential along the ring decreases. Consequently, the speed of sound corresponding to the minimum chemical potential is also reduced, leading to a smaller critical rotation rate.

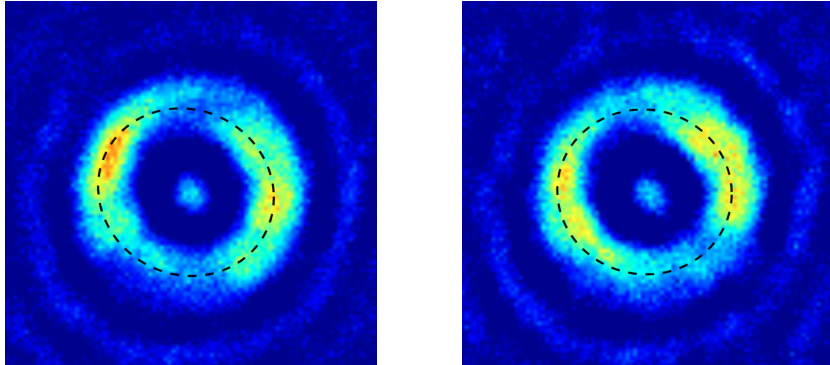


Figure 5.6 — In situ pictures of the double-moon shaped atomic cloud. These two pictures are taken during the rotation process, showing that the axis of the large atomic density is rotating.

5.3.1.2 Experimental sequences and results

We have discussed how to confine and rotate the atoms in the ring trap, now we will detect the circulation through the vertical images after TOF. Through the 1D model in section 5.1.1, we have seen that the appearance of a central hole after TOF expansion indicates a non-zero circulation of the superfluid. A larger size of the hole within the cloud corresponds to a larger circulation ℓ .

The effective rotation frequency of the superfluid after the rotating bucket process depends on three essential parameters: the applied rotation frequency Ω_{rot} , the duration

of the rotating phase t_{rot} and the amplitude of the deformation. During the rotation process, we set the peak-to-peak amplitude of the deformation to 1 kHz ($\eta = 10^{-4}$) and apply 2.5 turns of the rotating bucket. The exact experimental sequence is the following: after forming the ring and waiting for $t_1 = 500$ ms the atoms are set into rotation using the parameters given above, and then we let them rotate for another $t_2 = 500$ ms, after that we release the trap and let the atoms expand freely for a duration of the TOF of 23 ms which includes a 3 ms Stern-Gerlach procedure in the beginning of the TOF. Finally, we take an absorption image of the cloud along the vertical axis.

The TOF images corresponding to different applied rotation frequency Ω are shown in Fig. 5.7. The central holes are the signature of the circulation. As the applied rotation frequency increases, the size of the hole becomes larger. We can observe this hole for rotation rates from $\Omega \simeq 2\pi \times 7$ Hz to $\Omega \simeq 2\pi \times 30$ Hz. The expected critical rotation rate determined in beginning of this section for a very weak perturbation is 17.9 Hz. Taking into account the modulation of the trap bottom, the new critical rotation rate corresponding to the local minimum of the chemical potential ($\sim h \times 2.5$ kHz) becomes 16.3 Hz. It is still much larger than the rotation rate 7 Hz at which we first observe the hole. This could be caused by additional defects due to the roughness of the optical potential that have not been taken into account in the determination of the minimum local density and thus the critical rotation rate.

Fig. 5.7 shows that the size of the central hole in the expanded cloud depends on the circulation: the larger the winding number ℓ , the larger the size of the hole. Since the elementary rotation rate of our ring is $\Omega_0 = 2\pi \times 0.22$ Hz, the minimum achievable rotation rate to generate circulation is 7 Hz which is 32 times Ω_0 . We can not declare that the first observable central hole at 7 Hz corresponds to $\ell = 1$ nor $\ell = 32$. Once vortices have started to enter the central hole, their number also depend on the duration of the excitation and may be comprised between these two extreme values. In principle, classifying the hole sizes in histograms should enable to distinguish between different circulation states. However, the hole areas created with this rotation methods do not present well separated sizes, rather a continuous increase as a function of the applied frequency. Therefore, using this method to rotate the cloud can easily generate circulations of the superfluid but it is difficult to distinguish different circulations ℓ . Creating two potential minima to let vortices enter or exit may be not so controllable nor fully understood, and would need further investigation.

There is another method to prepare a circulation state in the ring which was used by many groups and well understood. This method uses a blue detuned laser to stir the ring. It should generate a circulation of $\ell = 1$ with a stirring frequency larger than $\Omega_0/2 = 2\pi \times 0.11$ Hz. In the following, we will use this method to rotate the atoms in order to prepare small quantized circulations in the ring.

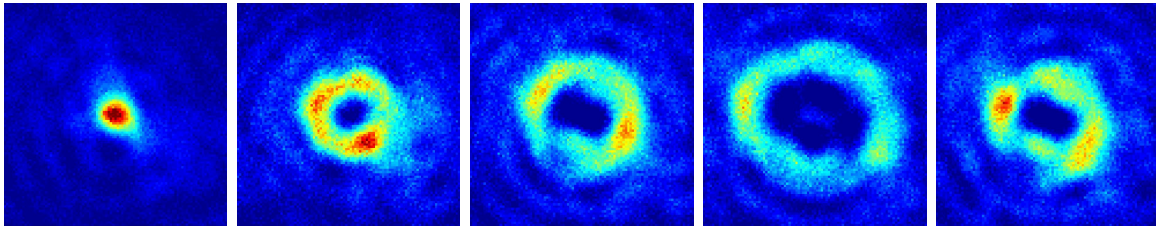


Figure 5.7 – Vertical ring pictures after the rotating phase with a quadrupole deformation, 500 ms holding time in the uniform ring trap and 23 ms TOF with 3 ms Stern-Gerlach. From left to right, the applied rotation frequency are 0, 13, 15, 18, 30 Hz. The size of the images is $100 \times 100 \mu\text{m}^2$

5.3.2 A rotating laser stirrer

5.3.2.1 Principle

The second method to generate superfluid circulations is to use a blue-detuned laser stirrer whose position is controllable. This method has been used by many other groups to rotate atoms both confined in a connected trap [34, 133] or in a ring trap [125]. In the ring trap, the density dip created by the rotating blue-detuned laser can make the vortices enter, eventually leading to an increase of circulation. This method has successfully produced circulation quanta from $\ell = 1$ to $\ell \gtrsim 12$ [123]. We will try to use it to create circulation at lower rotation frequency which is comparable with the half of the elementary rotation rate $\Omega_0/2 = 2\pi \times 0.11$ Hz.

The blue-detuned laser beam has a wavelength $\lambda = 532$ nm with maximum intensity 11 mW. Its waist is $7 \mu\text{m}$ and its Rayleigh length $\sim 200 \mu\text{m}$. This beam is derived from a part of the ALS laser which generates the plug beam. The blue-detuned laser crosses a pair of acousto-optic modulators (AOM) that can deflect the beam in two directions and the deflecting angle depends on the applied frequency. Therefore, we can control the beam to impact any position of the cloud by modifying the applied frequency on the AOMs. In the experiment, we use four types of trajectories: linearly oscillation along x or y axis and circularly rotating clockwise or counterclockwise. In the following we only use the a circular rotating trajectory. In addition, the motion of the beam is controlled by these essential parameters: stirring center, stirring radius, stirring frequency and power of the laser stirrer.

5.3.2.2 Beam focusing and position alignment

The stirring beam is injected from above the trap, after passing through the atoms it hits the vertical camera. In order to protect the camera, an interferential filter is installed to prevent the green light to reach it. To rotate the atoms efficiently, we have to first optimize the beam to focus on the atomic position. The last lens that the stirring laser crosses just before reaching the atoms can be translated. Thus, we will scan the position of this lens and detect a maximum in intensity directly with the vertical camera. Indeed, we know that the image of the atoms inside the ring is well focused on the camera. If the beam is correctly focused onto the camera, it will also be

focused in the object plane where the atoms are. Before doing that, we lower the power of the stirring beam 0.03% of its maximum intensity and remove the interferential filter. The exposure time is set to 20 ms. We then plot the maximum intensity as a function of the position of the last lens, as shown in Fig. 5.8. The maximum intensity is largest once the beam is focused.

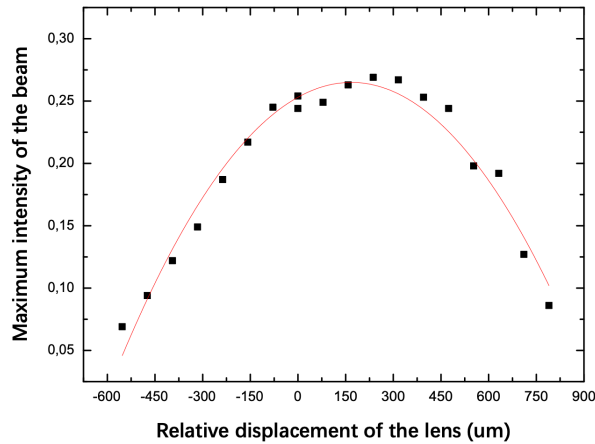


Figure 5.8 — Focusing the stirring beam on the vertical atomic position. Plot of the maximum intensity of the beam for different relative displacement of the last lens compared to the initial position, fitted by a parabola (red line). It gives the optimized position of the lens to focus the beam. The error on the center of the parabola deduced from the fit is $\pm 9 \mu\text{m}$.

After focusing the beam, the second alignment is to make the stirring center coincide with the center of the ring. We have tried to realize this alignment by centering the beam onto the connected cloud trapped at the bottom of the bubble. However, this method did not work very well due to the dipole oscillation of the cloud at the bottom. In the end, we optimize the beam center by detecting the superposition of the stirrer trajectory and the in situ absorption image of the ring. As the procedure of the beam focusing, the beam power is set to 0.03% of maximum before removing the filter. In this case, the intensity of the stirring beam corresponds to around 1% of the chemical potential, which means that the stirring beam can not really create an obvious atomic density dip. Since the filter was removed, the stirring beam could be caught by the camera. The vertical camera records the photons from the stirrer as well as the photons absorbed by the cloud, which results in a circular dark region indicating its trajectory, see Fig. 5.9. The rotation frequency is set to 100 Hz and the exposure time is 30 ms, which means that the exposure time is long enough to let the stirring beam complete several times a whole trajectory. The radius of the rotation is $23 \mu\text{m}$ which is the same as the radius of the ring. After setting these parameters, we produce a ring trap and confine atoms inside. 300 ms later, the stirring beam start to rotate and we take an in situ absorption image, shown in Fig. 5.9. When the trajectory of the stirring beam is

superimposed onto the ring, the center of the circular trajectory of the stirrer and the ring coincide.

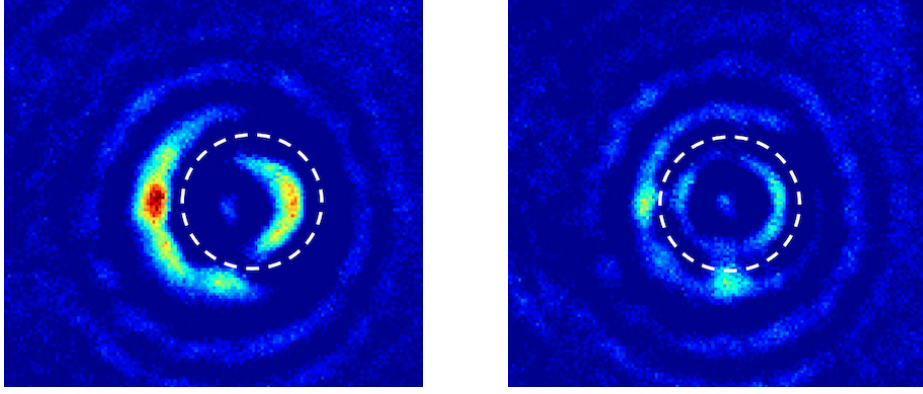


Figure 5.9 – In situ image of the superposition of the stirring beam and the atomic cloud. The estimated trajectory of the stirring beam is plotted in dashed white line. Left: Before optimization the rotation trajectory is off the atomic cloud. Right: After alignment the rotation trajectory coincides with the ring.

5.3.2.3 Preliminary experimental results

After the alignments, we look at TOF absorption images of the rotating ring excited by the stirring laser. In order to create small quantized currents with low stirring frequency, we have to adjust two parameters, the power of the stirring beam and the radius of the rotation, which determine the density dip created by such a repulsive optical barrier. We define the power of the stirrer p , which is the ratio between the real power and the maximum power (11 mW). The stirring laser with a power of $p = 0.02$ can create a zero of density on the ring when 10^5 atoms are trapped inside. This means that the potential barrier generated by the stirring beam with $p = 0.02$ is equivalent to the chemical potential of the ring with 10^5 trapped atoms. Before starting the experiment, we check the applied rotation frequency and the alignment of the stirring trajectory. We set the radius of the rotation to the radius of the ring and the power to $p = 0.15$. We then take the in situ images at different times during the stirring phase, as shown in Fig. 5.10. Once the trajectory of the density dip coincides with the ring and the period corresponds to the applied rotation rate, we start to generate and detect the superfluid flow.

After trying different parameters, we succeeded in lowering the stirring frequency necessary to produce a central hole after the standard TOF procedure down to 1.1 Hz. The experimental sequence is shown in Fig. 5.11: the cold ring is formed at time $t = 2$ s after the creation of the bubble trap, when the rf knife is 15 kHz higher than the potential bottom; 100 ms later, the stirring beam power is ramped up in 200 ms from 0 to $p = 0.13$ while rotating at 1.1 Hz with a radius of 35 μm ; then the beam stirs the annular gas for 500 ms with the power $p = 0.13$ and is ramped down to $p = 0$ in 500 ms

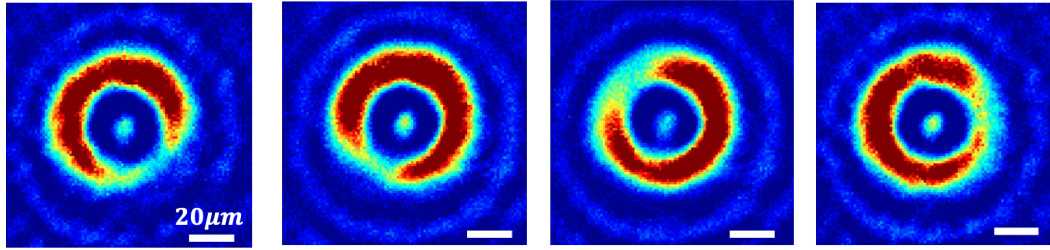


Figure 5.10 — In situ pictures of the ring excited by the stirring beam, taken at different times of the stirring phase. The power of the stirring beam is $p = 0.15$ and the stirring frequency is 1 Hz. The pictures from left to right are taken at times 0.25, 0.5, 0.75, 1 s.

while rotating; after holding the atoms in the ring trap for another 300 ms, we release the quantum gas and take an absorption image from above after a TOF of 30 ms (with 3 ms Stern-Gerlach procedure).

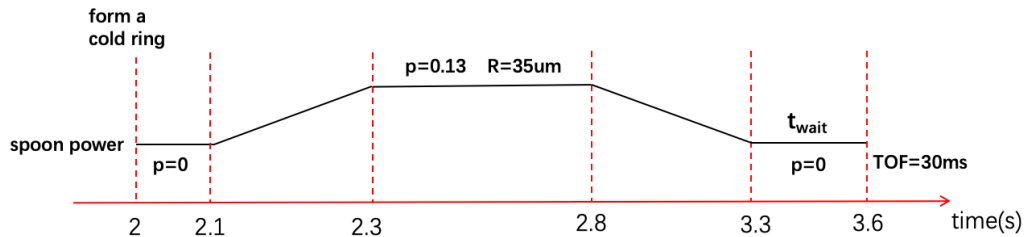


Figure 5.11 — Experimental sequence used to produce and detect the superfluid circulation.

Fig. 5.12 (a) illustrates how the blue detuned beam stirs the ring. The radius of the ring is $23\mu\text{m}$ while the stirring radius $35\mu\text{m}$. Such a radius and power of the stirring beam produce an optical barrier of around 30% of the chemical potential at ring position.

The corresponding experimental result is presented in Fig. 5.12 (b), showing a central hole within the cloud due to the destructive interference. Although using this method allowed us to lower the rotation frequency to observe a hole, 1.1 Hz is still 5 times larger than the elementary rotation rate. When rotating below this frequency, we observed a deformed connected cloud but never a clear hole within the cloud.

5.4 Improvement of the detection of the flow

In the experiment presented above, we could not observe a central hole by stirring the cloud at the elementary rotation rate (0.22 Hz). The technique of rotating the ring-shaped gas with a stirring beam was well investigated by the group of G. K. Campbell.

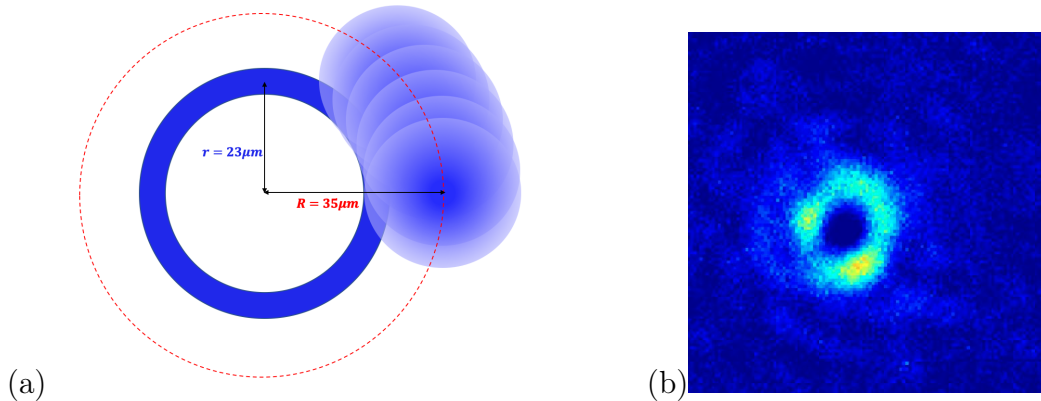


Figure 5.12 – (a): Illustration of the stirring procedure. The blue ring is the ring-shaped cloud and the blue disk indicates the stirring beam. The red dashed line represents the stirring trajectory of the center of the stirring beam with a radius $35 \mu\text{m}$. (b): Resulting vertical TOF image with a stirring frequency of 1.1 Hz . The central hole indicates the existence of a nonzero circulation. The image size is $120 \times 120 \mu\text{m}$.

Their ring trap was constructed by a pair of red-detuned laser beams, a horizontal sheet beam and a vertical ring beam, which is presented in Fig. 5.13(a). It was also difficult for their experiment to detect and analyse the central hole corresponding to a low circulation, so they provided a solution to magnify the hole size [123]. Instead of releasing the trap directly, they ramped down the red-detuned annular beam to about 10% of its initial power in 50 ms before releasing the trap and then detect the TOF absorption image. By doing so, the radial trapping frequency is reduced and the radial expansion is slower, which facilitates the detection of a small circulation. They presented the comparison of the TOF density profile with or without the "ramp-down" procedure, as shown in Fig. 5.13(b) and (c), which indicates that this procedure can make the central hole more visible.

5.4.1 Our strategy for magnifying the effect of the circulation

5.4.1.1 Reconnecting the annular gas

The configuration of our ring trap does not allow us to gradually load atoms into a harmonic trap by ramping down some laser. However, benefiting from the geometry of the bubble trap, we can load the rotating atoms in a connected harmonic trap by vertically shifting up the bubble while the light sheet beam is still on. The atoms then are pushed from the equator to the bottom of the bubble. When the light sheet pushes the atoms to the bottom, the local velocity increases since the radius is reduced but the angular momentum and the circulation are conserved during the reconnection procedure. As the relative position of the atoms on the bubble is modified, the Rabi coupling also changes. To avoid any unwanted evaporation, the rf knife is removed during the reconnection procedure.

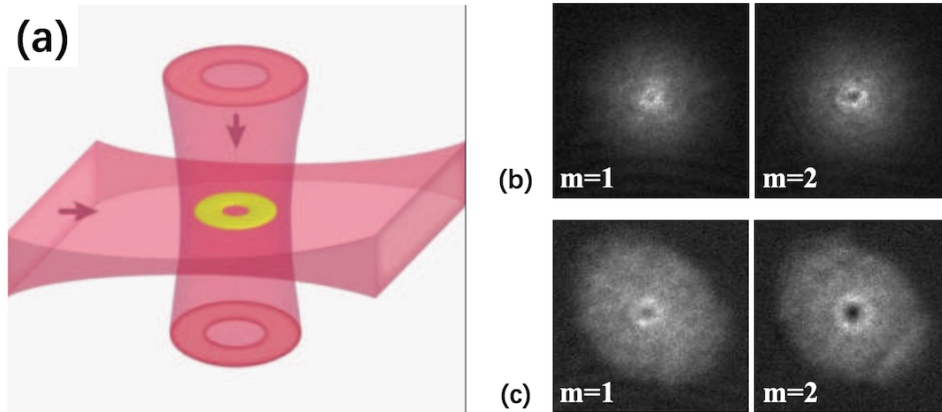


Figure 5.13 — (a): Scheme of the ring-shape trap that consists of a horizontal red detuned annular sheet beam and a vertical ring beam. Atoms are confined at the intersection of the two beams. Taken from [125]. (b): TOF absorption images of the ring with low circulation $\ell = 1, 2$, obtained by directly switching off the trap. (c): TOF absorption images of the annular gas with $\ell = 1, 2$, released from the trap after the "ramp-down" procedure. (b) and (c) are taken from [123].

Based on the sequence presented in Fig. 5.11, before releasing the trap we shift the bubble up in the vertical direction in 100 ms to reconnect the ring at the bottom while maintaining the vertical optical confinement. As soon as the ring is reconnected at the bottom, we switch off the trapping laser as well as the bubble trap and a vertical absorption image is performed after a 30 ms TOF. The resulting image is shown in Fig. 5.14. Compared the one with the same condition but released directly, this procedure leads to an extreme enhancement of the hole size after TOF in the case of a rotating ring.

Finally, by adjusting the parameters and using the reconnection procedure, we observe a clear central hole at a rotation rate of 0.15 Hz which is above $\Omega_0/2$ but below the elementary rotation frequency Ω_0 . For this rotation experiment at low frequency, we increase the duration of the ramp up and rotating phase to 500 ms and 2 s and reduce the rotation radius to 32 μm . After repeating many times for a given stirring frequency, the size of the central hole could be different, as shown in Fig. 5.15. The figure also shows that the atomic density along the central hole has fluctuations. It might be induced by optical defects in the double light sheet. In addition, when the double light sheet push atoms from the equator to the bottom at constant speed, the acceleration of the bubble in the beginning and the end is infinite. Consequently, the cloud position is not at the potential minimum of the double light sheet anymore. This effect could also affect the atomic cloud, leading to a density fluctuation of the cloud along the central hole.

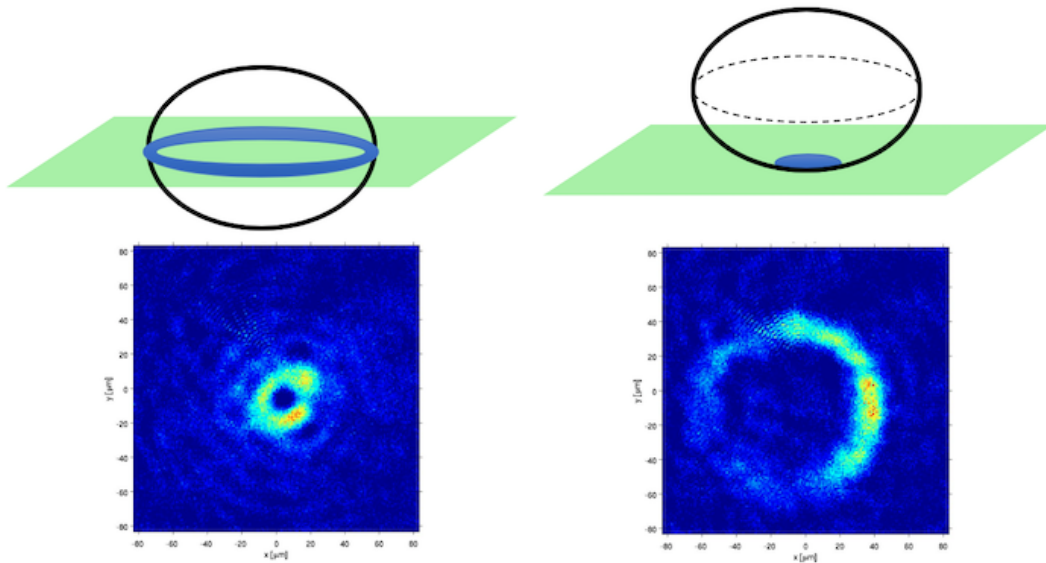


Figure 5.14 — Top: Principle of the reconnection procedure: the atoms are pushed from the equator to the bottom of the bubble. The green parallelogram indicates the confining plane in between the two light sheets while the atomic cloud is in blue. Bottom: TOF images of the expanding annular gas rotated with a stirring beam at 1.5 Hz with (right) or without (left) the reconnection procedure.

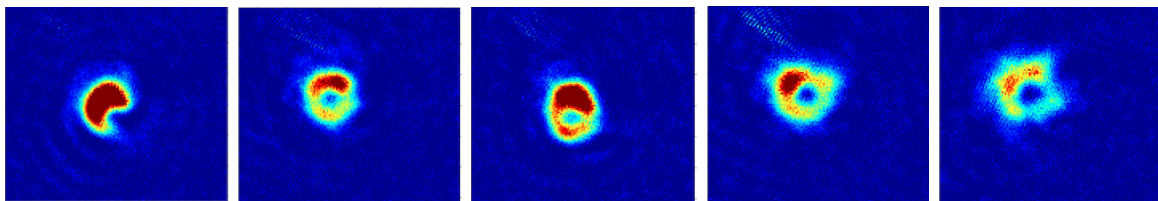


Figure 5.15 — TOF images of the ring after the reconnection and release procedure and 30 ms TOF. These pictures are taken with the same conditions, stirring frequency 0.2 Hz and radius 32 μm .

5.4.2 Statistics on the hole area

With the reconnection method, we were able to observe a small circulation generated at low stirring frequency. We may now wonder if the observed currents are indeed quantized. The superfluid currents corresponding to different winding numbers should lead to discrete hole sizes. If the measured area of the hole is discrete for different rotation rates, it proves that the superfluid flow is quantized. In order to look for this hole area quantization, we took around 200 images with a stirring frequency ranging from 0.15 to 0.3 Hz and measured the surface of the central hole.

The method for measuring the surface of the holes was developed by Romain Dubessy in the group. The hole size can be estimated through a Laplacian filter operation: after removing some background noise and smoothing the vertically integrated

atomic density profile, the boundaries of the holes are defined as the zero curvature contour line. The hole size is then given by the number of pixels counted inside the contour line. Using this method to measure the hole areas of these 200 images, we plot the histogram showing the number of occurrences of different areas, shown in Fig. 5.16. This histogram of the hole sizes shows a clear threshold for the smallest holes corresponding to $\ell = 1$ quantum of circulation. However it is not as expected constituted of two well separated peaks corresponding to $\ell = 1$ and $\ell = 2$.

It could be caused by three reasons: (i) the number of the images in the sample is not large enough and we have to take much more pictures to make the statistics; (ii) the hole size depends on the number of atoms and we have to make the atom number more stable; (iii) the method for measuring the hole area by counting the pixels is not so accurate and we should optimize the setup and the parameters to make the atomic density uniform around the hole and fit it by an ellipse. More generally, the fluctuations we observe on the images taken in the same condition, see Fig. 5.15, indicate that the experiment would benefit from an improved stability.

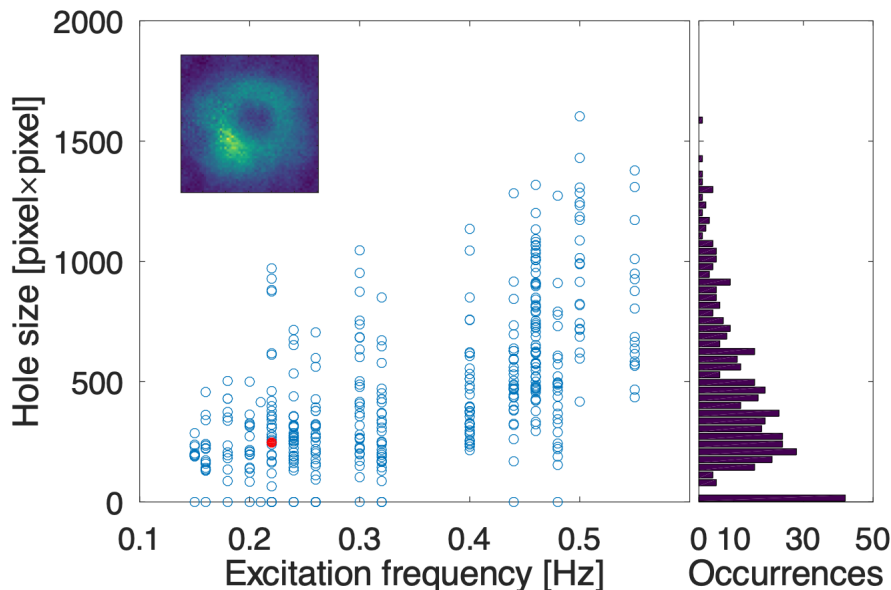


Figure 5.16 — Hole size as a function of the stirring frequency and the histogram of the hole sizes. The inset shows a typical hole seen in the TOF distribution corresponding to the data point marked in red.

5.4.3 Splitting into singly-charged vortices

Another most direct proof of the quantized current is to observe a multiply charged vortex splitting into several singly charged vortices. The equation (1.47) shows that for a given angular momentum the energy of a multiply charged vortex is larger than the

sum of singly charged vortices. In a connected gas, splitting into small vortices is thus energetically favorable. If one generates a circulation $\ell = 3$ in the ring trap presented in Fig. 5.13 and then reconnect the trap to make it harmonic, three well separated singly charged vortices will appear after the time-of-flight expansion [28, 29].

In order to observe this vortex splitting, we stir the atoms at a larger rotation frequency of $\Omega = 2\pi \times 0.5 \text{ Hz}$ for which we expect a circulation between $\ell = 2$ and $\ell = 3$. If the atoms are not held at the bottom of the bubble after the reconnection procedure, the TOF images show a large single hole indicating a multiply charged vortex. However, if the atoms undergo a free evolution in the reconnected trap for longer than 500 ms, the TOF images show 2 to 3 smaller separated holes within the cloud, which are the singly charged vortices, shown in Fig. 5.17. This is a strong indication for the previous presence of a quantized current in the ring.

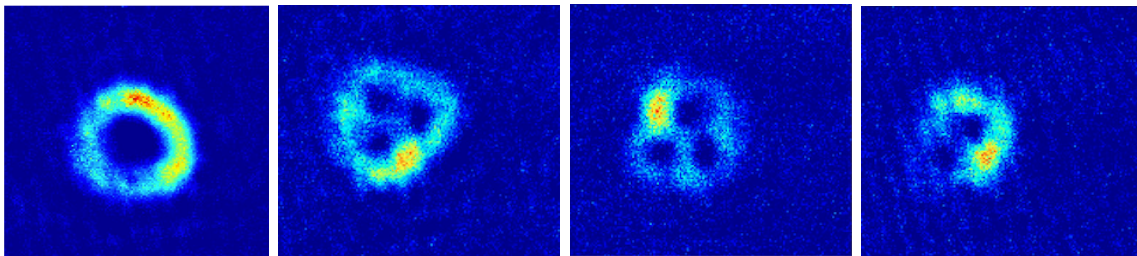


Figure 5.17 – TOF images of the atoms after reconnection procedure and free evolution in the reconnected trap. From left to right, the holding time in the reconnected trap is 0, 500, 600, 800 ms. During the waiting time in the reconnected trap, a multiply charged vortex splits into 2 or 3 singly charged vortices.

5.5 Conclusions

In this Chapter, I presented the principle of the ring trap produced by the double light sheet and the bubble trap. In addition, I introduced two methods for rotating the atoms inside: one is to introduce a quadrupole deformation of the ring trap that is set into rotation, the other one is to stir a blue detuned laser beam focused near the atoms.

The former method can create circulations in the ring but we can not determine the corresponding winding number ℓ for a given size of the central hole in the expanded cloud. In the limit a vanishing deformation amplitude, the critical rotation rate of the quadrupole deformed trap to excite the ring is 17.9 Hz, computed through the speed of sound of the ring with 10^5 atoms inside. Compared to the elementary rotation rate 0.22 Hz corresponding to $\ell = 1$, this critical frequency is very large. Therefore, this method is not well adapted to the production of a desired circulation, especially for small ℓ . The results we obtained with this method are not fully understood and would require further investigation.

The latter method was used by many other groups and is well understood. In a first set of experiments, we found that the lowest stirring frequency to produce a circulation that can be detected is 1.1 Hz. After adding the reconnection procedure, shifting the bubble and pushing the atoms from the equator to the bottom of the bubble before releasing them, we finally succeeded in detecting the circulation generated by stirring the laser at 0.15 Hz.

The histogram of the observed hole sizes shows a clear threshold in size for the smallest holes, which is strongly evidencing for the observation of elementary circulation corresponding to $\ell = 1$. In addition, after reconnection procedure and free evolution in the connected trap, we observed that a multiply charged vortex splits into two or three small vortices with single circulation $\ell = 1$. It was an evidence indicating that we have generated a quantized circulation of the superfluid in the ring trap. Further studies would involve the determination of a reliable protocol to prepare a well-defined circulation state and study its lifetime and decay mechanisms.

Chapter 6

Fast rotating superfluid in a bubble trap: from a connected gas to a dynamical ring

In a superfluid, the the ensemble of particles behave as a wave described by an amplitude and a phase. The velocity of the fluid is defined by the gradient of the phase, which implies that a superfluid is irrotational. Nevertheless, introducing vortices inside with lines of zero density leads the superfluid to rotate [6, 7, 74]. The rotation of such an irrotational superfluid attracts a lot of interest. When the superfluid rotates faster, it exhibits different properties. Once many vortices enter the cloud, as the rotation rate increases, the superfluid in the bubble trap can be roughly characterized by three different phases: an ordered vortex lattice, a dynamical ring with a multiply charged vortex in the center and a vortex lattice in the bulk, and a one-dimensional ring with a single multiply charged vortex called a giant vortex [134–136]. The first regime, the vortex lattice, was observed and studied experimentally [34, 35, 40]. In order to reach the second regime with a multiply charged vortex at the center, a harmonic plus a quartic trap is necessary, as the atoms need to rotate faster than the harmonic trapping frequency. Experimentally, this regime was investigated and approached more than ten years ago [137]. A density depletion could be observed in the trap center, although the density did not fully vanish. The third regime, even harder to reach experimentally, has never been observed yet.

The idea of rotating the superfluid at bottom of the bubble fast enough to get a ring was proposed by Romain Dubessy. The bubble trap is a smooth anharmonic trap with a weak anharmonicity which decreases the critical rotation rate to create a hole at the center. With our setup, we have been able to achieve the second regime where a fast rotating annular superfluid presents a vanishing density in the center, indicating a multiply charged vortex. This rotating annular gas, that we called a dynamical ring, is supersonic with a coarse-grained linear velocity reaching Mach 18 and survives more than a minute [94]. Here I will show the steps for achieving such a dynamical ring and examine its properties.

This chapter aims at investigating the fast rotating Bose gas in the bubble trap. In the first section, I will recall the theory of the fast rotating superfluid in a harmonic trap or in a harmonic plus quartic trap. At first I will explain how a rotating neutral atom can mimic a free charged particle in a magnetic field. I will then discuss the Lowest Landau Level for a fast rotating Bose gas. I will then present the three phases of the rotating superfluid with increasing rotation frequency. After that, I will discuss the collective modes of a rotating superfluid confined in a harmonic trap or a harmonic plus a quartic trap respectively. In the second section I will describe our strategy to achieve a superfluid rotating faster than the harmonic trapping frequency, give the trap geometry and the method for rotating the gas. The effective rotation frequency of the cloud can not be precisely controlled, so I will present several methods for measuring the effective rotating frequency through the in situ and TOF images directly or by exciting the quadrupole modes. After that, I will show the main experimental result: a long lived dynamical ring. I will give the evidences for its superfluid and supersonic character. In addition, I will then present the quadrupole mode in the dynamical ring, which has been predicted theoretically but never observed experimentally. Finally, I will present the outlook of the fast rotation experiment and give an idea of how far our dynamical ring is from the giant vortex regime.

6.1 Theory of rotating superfluids

6.1.1 Motivations for fast rotation

6.1.1.1 Analogy with an electron in a magnetic field

A rotating superfluid is worth investigating. An essential reason is its analogy with a 2D electron gas immersed in a strong magnetic field. In classical mechanics, an atom with mass M moving with a velocity of \mathbf{v} in a frame rotating around a rotation vector $\boldsymbol{\Omega}$ undergoes the Coriolis force:

$$\mathbf{F}_C = 2M\mathbf{v} \times \boldsymbol{\Omega}, \quad (6.1)$$

which is totally analogous to the Lorentz force on a moving electron of charge q in a magnetic field \mathbf{B} :

$$\mathbf{F}_L = q\mathbf{v} \times \mathbf{B}, \quad (6.2)$$

if we identify $q\mathbf{B}$ with $2M\boldsymbol{\Omega}$. In quantum mechanics, we can also write the Hamiltonian for the motion of one particle in a frame rotating around the z axis with angular frequency $\boldsymbol{\Omega} = \Omega\mathbf{e}_z$. The transformed Hamiltonian in the rotating frame writes $H_{\text{rot}} = H_0 - \Omega L_z$ where L_z is the projection of the angular momentum on the z axis. In this rotating frame, assuming the atom is confined in the $x-y$ horizontal plane, its position and momentum are noted as $\mathbf{r}(x, y)$ and $\mathbf{p}(p_x, p_y)$. The one-body Hamiltonian in the presence of a rotationally invariant trapping potential $V(r)$ can be written as:

$$H_{\text{rot}} = \frac{\mathbf{p}^2}{2M} + V(r) - \boldsymbol{\Omega} \cdot \mathbf{L} = \frac{\mathbf{p}^2}{2M} + V(r) - \Omega(xp_y - yp_x). \quad (6.3)$$

If the atom is confined in a harmonic trap with a trapping frequency ω_r , the Hamiltonian becomes:

$$\begin{aligned} H_{\text{rot}} &= \frac{1}{2M}[\mathbf{p}^2 - 2M\Omega\mathbf{p} \cdot (-y\mathbf{e}_x + x\mathbf{e}_y) + M^2\Omega^2(x^2 + y^2)] + \frac{1}{2}M(\omega_r^2 - \Omega^2)r^2 \\ &= \frac{(\mathbf{p} - M\mathbf{A}_C)^2}{2M} + V_{\text{eff}}(r), \end{aligned} \quad (6.4)$$

where the effective trapping potential is $V_{\text{eff}}(r) = \frac{1}{2}M(\omega_r^2 - \Omega^2)r^2$. Comparing with the harmonic trap potential, the additional term is the centrifugal potential due to the rotation. The effective trapping potential depends on the position as well as on the rotation frequency. The potential vector \mathbf{A}_C describing the field of Ω can be written as $\mathbf{A}_C = \Omega \times \mathbf{r}$. This Hamiltonian takes the same form of the Hamiltonian of an electron involved in a uniform magnetic field, which is given by:

$$H_e = \frac{(\mathbf{p} - q\mathbf{A}_L)^2}{2M}, \quad (6.5)$$

in which the vector potential \mathbf{A}_L for the magnetic field \mathbf{B} is $\mathbf{A}_L = \frac{1}{2}\mathbf{B} \times \mathbf{r}$. Comparing these two Hamiltonians (6.4) and (6.5), we see that studying the behavior of a rotating BEC confined in a harmonic trap can give the related behaviors of electron gases in an uniform magnetic field, provided $\Omega = \omega_r$. For this reason, rotation plays the role of a gauge field.

6.1.1.2 High rotation rate: Lowest Landau Level

Here we will discuss the case of atoms rotating very fast in the harmonic trap. As the rotation rate increases, the gas expands because of the centrifugal potential. When the rotation frequency is close to the trapping frequency, the radial trapping frequency becomes very small and the atomic cloud expands radially while the atomic density decreases, which may lead to a quasi two-dimensional atomic cloud.

We consider an atom confined in a two-dimensional isotropic harmonic trap with a trapping frequency ω_r and a ground state size $d_r = \sqrt{\hbar/M\omega_r}$. We use the quantum mechanical description of the trapped atoms, introducing the creation and annihilation operators of the harmonic oscillator. These operators along x axis are given by:

$$\hat{a}_x = \frac{1}{\sqrt{2}} \left(\frac{x}{d_r} + i\frac{p_x d_r}{\hbar} \right), \quad \hat{a}_x^\dagger = \frac{1}{\sqrt{2}} \left(\frac{x}{d_r} - i\frac{p_x d_r}{\hbar} \right). \quad (6.6)$$

The operators \hat{a}_y and \hat{a}_y^\dagger along y axis take the same form as (6.6). Since we look for the quantum states in a rotating frame, it is more appropriate to use the circularly polarized states in which basis the creation and annihilation operators can be written as:

$$\hat{a}_\pm = \frac{\hat{a}_x \mp i\hat{a}_y}{\sqrt{2}}, \quad \hat{a}_\pm^\dagger = \frac{\hat{a}_x^\dagger \pm i\hat{a}_y^\dagger}{\sqrt{2}} \quad (6.7)$$

The Hamiltonian of the harmonic oscillator can be written as:

$$H_0 = \hbar\omega_r(\hat{a}_x^\dagger\hat{a}_x + \frac{1}{2}) + \hbar\omega_r(\hat{a}_y^\dagger\hat{a}_y + \frac{1}{2}) \quad (6.8)$$

$$= \hbar\omega_r(\hat{a}_+^\dagger\hat{a}_+ + \hat{a}_-^\dagger\hat{a}_- + 1). \quad (6.9)$$

In this new basis, the angular momentum is given by:

$$L_z = \hbar(\hat{a}_+^\dagger \hat{a}_+ - \hat{a}_-^\dagger \hat{a}_-). \quad (6.10)$$

The eigenvalues of $\hat{a}_+^\dagger \hat{a}_+$ and $\hat{a}_-^\dagger \hat{a}_-$ are n_+ and n_- which are two non-negative integers. The operators \hat{a}_+^\dagger and \hat{a}_+ can create and annihilate one quantum with positive circular polarization. The expression of L_z shows that the angular momentum increases as $\hbar n_+$ and decreases as $\hbar n_-$. Taking the expressions above, one finds that the Hamiltonian in the rotating frame reads:

$$H_{\text{rot}} = \hbar\omega_r + \hbar(\omega_r - \Omega)\hat{a}_+^\dagger \hat{a}_+ + \hbar(\omega_r + \Omega)\hat{a}_-^\dagger \hat{a}_-. \quad (6.11)$$

Therefore, the corresponding eigenenergies of the Hamiltonian H_{rot} depend only on n_\pm . If we remove the energy of the fundamental state $\hbar\omega_r$, the eigenenergies reads:

$$E(n_+, n_-) = \hbar(\omega_r - \Omega)n_+ + \hbar(\omega_r + \Omega)n_- \quad (6.12)$$

$$= n\hbar\omega_r - m\hbar\Omega \quad (6.13)$$

where $n = n_+ + n_-$ describes the energy level of the non-rotating gas and $m = n_+ - n_-$ describes the angular momentum. The non negativity of n_\pm imposes that $|m| \leq n$. When the rotation frequency Ω is very close to the trapping frequency ω_r , the energy simply writes $E = 2n_- \hbar\omega_r$. All the states with $n = m$ have the same energy and form a degenerate ground state known as the Lowest Landau Level (LLL), shown in Fig. 6.1. The next level corresponds to $n - m = 2$ and is distant by an energy $2\hbar\omega_r$.

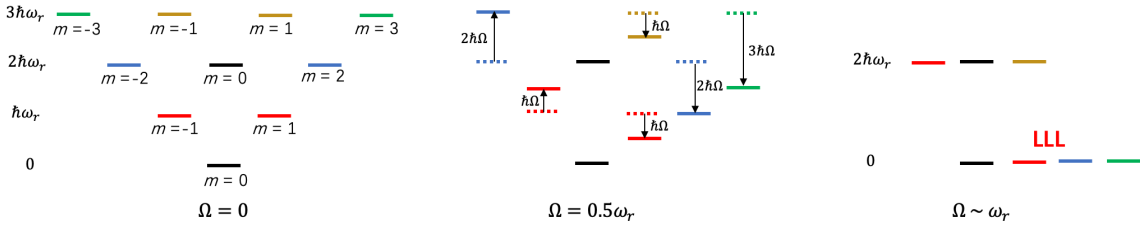


Figure 6.1 — Formation of the Lowest Landau Level with an increasing rotation frequency. From left to right, the rotation frequency increases from 0 to $0.5\omega_r$ and close to ω_r . The energy of a substate with angular momentum m is shifted by $m\hbar\Omega$.

6.1.1.3 Mean field LLL regime

In the previous paragraph we have examined the one-body Hamiltonian which shows a degenerate ground level of single particle states which appears when the rotation frequency equals the radial trapping frequency. In the real case, considering the interactions between the atoms, the atomic distribution on the substates depends on the interaction term gn , the Landau level spacing $2\hbar\Omega$ and the off-resonant energy $\hbar\delta = \hbar(\omega_r - \Omega)$. At first, I will introduce the Landau level parameter which describes

how close we are to the LLL. The Landau level parameter is the ratio between the interaction term and the Landau level spacing, which reads:

$$\Gamma_{LLL} = \frac{gn}{2\hbar\Omega}. \quad (6.14)$$

Under the mean field Thomas Fermi and the local density approximation, the characteristic interaction energy $gn(r)$ can be also regarded as the effective local chemical potential $\mu'(r) = \mu - V(r)$. If Γ_{LLL} is smaller than 1, then all the atoms stay in the LLL which is almost degenerate but with an energy spacing $\hbar\delta$, as shown in Fig. 6.2. The number of the states occupied in the LLL can be deduced as:

$$m_{\max} = \frac{gn}{\hbar\delta} \quad \text{if } \frac{gn}{\hbar\delta} \text{ is an integer, or } \left\lceil \frac{gn}{\hbar\delta} \right\rceil + 1 \quad \text{otherwise.} \quad (6.15)$$

Now I will introduce another parameter called the filling factor ν which describes the number of atoms occupying one given substate in the LLL. In this case with $\Gamma_{LLL} < 1$, the filling factor can be written as the total atom number divided by the number of occupied states: $\nu = N\hbar\delta/(gn)$.

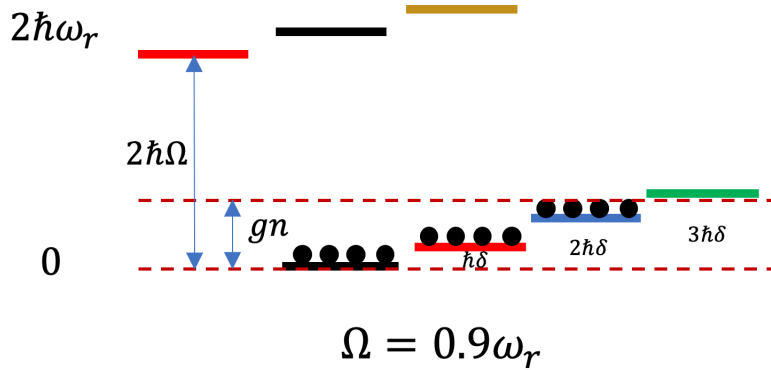


Figure 6.2 — Illustration of the occupation of the near-degenerate ground states. Here the interaction energy is smaller than the Landau level spacing, and the atoms occupy only the LLL. Each substate has 4 atoms indicating a filling factor $\nu = 4$.

We have mentioned that the signature of a rotating superfluid is the presence of quantized vortices, as shown in Fig. 1.3. At a high rotation rate, the trap is gradually open due to the centrifugal force, leading to a radial expansion and decrease of the atomic density. In Chapter 1, we have shown that the typical size of the vortex is, comparable with the healing length ξ and depends on the chemical potential. Therefore, as the rotation frequency increases, the size of the vortex core is getting larger and larger because the chemical potential decreases while the number of vortices increases due to an increasing angular momentum. When the interaction term gn decreases below $2\hbar\Omega$, all the atoms are in the LLL degenerate ground state. In this case, each vortex indicates

a substate of angular momentum m . So the number of vortices is equal to the number of the substates occupied $N_v = m_{\max}$. The filling factor thus represents the number of atoms per vortex. Experimentally, the group of E. A. Cornell rotated the quantum gas in a harmonic trap and first entered the Lowest Landau Level regime [40]. In their experiment, the minimal achievable filling factor is around $\nu = 500$. For a such high filling factor $\nu \gg 1$, the superfluid is in the mean-field LLL regime [138] and forms a vortex lattice. If the filling factor drops to 1 or even smaller, the mean field approach is not valid anymore and the system is described by a many-body ground state called the Laughlin state [139]. In this fast rotating two-dimensional BEC, the condensate wavefunction writes [140]

$$\Psi(x, y) = \mathcal{C} \prod_j (u - u_j)^2 e^{-|u|^2/2d_r^2}, \quad u = x + iy, \quad (6.16)$$

where $u_j = x_j + iy_j$ describe the vortex locations in complex notation while \mathcal{C} is a normalization constant. This is a highly correlated state because in the condensate the position of a single atom depends on the positions of the other atoms. In the fractional quantum Hall effect, with electrons, the filling factor can take fractional values, such as $\mu = 1/q$ where q is an odd integer. For bosons, q should instead be even. In this case, the system can be described by a highly correlated state whose wave function is proposed by Laughlin and takes the same form as equation (6.16) [51]. More details about these states and the relation with the quantum Hall regime can be found in [141, 142].

6.1.2 GPE solution in the rotating frame

6.1.2.1 Vortex lattice in the Thomas Fermi regime

In this section we consider a rotating superfluid in the presence of many vortices. We have seen that the vortices in the superfluid form a triangular vortex lattice. We recall the Feynman-Onsager relation describing the circulation of a superfluid:

$$\Gamma = \oint_{\mathcal{C}} \mathbf{v}(\mathbf{r}, t) \cdot d\mathbf{l} = \oint_{\mathcal{C}} \frac{\hbar}{M} \nabla \phi(\mathbf{r}, t) \cdot d\mathbf{l} = \ell \times 2\pi \frac{\hbar}{M}, \ell \in \mathbb{Z}. \quad (6.17)$$

Therefore, a singly charged vortex contributes a circulation of $2\pi\hbar/M$. We consider a closed area of surface S having N_v vortices inside, which leads to a total circulation $\Gamma_N = N_v 2\pi\hbar/M$. Stokes' theorem gives the corresponding circulation of a classical fluid $\Gamma_c = 2\Omega_{\text{eff}} S$ [143]. Comparing the two expressions of the circulation, we can deduce the density of vortices:

$$n_v = \frac{N_v}{S} = \frac{M\Omega_{\text{eff}}}{\pi\hbar} \quad (6.18)$$

in which Ω_{eff} is the effective rotation frequency defined by the average angular momentum per particle $\langle L_z \rangle$:

$$\Omega_{\text{eff}} = \frac{\langle L_z \rangle}{M\langle r^2 \rangle}, \quad \langle r^2 \rangle = \frac{2}{7} R_{\perp}^2 \quad (6.19)$$

where R_{\perp} is the Thomas-Fermi radius [6]. The mean area A per vortex is thus:

$$\frac{1}{n_v} = \frac{\pi \hbar}{M \Omega_{\text{eff}}} = \pi l^2 \quad (6.20)$$

where $l = (\hbar/M\Omega_{\text{eff}})^{1/2}$ is a "magnetic length" by analogy with the quantum Hall effect ($l_B = (\hbar/eB)^{1/2}$), which also defines the inter-vortex distance. Using $S = \pi R_{\perp}^2$, the number of vortices can be determined as:

$$N_v = \frac{R_{\perp}^2(\Omega_{\text{eff}})}{l^2} \quad (6.21)$$

where $R_{\perp}(\Omega_{\text{eff}})$ is the radial Thomas-Fermi radius of a rotating condensate with the effective rotation frequency Ω_{eff} . In a harmonic trap with radial and vertical trapping frequency ω_r and ω_z , as the rotation increases the radial trapping potential becomes $\frac{1}{2}M(\omega_r^2 - \Omega_{\text{eff}}^2)r^2$ due to the centrifugal force while the condensate gets more and more anisotropic, see Fig. 6.3. Since the trapping frequency is modified by the rotation, in the rotating frame, the Thomas-Fermi radii become [143, 144]:

$$R_{\perp}(\Omega_{\text{eff}}) = R_{\perp}(0) \left(1 - \frac{\Omega_{\text{eff}}^2}{\omega_r^2}\right)^{-3/10} \quad R_z(\Omega_{\text{eff}}) = R_z(0) \left(1 - \frac{\Omega_{\text{eff}}^2}{\omega_r^2}\right)^{1/5}, \quad (6.22)$$

which can also give the aspect ratio of a rotating BEC in the harmonic trap:

$$\frac{R_z(\Omega_{\text{eff}})}{R_{\perp}(\Omega_{\text{eff}})} = \frac{\sqrt{\omega_r^2 - \Omega_{\text{eff}}^2}}{\omega_z}. \quad (6.23)$$

This is valid provided that the gas stays in the Thomas-Fermi regime in the vertical direction, i.e. $R_z(\Omega_{\text{eff}}) > d_z$.

The critical temperature for Bose-Einstein condensation is proportional to the geometric mean trapping frequency which is reduced due to the rotation. Therefore, the ratio between the critical temperature with or without the rotation is given by [145]:

$$\frac{T_c(\Omega_{\text{eff}})}{T_c(0)} = \left(1 - \frac{\Omega_{\text{eff}}^2}{\omega_r^2}\right)^{1/3}. \quad (6.24)$$

6.1.2.2 Beyond the harmonic trapping frequency: giant vortex

In the previous paragraph we discussed the vortex lattice that happens for a rotation rate smaller than the radial trapping frequency. The rotation rate of a BEC confined in a harmonic trap can never exceed the trapping frequency. In order to achieve higher rotating rate compared with the trapping frequency, one solution is to confine the BEC in a harmonic plus a quartic trap [136, 137, 146]. The higher order confinement is able to trap the atoms for higher rotation rates. The horizontal trapping potential is given by:

$$V_{\text{tr}}(r) = \frac{1}{2}M\omega_r^2 \left(r^2 + \lambda \frac{r^4}{d_r^2}\right). \quad (6.25)$$

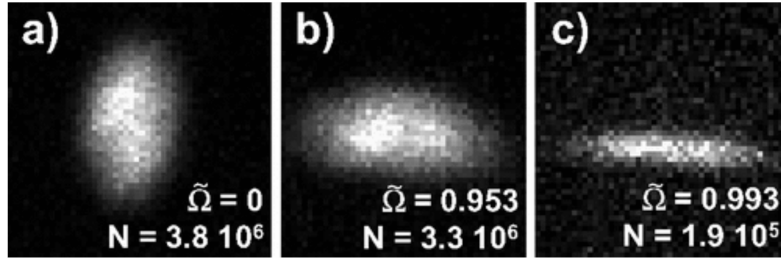


Figure 6.3 – Side view of the condensate in a harmonic trap. (a) A static BEC in the trap with aspect ratio $R_z/R_\perp = 1.57$. (b) This ratio reduced sharply for a rotation rate of $\Omega_{\text{eff}} = 0.953\omega_r$. (c) Rotation at $\Omega_{\text{eff}} = 0.993\omega_r$. Figures are taken from [40].

where λ is the coefficient of the quartic term and d_r is the harmonic oscillator length. For such a trap, rotating faster than the harmonic trapping frequency results in a Mexican hat potential with an anti-confinement at the center, creating a density hole. A density hole starts to form when the chemical potential is smaller than the potential barrier at the center. Thus the critical rotation rate for generating a hole at the center is given by [136]:

$$\Omega_h = \omega_r \left[1 + 2\sqrt{\lambda} \left(\frac{3\sqrt{\lambda}\tilde{g}}{2\pi} \right)^{1/3} \right]^{1/2}, \quad (6.26)$$

in the case of a quasi-2D gas and $\tilde{g} = g/(\sqrt{2\pi}d_z)$ is the dimensionless interaction constant for the quasi-2D system. The critical rotation rate is slightly larger than the trapping frequency due to the interactions between the atoms.

When the rotation rate is increased from below to above the harmonic trapping frequency, the gas will cross three different phases: ordered vortex lattice with many singly charged vortex, a central hole of multiply charged vortex in the center with vortex lattice in the bulk and a pure multiply charged vortex which is called a giant vortex, and is shown in Fig. 6.4. In the giant vortex regime, the thickness of the annular gas is too small to contain a single vortex, which means that the gas is in the 1D regime. This giant vortex state has been identified by several theoretical studies [134–136]. However, confined in such a potential, the atoms can not exactly reach the LLL which only happens in a harmonic trap.

6.1.3 Collective modes of a rotating trapped superfluid

6.1.3.1 In a harmonic trap

In Chapter 1 we have seen the collective modes of a non-rotating trapped superfluid. After linearizing the hydrodynamic equations, we obtain the dispersion relation of the eigenmodes. Here we recall the dispersion relation of a 3D ($\mu \gg \hbar\omega_z \gg \hbar\omega_r$) trapped oblate condensate under the hydrodynamic approximation:

$$\omega^2 = \omega_r^2 \left(\frac{4}{3}n^2 + \frac{4}{3}nm + 2n + m \right). \quad (6.27)$$

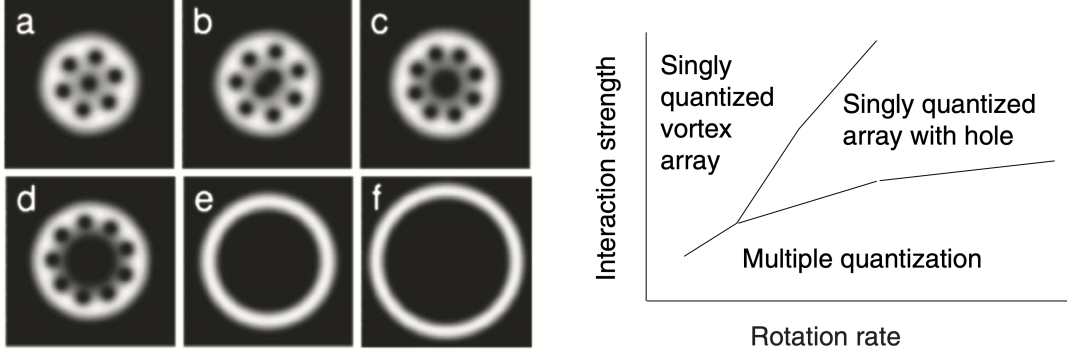


Figure 6.4 – Left: Numerical simulation of the GPE in the rotating frame describing a BEC confined in a harmonic plus a quartic trap with $\lambda = 0.5$. From (a) to (f): as the rotation rate increases, the cloud starts from a vortex lattice (a) to a central hole with vortex lattice in the bulk (b-d). Finally it reaches the giant vortex regime with a single multiply charged vortex at the center (e-f). Taken from [136] Right: The expected phase diagram of the ground state of a rapidly rotating BEC in the rotation-interaction space showing the three different phases. Figure is taken from [135].

where n gives the number of radial nodes and m corresponds to the z -axis projection of the angular momentum. There are two quadrupole modes $n = 0, m = \pm 2$ whose frequencies are ω_+ and ω_- . For a non-rotating condensate, the frequencies of these two modes are degenerate $\omega_+ = \omega_- = \sqrt{2}\omega_r$, as obtained from equation (1.49). The quadrupole out-of-phase oscillation of the condensate radii can be regarded as the superposition of two rotating elongated clouds corresponding to the mode $m = \pm 2$. They rotate at the same frequency $\omega_+/2$ but in opposite directions, as illustrated in Fig. 6.5. The figure also shows that if the elongated cloud rotates by half a turn it goes back to its initial shape, which indicates that the frequency of the quadrupole mode is twice the rotation frequency of the elongated clouds.

For a rotating condensate with a nonzero angular momentum, the frequencies of these two modes are not degenerate anymore. The frequency difference is determined by the effective rotation frequency of the condensate [81]:

$$\omega_+ - \omega_- = 2\Omega_{\text{eff}} \quad \omega_+^2 + \omega_-^2 = 4\omega_r^2, \quad (6.28)$$

which also provides a way to measure the effective rotation frequency of a rotating condensate. Combining these two relations above, we can deduce the frequencies of these two modes:

$$\omega_{\pm} = \sqrt{2\omega_r^2 - \Omega_{\text{eff}}^2} \pm \Omega_{\text{eff}}. \quad (6.29)$$

The equations show that as the effective rotation frequency of the condensate increases, the frequency of the mode $m = +2$ increases while the frequency of the mode $m = -2$ decreases.

The rotating superfluid can also be excited by a superposition of the two modes $m = \pm 2$, if a sudden deformation is applied. We can then observe an out-of-phase

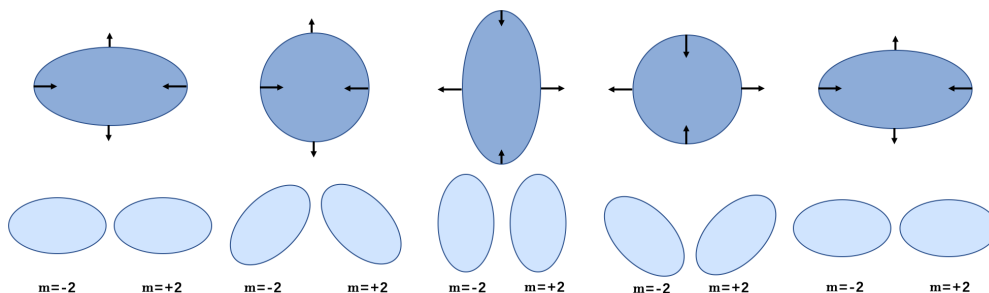


Figure 6.5 – Illustration of the quadrupole oscillation of a non-rotating condensate. The figures in the first line show the motion of the quadrupole mode for one period. The figures in the second line show half a period of the two rotating components which are the elongated clouds corresponding to the modes $m = \pm 2$. Again, this corresponds to half a period of a solid rotation but to a full period of the mode itself, as the final state is the same as the initial one.

oscillation of the cloud radii, with a rotation of the main axes. The mode $m = +2$ and $m = -2$ rotate with and against the atomic flow respectively. The rotation frequency of the axes is then Ω_{eff} . Experimentally, the quadrupole modes can be excited by rotating a quadrupole deformation of the trap. A resonance occurs when half a period of this deformation corresponds to the second line of Fig. 6.5, i.e. to full a period of the quadrupole mode. The deformation probe should thus rotate at half the frequency of the quadrupole modes:

$$\omega_{\pm}^{\text{rot}} = \frac{1}{2}(\Omega_{\text{eff}} \pm \sqrt{2\omega_r^2 - \Omega_{\text{eff}}^2}), \quad (6.30)$$

where we define that the direction of the atomic flow is positive. The details of exciting the quadrupole modes will be explained in section 6.3.2 and section 6.6.

6.1.3.2 In a harmonic plus quartic trap

In order to achieve a high rotation rate, the atoms should be confined in a trap with higher order confinement than a harmonic trap. Here we will discuss the quadrupole mode of a rotating condensate confined in a harmonic plus quartic trap. It has two phases distinguished by the formation of the central hole.

When $\Omega_{\text{eff}} < \Omega_h$, the cloud is still connected. Hence the frequencies of the quadrupole modes are similar to the case of a harmonic trap but with a correction due to the quartic term, which reads [147]:

$$\omega_{\pm} = \sqrt{\left(2 + 3\lambda \frac{R_{\perp}^2}{d_r^2}\right) \omega_r^2 - \Omega_{\text{eff}}^2} \pm \Omega_{\text{eff}}, \quad (6.31)$$

where we recall that R_{\perp} is the Thomas-Fermi radius of the condensate and d_r the harmonic oscillator length. In our case of a weak anharmonicity with $\lambda = 1.3 \times 10^{-4}$, the term with λ in the last equation is of order 0.15 which is much smaller than 2. The

frequencies of the two quadrupole modes are slightly shifted but their difference is still $2\Omega_{\text{eff}}$, as shown in Fig. 6.6.

When $\Omega_{\text{eff}} > \Omega_h$, the central hole with multiply quantized vortex is formed. Once the hole appears, the frequencies of the two modes will deviate, as predicted by M. Cozzini [146, 147]. In addition, after the formation of the central hole, there are four quadrupole modes: two modes with $m = -2$ and two modes with $m = +2$, shown in Fig. 6.6.

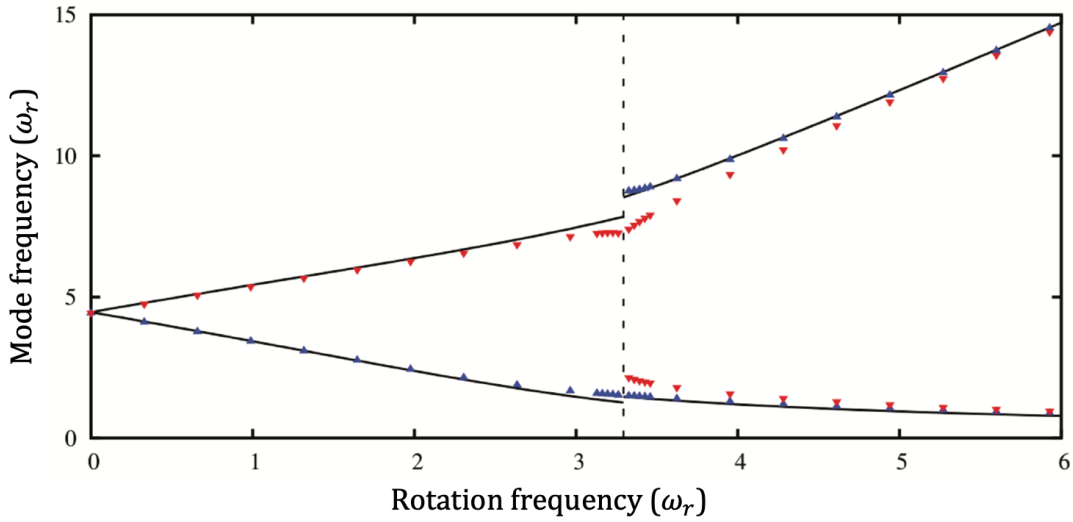


Figure 6.6 – Frequencies of the quadrupole modes $m = +2$ (blue upwards triangle) and $m = -2$ (red downwards triangle) in the harmonic plus quartic trap with $\lambda = 0.5$ in the rotating frame. The black dashed line indicates the critical frequency Ω_h . The solid black lines are the sum rule predictions, explained in [147]. Figure is taken from [147].

From the prediction in [146, 147], in the condition of large rotation frequency $\Omega_{\text{eff}} \gg \Omega_h$, the high-lying mode frequency becomes $\sqrt{6\Omega_{\text{eff}}^2 - 2\omega_r^2}$ and the low-lying mode frequency is proportional to $2\lambda R_-^2 / \Omega_{\text{eff}}$ where $R_-^2 = R_2^2 - R_1^2$, R_2 and R_1 are the outer and inner radius of the annular gas [147]. Therefore, as the rotation frequency increase, the frequency of the low-lying mode gets close to 0 but is always positive.

In the experiment, when one of the quadrupole modes are excited, we can observe that the cloud becomes elongated and rotates with respect to the direction of the rotating deformed trap at half the mode frequency. Since describing the motion of the deformed trap in the laboratory frame is easier than in the rotating frame, it is more clear to plot the resonant frequency, which is also half the mode frequency, as a function of the effective rotation frequency of the superfluid in the laboratory frame. Romain Dubessy computed these frequencies for our trap parameters using sum rules, and the result is shown in Fig. 6.7.

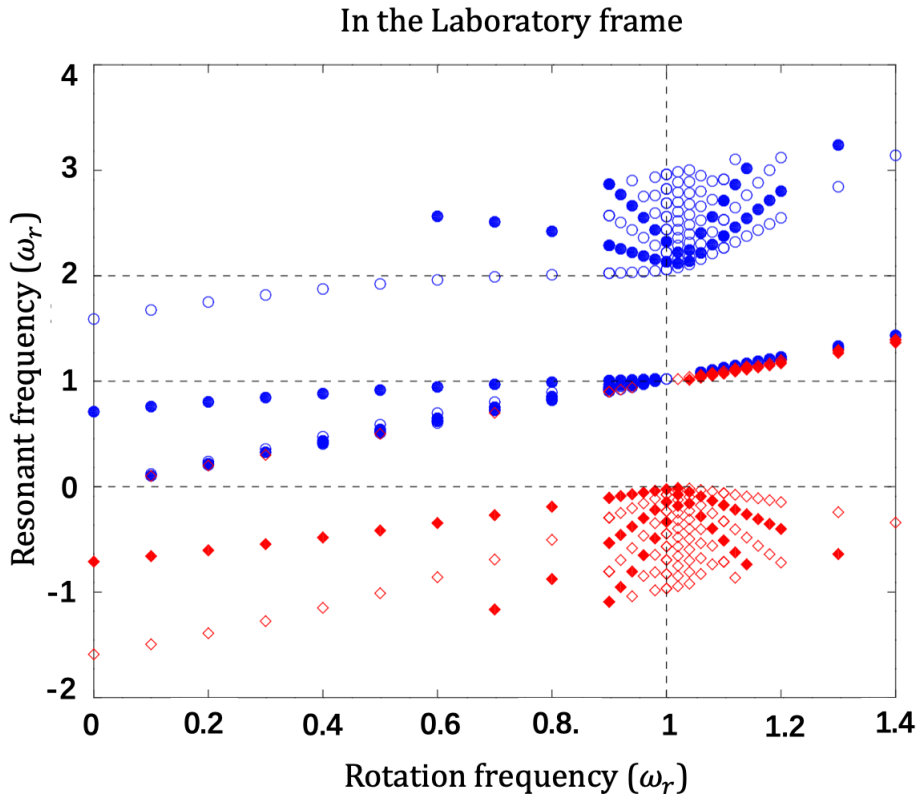


Figure 6.7 — Resonant frequencies as a function of the effective rotation frequency in the laboratory frame, in units of ω_r . The blue dots and the red diamonds indicate respectively the modes with $m = +2$ and the modes with $m = +2$ with different n . Numerical calculation realized by Romain Dubessy.

Figure 6.7 shows that, once the central hole appears, the two modes with $m = +2$ are excited around ω_r and $2\omega_r$ while the two modes with $m = -2$ are excited around ω_r and 0. Concentrating on the mode $m = -2$, we observe that as the rotation frequency increases but stays below the critical rotation frequency Ω_h , the resonant frequency of the mode $m = -2$ increases from its initial negative value $-\sqrt{2}\omega_r$ towards 0. Just after crossing Ω_h , there are two groups of modes, the resonant frequency of one mode stays close to zero but decreases to more negative values, while the resonant frequency of the other one mode jumps to ω_r and increases for an increasing rotation frequency. We remark that the mode whose resonant frequency stays close to zero always rotate against the atomic flow. In other words, its resonant frequency is always negative. We will investigate this mode of a fast rotating annular condensate in section 6.6, which will show a frequency not exactly in agreement with the theoretical prediction. Its resonant frequency may cross zero to be positive.

6.2 Fast rotating superfluids in a bubble trap

6.2.1 Potential in the rotating frame

In order to rotate the gas above the harmonic trapping frequency, we confine the condensate at the bottom of the bubble trap where it is equivalent to a harmonic plus a quartic trap. We have presented the bubble trap in Chapter 2. Here we recall the trapping potential and trapping frequencies at the bottom of the bubble. In the case where $\varepsilon = Mg/2\hbar\alpha \ll 1$ i.e. the effect of the magnetic gradient is much stronger than gravity, we can assume that the atoms are trapped on the surface of the bubble. Therefore the radial and vertical trapping frequencies at the bottom become, in the harmonic approximation:

$$\omega_r = \sqrt{\frac{g}{2r_b} \left(1 - \frac{\hbar\Omega_0}{Mgr_b}\right)^{1/2}} \quad (6.32)$$

$$\omega_z = 2\alpha\sqrt{\frac{\hbar}{M\Omega_0}}. \quad (6.33)$$

Assuming that the atoms remain on the resonant surface, the trapping potential in the rotating frame, beyond the harmonic approximation, can be written as:

$$V(r, z) = \hbar\Omega_1(r, z) + Mgz - \frac{1}{2}M\Omega_{\text{eff}}^2 r^2 \quad (6.34)$$

where the Rabi coupling and relation between the radius and the altitude are recalled:

$$\Omega_1(\mathbf{r}) = \frac{\Omega_0}{2} \left(1 - \frac{2z}{r_b}\right) \quad z = -\frac{\sqrt{r_b^2 - r^2}}{2}. \quad (6.35)$$

Therefore we can rewrite the total potential:

$$V(r) = \frac{\hbar\Omega_0}{2} - M\omega_r^2 r_b^2 \sqrt{1 - \frac{r^2}{r_b^2}} - \frac{1}{2}M\Omega_{\text{eff}}^2 r^2 \quad (6.36)$$

Expanding to fourth order in r and comparing with the expression of the harmonic plus a quartic trap in the equation (6.25), we can determine the quartic term coefficient λ at the bottom the bubble trap, which reads:

$$\lambda = \frac{d_r^2}{4r_b^2}. \quad (6.37)$$

In the fast rotation experiment, the current flowing in the quadrupole coils is 28.5 A, the dressing frequency is 300 kHz and the maximum Rabi coupling is 49.25 kHz, which determines the radial trapping frequency $\omega_r = 2\pi \times 33.7$ Hz and the semi-major axis of the bubble $r_b = 77.6$ μm . With these values, the parameter λ in our trap is 1.5×10^{-4} .

The expression of the critical rotation frequency to create the central hole Ω_h is given in equation (6.26), which depends on λ . Once we have the quartic term strength

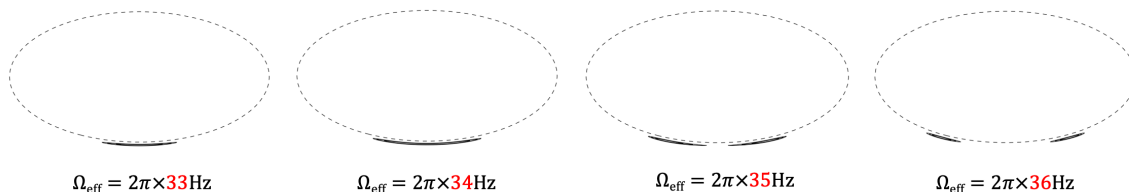


Figure 6.8 – Illustration of the realization of a fast rotating superfluid in a bubble trap. The black dashed line describes the side view of the bubble trap constructed by dressing the quadrupole trap. The solid black line indicates the isopotential that is 0.3 kHz above the minimum of the potential. The radial trapping frequency is $\omega_r = 2\pi \times 33.7\text{Hz}$. From left to right: as the rotation rate increases, the atomic cloud expands and climbs on the bubble’s sides leading to a central hole. Numerical calculation by H el ene Perrin.

λ , we can deduce the critical rotation frequency to produce the central hole in the bubble trap: $\Omega_h \simeq 1.05\omega_r$.

When the rotation frequency is above Ω_h , the central hole appears and the atoms climb on the edges of the bubble with an increasing r and z , see Fig. 6.8. Since the Rabi coupling is position dependent, the trapping frequencies will change as the atoms climb on the bubble. The new perpendicular and tangential oscillation frequencies at the position of the atoms can be computed as a function of the effective rotation frequency Ω_{eff} and the initial trapping frequencies ω_r and ω_z at the bottom of the bubble. The new perpendicular and tangential trapping frequencies at the location of the atoms corresponding to a rotation rate $\Omega_{\text{eff}} > \Omega_h$ can be written as:

$$\omega_{z'}^2 = \omega_z^2 \left[\frac{1 + 3\kappa^2}{2(1 + \kappa)} + \frac{\Omega_0^2}{\omega^2} \frac{3\kappa(9\kappa^4 - 7\kappa^2 - 2)}{8(1 + 3\kappa^2)} \right] - \frac{1 - \kappa^2}{1 + 3\kappa^2} \Omega_{\text{eff}}^2 \quad (6.38)$$

$$\omega_{r'}^2 = \omega_r^2 \frac{4}{\kappa} \frac{1 - \kappa^2}{1 + 3\kappa^2} \quad (6.39)$$

where $\kappa = \frac{\omega_r^2}{\Omega_{\text{eff}}^2} < 1$ and we remind that ω is the rf frequency. When the atoms climb on the bubble and form an annular gas, the perpendicular and tangential trapping frequencies in the trap modified by the centrifugal potential decrease.

6.2.2 Experimental rotation protocol

The method for rotating a superfluid is to realize a ‘rotating bucket’, which has been used previously for rotating superfluid helium [7] or a dilute BEC [34]. For dilute BECs, transferring angular momentum from a rotating anisotropic trap to the condensate has been already investigated in detail [133, 148].

The main idea is to deform the trap geometry from circular to elliptical and then rotating the main axis of the ellipse. In order to produce a rotational symmetrical trap, a circularly polarized rf field is necessary, which requires that the horizontal antennas H1 and H2 have the same amplitude and a $\pi/2$ phase difference. The polarization is

described in equation (2.84). During the rotating bucket phase, we first increase the rf amplitude of one horizontal antenna while decrease the rf amplitude of the other horizontal antenna by modifying Θ to make the polarization from circular to elliptical on purpose. In Chapter 2, we have seen that the Rabi coupling is determined by the local orientation of the static magnetic field as well as the local magnitude and the polarization of the rf field. Therefore, such an elliptically polarized rf field modifies the local Rabi coupling and creates a deformed trap. We then change Θ and Φ in the same time to rotate the deformation while keeping the anisotropy of the deformed trap constant. After rotating a given number of turns, Θ and Φ are set back to $\pi/4$ and $\pi/2$, resulting a rotationally symmetrical bubble trap again. In this way, we are able to rotate superfluids at the bottom of the bubble. The rotating procedure is shown in Fig. 6.9.

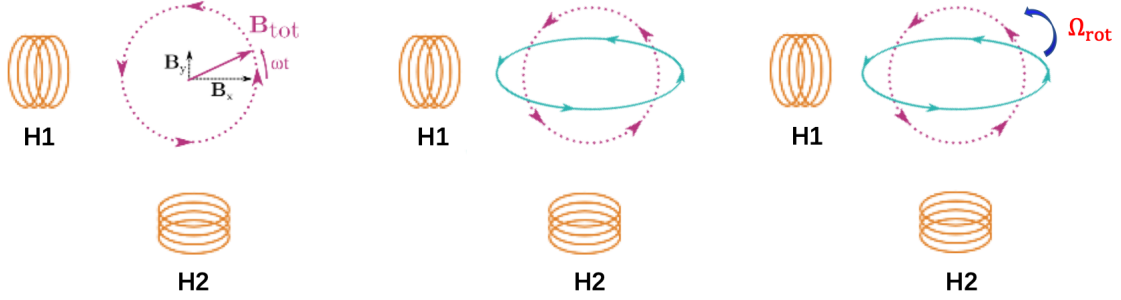


Figure 6.9 — Illustration of the rotation procedure. The dashed magenta circle describes the circularly polarized rf field generated by the first two antennas H1 and H2. The solid blue ellipse is the elliptically polarized rf field produced when the amplitudes are made slightly different, which make the polarization elliptical and the trap anisotropic. The deformed trap rotates with the main axis of the elliptical polarization at a frequency Ω_{rot} .

Although rotating the deformed trap enables to rotate the atoms, the effective rotation frequency Ω_{eff} of the gas is not exactly the same as the applied frequency Ω_{rot} . The real rotation frequency of the gas is affected by three factors: the applied rotation frequency, the duration of the rotation phase and the strength of the trap deformation. In the experiment, during the rotating phase, we apply 5.5 turns of the rotating bucket to rotate the gas for any applied rotation frequency. We use

$$\varepsilon_{\text{ani}} = \frac{\omega_x^2 - \omega_y^2}{\omega_x^2 + \omega_y^2} = \frac{\sqrt{1 - \eta}}{\frac{2MgR}{\hbar\Omega_0\sqrt{1 - \varepsilon^2}} - \sqrt{\eta}} \quad (6.40)$$

to describe the deformation of the trap. During the rotation phase, the anisotropy of the trap is $\varepsilon_{\text{ani}} = 0.14$.

Therefore, we need to determine the effective rotation frequencies of the superfluid after the rotation phase. The methods we implemented for this measurement are presented in the next section.

6.3 Measurement of the rotation rate

A superfluid is irrotational but in a rotating frame it can get angular momentum through the nucleation of vortices. The effective rotation frequency of the superfluid affects the expansion rate after TOF and the vortex density. Here I present four methods to measure Ω_{eff} in a rotating superfluid.

6.3.1 Analysis of the in situ atomic density distribution

This method of measuring the rotation frequency consists in a direct analysis of the atomic density distribution of the rotating cloud inside the trap because the density profile of the cloud is modified by the centrifugal force. In the following, we will discuss two situations: a connected rotating gas and an annular rotating gas.

When the rotation frequency is below Ω_h , the cloud is still connected. The effective trapping potential is modified by the centrifugal force, as shown in Fig. 6.10. The effective potential can be written as $V_{\text{eff}}(r, z) = V_{\text{tr}}(r, z) - \frac{1}{2}M\Omega_{\text{eff}}^2 r^2$. The typical atom number in the rotating superfluid is 10^5 . We can thus neglect the kinetic term and take the Thomas-Fermi approximation. After doing so, we can describe the atomic density distribution as a function of the rotation rate, which reads:

$$n(r) = \frac{1}{g} \left[\mu - V_{\text{tr}}(r) + \frac{1}{2}M\Omega_{\text{eff}}^2 r^2 \right]. \quad (6.41)$$

In this way, we obtain the effective rotation frequency by fitting the density profile of the cloud. For a given chemical potential and trapping potential, presented in equation (6.41), as Ω_{eff} increases the r satisfying $n(r) = 0$ becomes larger, which indicates that the Thomas-Fermi radius R_{\perp} also increases.

This method for determining the effective rotation frequency through the in situ atomic density distribution is very convenient as it is not necessary to take a series of pictures. However, compared to other methods presented in the following, we found that the results obtained by this method are not very accurate for the connected clouds, which may be caused by the limit of the high density absorption imaging or the dipole oscillation of the cloud.

We assume that the trap is a harmonic plus a quartic trap as in(6.25) such that the atoms are always confined even for a large rotation rate. When the rotation frequency is above Ω_h , the central hole appears and the cloud becomes an annular gas. In this case, we can determine Ω_{eff} directly from the in situ density profiles of the annular gas. We first perform an azimuthal integration of the density profiles to obtain the mean radial profile of the annular gas. After considering the effect of the centrifugal force, the effective trapping potential modified by the rotation frequency can be written as:

$$V_{\text{eff}}(r) = \frac{1}{2}M\omega_r^2 \left(r^2 + \lambda \frac{r^4}{d_r^2} \right) - \frac{1}{2}Mr^2\Omega_{\text{eff}}^2. \quad (6.42)$$

Since the maximum atomic density occurs at the minimum of the trapping potential where the derivative of the position is zero, we can deduce the relation between the

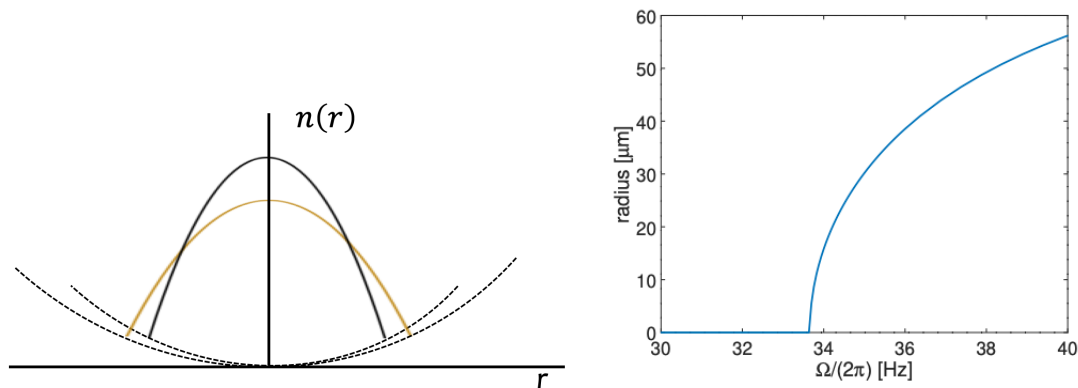


Figure 6.10 — Left: Illustration of the atomic density distribution for a zero or nonzero rotation rate below Ω_h . The centrifugal force leads to a trap opening and a modified density profile. Right: The radius of the annular rotating gas as a function of the effective rotation frequency. It starts to be nonzero above Ω_h .

rotation frequency and the radius of the ring by solving the equation $dV_{\text{eff}}(r)/dr = 0$. In the end, Ω_{eff} can be written as a function of the radius of the ring r_0 :

$$\Omega_{\text{eff}} = \omega_r \sqrt{1 + \frac{2\lambda r_0^2}{d_r^2}}, \quad (6.43)$$

which is plotted in Fig. 6.10. Using this method to fit the annular gas and to determine the rotation frequencies is more accurate than fitting the connected cloud, as we just need to point the maximum density radius and not to determine a width. Therefore, once the central hole appears, we use this method to determine the effective rotation frequency of the superfluid.

6.3.2 Exciting the quadrupole modes of a rotating superfluid

For a connected rotating superfluid, the effective rotation frequency measured by the method of resonantly exciting quadrupole modes is accurate. The principle of this method is to excite the quadrupole modes $m = \pm 2$ resonantly and deduce the effective rotation frequency through the difference of these two quadrupole modes through Eq. (6.31).

After rotating the atoms at the bottom of the bubble, we slightly deform the trap again with an anisotropy of $\varepsilon_{\text{ani}} = 0.065$ and then rotate the trap at Ω_{probe} . The resonance occurs at $\Omega_{\text{probe}} = \pm\omega_{\pm}/2$ while scanning Ω_{probe} from negative (opposite to the flow) to positive (in the same direction of the flow). Here we define the sign of the frequency with respect to the direction of the atomic flow. Once the resonance occurs, the cloud becomes elongated and rotates to follow the deformed trap. We let the atoms rotate in the deformed trap for a while and take an in situ image while the trap is still rotating. We then plot the anisotropy of the cloud as a function of the excitation frequency, as shown in Fig. 6.11. The anisotropy of the resonant cloud

$\zeta = R_{\text{long}}/R_{\text{short}}$ depends on the duration of the excitation time t , the dissipation Γ and the detuning from the resonant frequency $\omega_{\pm} - 2\Omega_{\text{probe}}$, and reads: [149].

$$\zeta(\Omega_{\text{probe}}) = 1 + \sum_{m=\pm} \zeta_{0,m} \sqrt{\frac{1 + e^{-2\Gamma_m t} - 2e^{-\Gamma_m t} \cos[(\omega_m - 2\Omega_{\text{probe}})t]}{(\omega_m - 2\Omega_{\text{probe}})^2 + \Gamma_m^2}} \quad (6.44)$$

where $\zeta_{0,\pm}$ describes the constant amplitudes for the mode $m = \pm$ and Γ_m is the mode damping rate. After fitting the curve by this model, we determine the frequencies of the quadrupole modes ω_{\pm} , leading to measure the effective rotation frequency $\Omega_{\text{eff}} = (\omega_+ - \omega_-)/2$.

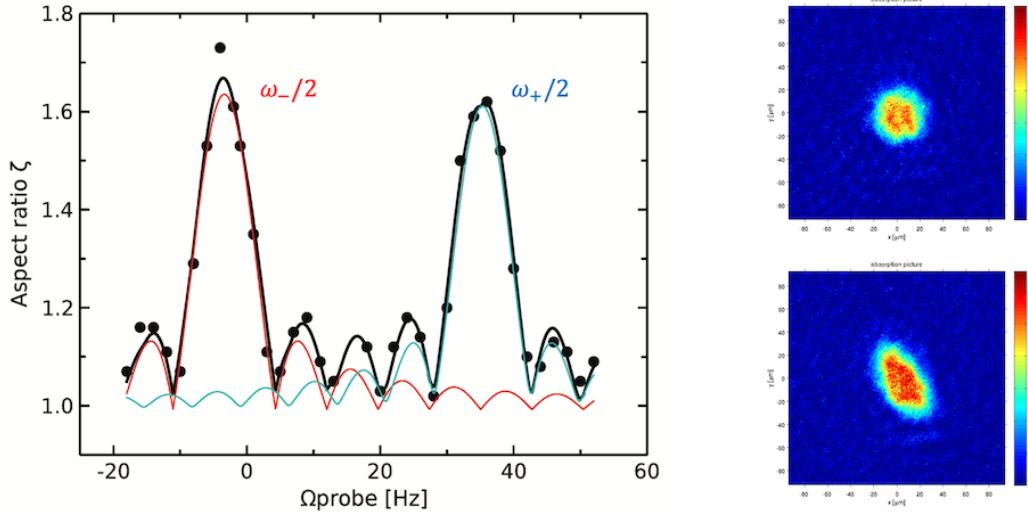


Figure 6.11 – Left: Cloud anisotropy ζ as a function of the probe frequency Ω_{probe} . There are two peaks at $\omega_{-2}/2$ and $\omega_{+2}/2$ that are resonant with the mode $m = -2$ and $m = +2$ respectively. In the rotation phase, we apply a rotation rate 27 Hz and 5.5 turns with an anisotropy of the trap $\varepsilon_{\text{ani}} = 0.14$. After waiting another 10 s in the rotationally invariant trap, we apply this second resonant excitation with a small anisotropy of the trap $\varepsilon_{\text{ani}} = 0.03$. After fitting the curve by Eq. (6.44), we find $\omega_{-2}/2\pi = -6.8(2)$ Hz and $\omega_{+2}/2\pi = 70.7(2)$ Hz, leading to the effective rotation frequency 31.9(3) Hz. Right, top: In situ image of the non-resonant cloud in the rotating deformed trap. Right, bottom: In situ image of the cloud at resonance with the rotating deformed trap. The excited cloud becomes very elongated.

6.3.3 Analysis of the vortex density in the time-of-flight images

Previously, we have examined the methods for measuring the effective rotation frequency by analysing the trapped cloud. Here we will discuss the methods to analyse the cloud after time-of-flight. For a rotation frequency below the radial trapping frequency, the rotating superfluid exhibits a vortex lattice which is related to the effective

rotation frequency. We recall the relation between the vortex density and the rotation frequency [6]:

$$n_v = \frac{M\Omega_{\text{eff}}}{\pi\hbar}. \quad (6.45)$$

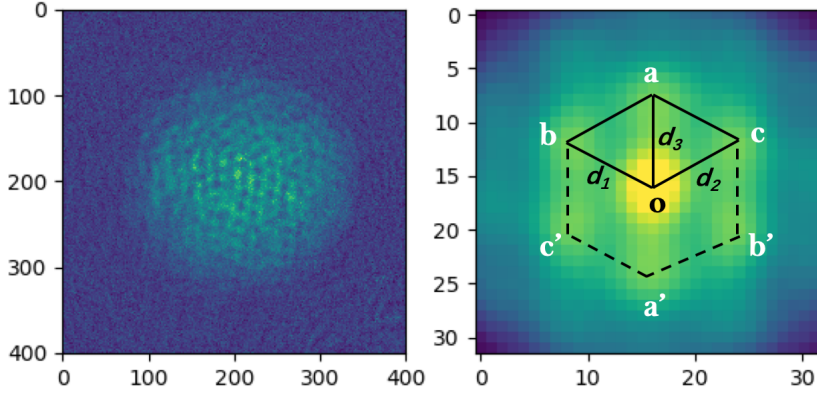


Figure 6.12 — Left: Time-of-flight picture with vortex lattice. Before the 23 ms TOF, the gas was rotated at 27 Hz and 5.5 turns with an anisotropy of $\varepsilon_{\text{ani}} = 0.14$ then held in the symmetrical trap for another 10 s. The effective rotation frequency determined by this method is 33 Hz. Right: Autocorrelation of the left picture. It is obtained by displacing the vortex lattice in the left picture for various distances in different directions and analysing how perfectly the shifted lattice overlaps with the initial lattice. For example, the first order peak at (a) means that if the vortex lattice is shifted along $\vec{o}\vec{a}$ for a distance d_3 , the new vortex lattice almost coincides with the initial lattice. Autocorrelation realized by Avinash Kumar.

This equation shows that we can determine the effective rotation frequency Ω_{eff} by analysing the vortex density of the trapped cloud. However, the vortex lattice in the trapped cloud is too small to observe, so we concentrate on the vortex lattice in the expanding cloud after TOF. We assume that the total number of the vortices is conserved during the period of TOF. We first determine the vortex density of the TOF cloud n'_v and then deduce the vortex density of the trapped cloud n_v .

Since the vortex lattice takes the form of a triangular lattice, the autocorrelation of the ordered vortex lattice gives the typical inter-vortex distance and the mean area per vortex. Fig. 6.12 shows a TOF image with ordered vortex lattice and its autocorrelation. The autocorrelation picture has six maxima (noted a, b, c, a', b', c' in Fig 6.12) forming a hexagon. The maximum in a indicates that if we shift the initial picture along $\vec{o}\vec{a}$ the shifted picture significantly overlaps with the initial picture. The maxima in the autocorrelation picture should be centrosymmetrical, because the overlap between the initial picture and the picture shifted along \vec{d} is the same as the overlap

between the initial picture and the picture shifted along $-\vec{d}$. As shown in Fig 6.12, we have $\vec{o}\vec{a} = -\vec{o}\vec{a}' = \vec{d}_3$, $\vec{o}\vec{b} = -\vec{o}\vec{b}' = \vec{d}_1$ and $\vec{o}\vec{c} = -\vec{o}\vec{c}' = \vec{d}_2$. Therefore, we can deduce the mean inter-vortex distance by only taking the average of $|\vec{d}_1|$, $|\vec{d}_2|$ and $|\vec{d}_3|$. It reads:

$$\bar{d} = \frac{1}{3} \sum_{i=1}^{n=3} d_i. \quad (6.46)$$

The surface of an equilateral triangle with side length \bar{d} is half of the unit area per vortex, because the sum of the internal angle is π which is the half of the perigon 2π . Therefore the vortex density after TOF can be deduced as:

$$n'_v = \frac{1}{s} = \frac{2}{\sqrt{3} \cdot \bar{d}^2}. \quad (6.47)$$

As a consequence, the vortex density of the in situ cloud should be:

$$n_v = \frac{\pi r^2}{\pi R^2} \cdot n'_v \quad (6.48)$$

where r and R are the Thomas Fermi radii of the in situ and the TOF cloud. We then determine the effective rotation frequency:

$$\Omega_{\text{eff}} = \frac{h}{\sqrt{3}M\bar{d}^2} \cdot \frac{r^2}{R^2}. \quad (6.49)$$

This method needs a well ordered vortex lattice such that we can determine an accurate inter-vortex distance. In order to obtain a clear ordered vortex lattice, we use the Stern-Gerlach method to separate the cloud with different Zeeman substates. The stray magnetic field may shift the cloud with $|m_F = \pm 1\rangle$, so the Stern-Gerlach procedure is able to avoid the superposition of the three clouds and the associated loss of contrast. After the Stern-Gerlach procedure, only the cloud with the state $|m_F = 0\rangle$ will be detected and analysed. Since during the Stern-Gerlach procedure we lose about half of the atoms, we should have enough atoms after the rotation phase. This method for measuring the effective rotation rate is accurate but it requires a high quality of the TOF pictures, for instance a clear ordered vortex lattice and enough atom number. In addition, it is only useful for the connected cloud with a vortex lattice whose rotation frequency should be smaller than the radial trapping frequency.

6.3.4 Size of the expanding cloud

Here we also present another method for analysing the TOF image, where it is not necessary to have an ordered vortex neither a connected gas. The method is to perform a time-of-flight expansion: we abruptly turn off the trapping potential and let the atoms fall for a duration t_{TOF} . The cloud undergoes a fast radial expansion, which can determine Ω_{eff} by using the ballistic model. The principle is shown in Fig. 6.13. We treat the gas as a classical fluid with a rigid rotation frequency of Ω_{eff} , so all the atoms at the edge of the cloud have a tangential velocity of $\Omega_{\text{eff}}r$ where r is deduced from the

Thomas-Fermi radius of the in situ image. This approach is justified when a vortex lattice is present, as the coarse-grained average velocity field is then the one of a solid body. The square of the Thomas-Fermi radius after t_{TOF} writes:

$$R^2 = r^2 + r^2 \Omega_{\text{eff}}^2 \cdot t_{\text{TOF}}^2. \quad (6.50)$$

We can first measure the Thomas-Fermi radius of the in situ cloud then measure the radius after the free expansion for a given TOF. Inserting r , TOF duration t_{TOF} and the radius R after TOF into the equation (6.50) can determine the effective rotation frequency Ω_{eff} . A more accurate way is to plot the square of the cloud radius after TOF as a function of the square of the TOF duration and fit it by a straight line. The gradient of the line is $r^2 \Omega_{\text{eff}}^2$.

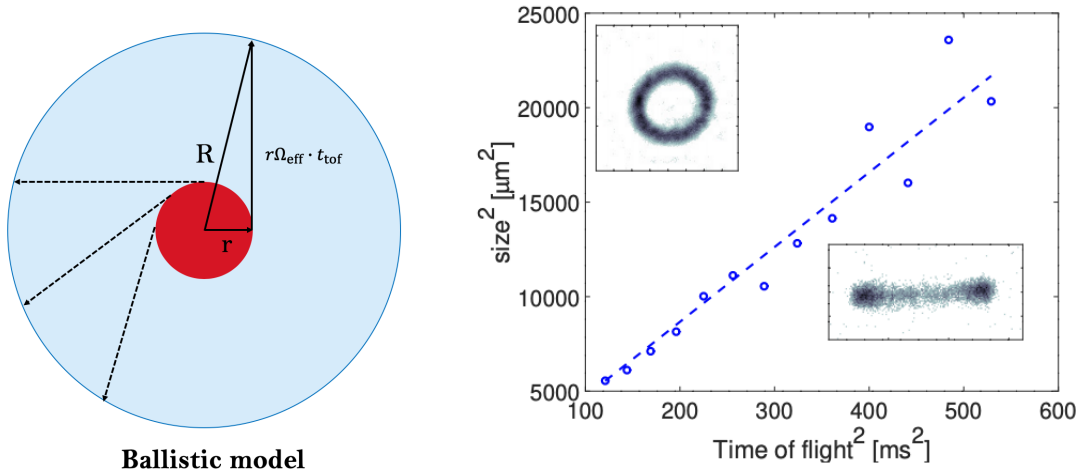


Figure 6.13 – Left: Illustration of the expansion in the ballistic model. The central area in red describes the in situ cloud. The light blue disk represents the cloud after TOF with a radius R . Right: Time-of-flight expansion of an annular cloud above Ω_h . Open blue circles: square of the measured radius R^2 as a function of the time-of-flight square t_{TOF}^2 . The dashed line is a linear fit. The top left inset shows the top view of the in situ cloud. The bottom right inset shows the side view of a typical time-of-flight image at $t_{\text{TOF}} = 23$ ms. $\Omega_{\text{eff}} = 1.06\omega_r$ from these data.

The accuracy of the rotation rate determined by this method depends on the accuracy of the mean radii of the in situ and TOF cloud. When $\Omega_{\text{eff}} > \Omega_h$ and the cloud becomes an annular gas, both the radius and the rotation rate are accurate. However, for a connected gas with a vortex lattice, the mean radius of the cloud after TOF is not so accurate because of the density fluctuations due to the vortices. In addition, since this method requires both the in situ and TOF images, we need to modify the vertical position of the camera for each given t_{TOF} , which is not very convenient.

6.4 A long-lived dynamical ring

In the previous section, when I introduced the methods for measuring the effective rotation rates I mentioned that we obtain an annular gas for a large rotation rate. As the rotation rate increases, the atoms climb on the edges of the bubble trap and form such a dynamical ring. This ring can survive for more than one minute. In this section, I will present the formation of the long-lived dynamical ring as well as the effect of the rf knife on the ring formation.

6.4.1 Formation of the dynamical ring

The experimental procedure is presented in Fig. 6.14. We change the trap geometry by modifying the dressing field polarization. Over a time $t_{\text{ramp}} = 400 \mu\text{s}$ we linearly increase ε_{ani} up to its maximal value 0.18, then rotate the trap axes at angular frequency $\Omega_{\text{rot}} = 2\pi \times 31 \text{ Hz}$ for $t_{\text{rot}} = 177 \text{ ms}$ (5.5 turns) and finally return to the isotropic trap over t_{ramp} .

After this procedure we let the cloud evolve in the rotationally symmetric trap for a finite time t and take an absorption image of the in situ atomic distribution, as presented in Fig. 6.14. During the stirring phase the density profile is strongly deformed, as is clear on the second image. Once the rotating phase is over and the trap returns to isotropic, which we take as $t = 0$, the cloud shape goes back to circular with an increased radius due to its higher angular momentum. We have mentioned that, in the frame co-rotating with the atomic flow at Ω_{eff} , the effective potential modified by the centrifugal force reads $V_{\text{eff}}(r, z) = V(r, z) - M\Omega_{\text{eff}}^2 r^2/2$, leading to a reduced effective radial trapping frequency and an increased size of the cloud. As the cloud expands, the chemical potential is reduced and the gas enters the quasi-2D regime $\mu < \hbar\omega_z$. We will discuss the chemical potential in more detail in section 6.5.4.

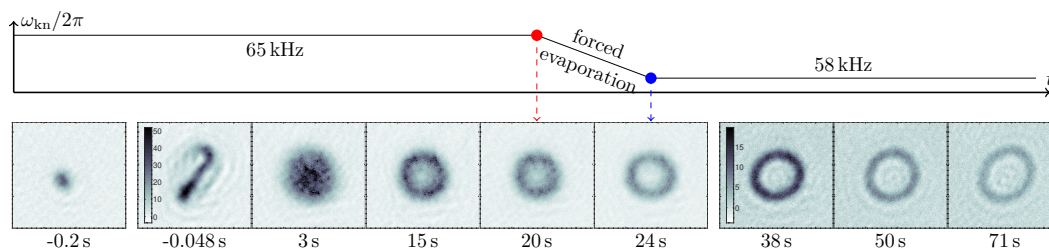


Figure 6.14 — Sketch of the experimental procedure (see text for detail on the stirring, evaporation and optional spectroscopy stages) and in situ images of the atomic distribution. The first image on left shows a cloud at rest before the stirring procedure: for this image only $\sim 10\%$ of the atoms are imaged. As the cloud is set into rotation the peak density decreases and for the sake of clarity we use two different color scales for pictures taken before and after $t = 25 \text{ s}$, for which the darkest pixels correspond to densities of $50 \mu\text{m}^{-2}$ and $20 \mu\text{m}^{-2}$, respectively.

As Fig. 6.14 shows, we apply an rf knife on the atoms to do evaporative cooling during the whole sequence. In our experiment there are two rf antennas used for evaporation, an antenna of horizontal axis called "horizontal antenna" and located on the side of the science cell and an antenna of vertical axis placed below the science cell and called the "vertical antenna". After forming an annular gas, we prefer to use the "vertical antenna" which preserves the rotational symmetry of the trap. But before that, when atoms are confined at the very bottom where the quantisation axis is aligned with the rf field generated by the vertical antenna, this vertical antenna cannot evaporate efficiently the atoms trapped at the bottom. So during the dressing and stirring phase as well as the first 2s waiting time, we still use the horizontal antenna at 365 kHz to evaporate the cloud. From $t = 2$ s on, the vertical antenna at 65 kHz replaces the horizontal one. The rf frequency in the vertical antenna is ramped down to 58 kHz from $t = 20$ s to $t = 24$ s in order to cool the cloud further, this is the forced evaporation stage in Fig. 6.14.

After a few seconds, a density depletion appears at the center of the cloud which is a signature of Ω_{eff} exceeding ω_r . After the stage of forced evaporation, a macroscopic hole appears in the density profile, indicating that Ω_{eff} is now above Ω_h , and leading to the formation of a dynamical ring with a typical radius of $\sim 30 \mu\text{m}$. Fig. 6.14 shows that the dynamical ring is able to survive for more than one minute. Such a long lifetime shows that the dissipation of the annular flow is very small.

6.4.2 Time evolution of the effective rotation frequency

From the time evolution of the density as the dynamical ring forms, we find that the atoms are accelerated while rotating in the isotropic trap. We plot in Fig. 6.15 the effective rotation frequency measured by analysing the in situ image (see section 6.3.1) as a function of the waiting time. After the stirring phase the cloud rotation accelerates and reaches a steady state value of $\Omega \simeq 1.02\omega_r$ around $t = 12$ s in the presence of a rf knife at $\omega_{\text{kn}} = 2\pi \times 65$ kHz. Applying the forced evaporation phase, ramping down the knife from 65 kHz to 58 kHz in 4s, leads to a significant increase of the rotation frequency, as shown in the grey region of Fig. 6.15.

During the forced evaporation phase, the rotation frequency increases and becomes larger than the critical rotation frequency Ω_h for which a dynamical ring is expected to form. At later times, the effective rotation frequency increases, which results in the formation of a faster rotating dynamical ring. This effect of the acceleration is due to the effect of the vertical evaporation antenna that selectively evaporates the atoms with lower angular momentum states, as we will explain now.

The rf field generated by the evaporation antenna also couples with the static magnetic field, as the dressing rf field. But the coupling strength between atomic spin and the rf field generated by the evaporation antenna is much smaller than the coupling strength between the spin and the rf field produced by the dressing antennas. We thus can neglect the coupling caused by the evaporation antenna in the estimation of the potential depth. The relative depth of the trap can be deduced from the difference

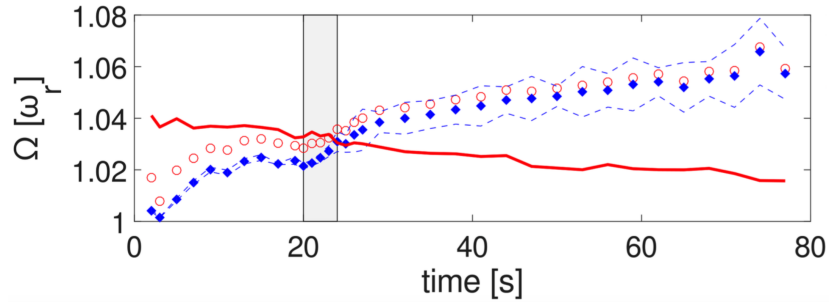


Figure 6.15 – Time evolution of the effective rotation frequency Ω (blue diamonds) and systematic uncertainty induced by the anisotropy of the dynamical ring (dashed blue lines), as measured from an elliptic fit of the annular shape. The light gray shaded area indicates the time span during which the forced evaporation is performed. The solid red line shows the value of Ω_h for each time, which is the critical rotation frequency leading to an annular two-dimensional density profile [150, 151]. The open red circles show the same data when we take into account the optical resolution $\sigma = 4 \mu\text{m}$.

between the RF knife frequency ω_{kn} and the local Rabi coupling $\Omega_1(r)$, which reads:

$$\hbar\omega_{\text{trap}} = \hbar(\omega_{\text{kn}} - \Omega_1(r)). \quad (6.51)$$

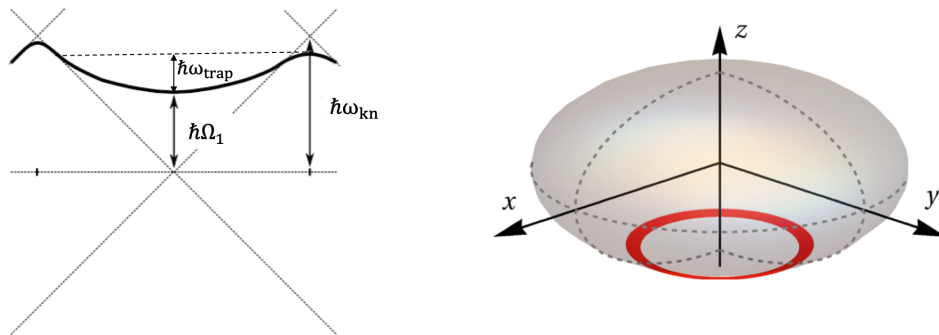


Figure 6.16 – Left: Sketch of the relative depth of the trap as determined by the rf-knife frequency ω_{kn} and the Rabi coupling Ω_1 . The dressed state is open on both sides of the resonance due to the presence of the RF knife [107]. Right: Illustration of the dynamical ring (red ring) climbing on the sides of the bubble (gray ellipsoid). The altitude of the annular gas is higher than the bottom, leading to a smaller Rabi coupling compared to the one at the bottom.

A sketch of the relative trap depth is shown in Fig. 6.16. In Chapter 2 we have shown that the Rabi coupling is position dependent and the maximum occurs at the

bottom of the bubble. When the atoms climb further away from the trap center, the local Rabi coupling $\Omega_1(r)$ decreases and the relative depth of the trap ω_{trap} with respect to the rf knife frequency increases. Therefore, the rf knife removes the atoms situated close to the bottom more efficiently. Once these atoms with lower angular momentum are removed, the average angular momentum per particle will increase. The function of the rf knife is thus not only evaporative cooling, but also accelerating the rotation.

6.5 Evidence of superfluidity

The dynamical ring has a clear macroscopic hole in the center, it seems close to the giant vortex state. However, all these achievements depend on the dynamical ring being a superfluid instead of a thermal gas. Therefore, we have to figure out if the dynamical ring is superfluid or not.

6.5.1 The most direct proof we are waiting for

In section 6.1.2 we have discussed the three different phases as a function of an increasing rotation rate. Since the dynamical ring is not in the giant vortex regime, if it is a superfluid it is supposed to have a large central multiply charged vortex and singly charged vortices in the bulk. The most direct way to confirm the superfluid character is to observe a vortex lattice in the bulk of the annular gas after time-of-flight expansion. The expected atomic distribution from Gross-Pitaevskii equation is shown in Fig. 6.17(a). Fig. 6.17(b) shows the vertical TOF image of the dynamical ring which was rotated at 31 Hz for 177 ms and rotating in the isotropic trap for 20 s [100].

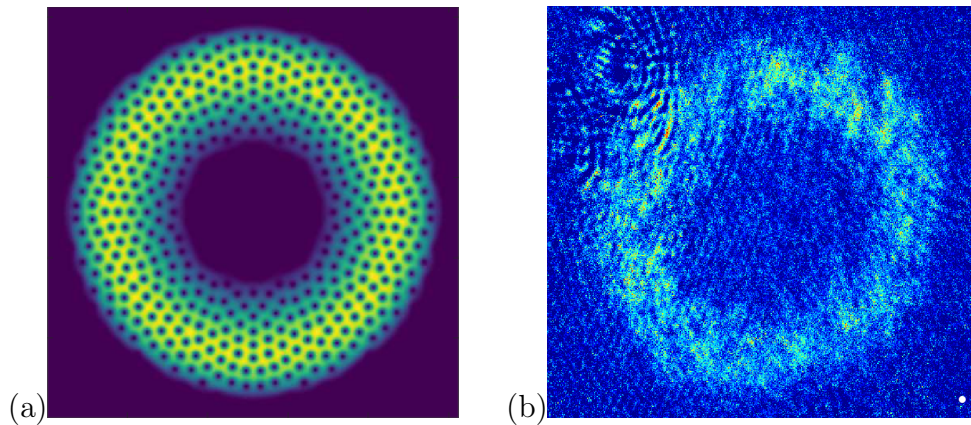


Figure 6.17 — (a) Gross-Pitaevskii simulation of the in situ atomic density distribution for a gas rotating at 35 Hz at the bottom of the bubble trap, realized by Romain Dubessy. (b) Pictures of the dynamical ring at $t = 20$ s, taken after a TOF of 23 ms. Picture taken from [100].

From the time-of-flight picture, we can observe some density fluctuations, but the

contrast is too low to claim that a vortex lattice is present in the bulk of the ring. Moreover, the fluctuations of the atomic density are very large. In addition, observing the vortices would require a time-of-flight duration long enough for the vortex size to overcome the optical resolution. However, for such a duration the atomic density drops dramatically due to the fast radial expansion and falls below our detection threshold. So we can't conclude that the dynamical ring is superfluid by only detecting its TOF image.

6.5.2 Estimating the ring temperature

6.5.2.1 Temperature measurement under an assumption of a pure thermal gas

Although we can not conclude that the dynamical ring is superfluid from the vertical TOF image, we can exclude the possibility that the gas is in a pure thermal state by using a proof of contradiction.

After getting a dynamical ring in the bubble trap as presented in Fig. 6.14, we release the gas from the trap and let it freely expand for various time-of-flight durations before taking the horizontal TOF images. It gives the atomic density integrated along the imaging axis y . We then integrate the data along x axis to get a vertical density profile, which can be nicely fitted by a Gaussian distribution.

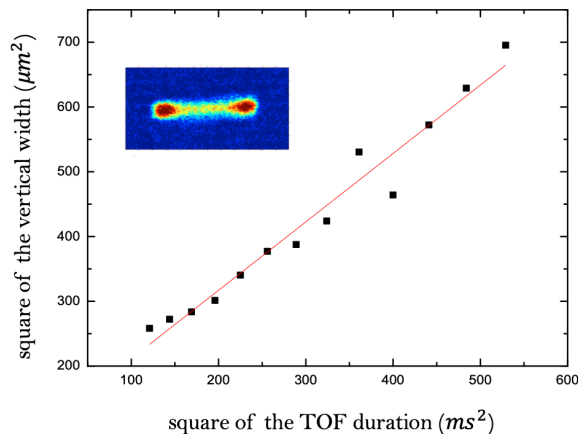


Figure 6.18 – Evolution of the square of the cloud $1/\sqrt{e}$ -radius as a function of t_{TOF}^2 . A linear fit of the data (red solid line) gives a slope of $1.05(6) \mu\text{m}^2/\text{ms}^2$. Inset: dynamical ring after a TOF of 19 ms, taken from the side.

In the beginning, we assume that the gas is thermal and that its temperature can be deduced from its vertical expansion. The vertical position variance $\sigma_r(t)^2$ can be related to the initial position variance $\sigma_r(0)^2$ and the initial velocity variance $\sigma_v(0)^2$ through

$$\sigma_r(t_{\text{TOF}})^2 = \sigma_r(0)^2 + \sigma_v(0)^2 \cdot t_{\text{TOF}}^2. \quad (6.52)$$

If the gas is thermal and satisfies $k_B T \gg \hbar\omega_z$, its velocity distribution should obey Maxwell-Boltzmann distribution. The standard deviation in velocity $\sigma_v(0)$ can be written as $\sqrt{\frac{k_B T}{M}}$, where k_B is the Boltzmann constant and M is the atomic mass. The relation then writes

$$\sigma_r(t_{\text{TOF}})^2 = \sigma_r(0)^2 + \frac{k_B T}{m} \cdot t_{\text{TOF}}^2. \quad (6.53)$$

From the equation above, we find that the vertical position variance $\sigma_r(t_{\text{TOF}})^2$ is linear with the square of the t_{TOF} . The temperature thus is determined by its slope which is $1.05 \mu\text{m}^2/\text{ms}^2$. We deduce the temperature of the ring-shape cloud $T = 13.0 \text{ nK}$. If it is a pure thermal cloud with 7×10^4 atoms at 13 nK , we can calculate that the corresponding phase space density is around 20. Such a high phase space density indicates a BEC which in turns contradicts our initial assumption that it is a thermal gas. If all the atoms stay in the ground state of the vertical direction, the expansion slope is $\sigma_{v0}^2 = \hbar\omega_z/2M = 0.826 \mu\text{m}^2/\text{ms}^2$ where $\omega_z = 360 \text{ Hz}$ is taken at the bottom of the bubble trap. Our measured expansion slope is 1.27 times of the slope corresponding to the situation where about 80% of the atoms are in the vertical ground state.

We can estimate more precisely the temperature if we take into account the discrete trapping states in the vertical direction. The momentum or velocity width in the trap at finite temperature is related to the mean excitation $\langle n_z \rangle$ in the vertical harmonic trap through $\sigma_v(0)^2 = (\langle n_z \rangle + 1/2)\hbar\omega_z/M$. $\langle n_z \rangle$ is related to the temperature through $\langle n_z \rangle = 1/[\exp(\hbar\omega_z/k_B T) - 1]$. This allows us to write the temperature as a function of the measured velocity width:

$$k_B T = \frac{\hbar\omega_z}{\ln\left(1 + \frac{1}{\langle n_z \rangle}\right)} = \frac{\hbar\omega_z}{\ln\left(\frac{\sigma_v(0)^2 + \sigma_{v0}^2}{\sigma_v(0)^2 - \sigma_{v0}^2}\right)} = \frac{\hbar\omega_z}{\ln\left(\frac{2M\sigma_v(0)^2 + \hbar\omega_z}{2M\sigma_v(0)^2 - \hbar\omega_z}\right)}. \quad (6.54)$$

We find a temperature of about 10 nK , extremely small. The motion in the vertical direction appears to be frozen. In order to also gain information on the horizontal degrees of freedom, we performed another analysis focused on the density distribution in the horizontal plane.

6.5.3 Analysis of the in situ azimuthal density profile

Up to now, we have studied the characteristics of the TOF annular gases to investigate their superfluid or degenerate character. Now we will concentrate on the in situ density profile of the dynamical ring in order to verify if it corresponds to the atomic density distribution of a 2D superfluid. In addition, we will also compare it to the density profile of a normal gas at the critical temperature T_c of the BKT transition [52, 53, 152].

We first take the dynamical ring at $t = 35 \text{ s}$ and take an azimuthal integration along the radius, which is plotted in magenta circle in Fig. 6.19. We then use a zero temperature Thomas-Fermi model, which is convolved with a Gaussian of $\sigma \simeq 4 \mu\text{m}$ to take into account the imaging resolution, to fit the density profile. This fit is plotted in blue solid line in Fig. 6.19, which is in perfect agreement with the experimental result. It is consistent with the fact that the dynamical ring is a superfluid.

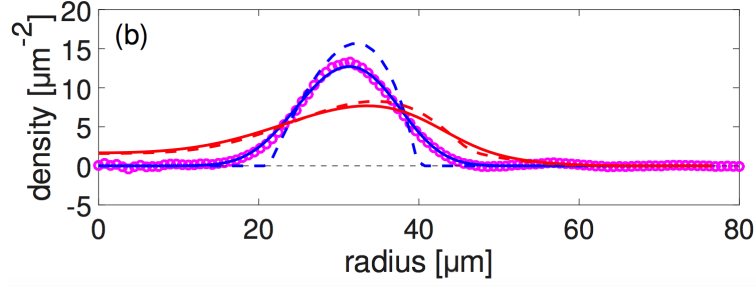


Figure 6.19 – Radial density profile at $t = 35$ s (open magenta circles) compared to two models of a quasi-2D gas: a semi-classical density profile at the critical temperature (solid red line) and a Thomas-Fermi density profile (solid blue line). The two models include a 2D convolution with a Gaussian of $\sigma \simeq 4 \mu\text{m}$ to take into account the optical resolution. The dashed lines show the models before the convolution.

In order to double check the result, this time we use a semi-classical Hartree-Fock model [153,154] to approximate the in situ density profile in $V_{\text{eff}}(r, z)$ close to the critical temperature. This would be the case if the gas were normal but close to the superfluid critical temperature. We know the total number of the atoms and the effective trap geometry of the rotating gas. If we assume that this total number of atoms is equal to the critical atom number for superfluidity, we can plot the density profile of the cloud at the critical temperature, which corresponds to the red solid line in Fig. 6.19. With the same atom number, the maximum density of the dynamical ring is much larger than the one at the critical temperature. Therefore we find that our dynamical ring must be well below the degeneracy temperature. Combining this finding with the results of the fit with the Thomas-Fermi model, we conclude that the dynamical ring is a superfluid.

6.5.4 Properties of the dynamical ring

Using the Thomas-Fermi model we can estimate the properties of the cloud. For the dynamical ring at $t = 35$ s the Thomas-Fermi profile shown in Fig. 6.19 has about $N = 4 \times 10^4$ atoms and the average radius of the ring at equilibrium is $r_{\text{eq}} \simeq 30 \mu\text{m}$. We then deduce the effective rotation frequency of the dynamical ring using equation (6.43), and we have $\Omega_{\text{eff}} = 2\pi \times 35.4 \text{ Hz} = 1.05\omega_r$. From the radius and the effective rotation frequency, one can determine the average angular momentum per particle: $\langle L_z \rangle / N \simeq 317\hbar$.

Let us now estimate the value of the chemical potential. A first rough estimation can be made by modelling the effective trap, including the rotational term, by a ring potential with harmonic trapping ω'_z in the vertical direction and ω'_r around the equilibrium radius r_{eq} . Through equations (6.38) and (6.39), we deduce the perpendicular and tangential trapping frequencies the dynamical ring, which read: $\omega'_z / 2\pi = 337.5 \text{ Hz}$, $\omega'_r / 2\pi = 16.9 \text{ Hz}$. If we assume that the gas is in the three-dimensional regime, the

chemical potential is given by [87]:

$$\mu_{3D} = \hbar \sqrt{\omega'_z \omega'_r} \sqrt{\frac{2Na}{\pi r_{\text{eq}}}} \quad (6.55)$$

where $a = 5.3 \text{ nm}$ is the scattering length of rubidium atoms. Using this expression for μ , we find $\mu_{3D}/\hbar = 2\pi \times 144.9 \text{ Hz}$ which is smaller than the transverse oscillation frequency, in contradiction with the 3D assumption. This means that the dynamical ring is in the quasi-2D regime.

A better estimation of the chemical potential can then be given using the full harmonic plus quartic potential modified by the centrifugal potential, following the approach of Ref. [147] which is valid for a two-dimensional gas. The chemical potential of such a quasi-2D superfluid is given by [147]:

$$\mu = \frac{\hbar \omega_r}{8\lambda} \left(\frac{12\lambda^2 \tilde{g}}{\pi} \right)^{2/3}, \quad (6.56)$$

where ω_r is the radial oscillation frequency at the harmonic oscillation and $d_z = \sqrt{\hbar/M\omega_z}$ is the size of the vertical harmonic groundstate in the nonrotating trap and $\tilde{g} = \sqrt{8\pi}a/d_z$ is the dimensionless interaction constant in two dimensions. With this formula, we find $\mu/\hbar \simeq 2\pi \times 84 \text{ Hz}$.

Interestingly, with this value of the chemical potential the estimated peak speed of sound $c = \sqrt{\mu/M} \simeq 0.62 \text{ mm/s}$ at the peak radius r_{eq} is much smaller than the local coarse-grained fluid velocity $v = \Omega r_m \simeq 6.9 \text{ mm/s}$: the superfluid is therefore rotating at a supersonic velocity corresponding to a Mach number of 11. If we compare it to the radial average speed of sound of this very thin gas $c = \sqrt{\bar{\mu}/M} = \sqrt{4\mu/5M} \simeq 0.55 \text{ mm/s}$ we even find Mach 12.4.

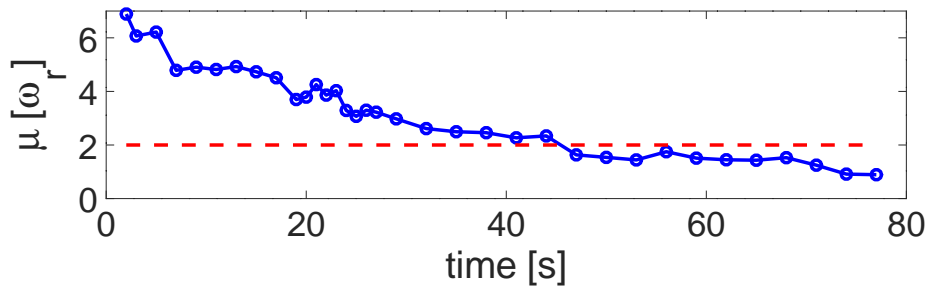


Figure 6.20 — Time evolution of the chemical potential in units of the harmonic trapping frequency. The red dashed line indicates $\mu = 2\hbar\omega_r$.

Moreover, due to the continuous acceleration of the rotation, the dynamical ring radius grows gradually with time and the atomic number decreases with the waiting time which results in a decrease of the chemical potential and an increase of the Mach number. The time evolution of the chemical potential is presented in Fig. 6.20. For

$t > 45$ s the chemical potential is below $2\hbar\omega_r$ and the highest measured Mach number is above 20.

We have discussed the Lowest Landau Level regime previously. For a Bose gas rotating in a harmonic trap, when the interaction energy gn is smaller than $2\hbar\Omega_{\text{eff}}$, the atoms stay in the LLL ground state. In our case, we have a harmonic plus quartic trap, such that the LLL doesn't strictly exist. However, there is still a family of quasidegenerate states in the fast rotation regime, with an energy gap of $2\hbar\omega_r$ to the next family of states. After a holding time of about 50 s, the chemical potential drops below this gap and we can say that the atoms occupy only this family of lower states. The many-body character of the wavefunction is however not clear, and this work calls for further investigation in this direction.

6.6 Quadrupole modes of the dynamical ring

In section 6.3.2 we have described how to excite the quadrupole mode for measuring the effective rotation frequency of the connected gas at the bottom of the bubble trap. In the case where a hole has formed, we can observe that the dynamical rings in Fig. 6.14 are not always perfectly round. An anisotropy develops after the forced evaporation stage and rotates. For a connected cloud rotating at $\Omega_{\text{eff}} < \Omega_h$, the energies of the $m = \pm 2$ quadrupole modes are non degenerate [82, 155]. Such quadrupole modes have also been predicted for a dynamical ring formed in a harmonic plus quartic trap [146] but never observed up to now. Here we investigate these modes of a dynamical ring by using a surface mode spectroscopy scheme [149].

Fig. 6.14 shows the experimental procedure and the evolution of the dynamical ring. We have seen the experimental procedure of exciting the quadrupole modes resonantly in section 6.3.2. During the resonant excitation phase, we selectively excite a quadrupole mode $m = -2$ by rotating a small trap anisotropy $\varepsilon_{\text{ani}} = 0.01$ for a duration $\tau = 1$ s once the ring is formed. For each excitation frequency Ω_{exc} , the cloud is imaged in situ just after excitation and the cloud anisotropy $\zeta = r_{\text{long}}/r_{\text{short}}$ is plotted as a function of Ω_{exc} . For a connected elliptical cloud, r_{long} and r_{short} are the Thomas Fermi radii of the long and short axes. For the ring-shaped elliptical cloud, the long and short axes are defined as the distance from the center of the density peaks along the ellipse.

We have discussed above how the RF knife is able to accelerate the cloud during evaporative cooling. Therefore, we can prepare clouds with different effective rotation frequencies by selecting the sample at different waiting time. We hence realize the resonant excitation experiment, through deforming the trap and rotating the deformed trap at various frequencies, at different times t in order to be sure the rotation frequencies are different before the resonant excitation phase.

Figure 6.21 shows the result of this quadrupole mode spectroscopy, focusing on the $m = -2$ mode for increasing rotation frequencies corresponding to times $t = 2.5$ s, 5 s, 20 s, 26 s and 50 s. They are fitted by a Lorentzian distribution instead of the model in equation (6.44), since we are mostly interested in the resonant frequency. By convention we set that Ω_{exc} is negative when the excitation anisotropy is rotated

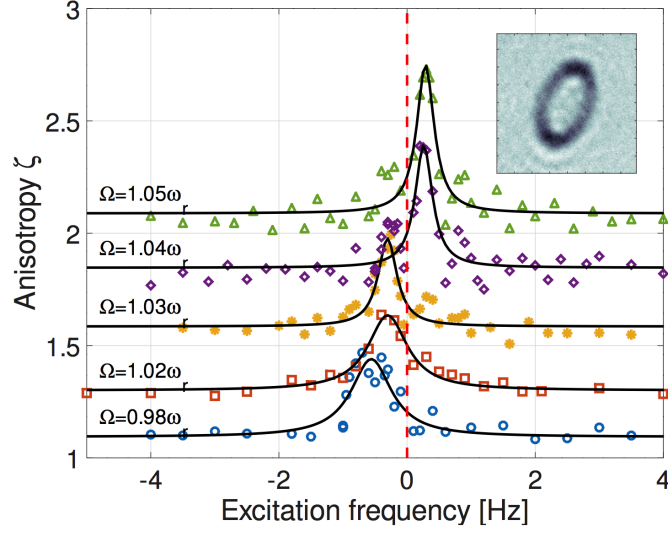


Figure 6.21 — Cloud anisotropy ζ as a function of the probe frequency Ω_{exc} for different holding times $t = 2.5$ s, 5 s, 20 s, 26 s and 50 s from bottom to top, corresponding to effective rotation rates $\Omega/\omega_r \simeq 0.98, 1.02, 1.03, 1.04$ and 1.05 (circle, square, star, diamond and triangle symbols respectively). The black solid curves are Lorentzian fits to the data. Inset: example of resonantly excited dynamical ring.

against the direction of the atomic flow. The resonant spectroscopy of the connected cloud shows that the $m = -2$ quadrupole mode resonance occurs at negative frequency since the behavior of the quadrupole modes of the connected cloud trapped in the bubble is similar to the $m = -2$ mode in a harmonic trap, before the appearance of the central hole. Surprisingly, when the rotation frequency increases and $\Omega > \Omega_h$, this resonance shifts towards positive frequencies, which means that the two quadrupole modes $m = \pm 2$ are now both co-rotating with the flow. This is not expected, as Ref. [146] always predicts a negative value for the $m = -2$ resonant quadrupole frequency.

In order to verify that the direction of the rotating mode $m = -2$ is really co-rotating with the flow, we take many in situ images with different waiting times after the 1 s resonant excitation phase and observe the rotating direction of the anisotropic ring. The four figures in Fig. 6.22(b) show that the trap deformation rotates counterclockwise during the stirring phase. Once the dynamical ring quadrupole mode $m = -2$ is excited resonantly, the ring becomes an ellipse and rotates in the same direction than the flow, as shown in Fig. 6.22(a).

Moreover, the rotation rate of the ellipse in Fig. 6.22(a) is supposed to follow the resonant probe frequency of the mode $m = -2$ which is $\omega_-/2$. We take pictures of the rotating ellipse at different times and determine its rotation rate through the time evolution of the angle, shown as the inner picture of the Fig. 6.23. Fig. 6.22 presents the rotation rate of the ellipse, $0.801(6) \text{ rad} \cdot \text{s}^{-1}$ and the resonant frequency of the spectroscopy $0.98(11) \text{ rad} \cdot \text{s}^{-1}$. These two frequencies are in fair agreement, showing

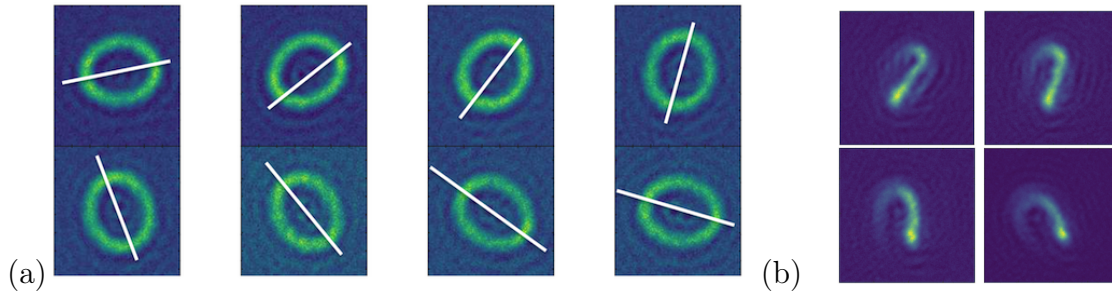


Figure 6.22 – (a): The ring anisotropy rotates counterclockwise at a very low angular velocity. Pictures are taken every 1 s from left to right after the end of the forced evaporation phase. The white lines are the long axis of the ellipse, showing that the ellipse rotates counterclockwise. (b): Four pictures taken during the stirring phase, at time $t = -60$ ms, -58 ms, -56 ms and -54 ms. Reading order from left to right, from top to bottom.

that the elliptical excited ring rotates at the resonant frequency of the spectroscopy, the difference being probably explained by the fact that the rotation frequency could be slightly different if the time at which the spectroscopy was made is not exactly the time at which the elliptic deformation occurred. It also ensures that both the quadrupole modes $m = \pm 2$ are co-rotating with the atomic flow, which doesn't agree with the theoretical prediction in [146, 147].

We also tried to excite the mode $m = +2$ through rotating a deformed trap with a small anisotropy $\varepsilon_{\text{ani}} = 0.01$ at different rotating frequencies between 10 Hz and 70 Hz. However, this mode was much more difficult to excite than the mode $m = -2$. In the end, we could not observe a resonant peak as the one of the mode $m = -2$. If we increase the anisotropy of the deformed trap to $\varepsilon_{\text{ani}} = 0.03$ and decrease the excitation duration to 25 ms, the resonant peak corresponding to the mode $m = +2$ appears with a resonant frequency around 40 Hz.

6.7 Outlook

6.7.1 Reaching the giant vortex regime

In this chapter I have presented our results showing that we have achieved a dynamical ring with a multiply charged vortex in the center and vortices in the bulk. The next interesting step would be to try to reach the giant vortex regime. As the phase diagram in Fig. 6.4 shows, in order to realize a phase transition from the dynamical ring to the giant vortex, we can increase the rotation rate Ω_{eff} or decrease the interaction strength. On the one hand, increasing the rotation rate to values much larger than $1.06\omega_r$ is too difficult to reach in our experiment. On the other hand, decreasing the interaction strength requires to increase the quartic strength λ or decrease the number of atoms. For our experiment, since changing the anharmonicity λ is not realistic, we can reach the giant vortex state with the current ring rotation frequency by lowering the atom

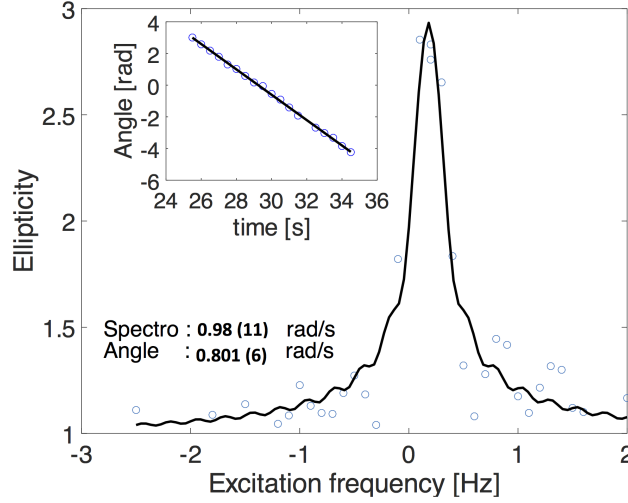


Figure 6.23 — Comparing the rotation frequency of the ellipse and the resonant frequency of the quadrupole mode. The inner picture represents the angle as a function of time together with a linear fit.

number. Fig. 6.24 presents the result of a GPE simulation made with $N = 400$ atoms: a giant vortex is formed at $\Omega_{\text{eff}} = 1.06\omega_r$. Waiting for a long time and decreasing the rf knife frequency would allow us to reach such a small atom number. But a high sensitivity detection setup is then required, which is not currently implemented on our setup. However, such sensitivities are possible and within reach of single atom detection schemes realized by other groups [156].

6.7.2 Dissipation of the supersonic flow

In section 6.3.2 we showed that when the temperature of the cloud is very low, the damping of the quadrupole mode will be very small and limited by the Fourier transform. In addition, the trapping potential is very smooth and the dynamical ring has little dissipation such that it can survive for a long time with the atomic velocity more than ten times of the superfluid speed of sound. In order to study how a localized defect would dissipate a superfluid flow at such a supersonic speed, we would like to use the blue detuned beam that we developed to stir the static annular gas (see Chapter 5) as an obstacle to perturb the dynamical ring. We are able to align the position of the circular trajectory of the obstacle with the dynamical ring by using the same method presented in Section 5.3.2.2. Changing the parameters of the obstacle, such as position, intensity or rotation frequency, modifies the perturbation strength. We can measure the evolution of the effective rotation frequency in the absence of the selectively evaporative rf knife or the atom number with the knife as a function of the perturbation strength. This experiment may complement to even higher speeds the theoretical and recent experimental works [157–160] showing that obstacles moving at velocities far exceeding the Landau critical velocity do not necessarily create a significant amount

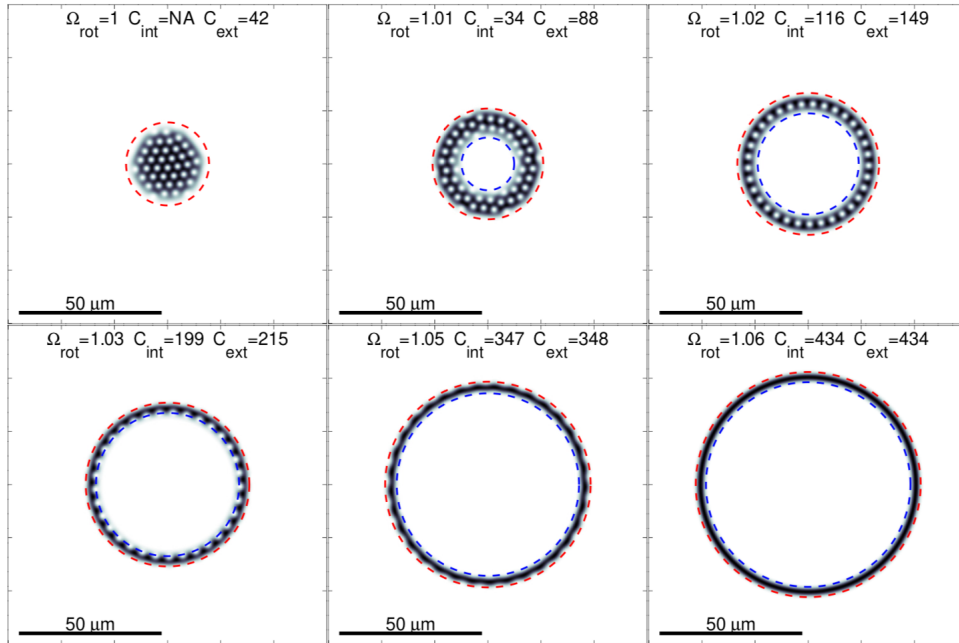


Figure 6.24 — GPE simulation for 400 atoms rotating in the bubble trap for different Ω_{eff} in units of ω_r . The blue (red) dashed lines are the contours along which the circulation C_{int} (C_{ext}) has been computed. The difference between the circulations of the inner contour and the outer contour indicates the number of vortices present in the bulk of the ring. When $\Omega_{\text{rot}} = 1.06\omega_r$, the inner contour and the outer contour have the same circulation, proving that the dynamical ring is in the 1D giant vortex regime. Simulations realized by Romain Dubessy.

of excitations. This work will be realized in the near future.

General conclusion

In this manuscript, I have shown three ring-shaped superfluids, a levitating ring, a trapped ring situated at the equator of the bubble trap and a fast-rotating dynamical ring. They are all confined on the surface of the bubble trap but with different formation mechanisms.

The levitating ring is formed in a microgravity environment and confined on the bubble surface. During my PhD, we proposed a method to compensate gravity which is taking advantage of the inhomogeneous distribution of the local Rabi coupling. We then designed the related experiments to test the theoretical prediction and to ensure a perfectly circularly polarized rf field. After observing an unexpected ring instead of a bubble-shaped cloud, we improved the initial analytical model by taking the inhomogeneous transverse confinement into account which allowed us to qualitatively explain the formation of the levitating ring. As recently NASA has launched the Cold Atom Laboratory (CAL) to the International Space Station (ISS) [65] to produce ultracold degenerate quantum gases and one of the experiments aims at investigating the gas confined in a microgravity bubble trap [67], our study of the levitating ring could be helpful for the study of cold atoms in microgravity environment, especially for the related experiment in the ISS. By now, we did not probe the coherence of the levitating ring. In the near future, we plan to evaporatively cool down the levitating ring with the antenna of vertical axis, avoiding to breaking the rotational symmetry, in order to study the properties of the levitating ring further.

As for the trapped ring, it is confined directly in the ring trap which is constructed by the combination of a double blue detuned light sheet and the bubble trap. The circulation of the ring is determined by the phase winding around one circle. The wavefunction at a certain position of the ring should be single-valued, so the winding phase has to be an integer times 2π , resulting in a quantized circulation. In the beginning of my PhD, the implementation of the ring trap was almost done by the two previous PhD students. My work, during my PhD, was to set the ring into rotation and prove that the circulation of the ring is quantized. In this manuscript, we recall the principle and experimental realization of the ring-shape trap. In addition, we also showed two methods to set the ring into rotation: one method is rotating a quadrupole deformation of the ring trap, and the other one is stirring the annular gas with a blue

detuned laser.

The former method is able to create circulations in the ring, but it is difficult to determine precisely the corresponding winding number. The critical rotation rate to excite the ring and introduce vortices, computed through the speed of sound of the ring, is much larger than the elementary rotation rate. As a consequence, using this method is difficult to produce a desired circulation, especially a small one. The latter method was used by many other groups and it was understood much better than the last method. After improving the detection sensitivity of the circulation by implementing a reconnection procedure, shifting the bubble and pushing the rotating superfluid from the equator to the bottom of the bubble before releasing them, we finally succeeded in detecting the circulation of the first circulation quanta. Moreover, we also observed that a multiply charged vortex is separated into two or three small singly charged vortices, which was an evidence of a quantized circulation.

As for the perspective of the trapped ring, on one hand, in order to generate any desired circulation accurately, we would like to use the phase imprinting technique [161] to rotate the ring. The idea is to imprint a given phase on the ring through an helix of light intensity, generated by a Spatial Light Modulator (SLM). This method was investigated theoretically [161] and the realization of the light profile has been obtained experimentally in the lab. On the other hand, increasing the power of the double light sheet and the magnetic gradient while decreasing the chemical potential allow the ring to reach quasi-2D or quasi-1D regimes. A quasi-1D ring is attractive since it can be regarded as a uniform ring satisfying periodic boundary conditions. Reaching such a low-dimensional regime requires a chemical potential for a quasi-1D ring smaller than both the radial and vertical trapping frequencies. The challenge here will be to produce a quasi-1D ring with a small chemical potential due to the residual optical defects and the inhomogeneous potential.

The superfluid dynamical ring, obtained by rotating a superfluid initially at the bottom of the bubble trap, is formed due to the centrifugal force. The linear velocity of the superfluid dynamical ring is more than Mach 18, indicating a supersonic velocity. In addition, the dynamical ring can survive for more than one minute, showing that the adiabatic potential is too smooth to dissipate the atomic flow. In the manuscript, we also demonstrated the quadrupole modes of rotating connected or annular superfluids. Surprisingly, we found that both of the quadrupole modes for the dynamical ring are co-rotating with the atomic flow, which does not agree with the previous theoretical prediction. This thesis presents the first experimental realization of a superfluid dynamical ring and the first observation of the quadrupole modes of the dynamical ring.

Theoretical and recent experimental works [157–159] indicated that obstacles moving at velocities far exceeding the speed of sound do not necessarily create a significant amount of excitations. The heating rate may become maximum when the velocity of the obstacle is close to the speed of sound [160]. In our setup, it will be very interesting to study how a localized defect would dissipate the superfluid flow at such a supersonic speed. To this aim, we plan to add a local obstacle to perturb the dynamical ring in order to investigate the decay of rotation as a function of the laser parameters,

such as position and intensity. The blue detuned laser stirrer which had been used to stir the trapped ring can be used for this purpose. We can use the same method as presented in Section 5.3.2.2 to adjust the laser position with respect to the dynamical ring. Analyzing the resulting data and compare it to theory will be the main challenges here.

As described in Chapter 6, rotating a superfluid rapidly in an anharmonic trap, such as a harmonic plus quartic trap or a bubble trap, crosses three phases: vortex lattice, multiply charged vortex in center with vortex lattice in bulk, and giant vortex. The giant vortex, as a one-dimensional irrotational flow with a large rotation rate, is a phase never observed yet. We demonstrated that our superfluid dynamical ring is one important step towards this giant vortex. After a series of numerical simulations by Romain Dubessy, we found that the giant vortex regime should be accessible in our experimental system for an atom number of 400 atoms with the maximum achievable rotation rate in the experiment. Although such a small atomic density is below our current detection sensitivity, it is still within reach of single atom detection schemes [156]. Future experiments in this direction could build on the results presented in this manuscript to access unprecedented regimes of rotation.

Appendices

Measurement of the gradient of the quadrupole trap

In Chapter 2 we have explained that a rf dressed quadrupole trap results in a bubble trap, and this dressing process take place in the science cell. After forming the bubble trap, measuring the magnetic gradient α precisely allows us to obtain a more accurate information about the trap. In fact, the most interesting parameter is the constant gradient $b = \alpha/I$, which only depends on our own configuration of the magnetic trap. Once having this constant gradient b , it is accessible to the magnetic gradient with any current. In the following I will present a method of measuring the constant gradient. The main idea of measuring the gradient is that we increase the rf frequency for a certain flowing current while the semi-minor axis increases correspondingly. A reminder of the expression of the vertical equilibrium position considering gravity is written:

$$R = \frac{\omega_{\text{rf}}}{2\alpha} \left(1 + \frac{\varepsilon}{\sqrt{1 - \varepsilon^2}} \frac{\Omega_0}{\omega_{\text{rf}}} \right) = \frac{\omega_{\text{rf}}}{2\alpha} + \frac{\varepsilon}{\sqrt{1 - \varepsilon^2}} \frac{\Omega_0}{2\alpha}. \quad (\text{A.1})$$

where ε is defined $Mg/2\hbar\alpha$. In this configuration of the quadrupole trap, α describe the horizontal magnetic gradient, half of the vertical one, which is proportional to the flowing current. From the last equation, one finds the first term is the semi-minor axis of the resonant ellipsoid surface and the second term corresponds to the correction of gravity. For a given Rabi coupling and a flowing current, the second term becomes a constant that doesn't depend on the rf frequency. If we plot the vertical position of atoms after a duration of time-of-flight(TOF) for a different dressing frequencies, which is supposed to be a straight line whose gradient indicates the inverse of the vertical gradient of the magnetic trap. We can also describe the rf frequency as a function of the vertical position as:

$$\omega_{\text{rf}} = 2\alpha R - \frac{\varepsilon\Omega_0}{\sqrt{1 - \varepsilon^2}}. \quad (\text{A.2})$$

in which the gradient of the plotting curve gives the magnetic gradient. In order to minimize the errors due to the dipole oscillation and get an accurate vertical position,

for a fixed current and rf frequency, we also plot the vertical positions at different waiting time.(see Fig.A.1) Fitting the curve with a sine function presents the center of the motion, which minimizes the error bars. By using this method, we measure the value of $\alpha/2\pi$ with three different flowing currents: 36 A, 45 A and 60 A, which are 5.2(1), 6.6(2) and 8.5(5) MHz · mm⁻¹. It then gives the constant gradients per ampere by dividing the currents into the magnetic gradient α respectively. Finally, after averaging the three values for different currents, we obtain an accurate constant gradient per ampere, which is $b = 2.071 \pm 0.16 \text{ G} \cdot \text{cm}^{-1} \cdot \text{A}^{-1}$.

Fig. A.1 shows one case of 36A as well as the vertical oscillation of the cloud confined in the bubble trap with dressing frequency 3 MHz.

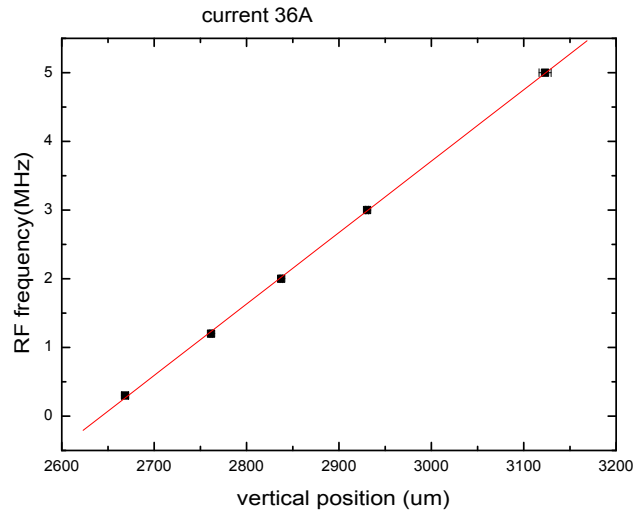


Figure A.1 — Left: Plot the setting rf frequency as a function of the measured vertical position of the atoms after TOF while the flowing current is always 36 A. The gradient of the resulting curve indicates the vertical magnetic gradient for 36 A.

Appendix **B**

Loading atoms to the equator of the compressed bubble trap

In order to shift the relative position between the bubble and the light sheet, there is a pair of coils in Helmholtz configuration situated below and above the science cell generating a vertical bias magnetic field, which can displace the bubble vertically. So the equilibrium of the vertical position is determined by the sum of two magnetic fields: one is generated by the quadrupole coils with an amplitude $-2bZ \times I_{\text{quad}}$ where $b = 2.071 \text{G} \cdot \text{cm}^{-1} \cdot \text{A}^{-1}$ is the horizontal magnetic gradient and Z is the vertical distance away from the quadrupole trap center; the other one is produced by the vertical bias field with an amplitude $B_b \times I_{\text{bias}}$. Therefore, the new center of the quadrupole field is given by seeing:

$$B_b \times I_{\text{bias}} - 2bZ \times I_{\text{quad}} = 0. \quad (\text{B.1})$$

Applying a current I_{bias} in the bias coils can shift the bubble vertically by a distance Z and a given current I_{quad} in the quadrupole coils. The conversion between the vertical displacement in distance and the change of the current in bias coils can be described as:

$$Z = \frac{I_{\text{bias}}}{I_{\text{quad}}} \times \frac{B_b}{2b} = I_{\text{bias}} \times \frac{\beta}{I_{\text{quad}}}, \quad (\text{B.2})$$

where $\beta = 2266 \mu\text{m}$ is constant for a given geometry of the coils and is calibrated by plotting the vertical position of the cloud after TOF as a function of I_{bias} for a certain I_{quad} [100].

To shift the bubble and make the altitude of the atoms correspond to the center of the light sheet, after vertically shifting the bubble to a certain position, we switch off the trap including the quadrupole currents and the rf antennas while switching on the double light sheet for 0.1 ms with its maximum power. Since the blue-detuned light sheet applies a repulsive force on the atoms, one can deduce their relative position through the atomic shape and center of mass in the horizontal TOF pictures. If the altitude of atoms is aligned with the two maxima or the central minimum of the light sheet, the vertical expansion of the cloud after TOF is symmetric and the vertical position of the center of mass after TOF coincides with the position after free fall, which is

shown in Fig. B.1. The distance between the two potential maxima of the double light sheet is about $10\ \mu\text{m}$, and the corresponding current shifting in the bias coils is $0.15\ \text{A}$, which also can be checked with equation (B.2). During scanning the bias current and shifting the bubble, there are three times that the cloud expands symmetrically after touching the double light sheet. It occurs when the atoms are aligned with the two potential maxima and the potential minimum of the double light sheet, noted "b" and "a" respectively in Fig B.1. In order to avoid to align the atoms with the maxima of the light sheet, we scan the current I_{bias} from a value smaller than the expected value. Once the expansion after TOF becomes extremely large and symmetric we check the position of the other maximum by adding $0.15\ \text{A}$. If the expansion is still symmetric we conclude that the good bias current corresponding to the potential minimum is between these two values. After scanning the bias current and getting another symmetrical expanding cloud, we load the atoms in the potential minimum of the double light sheet. We check that the cloud is indeed at the minimum by looking at the position of the center of mass after TOF.

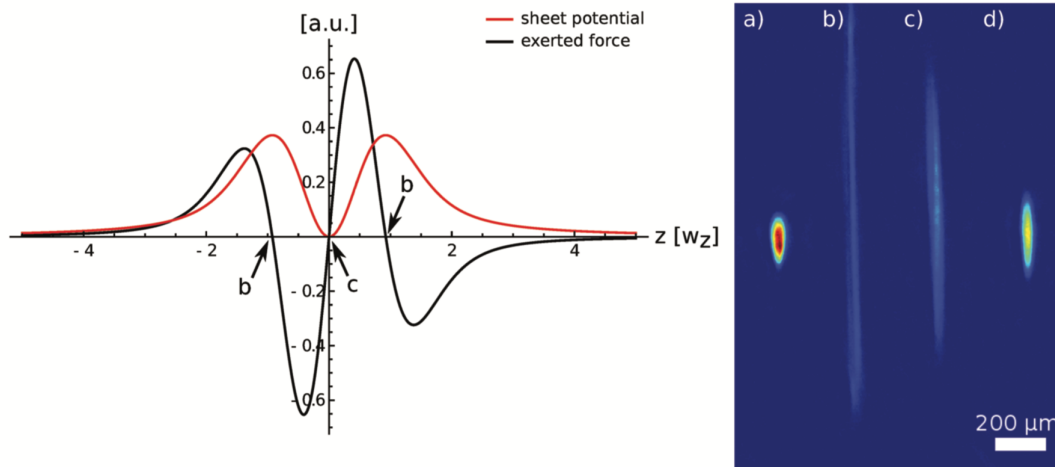


Figure B.1 – Left: Vertical optical intensity distribution of the light sheet (red line) and its derivative indicating the force applying on the atoms (black line). The atoms do not undergo a force when they are located at the two maxima (noted b) and minimum (noted c) of the light sheet. Right: Horizontal images of the atoms after 23 ms TOF. (a) indicates the atoms at the bottom of the bubble without the light sheet. (b) corresponds to the atoms located at a maximum of the double light sheet, which also expands symmetrically. (c) corresponds to the atoms in the central minimum of the light sheet, which indicates a successful loading of the atoms into the light sheet. (d) shows the TOF image of the atomic cloud after loading into the light sheet with a power $P_0 = 300\ \text{mW}$. The cloud expands larger than (a) since the vertical trapping frequency generated by the light sheet is more important than the transverse trapping frequency at the bottom of the bubble.

After aligning the atoms with the minimum of the light sheet, we note the current in the bias coils as I_{bias} . During the third process of loading the atoms into the light sheet, we hold the atoms at the bottom of the aligned bubble and then ramp the power of the light sheet from 0 to P_0 in 400 ms. Before compressing the bubble, atoms are maintained in the double light sheet for another 100 ms.

Increasing the magnetic gradient and compressing the bubble lead to increase the atomic density and the chemical potential, which also make it easier to reach condensation. During the last step, we first shift down the bubble for a distance of Δz in 50 ms, resulting in a ring trap whose radius r is already the goal radius at the equator of the final ring trap, as shown as Fig.B.2(a) and (b). After that, we ramp the current in the quadrupole coils from 28.5 A to 90 A in 200 ms to compress the bubble while changing the current in the bias coils in order to always keep the radius of the ring constant, as shown in Fig.B.2(c). Keeping the same radius during the bubble compression can avoid displacing the atoms and minimize the heating and losses of the atoms. The final current in the bias coils after compressing the bubble is given by:

$$I_{\text{fin}} = I_{\text{bias}} \frac{I_2}{I_1} + \frac{r_b}{2} \times \frac{I_2}{\beta} + Z_g \times \frac{I_2}{\beta}, \quad (\text{B.3})$$

where $I_1 = 28.5$ and $I_2 = 90$ are the initial and final currents in the quadrupole coils, r_b is the semi-major radius of the bubble with 28.5 A, determined by equation (2.61). On the right hand side of the equation (B.3), the first term serves to fix the position of zero magnetic field. The second term is shifting down the bubble for a distance of semi-minor radius $r_b/2$. In addition, the last term corresponds to the correction of the gravity, which is around $2.6 \mu\text{m}$ deduced by equation (2.74). An illustration showing the role of these three contributions is presented Fig. B.2(d).

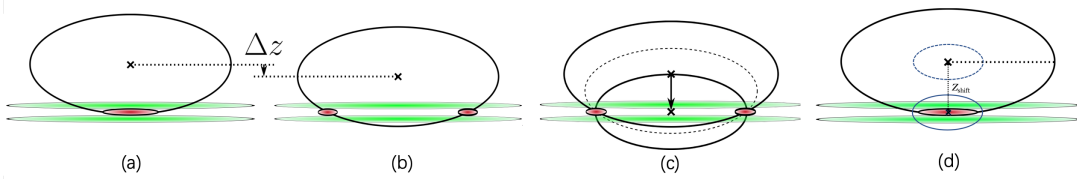


Figure B.2 — Illustration of the processes for loading the atoms into the ring trap at the equator of the bubble. (a)(b) show the vertical shift to make a ring trap whose size is the same as final trap. (c) indicates the compressing process while keeping the same size of ring trap. (d) is not one step of the loading procedure but it shows the idea of how to determine the final current in the bias. The small ellipse drawn in dashed line indicates the bubble trap after being compressed while remaining the same center. Z_{shift} presents the distance between the initial center of the bubble trap and the center of the double light sheet. It consists of the semi-minor radius of the large bubble drawn in solid line and the distance between the position where atoms are trapped and the very bottom of the resonant surface.

Bibliography

- [1] A. EINSTEIN, “Quantentheorie des einatomigen idealen Gases”. *Sitzungsber. Kgl. Preuss. Akad. Wiss.*, 261–267 (1924).
- [2] A. EINSTEIN, “Quantentheorie des einatomigen idealen Gases. Zweite Abhandlung”. *Sitzungsber. Kgl. Preuss. Akad. Wiss.*, 3–14 (1925).
- [3] P. KAPITZA, “Viscosity of Liquid Helium below the λ -Point”. *Nature* **141**, 74 (1938).
- [4] J.F. ALLEN and A.D. MISENER, “Flow of Liquid Helium II”. *Nature* **141**, 75 (1938).
- [5] D.R. ALLUM, P.V.E. MCCLINTOCK, A. PHILLIPS and R.M. BOWLEY, “The breakdown of superfluidity in liquid ^4He : an experimental test of Landau’s theory”. *Philosophical Transactions of the Royal Society of London A: Mathematical, Physical and Engineering Sciences* **284** (1320), 179–224 (1977).
- [6] R.P. FEYNMAN, “Chapter II Application of Quantum Mechanics to Liquid Helium”. volume 1 of *Progress in Low Temperature Physics* pages 17 – 53, Elsevier (1955).
- [7] V.F. VINEN, “The detection of single quanta of circulation in liquid helium II”. *Proceedings of the Royal Society of London A: Mathematical, Physical and Engineering Sciences* **260** (1301), 218–236 (1961).
- [8] G. B. HESS and W. M. FAIRBANK, “Measurements of Angular Momentum in Superfluid Helium”. *Phys. Rev. Lett.* **19**, 216–218 (Jul 1967).
- [9] E. J. YARMCHUK, M. J. V. GORDON and R. E. PACKARD, “Observation of Stationary Vortex Arrays in Rotating Superfluid Helium”. *Phys. Rev. Lett.* **43**, 214–217 (Jul 1979).
- [10] D. J. WINELAND, R. E. DRULLINGER and F. L. WALLS, “Radiation-Pressure Cooling of Bound Resonant Absorbers”. *Phys. Rev. Lett.* **40**, 1639–1642 (1978).

-
- [11] W. NEUHAUSER, M. HOHENSTATT, P. TOSCHEK and H. DEHMELT, “Optical-Sideband Cooling of Visible Atom Cloud Confined in Parabolic Well”. *Phys. Rev. Lett.* **41**, 233–236 (1978).
- [12] S. CHU, L. HOLLBERG, J. E. BJORKHOLM, A. CABLE and A. ASHKIN, “Three-dimensional viscous confinement and cooling of atoms by resonance radiation pressure”. *Phys. Rev. Lett.* **55**, 48–51 (1985).
- [13] ALAN L. MIGDALL, JOHN V. PRODAN, WILLIAM D. PHILLIPS, THOMAS H. BERGEMAN and HAROLD J. METCALF, “First Observation of Magnetically Trapped Neutral Atoms”. *Phys. Rev. Lett.* **54**, 2596–2599 (Jun 1985).
- [14] S. CHU, J.E. BJORKHOLM, A. ASHKIN and A. CABLE, “Experimental observation of optically trapped atoms”. *Phys. Rev. Lett.* **57** (3), 314–317 (1986).
- [15] E.L. RAAB, M. PRENTISS, A. CABLE, S. CHU and D.E. PRITCHARD, “Trapping of neutral sodium atoms with radiation pressure”. *Phys. Rev. Lett.* **59** (23), 2631–2634 (1987).
- [16] C. COHEN-TANNOUJDI, “Nobel Lecture: Manipulating atoms with photons”. *Rev. Mod. Phys.* **70**, 707 (1998).
- [17] S. CHU, “Nobel Lecture: The manipulation of neutral particles”. *Rev. Mod. Phys.* **70**, 685 (1998).
- [18] W. D. PHILLIPS, “Nobel Lecture: Laser cooling and trapping of neutral atoms”. *Rev. Mod. Phys.* **70**, 721 (1998).
- [19] M.H. ANDERSON, J.R. ENSHER, M.R. MATTHEWS, C.E. WIEMAN and E.A. CORNELL, “Observation of Bose-Einstein condensation in a dilute atomic vapor”. *Science* **269**, 198–201 (1995).
- [20] K.B. DAVIS, M.-O. MEWES, M.R. ANDREWS, N.J. VAN DRUTEN, D.S. DURFEE, D.M. KURN and W. KETTERLE, “Bose-Einstein condensation in a gas of sodium atoms”. *Phys. Rev. Lett.* **75** (22), 3969–3973 (1995).
- [21] E. A. CORNELL and C. E. WIEMAN, “Nobel Lecture: Bose-Einstein condensation in a dilute gas, the first 70 years and some recent experiments”. *Rev. Mod. Phys.* **74**, 875 (2002).
- [22] W. KETTERLE, “When atoms behave as waves: Bose-Einstein condensation and the atom laser”. *Rev. Mod. Phys.* **74**, 1131 (2002).
- [23] S. JOCHIM, M. BARTENSTEIN, A. ALTMAYER, G. HENDL, S. RIEDL, C. CHIN, J. H. DENSCHLAG and R. GRIMM, “Bose-Einstein Condensation of Molecules”. *Science* **302** (2003).

- [24] J. KASPRZAK, M. RICHARD, S. KUNDERMANN, A. BAAS, P. JEAMBRUN, J. M. J. KEELING, F. M. MARCHETTI, M. H. SZYMANSKA, J. L. ANDRÉ, R. AMD STAEHLI, V. SAVONA, P.B. LITTLEWOOD, B. DEVEAUD and LE SI DANG, “Bose–Einstein condensation of exciton polaritons”. *nature* **443**, 409–413 (2006).
- [25] J. KLAERS, J. SCHMITT, F. VEWINGER and M. WEITZ, “Bose–Einstein condensation of photons in an optical microcavity”. *Nature* **468**, 545–548 (2010).
- [26] M. GREINER, O. MANDEL, T. ESSLINGER, T.W. HÄNSCH and I. BLOCH, “Quantum Phase Transition from a Superfluid to a Mott Insulator in a Gas of Ultracold Atoms”. *Nature* **415**, 39 (2002).
- [27] D. JAKSCH, C. BRUDER, J. I. CIRAC, C. W. GARDINER and P. ZOLLER, “Cold Bosonic Atoms in Optical Lattices”. *Phys. Rev. Lett.* **81**, 3108–3111 (Oct 1998).
- [28] C. RYU, M. F. ANDERSEN, P. CLADÉ, V. NATARAJAN, K. HELMERSON and W. D. PHILLIPS, “Observation of Persistent Flow of a Bose–Einstein Condensate in a Toroidal Trap”. *Phys. Rev. Lett.* **99**, 260 401 (2007).
- [29] STUART MOULDER, SCOTT BEATTIE, ROBERT P. SMITH, NAAMAN TAMMUZ and ZORAN HADZIBABIC, “Quantized supercurrent decay in an annular Bose–Einstein condensate”. *Phys. Rev. A* **86**, 013 629 (Jul 2012).
- [30] STEPHEN ECKEL, JEFFREY G. LEE, FRED JENDRZEJEWSKI, NOEL MURRAY, CHARLES W. CLARK, CHRISTOPHER J. LOBB, WILLIAM D. PHILLIPS, MARK EDWARDS and GRETCHEN K. CAMPBELL, “Hysteresis in a quantized superfluid ‘atomtronic’ circuit”. *Nature* **506** (7487), 200–203 (02 2014).
- [31] I. CHIORESCU, Y. NAKAMURA, C.J.P.M. HARMANS and J.E. MOOIJ, “Coherent quantum dynamics of a superconducting flux qubit”. *Science* **299** (5614), 1869–1871 (Mar 21 2003).
- [32] C. RYU, P. W. BLACKBURN, A. A. BLINOVA and M. G. BOSHIER, “Experimental Realization of Josephson Junctions for an Atom SQUID”. *Phys. Rev. Lett.* **111**, 205 301 (Nov 2013).
- [33] LUIGI AMICO, GERHARD BIRKL, MALCOLM BOSHIER and LEONG-CHUAN KWEK, “Focus on atomtronics-enabled quantum technologies”. *New Journal of Physics* **19** (2), 020 201 (2017).
- [34] K. W. MADISON, F. CHEVY, W. WOHLLEBEN and J. DALIBARD, “Vortex formation in a stirred Bose–Einstein condensate”. *Phys. Rev. Lett.* **84**, 806 (2000).
- [35] J. R. ABO-SHAER, C. RAMAN, J. M. VOGELS and W. KETTERLE, “Observation of Vortex Lattices in Bose–Einstein Condensates”. *Science* **292**, 476 (2001).

- [36] Y. LIN, R. COMPTON, K. JIMÉNEZ-GARCÍA, J. V. PORTO and B. SPIELMAN, “Synthetic magnetic fields for ultracold neutral atoms”. *Nature* **462**, 628–632 (2009).
- [37] JEAN DALIBARD, FABRICE GERBIER, GEDIMINAS JUZELIŪNAS and PATRIK ÖHBERG, “*Colloquium*: Artificial gauge potentials for neutral atoms”. *Rev. Mod. Phys.* **83**, 1523–1543 (Nov 2011).
- [38] M. AIDELSBURGER, M. ATALA, S. NASCIMBÈNE, S. TROTZKY, Y.-A. CHEN and I. BLOCH, “Experimental Realization of Strong Effective Magnetic Fields in an Optical Lattice”. *Phys. Rev. Lett.* **107**, 255 301 (Dec 2011).
- [39] M. R. MATTHEWS, B. P. ANDERSON, P. C. HALJAN, D. S. HALL, C. E. WIEMAN and E. A. CORNELL, “Vortices in a Bose–Einstein Condensate”. *Phys. Rev. Lett.* **83** (13), 2498–2501 (Sep 1999).
- [40] V. SCHWEIKHARD, I. CODDINGTON, P. ENGELS, V.P. MOGENDORFF and E.A. CORNELL, “Rapidly rotating Bose-Einstein condensates in and near the lowest Landau level”. *Phys. Rev. Lett.* **92** (4), 040 404, 1–4 (2004).
- [41] N. R. COOPER, N. K. WILKIN and J. M. F. GUNN, “Quantum Phases of Vortices in Rotating Bose–Einstein Condensates”. *Phys. Rev. Lett.* **87** (12), 120 405 (Aug 2001).
- [42] R. LANDIG, L. HRUBY, N. DOGRA, M. LANDINI, R. MOTTL, T. DONNER and T. ESSLINGER, “Quantum phases from competing short- and long-range interactions in an optical lattice”. *Nature* **532**, 476 (Apr 2016).
- [43] J. LÉONARD, A. MORALES, P. ZUPANCIC, T. ESSLINGER and T. DONNER, “Supersolid formation in a quantum gas breaking a continuous translational symmetry”. *Nature* **543**, 87 (Mar 2017).
- [44] M. SCHELLEKENS, R. HOPPELER, A. PERRIN, J. VIANA GOMES, D. BOIRON, A. ASPECT and C. I. WESTBROOK, “Hanbury Brown Twiss Effect for Ultracold Quantum Gases”. *Science* **310** (5748), 648–651 (2005).
- [45] RAPHAEL LOPES, ALMAZBEK IMANALIEV, ALAIN ASPECT, MARC CHENEAU, DENIS BOIRON and CHRISTOPH I WESTBROOK, “Atomic Hong–Ou–Mandel experiment”. *Nature* **520**, 66–68 (2015).
- [46] R. ISLAM, R. MA, P. M. PREISS, M. ERIC TAI, A. LUKIN, M. RISPOLI and M. GREINER, “Measuring entanglement entropy in a quantum many-body system”. *Nature* **528**, 77 (Dec 2015).
- [47] H. KADAU, M. SCHMITT, M. WENZEL, C. WINK, T. MAIER, I. FERRIER-BARBUT and T. PFAU, “Observing the Rosensweig instability of a quantum ferrofluid”. *Nature* **530**, 194 (Feb 2016).

- [48] M. SCHMITT, M. WENZEL, F. BÖTTCHER, I. FERRIER-BARBUT and T. PFAU, “Self-bound droplets of a dilute magnetic quantum liquid”. *Nature* **539**, 259 (Nov 2016).
- [49] C. R. CABRERA, L. TANZI, J. SANZ, B. NAYLOR, P. THOMAS, P. CHEINEY and L. TARRUELL, “Quantum liquid droplets in a mixture of Bose-Einstein condensates”. *Science* **359** (6373), 301–304 (2018).
- [50] ALEXANDER MIL, TORSTEN V. ZACHE, APOORVA HEGDE, ANDY XIA, ROHIT P. BHATT, MARKUS K. OBERTHALER, PHILIPP HAUKE, JÜRGEN BERGES and FRED JENDRZEJEWSKI, “A scalable realization of local U(1) gauge invariance in cold atomic mixtures”. *Science* **367**, 1128–1130 (2020).
- [51] L. PRICOUPENKO, H. PERRIN and M. OLSHANII (editors), *Quantum Gases in Low Dimensions*, J. Phys. IV France (2004).
- [52] V. BEREZINSKII, “Destruction of long-range order in one-dimensional and 2-dimensional systems having a continuous symmetry group, 2 - quantum systems”. *Sov. Phys. JETP-USSR* **34**, 610 (1972).
- [53] J.M. KOSTERLITZ and D.J. THOULESS, “Ordering, metastability and phase transitions in two-dimensional systems”. *J. Phys. C : Solid State Phys.* **6**, 1181–1203 (1973).
- [54] T. KINOSHITA, T. R. WENGER and D. S. WEISS, “Observation of a one-dimensional Tonks-Girardeau gas”. *Science* **305**, 1125 (2004).
- [55] HEPENG YAO, DAVID CLÉMENT, ANNA MINGUZZI, PATRIZIA VIGNOLO and LAURENT SANCHEZ-PALENCIA, “Tan’s Contact for Trapped Lieb-Liniger Bosons at Finite Temperature”. *Phys. Rev. Lett.* **121**, 220 402 (Nov 2018).
- [56] Y. ABOU EL-NEAJ ET AL., “AEDGE: Atomic Experiment for Dark Matter and Gravity Exploration in Space”. *EPJ Quantum Technology* **7** (1), 6 (2020).
- [57] D. SCHLIPPERT, J. HARTWIG, H. ALBERS, L. L. RICHARDSON, C. SCHUBERT, A. ROURA, W. P. SCHLEICH, W. ERTMER and E. M. RASEL, “Quantum Test of the Universality of Free Fall”. *Phys. Rev. Lett.* **112**, 203 002 (May 2014).
- [58] J. WILLIAMS, S. CHIOW, N. YU and H. MÜLLER, “Quantum test of the equivalence principle and space-time aboard the International Space Station”. *New Journal of Physics* **18** (2), 025 018 (feb 2016).
- [59] H. MÜNTINGA, H. AHLERS, M. KRUTZIK, [...] and E. M. RASEL, “Interferometry with Bose-Einstein Condensates in Microgravity”. *Phys. Rev. Lett.* **110**, 093 602 (Feb 2013).
- [60] V. XU, M. JAFFE, C. D.PANDA, S. KRISTENSEN, L. W.CLARK and H. MÜLLER, “Probing gravity by holding atoms for 20 seconds”. *Science* **366**, 745–749 (2019).

- [61] KOSUKE SHIBATA, HIDEHIKO IKEDA, RYOTA SUZUKI and TAKUYA HIRANO, “Compensation of gravity on cold atoms by a linear optical potential”. *Phys. Rev. Research* **2**, 013 068 (Jan 2020).
- [62] A.E. LEANHARDT²⁰⁰³, T.A. PASQUINI, A. SABA, A. SCHIROTZEK, Y. SHIN, D. KIELPINSKI, D.E. PRITCHARD and W. KETTERLE, “Cooling Bose-Einstein Condensates Below 500 Picokelvin”. *Science* **301**, 1513–1515 (2003).
- [63] G. KLEINE BÜNING, J. WILL, W. ERTMER, C. KLEMPT and J. ARLT, “A slow gravity compensated atom laser”. *Applied Physics B* **100**, 117–123 (2010).
- [64] DENNIS BECKER, MAIKE D. LACHMANN, STEPHAN T. SEIDEL, [...] and ERNST M. RASEL, “Space-borne Bose–Einstein condensation for precision interferometry”. *Nature* **562**, 391–395 (2019).
- [65] E.R. ELLIOTT, M.C. KRUTZIK, J.R. WILLIAMS, R.J. THOMPSON and D.C. AVELINE, “NASA’s Cold Atom Lab (CAL): system development and ground test status”. *npj Microgravity* **4** (Aug 2019).
- [66] HUBERT AMMANN and NELSON CHRISTENSEN, “Delta Kick Cooling: A New Method for Cooling Atoms”. *Phys. Rev. Lett.* **78**, 2088–2091 (Mar 1997).
- [67] N. LUNDBLAD, R. A. CAROLLO, C. LANNERT, M. J. GOLD, X. JIANG, D. PASELTINER, N. SERGAY and D. C. AVELINE, “Shell potentials for microgravity Bose–Einstein condensates”. *npj Microgravity* **5**, 010 402 (Dec 2019).
- [68] L. PITAEVSKII and S. STRINGARI, *Bose-Einstein condensation*. Oxford University Press (2003).
- [69] F. DALFOVO, S. GIORGINI, L.P. PITAEVSKII and S. STRINGARI, “Theory of Bose-Einstein condensation in trapped gases”. *Rev. Mod. Phys.* **71** (3), 463–512 (1999).
- [70] C. PETHICK and H. SMITH, *Bose-Einstein condensation in dilute gases*. Cambridge University Press (2008).
- [71] S. STRINGARI, “Collective excitations of a trapped Bose-condensed gas”. *Phys. Rev. Lett.* **77** (12), 2360–2363 (1996).
- [72] J.T.M. WALRAVEN, *Quantum Gases* (2017). [Lecture notes, course given at the university of Amsterdam](#), note.
- [73] L.D. LANDAU, “The theory of syperfluidity of helium II”. *J.Phys. USSR* **5**, 71 (1941).
- [74] L. ONSAGER, “Statistical hydrodynamics”. *Il Nuovo Cimento Series 9* **6** (2), 279–287 (1949).

- [75] O. M. MARAGÒ, S. A. HOPKINS, J. ARLT, E. HODBY, G. HECHENBLAIKNER and C. J. FOOT, “Observation of the Scissors Mode and Evidence for Superfluidity of a Trapped Bose-Einstein Condensed Gas”. *Phys. Rev. Lett.* **84**, 2056–2059 (Mar 2000).
- [76] G. BISMUT, B. PASQUIOU, E. MARÉCHAL, P. PEDRI, L. VERNAC, O. GORCEIX and B. LABURTHE-TOLRA, “Collective Excitations of a Dipolar Bose-Einstein Condensate”. *Phys. Rev. Lett.* **105** (4), 040 404 (Jul 2010).
- [77] KARINA MERLOTI, ROMAIN DUBESSY, LAURENT LONGCHAMBON, MAXIM OLSHANII and HÉLÈNE PERRIN, “Breakdown of scale invariance in a quasi-two-dimensional Bose gas due to the presence of the third dimension”. *Phys. Rev. A* **88**, 061 603 (Dec 2013).
- [78] CAMILLA DE ROSSI, ROMAIN DUBESSY, KARINA MERLOTI, MATHIEU DE GOËR DE HERVE, THOMAS BADR, AURÉLIEN PERRIN, LAURENT LONGCHAMBON and HÉLÈNE PERRIN, “Probing superfluidity in a quasi two-dimensional Bose gas through its local dynamics”. *New Journal of Physics* **18** (6), 062 001 (2016).
- [79] S. STRINGARI, “Dynamics of Bose-Einstein condensed gases in highly deformed traps”. *Phys. Rev. A* **58**, 2385–2388 (Sep 1998).
- [80] ENRICO VOGT, MICHAEL FELD, BERND FRÖHLICH, DANIEL PERTOT, MARCO KOSCHORRECK and MICHAEL KÖHL, “Scale Invariance and Viscosity of a Two-Dimensional Fermi Gas”. *Phys. Rev. Lett.* **108**, 070 404 (Feb 2012).
- [81] FRANCESCA ZAMBELLI and SANDRO STRINGARI, “Quantized Vortices and Collective Oscillations of a Trapped Bose-Einstein Condensate”. *Phys. Rev. Lett.* **81**, 1754–1757 (Aug 1998).
- [82] F. CHEVY, K. W. MADISON and J. DALIBARD, “Measurement of the Angular Momentum of a Rotating Bose-Einstein Condensate”. *Phys. Rev. Lett.* **85**, 2223–2227 (Sep 2000).
- [83] O. ZOBAY and B.M. GARRAWAY, “Two-dimensional atom trapping in field-induced adiabatic potentials”. *Phys. Rev. Lett.* **86** (7), 1195–1198 (2001).
- [84] Y. COLOMBE, B. MERCIER, H. PERRIN and V. LORENT, “Loading a dressed Zeeman trap with cold atoms”. In *Proceedings of the Euroschool on quantum gases in low dimensions, Les Houches 2003*, volume 116, edited by L. PRICOUPENKO, H. PERRIN and M. OLSHANII 247, J. Phys. IV (2004).
- [85] Y. COLOMBE, E. KNYAZCHYAN, O. MORIZOT, B. MERCIER, V. LORENT and H. PERRIN, “Ultracold atoms confined in rf-induced two-dimensional trapping potentials”. *Europhys. Lett.* **67** (4), 593–599 (2004).

- [86] T. SCHUMM, S. HOFFERBERTH, L.M. ANDERSSON, S. WILDERMUTH, S. GROTH, I. BAR-JOSEPH, J. SCHMIEDMAYER and P. KRÜGER, “Matter wave interferometry in a double well on an atom chip”. *Nature Phys.* **1**, 57 (2005).
- [87] O. MORIZOT, Y. COLOMBE, V. LORENT, H. PERRIN and B.M. GARRAWAY, “Ring trap for ultracold atoms”. *Phys. Rev. A* **74**, 023 617 (2006).
- [88] W. H. HEATHCOTE, E. NUGENT, B. T. SHEARD and C. J. FOOT, “A ring trap for ultracold atoms in an RF-dressed state”. *New Journal of Physics* **10** (4), 043 012 (2008).
- [89] N. LUNDBLAD, P. J. LEE, I. B. SPIELMAN, B. L. BROWN, W. D. PHILLIPS and J. V. PORTO, “Atoms in a Radio-Frequency-Dressed Optical Lattice”. *Phys. Rev. Lett.* **100**, 150 401 (Apr 2008).
- [90] IGOR LESANOVSKY and WOLF VON KLITZING, “Time-Averaged Adiabatic Potentials: Versatile Matter-Wave Guides and Atom Traps”. *Phys. Rev. Lett.* **99** (8), 083 001 (Aug 2007).
- [91] B. E. SHERLOCK, M. GILDEMEISTER, E. OWEN, E. NUGENT and C. J. FOOT, “Time-averaged adiabatic ring potential for ultracold atoms”. *Phys. Rev. A* **83**, 043 408 (Apr 2011).
- [92] K. MERLOTI, R. DUBESSY, L. LONGCHAMBON, A. PERRIN, P.-E. POTTIE, V. LORENT and H. PERRIN, “A two-dimensional quantum gas in a magnetic trap”. *New Journal of Physics* **15** (3), 033 007 (2013).
- [93] R. DUBESSY, C. DE ROSSI, T. BADR, L. LONGCHAMBON and H. PERRIN, “Imaging the collective excitations of an ultracold gas using statistical correlations”. *New Journal of Physics* **16** (12), 122 001 (2014).
- [94] Y. GUO, R. DUBESSY, M. DE GOER DE HERVE, A. KUMAR, T. BADR, A. PERRIN, L. LONGCHAMBON and H. PERRIN, “Supersonic Rotation of a Superfluid: A Long-Lived Dynamical Ring”. *Phys. Rev. Lett.* **124**, 025 301 (Jan 2020).
- [95] HÉLÈNE PERRIN and BARRY M. GARRAWAY, “Chapter Four - Trapping Atoms With Radio Frequency Adiabatic Potentials”. *volume 66 of Advances In Atomic, Molecular, and Optical Physics* pages 181 – 262, Academic Press (2017).
- [96] A. MESSIAH, *Quantum Mechanics*. North Holland, John Wiley & Sons (1966).
- [97] C. COHEN-TANNOUDJI, *Atomes ultra-froids – Piégeage non dissipatif et refroidissement évaporatif*. *Cours de physique atomique et moléculaire, Collège de France, année 1996-1997*, note.
- [98] D.T. PEGG and G.W. SERIES, “Semi-classical theory of the Hanle effect with transverse static and oscillating magnetic fields”. *J. Phys. B: Atom. Mol. Phys.* **3**, L33 (1970).

- [99] D T PEGG, “Misalignment effects in magnetic resonance”. *Journal of Physics B: Atomic and Molecular Physics* **6** (2), 241 (1973).
- [100] M. DE GOËR DE HERVE, *Superfluid dynamics of annular Bose gas*. PhD thesis, University Paris 13 (2018).
- [101] THOMAS LIENNARD, *Construction d’un montage de condensation de Bose–Einstein de rubidium et étude théorique d’un superfluide en rotation dans un anneau*. PhD thesis, Université Paris-Nord - Paris XIII (2011).
- [102] KARINA MERLOTI, *Condensat de Bose–Einstein dans un piège habillé: modes collectifs d’un superfluide en dimension deux*. PhD thesis, Université Paris 13 (2013).
- [103] CAMILLA DE ROSSI, *Gaz de Bose en dimension deux : modes collectifs, superfluidité et piège annulaire*. PhD thesis, Université Paris 13 (2016).
- [104] DANIEL A. STECK, “Rubidium 87 D Line Data” (Sep 2001).
- [105] R. DUBESSY, K. MERLOTI, L. LONGCHAMBON, P.-E. POTTIE, T. LIENNARD, A. PERRIN, V. LORENT and H. PERRIN, “Rubidium-87 Bose-Einstein condensate in an optically plugged quadrupole trap”. *Phys. Rev. A* **85**, 013643 (Jan 2012).
- [106] E. MAJORANA, “Atomi orientati in campo magnetico variabile”. *Nuovo Cimento* **9**, 43–50 (1932).
- [107] C.L. GARRIDO ALZAR, H. PERRIN, B.M. GARRAWAY and V. LORENT, “Evaporative cooling in a radio-frequency trap”. *Phys. Rev. A* **74**, 053413 (2006).
- [108] L. CHOMAZ, L. CORMAN, T. YEFSAH, R. DESBUQUOIS and J. DALIBARD, “Absorption imaging of a quasi-two-dimensional gas: a multiple scattering analysis”. *New Journal of Physics* **14** (5), 055001 (2012).
- [109] G. REINAUDI, T. LAHAYE, Z. WANG and D. GUÉRY-ODELIN, “Strong saturation absorption imaging of dense clouds of ultracold atoms”. *Opt. Lett.* **32** (21), 3143–3145 (Nov 2007).
- [110] LAURIANE CHOMAZ, *Coherence and superfluidity of Bose gases in reduced dimensions: from harmonic traps to uniform fluids*. PhD thesis, Ecole Normale Supérieure (novembre 2014).
- [111] DAVID C. AVELINE, JASON R. WILLIAMS, ETHAN R. ELLIOTT, CHELSEA DUTENHOFFER, JAMES R. KELLOGG, JAMES M. KOHEL, NORMAN E. LAY, KAMAL OUDRHIRI, ROBERT F. SHOTWELL, NAN YU and ROBERT J. THOMPSON, “Observation of Bose–Einstein condensates in an Earth-orbiting research lab”. *Nature* **582**, 193–197 (2020).

- [112] KUEI SUN, KARMELA P ADAVIĆ, FRANCES YANG, SMITHA VISHVESHWARA and COURTNEY LANNERT, “Static and dynamic properties of shell-shaped condensates”. *Phys. Rev. A* **98**, 013 609 (Jul 2018).
- [113] A. TONONI, F. CINTI and L. SALASNICH, “Quantum Bubbles in Microgravity”. *Phys. Rev. Lett.* **125**, 010 402 (Jun 2020).
- [114] A. TONONI and L. SALASNICH, “Bose-Einstein Condensation on the Surface of a Sphere”. *Phys. Rev. Lett.* **123**, 160 403 (Oct 2019).
- [115] KARMELA P ADAVIĆ, KUEI SUN, COURTNEY LANNERT and SMITHA VISHVESHWARA, “Vortex-antivortex physics in shell-shaped Bose-Einstein condensates”. *Phys. Rev. A* **102**, 043 305 (Oct 2020).
- [116] S. HOFFERBERTH, B. FISCHER, T. SCHUMM, J. SCHMIEDMAYER and I. LESANOVSKY, “Ultracold atoms in radio-frequency dressed potentials beyond the rotating-wave approximation”. *Phys. Rev. A* **76**, 013 401 (Jul 2007).
- [117] S. GUPTA, K. W. MURCH, K. L. MOORE, T. P. PURDY and D. M. STAMPER-KURN, “Bose-Einstein Condensation in a Circular Waveguide”. *Phys. Rev. Lett.* **95**, 143 201 (2005).
- [118] A. S. ARNOLD, C. S. GARVIE and E. RIIS, “Large magnetic storage ring for Bose-Einstein condensates”. *Phys. Rev. A* **73**, 041 606 (2006).
- [119] P NAVEZ, S PANDEY, H MAS, K POULIOS, T FERNHOLZ and W VON KLITZING, “Matter-wave interferometers using TAAP rings”. *New Journal of Physics* **18** (7), 075 014 (2016).
- [120] S. ECKEL, A. KUMAR, T. JACOBSON, I. B. SPIELMAN and G. K. CAMPBELL, “A Rapidly Expanding Bose-Einstein Condensate: An Expanding Universe in the Lab”. *Phys. Rev. X* **8**, 021 021 (Apr 2018).
- [121] L. CORMAN, L. CHOMAZ, T. BIENAIMÉ, R. DESBUQUOIS, C. WEITENBERG, S. NASCIMBÈNE, J. DALIBARD and J. BEUGNON, “Quench-Induced Supercurrents in an Annular Bose Gas”. *Phys. Rev. Lett.* **113**, 135 302 (Sep 2014).
- [122] M. AIDELSBURGER, J. L. VILLE, R. SAINT-JALM, S. NASCIMBÈNE, J. DALIBARD and J. BEUGNON, “Relaxation Dynamics in the Merging of N Independent Condensates”. *Phys. Rev. Lett.* **119**, 190 403 (Nov 2017).
- [123] NOEL MURRAY, MICHAEL KRYGIER, MARK EDWARDS, K. C. WRIGHT, G. K. CAMPBELL and CHARLES W. CLARK, “Probing the circulation of ring-shaped Bose-Einstein condensates”. *Phys. Rev. A* **88**, 053 615 (Nov 2013).
- [124] F. JENDRZEJEWSKI, S. ECKEL, N. MURRAY, C. LANIER, M. EDWARDS, C. J. LOBB and G. K. CAMPBELL, “Resistive Flow in a Weakly Interacting Bose-Einstein Condensate”. *Phys. Rev. Lett.* **113**, 045 305 (Jul 2014).

- [125] K. C. WRIGHT, R. B. BLAKESTAD, C. J. LOBB, W. D. PHILLIPS and G. K. CAMPBELL, “Driving Phase Slips in a Superfluid Atom Circuit with a Rotating Weak Link”. *Phys. Rev. Lett.* **110**, 025 302 (Jan 2013).
- [126] A. RAMANATHAN, K. C. WRIGHT, S. R. MUNIZ, M. ZELAN, W. T. HILL, C. J. LOBB, K. HELMERSON, W. D. PHILLIPS and G. K. CAMPBELL, “Superflow in a Toroidal Bose-Einstein Condensate: An Atom Circuit with a Tunable Weak Link”. *Phys. Rev. Lett.* **106**, 130 401 (Mar 2011).
- [127] SCOTT BEATTIE, STUART MOULDER, RICHARD J. FLETCHER and ZORAN HADZIBABIC, “Persistent Currents in Spinor Condensates”. *Phys. Rev. Lett.* **110**, 025 301 (Jan 2013).
- [128] JEAN DALIBARD, *Cohérence et superfluidité dans les gaz atomiques. Course “Atomes et rayonnement ”*, Collège de France, year 2015-2016, note.
- [129] MARCO COMINOTTI, DAVIDE ROSSINI, MATTEO RIZZI, FRANK HEKKING and ANNA MINGUZZI, “Optimal Persistent Currents for Interacting Bosons on a Ring with a Gauge Field”. *Phys. Rev. Lett.* **113**, 025 301 (Jul 2014).
- [130] F. PIAZZA, L. A. COLLINS and A. SMERZI, “Vortex-induced phase-slip dissipation in a toroidal Bose-Einstein condensate flowing through a barrier”. *Phys. Rev. A* **80**, 021 601 (2009).
- [131] Y. CASTIN and R. DUM, “Bose-Einstein condensates in time dependent traps”. *Phys. Rev. Lett.* **77** (27), 5315–5319 (1996).
- [132] R. DUBESSY, T. LIENNARD, P. PEDRI and H. PERRIN, “Critical rotation of an annular superfluid Bose-Einstein condensate”. *Phys. Rev. A* **86**, 011 602 (Jul 2012).
- [133] K. W. MADISON, F. CHEVY, V. BRETIN and J. DALIBARD, “Stationary states of a rotating Bose-Einstein condensate: Routes to vortex nucleation”. *Phys. Rev. Lett.* **86**, 4443 (2001).
- [134] KENICHI KASAMATSU, MAKOTO TSUBOTA and MASAHITO UEDA, “Giant hole and circular superflow in a fast rotating Bose-Einstein condensate”. *Phys. Rev. A* **66**, 053 606 (Nov 2002).
- [135] G M KAVOULAKIS and GORDON BAYM, “Rapidly rotating Bose-Einstein condensates in anharmonic potentials”. *New Journal of Physics* **5** (1), 51 (2003).
- [136] ALEXANDER L. FETTER, B. JACKSON and S. STRINGARI, “Rapid rotation of a Bose-Einstein condensate in a harmonic plus quartic trap”. *Phys. Rev. A* **71**, 013 605 (Jan 2005).
- [137] V. BRETIN, S. STOCK, Y. SEURIN and J. DALIBARD, “Fast rotation of a Bose-Einstein condensate”. *Phys. Rev. Lett.* **92** (5), 050 403, 1–4 (2004).

- [138] TIN-LUN HO, “Bose-Einstein Condensates with Large Number of Vortices”. *Phys. Rev. Lett.* **87**, 060 403 (Jul 2001).
- [139] R. B. LAUGHLIN, “Nobel Lecture: Fractional quantization”. *Rev. Mod. Phys.* **71**, 863–874 (Jul 1999).
- [140] GORDON BAYM, “Vortex lattices in rapidly rotating Bose-Einstein condensates: Modes and correlation functions”. *Phys. Rev. A* **69**, 043 618 (Apr 2004).
- [141] N. R. COOPER, “Rapidly rotating atomic gases”. *Advances in Physics* **57** (6), 539–616 (2008).
- [142] JEAN DALIBARD, *Le magnétisme artificiel pour les gaz d’atomes froids*. Course “Atomes et rayonnement”, Collège de France, year 2013-2014, note.
- [143] A. L. FETTER, “Rotating trapped Bose-Einstein condensates”. *Laser Physics* **18**, 023 637 (Nov 2008).
- [144] C. RAMAN, J. R. ABO-SHAER, J. M. VOGELS, K. XU and W. KETTERLE, “Vortex Nucleation in a Stirred Bose-Einstein Condensate”. *Phys. Rev. Lett.* **87**, 210 402 (Nov 2001).
- [145] S. STRINGARI, “Phase Diagram of Quantized Vortices in a Trapped Bose-Einstein Condensed Gas”. *Phys. Rev. Lett.* **82**, 4371–4375 (May 1999).
- [146] M. COZZINI, A. L. FETTER, B. JACKSON and S. STRINGARI, “Oscillations of a Bose-Einstein Condensate Rotating in a Harmonic Plus Quartic Trap”. *Phys. Rev. Lett.* **94**, 100 402 (Mar 2005).
- [147] M. COZZINI, “Diffused vorticity approach to the oscillations of a rotating Bose-Einstein condensate confined in a harmonic plus quartic trap”. *Pramana* **66** (1), 31–42 (Jan 2006).
- [148] F. CHEVY, *Dynamique d’un condensat de Bose-Einstein*. PhD thesis, Université Pierre et Marie Curie – Paris VI (2001).
- [149] V. BRETIN, P. ROSENBUSCH, F. CHEVY, G. V. SHLYAPNIKOV and J. DALIBARD, “Quadrupole Oscillation of a Single-Vortex Bose-Einstein Condensate: Evidence for Kelvin Modes”. *Phys. Rev. Lett.* **90**, 100 403 (Mar 2003).
- [150] ALEXANDER L. FETTER, “Rotating vortex lattice in a Bose-Einstein condensate trapped in combined quadratic and quartic radial potentials”. *Phys. Rev. A* **64**, 063 608 (Nov 2001).
- [151] UWE R. FISCHER and GORDON BAYM, “Vortex States of Rapidly Rotating Dilute Bose-Einstein Condensates”. *Phys. Rev. Lett.* **90**, 140 402 (Apr 2003).

- [152] V. BEREZINSKII, “Destruction of long-range order in one-dimensional and 2-dimensional systems having a continuous symmetry group, 1 - classical systems”. *Sov. Phys. JETP-USSR* **32**, 493 (1971).
- [153] MARKUS HOLZMANN and WERNER KRAUTH, “Kosterlitz-Thouless Transition of the Quasi-Two-Dimensional Trapped Bose Gas”. *Phys. Rev. Lett.* **100**, 190 402 (May 2008).
- [154] MARKUS HOLZMANN, MAGUELONNE CHEVALLIER and WERNER KRAUTH, “Semiclassical theory of the quasi-two-dimensional trapped Bose gas”. *Eur. Phys. Lett.* **82**, 30 001 (2008).
- [155] P. C. HALJAN, B. P. ANDERSON, I. CODDINGTON and E. A. CORNELL, “Use of Surface-Wave Spectroscopy to Characterize Tilt Modes of a Vortex in a Bose-Einstein Condensate”. *Phys. Rev. Lett.* **86**, 2922–2925 (Apr 2001).
- [156] R. BÜCKER, A. PERRIN, S. MANZ, T. BETZ, CH. KOLLER, T. PLISSON, J. ROTTMANN, T. SCHUMM and J. SCHMIEDMAYER, “Single-particle-sensitive imaging of freely propagating ultracold atoms”. *New Journal of Physics* **11** (10), 103 039 (2009).
- [157] NICOLAS PAVLOFF, “Breakdown of superfluidity of an atom laser past an obstacle”. *Physical Review A* **66** (1), 013 610 (jul 2002).
- [158] A. PARIS-MANDOKI, J. SHEARRING, F. MANCARELLA, T. M. FROMHOLD, A. TROMBETTONI and P. KRÜGER, “Superfluid flow above the critical velocity”. *Scientific Reports* **7** (1), 9070 (dec 2017).
- [159] D. I. BRADLEY, S. N. FISHER, A. M. GUÉNAULT, R. P. HALEY, C. R. LAWSON, G. R. PICKETT, R. SCHANEN, M. SKYBA, V. TSEPELIN and D. E. ZMEEV, “Breaking the superfluid speed limit in a fermionic condensate”. *Nature Physics* **12** (11), 1017–1021 (nov 2016).
- [160] VIJAY PAL SINGH and LUDWING MATHEY, “Collective modes and superfluidity of a two-dimensional ultracold Bose gas” (2020). <https://arxiv.org/abs/2010.00013>.
- [161] AVINASH KUMAR, ROMAIN DUBESSY, THOMAS BADR, CAMILLA DE ROSSI, MATHIEU DE GOËR DE HERVE, LAURENT LONGCHAMBON and HÉLÈNE PERRIN, “Producing superfluid circulation states using phase imprinting”. *Phys. Rev. A* **97**, 043 615 (Apr 2018).

Résumé

Les gaz quantiques dégénérés constituent une plate-forme idéale pour étudier la superfluidité. Un superfluide annulaire a de nombreuses propriétés subtiles dues à sa géométrie topologique. Dans ce manuscrit, nous présentons trois superfluides annulaires, obtenus par trois mécanismes différents.

Le point de départ des expériences est un superfluide confiné au fond d'un piège en forme de bulle, produit par l'habillage des atomes dans un piège quadrupolaire avec des photons radiofréquence (rf). Ce piège adiabatique, présentant une excellente régularité, permet de réaliser ces trois superfluides annulaires.

Le premier est un anneau en lévitation, formé à la surface du piège bulle par compensation de la gravité. Nous étudions la structure prise par le nuage atomique, liée à l'effet fin de la polarisation rf et au fort couplage rf. Le second est un piège annulaire, formé à l'équateur de la bulle avec une double nappe lumineuse désaccordée vers le bleu. Nous avons placé le gaz annulaire en rotation par deux méthodes, ce produisant ainsi un courant superfluide permanent et une circulation quantifiée. Enfin, nous avons réalisé un anneau dynamique, qui se forme sous l'effet de la force centrifuge lorsque l'on place les atomes de la bulle en rotation rapide. Il s'agit d'un superfluide supersonique de longue durée de vie dont la vitesse linéaire peut atteindre Mach 18. Nous mettons également en évidence un mode collectif d'un tel superfluide en rotation rapide. La réalisation expérimentale de l'anneau dynamique est une étape importante vers le régime du vortex géant.

Mots-clefs : Condensats de Bose-Einstein, potentiels adiabatiques, microgravité, superfluide, vortex, rotations rapides, modes collectifs, vortex géant

Abstract

Degenerate quantum gases offer an ideal platform to study superfluidity. An annular superfluid has many subtle properties due to its topological geometry. In this manuscript, we present three ring-shaped superfluids, obtained with different formation mechanisms.

The starting point of the experiments is a superfluid confined at the bottom of a bubble-shaped trap, generated by dressing atoms in a quadrupole trap with radio-frequency (rf) photons. Taking advantage of the smoothness of such an adiabatic trap allows us to realize these three annular superfluids.

The first one is a levitating ring, formed on the surface of the bubble trap by compensating gravity. We study the structure taken by the atomic cloud related to fine effect of the rf polarization and the strong rf coupling. The second one is a ring trap, formed at the equator of the bubble with an additional blue detuned double light sheet. We set the annular gas into rotation by two methods, resulting in a persistent superfluid current and a quantized circulation. The last one is a fast-rotating dynamical ring, which forms under the effect of the centrifugal force. It is a long-lived supersonic superfluid whose linear velocity can reach Mach 18. We also evidence a collective mode of such a rapid rotating superfluid. The experimental realization of the dynamical ring is an important step towards the giant vortex regime.

Keywords: Bose-Einstein condensates, adiabatic potentials, microgravity, superfluidity, vortex, fast rotations, collective modes, giant vortex